

A Thesis Submitted for the Degree of PhD at the University of Warwick

Permanent WRAP URL:

<http://wrap.warwick.ac.uk/161246>

**Copyright and reuse:**

This thesis is made available online and is protected by original copyright.

Please scroll down to view the document itself.

Please refer to the repository record for this item for information to help you to cite it.

Our policy information is available from the repository home page.

For more information, please contact the WRAP Team at: [wrap@warwick.ac.uk](mailto:wrap@warwick.ac.uk)



---

# **Development of Techniques for Mapping Analytes and Properties at Interfaces**

by  
**James Teahan**

---

## **Thesis**

Submitted to the University of Warwick  
for the degree of  
**Doctor of Philosophy**

---

Supervisors: Dr. Nikola Chmel, Prof. Patrick R. Unwin, Prof. Melissa Hanna-Brown  
MAS Centre for Doctoral Training  
September 2019



*“All models are wrong, but some are useful.”*

George Box

# Contents

<b>List of Figures.....</b>	<b>vi</b>
<b>List of Tables.....</b>	<b>viii</b>
<b>Abbreviations.....</b>	<b>ix</b>
<b>Acknowledgements.....</b>	<b>xi</b>
<b>Declaration.....</b>	<b>xii</b>
<b>Abstract.....</b>	<b>xiv</b>
<b>1 Introduction .....</b>	<b>1</b>
1.1 Thesis Summary .....	1
1.2 Interfacial Properties and Processes .....	2
1.2.1 The Importance of Single Entity Measurements.....	2
1.2.2 The Role of the Electrical Double Layer .....	2
1.2.3 Models of the Double Layer .....	3
1.2.4 The Gouy-Chapman Model.....	5
1.2.5 Mass Transport.....	7
1.2.6 Electroosmotic Flow .....	8
1.2.7 Electrohydrodynamics.....	11
1.3 Processes at Active Surfaces .....	12
1.3.1 Reactions at Electrodes .....	12
1.3.2 Analytical Expressions for Charge Transfer .....	14
1.3.3 Ultramicroelectrodes .....	15
1.3.4 Bulk Investigations of Electrodes .....	17
1.3.5 Soft Interfaces .....	17
1.3.6 Electrohydrodynamics of Living Cells .....	19
1.4 Techniques for <i>in situ</i> Functional Mapping .....	20
1.4.1 Optical Microscopy .....	20
1.4.2 Electron Microscopy .....	22
1.4.3 Scanning Probe Microscopy .....	22

1.4.4	Multi-Microscopy Methods .....	26
1.5	Scanning Ion Conductance Microscopy.....	26
1.5.1	Technique Fundamentals .....	26
1.5.2	Feedback Types and Scanning Regimes .....	28
1.5.3	Quantifying the SICM Response with FEM .....	32
1.6	SICM Functional Mapping .....	36
1.6.1	Ion Flux Quantification .....	37
1.6.2	Charge Mapping.....	38
1.6.3	Functional Mapping of Complex Surfaces .....	39
1.7	References .....	40
<b>2</b>	<b>Surface Effects on Electroosmotic Flow-Delivery of Neutral Molecules using Scanning Ion Conductance Microscopy (SICM).....</b>	<b>53</b>
2.1	Abstract .....	54
2.2	Introduction .....	54
2.3	Materials and Methods.....	58
2.3.1	Solutions.....	58
2.3.2	Nanopipettes.....	58
2.3.3	Quasi-Reference Counter Electrodes .....	59
2.3.4	CF-UME Fabrication and Bulk HQ Voltammetry.....	59
2.3.5	Instrumentation .....	59
2.3.6	SICM Delivery and Sensing.....	60
2.3.7	FEM Simulations .....	61
2.4	Results and Discussion.....	64
2.4.1	Preliminary Experiments.....	64
2.4.2	Efficacy of Hold Potentials .....	64
2.4.3	Delivery with $V_{\text{efflux}}$ .....	73
2.5	Conclusions .....	83

2.6	References .....	84
<b>3</b>	<b>Scanning Ion Conductance Microscopy Potential Controlled Acid Delivery: A Tool to Assess Dental Corrosion .....</b>	<b>87</b>
3.1	Abstract .....	88
3.2	Introduction .....	88
3.3	Materials and Methods .....	92
3.3.1	Solutions .....	92
3.3.2	Substrates .....	92
3.3.3	Fluoride and citric acid treatments .....	93
3.3.4	Kapton tape control .....	93
3.3.5	Pellicle layer deposition .....	94
3.3.6	Statistical analysis .....	94
3.3.7	SICM methodology .....	94
3.4	Theory and Simulations .....	98
3.4.1	FEM Model .....	98
3.4.2	Simulation Methodology and Validation .....	102
3.5	Results and discussion .....	105
3.5.1	Parameter testing .....	105
3.5.2	Probe and sample variability .....	106
3.5.3	Taped enamel Vs sound enamel .....	107
3.5.4	Citric acid and fluoride treatments .....	107
3.5.5	Pellicle layer SICM enamel dissolution with topographical images. 117	
3.6	Conclusions .....	119
3.7	References .....	121
<b>4</b>	<b>Nanoscale analysis of live bacteria using Scanning Ion Conductance Microscopy: towards bioelectrical models of the bacterial cell envelope .....</b>	<b>125</b>
4.1	Abstract .....	126

4.2	Introduction .....	126
4.3	Methods.....	129
4.3.1	Chemicals.....	129
4.3.2	Nanopipettes fabrication and characterization .....	130
4.3.3	Instrumentation. ....	130
4.3.4	Bacterial Strains .....	131
4.3.5	Bacterial cultures.....	131
4.3.6	Bacterial Culturing in M9m .....	132
4.3.7	Bacterial Substrates.....	133
4.3.8	Electron microscopy of bacteria.....	135
4.3.9	Fluorescence microscopy .....	136
4.3.10	SICM Scanning Regime.....	137
4.3.11	Growth and viability of bacterial strains.....	138
4.4	FEM Simulations and Model Parameterisation .....	142
4.4.1	General Details and <i>E. coli</i> Model .....	142
4.4.2	<i>B. Subtilis</i> Model .....	144
4.5	Results and Discussion.....	149
4.5.1	Probing the gram-negative cell envelope: <i>E. coli</i> .....	149
4.5.2	Scanned-Potential Measurements of Gram-negative <i>E.coli</i> Cells ...	153
4.5.3	Probing the gram-positive cell envelope: <i>B. subtilis</i> .....	155
4.5.4	Potential scans across gram-positive <i>B. subtilis</i> cells .....	156
4.5.5	Further studies into the cell envelope-solution interface .....	159
4.5.6	FEM simulations of the gram-positive cell envelope .....	160
4.6	Conclusions .....	164
4.7	References.....	165
<b>5</b>	<b>Conclusions and Outlook.....</b>	<b>172</b>

# List of Figures

Figure 1.1 Schematic of the double layer at a conductive interface. ....	4
Figure 1.2 Schematic of the EOF and ion distribution in a negatively charged channel. .....	10
Figure 1.3 Schematic of the electron transfer processes according to electrode potential.....	13
Figure 1.4 Diffusion profile at a macro electrode and a UME.....	16
Figure 1.5 Schematic of a standard SICM experimental configuration and example topography.....	27
Figure 1.6 Main scanning procedures of SICM. ....	29
Figure 1.7 Diagram of SICM feedback regimes used herein.....	31
Figure 1.8 TEM of a typical nanopipette used in SICM experiments with the COMSOL simulation domain built from it.....	33
Figure 1.9 SICM functional mapping potential control regimes. ....	36
Figure 2.1 SICM delivery methodology. ....	55
Figure 2.2 Scanning transmission electron microscopy (STEM) image of a representative nanopipette.....	58
Figure 2.3 HQ voltammetry on a CF UME.....	61
Figure 2.4 Schematic (not to scale) of FEM simulation domain with the main boundaries labelled.....	62
Figure 2.5 Holding potential efficacy for delivery of HQ. ....	65
Figure 2.6 Simulated approach curves of a nanopipette at hold biases. ....	66
Figure 2.7 FEM simulations of hold biases. ....	67
Figure 2.8 FEM simulations of hold biases in bulk and at an inert surface.....	68
Figure 2.9 Simulated flow profiles at hold potentials. ....	70
Figure 2.10 Steady-state simulations of hold biases at approached distances. ....	72
Figure 2.11 Functional mapping of HQ oxidation on a 7 $\mu\text{m}$ CF-UME.....	73
Figure 2.12 Simultaneously obtained maps of SICM HQ delivery. ....	74
Figure 2.13 Analysis of substrate currents during HQ delivery when $V_{\text{efflux}} = 0.2 \text{ V}$ . 76	
Figure 2.14 Analysis of substrate currents during HQ delivery when $V_{\text{efflux}} = 0.4 \text{ V}$ . .....	77
Figure 2.15 FEM simulations of HQ delivery to a 7 $\mu\text{m}$ CF-UME 30 nm from the pipette orifice. ....	81



Figure 2.16 Phase portraits of flow during HQ delivery.....	82
Figure 3.1 Procedure for experimental surface treatments. ....	93
Figure 3.2 SICM procedure.....	97
Figure 3.3 Schematic and results from FEM simulations. ....	99
Figure 3.4 Scanning transmission electron microscopy (STEM) image of a representative nanopipette.....	100
Figure 3.5 AC amplitude at different rate constants. ....	104
Figure 3.6 FEM simulations of the relationship between the etching rate and $k_0$ ....	105
Figure 3.7 Etching depth vs. time for different delivery biases. ....	106
Figure 3.8 Summary figures of recorded etch depths. ....	108
Figure 3.9 Individual sample distributions for etch pit depth. ....	111
Figure 3.10 FEM simulation of the SICM proton delivery and surface tracking process on enamel with various surface treatments. ....	112
Figure 3.11 FEM simulations of species distributions.....	113
Figure 3.12 Volcano plot of all treatments for each enamel sample.....	115
Figure 3.13 SICM topography images of etch pit arrays on a) sound bovine enamel and b) with adhered pellicle layer. ....	118
Figure 4.1 Illustration of a simplified bacteria cell envelope.....	128
Figure 4.2 STEM images of a typical nanopipette used herein. Pore diameter approximately 180 nm.....	130
Figure 4.3 Details of the SICM scanning regimes. ....	137
Figure 4.4 Mean optical density growth curves. ....	139
Figure 4.5 Growth of bacterial strains in the presence of KCl.....	141
Figure 4.6 Schematic (not to scale) of FEM simulation domain. ....	143
Figure 4.7 Cryo-TEM of <i>B. subtilis</i> . ....	145
Figure 4.8 FEM simulations for functional mapping of <i>B. subtilis</i> . ....	148
Figure 4.9 SICM pulsed-potential scan of <i>E. coli</i> . ....	149
Figure 4.10 Scanning Electron Microscopy (SEM) image of <i>E. coli</i> (wild type) cell. .....	150
Figure 4.11 <i>E. coli</i> pulsed-potential scan and simulations.....	151
Figure 4.12 FEM simulation of pulse-potential SICM measurements at charged surfaces.....	153
Figure 4.13 Scanned-Potential SICM mapping of <i>E. coli</i> .....	155

Figure 4.14 SICM pulsed-potential mapping of <i>B. subtilis</i> . ....	156
Figure 4.15 Scanned-potential SICM maps of <i>B. subtilis</i> .....	157
Figure 4.16 SEM of <i>B. subtilis</i> ( $\Delta$ hag). ....	158
Figure 4.17 Scanning Electron Microscopy (SEM) image of <i>B. subtilis</i> ( $\Delta$ hag). ....	158
Figure 4.18 Confocal microscopy of <i>B. subtilis</i> ( $\Delta$ hag). Bacteria are stained with Alexa Fluor 594 (red) and SYBR Green (green) to show the location of EPS and bacteria, respectively. ....	159
Figure 4.19 Pulsed-potential SICM of a <i>B. subtilis</i> mutant with no EPS. ....	160
Figure 4.20 FEM simulations of the pulse-potential SICM at the gram-positive cell wall with charge concentration of 100 mM. ....	162

## List of Tables

Table 2.1 Simulated delivery currents under different conditions.....	80
Table 3.1 Table of species properties used in FEM. ....	102
Table 3.2 Summary table of etch pit depth and FEM calculated dissolution rates..	109
Table 3.3 Pairwise analysis of aggregated data. ....	110
Table 3.4 Pairwise analysis of treatments from individual samples. ....	116
Table 4.1 Full M9m media components. ....	132
Table 4.2 Quantities and concentrations for M9m minimal salts. ....	132
Table 4.3 Quantities and concentrations for 1000x Trace metal solution.....	133
Table 4.4 Quantities and concentrations for 5-vitamin solution.....	133
Table 4.5 Parameters measured from Cryo-TEM images.....	145

# Abbreviations

AC	Alternating Current
AFM	Atomic Force Microscopy
BM-SICM	Bias Modulated Scanning Ion Conductance Microscopy
BQ	Benzoquinone
CV	Cyclic Voltammogram
CF	Carbon Fiber
Cryo-TEM	Cryogenic Transmission Electron Microscopy
DC	Direct Current
DM-SICM	Distance Modulated Scanning Ion Conductance Microscopy
DNA	Deoxyribonucleic Acid
EFM	Electrostatic Force Microscopy
EOF	Electroosmotic Flow
EPS	Extracellular Polymeric substances
FEM	Finite Element Method
FPGA	Field Programmable Gate Array
HOMO	Highest Occupied Molecular Orbital
HQ	Hydroquinone
ICR	Ion Current Rectification
LUMO	Lowest Unoccupied Molecular Orbital
QRCE	Quasi-Reference Counter Electrode
SECCM	Scanning Electrochemical Cell Microscopy
SECM	Scanning Electrochemical Microscopy
SEM	Scanning Electron Microscopy
SEPM	Scanning Electrochemical Probe Microscopy
SERS	Surface Enhanced Raman Spectroscopy
SICM	Scanning Ion Conductance Microscopy
SPM	Scanning Probe Microscopy
SPR	Surface Plasmon Resonance
TEM	Transmission Electron Microscopy
UME	Ultramicroelectrode

# Acknowledgements

I would first like to thank all people involved in supervision of my project in the last 4 years for their support and advice. This includes (but is probably not limited to) Prof. Patrick Unwin for his encouragement and unwavering enthusiasm for research and Dr. Nikola Chmel for his patience and composure when coordinating so much. I'd also like to thank Prof. Melissa Hanna-Brown and Dr. Raymond Chen at Pfizer for support, advice and encouragement.

Also everyone in the MAS-CDT for the distractions, the trips, and general ridiculousness which has made the time at Warwick enjoyable. Especially Naomi Grew and Steven Brown for keeping us all on track no matter how much we try to wander off.

I would like to acknowledge everyone in the Warwick Electrochemistry and Interfaces Group and Biophysical Chemistry Group for developing and maintaining such a high standard of equipment and research, and for all the sacrifices individuals make to keep group resources going. Particularly Dr. David Perry without whom this work would not have been possible, everyone (Bryn Jones, Kelsey Cremin, Baoping Chen, Gabriel Meloni) who provided interesting problems and experiments to simulate, and Ian McPherson for following me down so many rabbit holes (and often digging me out). Thank you to Alexandra Borrill for spending so much time teaching me electrochemistry, for interesting discussions, and generally keeping me going. I would also like to thank everyone who created such an enjoyable atmosphere in an effort to keep everyone else sane; for Dangerous Wednesdays, Boulderling Fridays, and Squash Tuesdays.

Most of all, I would like to thank all of my friends and family for their support and understanding throughout my PhD and putting up with the chaos and disorganisation generated throughout.

# Declaration

This thesis is submitted to the University of Warwick in support of my application for the degree of Doctor of Philosophy. The work presented in this thesis is entirely my own work, except where acknowledged below. I confirm that this thesis has not been submitted as any previous application for a degree at another university. Parts of this thesis are being submitted for publication:

Substrate Effects on Delivery of Species with Electroosmotic Flow using Scanning Ion Conductance Microscopy (SICM)

**Teahan J.**, Perry D., Chen B., and Unwin P.R.,

SICM Biased Induced Acid Dissolution: A Tool to Assess Dental Corrosion

Jones B., **Teahan J.**, Perry D., and Unwin P.R.,

Experiments were performed by Bryn Jones with help in experimental design from the author and Dr. David Perry. Simulations and data analysis were performed by the author. This work also forms the basis for a chapter in the PhD thesis of Bryn Jones.

Nanoscale analysis of live bacteria using Scanning Ion Conductance Microscopy: towards bioelectrical models of the bacterial cell envelope

Cremin K., Jones B., **Teahan J.**, Meloni G.N., Zerfass C., Soyer O., Unwin P.R,

Experiments were performed by Kelsey Cremin and Bryn Jones with help in experimental design from the author. All FEM models were built by the author and simulations were performed by the author with assistance from Kelsey Cremin. This work also forms the basis for thesis chapters of Kelsey Cremin and Bryn Jones.

In addition to the above, I have contributed to the following publications that are not included in this thesis:

Multi-site rate control analysis identifies ribosomal scanning as the sole high-capacity/low-flux-control step in mRNA translation

Fireczuk, H.; **Teahan, J.**; Mendes, P.; McCarthy, J.

*FEBS Journal*, **2019**, doi:10.1111/febs.15059

3'-5' crosstalk contributes to transcriptional bursting

Cavallaro, M.; Walsh, M.D.; Jones, M.; **Teahan, J.**; Tiberid, S.; Finkenstädt, B.; Hebenstreit, D.

Submitted, doi:10.1101/514174

# Abstract

Scanning ion conductance microscopy (SICM) is a powerful and non-invasive tool which allows substrates to be probed at the nanoscale. Recently developed SICM functional mapping methodologies are capable of providing detailed information about interfacial properties and processes. Interaction of these techniques with complex active surfaces are not fully understood and much of the previous work in this area has been performed on ideal or model substrates. This thesis aims to extend the use of SICM functional mapping towards analysis of complex substrates and real-world samples.

Through application of potential control programs and extensive finite element method (FEM) simulation, the interactions between the SICM probe and substrate can be elucidated to explain the ion current response. SICM delivery methodologies are applied to examine the effects of substrate charge and activity upon electroosmotic flow (EOF) in the nanopipette. This allows better informed selection of delivery parameters for the quantitative delivery of neutral species with SICM. Real-time tracking of active dissolution at an enamel surface at the nanoscale is achieved through the controlled delivery of protons and the effects of surface treatments upon the effective heterogeneous rate constant are calculated through FEM. Multiple functional mapping methodologies are combined to probe the bioelectrical properties of live bacteria and FEM is used to further understanding of the structural and dynamic properties of the bacterial cell envelope. Through the combination of experiments with theoretical modelling of the interactions occurring in SICM systems, this work also contributes to understanding of the fundamental processes underpinning SICM measurements.



# 1 Introduction

## 1.1 Thesis Summary

The work herein is concerned with the advancement of scanning ion conductance microscopy (SICM) with the aim of furthering capabilities to probe complex interfaces *in situ*. SICM is coupled with finite element method simulations (FEM) to allow elucidation of a range of interfacial properties and processes. Building upon previous work, FEM methodologies are extended to more complex interfaces to allow a new range of systems to be probed.

SICM methodologies for the delivery of neutral species are refined and the effects of interfacial processes upon delivery are examined for the first time. FEM is used to demonstrate surface charge induced flow separation for the first time and the effects of this phenomena upon delivery of neutral species are quantified. This improves understanding of the parameters affecting quantitative delivery of species with SICM and phenomena underlying SICM as a whole.

Controlled proton delivery through SICM is used to examine surface dissolution kinetics using a surface tracking regime. Simulations are employed to quantify proton delivery and examine processes relating to surface dissolution. SICM delivery is demonstrated to be a powerful tool for quantifying surface kinetics due to the application of high mass transport conditions which induce a fully surface limited regime. This allows quantification of enamel dissolution kinetics with previously inaccessible resolution, providing information on the heterogeneity and structure of enamel substrates.

Sophisticated potential control methodologies in SICM are applied to live bacteria for the first time to probe the convoluted interactions between individual living bacteria and their local microenvironments. FEM simulations are used to analyse the surficial properties of gram-negative and gram-positive bacteria, advancing understanding of the complex interface of the cell envelope.

Overall, experimental and theoretical treatment of SICM experiments are extended to new and increasingly complex systems, providing a basis for further application of SICM across a range of fields.

## **1.2 Interfacial Properties and Processes**

### **1.2.1 The Importance of Single Entity Measurements**

The interaction of any material with its external environment is mediated by properties and processes at the interface between the two. Most biological and many chemically relevant interfaces are between that of an aqueous phase and a solid or semi-solid of varying complexity.<sup>1</sup> While many materials seem homogeneous at the microscale and above, on the nanoscale they can be extremely heterogeneous and instead comprise of an ensemble of individual sites and single entities across the material surface.<sup>2-4</sup> The characteristics of these interfaces are a sum of the ensemble of distinct responses of the individual entities which constitute the material as a whole.

The bulk or ensemble properties of an interface are easily accessible by an array of traditional assays and electrochemical techniques which interrogate an entire surface or population, and thereby the cumulative or average response of the ensemble.<sup>5</sup> Measurements made at the nanoscale can reveal the characteristics of individual sites and entities, deconvoluting the distinct processes and properties occurring at each site and providing far more information towards elucidation of the underlying mechanisms.<sup>6</sup> Single entity measurements have proven useful in the investigation of nanomaterial catalysts,<sup>4</sup> polycrystalline interfaces,<sup>7-9</sup> biological membranes,<sup>10-12</sup> and cellular populations.<sup>13-15</sup> Nanoscale functional mapping techniques such as SICM are therefore important in furthering understanding across a range of fields and this thesis is concerned with the application of this technique to increasingly complex real-world systems. For these techniques to provide meaningful information on such systems it is necessary to fully understand the characteristics of interfaces and the mechanisms through which they can be probed.

### **1.2.2 The Role of the Electrical Double Layer**

Any interface between a fluid and another phase causes the formation of an interfacial structure of solvent and ions, commonly known as the electrical double layer (Figure 1.1).<sup>1,5</sup> The double layer is a manifestation of the surface and solution properties and is fundamental to the thermodynamic, kinetic, and transport phenomena observed at an interface.<sup>16</sup> The interfacial properties of a system underpin all electrochemical measurements and give rise to more complex phenomena which dominate nanoscale techniques such as SICM.<sup>6</sup> As such, defining the characteristics and formation of the

double layer is foundational to the understanding of many important systems including colloidal dispersions,<sup>17</sup> biological interfaces,<sup>18</sup> capacitors,<sup>19</sup> and electrode reactions.<sup>20,21</sup>

Double layers arise from two dominant mechanisms; specific adsorption of species to the surface and compensation of surface charge by the accumulation of charged ions in solution. The charge of a surface is defined by the chemical moieties at the interface and the degree of dissociation of these groups in solution. These chemical moieties can be formed from polymers,<sup>22</sup> biological molecules,<sup>23,24</sup> or surface termination groups<sup>25</sup> and are a dominant factor in interfacial phenomena. Conductive materials such as metals and other common electrode materials can also possess a potential bias with respect to the solution, causing an interfacial electric field which also perturbs the ionic distribution. The potential difference between the electrode material and the interfacial species also defines the charge transfer processes which can occur. Specific interactions between the electrolyte and surface can also occur, changing the effective charge of the surface and double layer composition and even the internal charge distribution of the material.<sup>26</sup> For full understanding of the interface it is necessary to build mathematical descriptions of these underlying phenomena.

### **1.2.3 Models of the Double Layer**

There is a long history of investigation into the double layer and a number of analytical solutions for double layer composition based upon continuum models of varying complexity. The first descriptions of the double layer were formed by Helmholtz in 1879 to describe the capacitive behaviour of electrodes in electrolytes due to the charge separation between the electrode surface and the ions in solution.<sup>27</sup> This model generally describes the compensation of surface charge by the appropriate counterion and the accumulation of these ions at the interface. This concept was later used by Stern (1924),<sup>28</sup> who integrated it with Gouy-Chapman theory (1910)<sup>29,30</sup> which forms the basis of most successful continuum models of the double layer by introducing Maxwell-Boltzmann statistics.<sup>31</sup> It was assumed that the closest possible approach of ions to the surface would be limited by their hydration shell and a layer of water at the surface, known as the outer Helmholtz plane (Figure 1.1A). Grahame modified this theory to include ion-surface interactions in which ions can be partially desolvated, adsorbing to the surface to form the inner Helmholtz plane.<sup>32</sup>

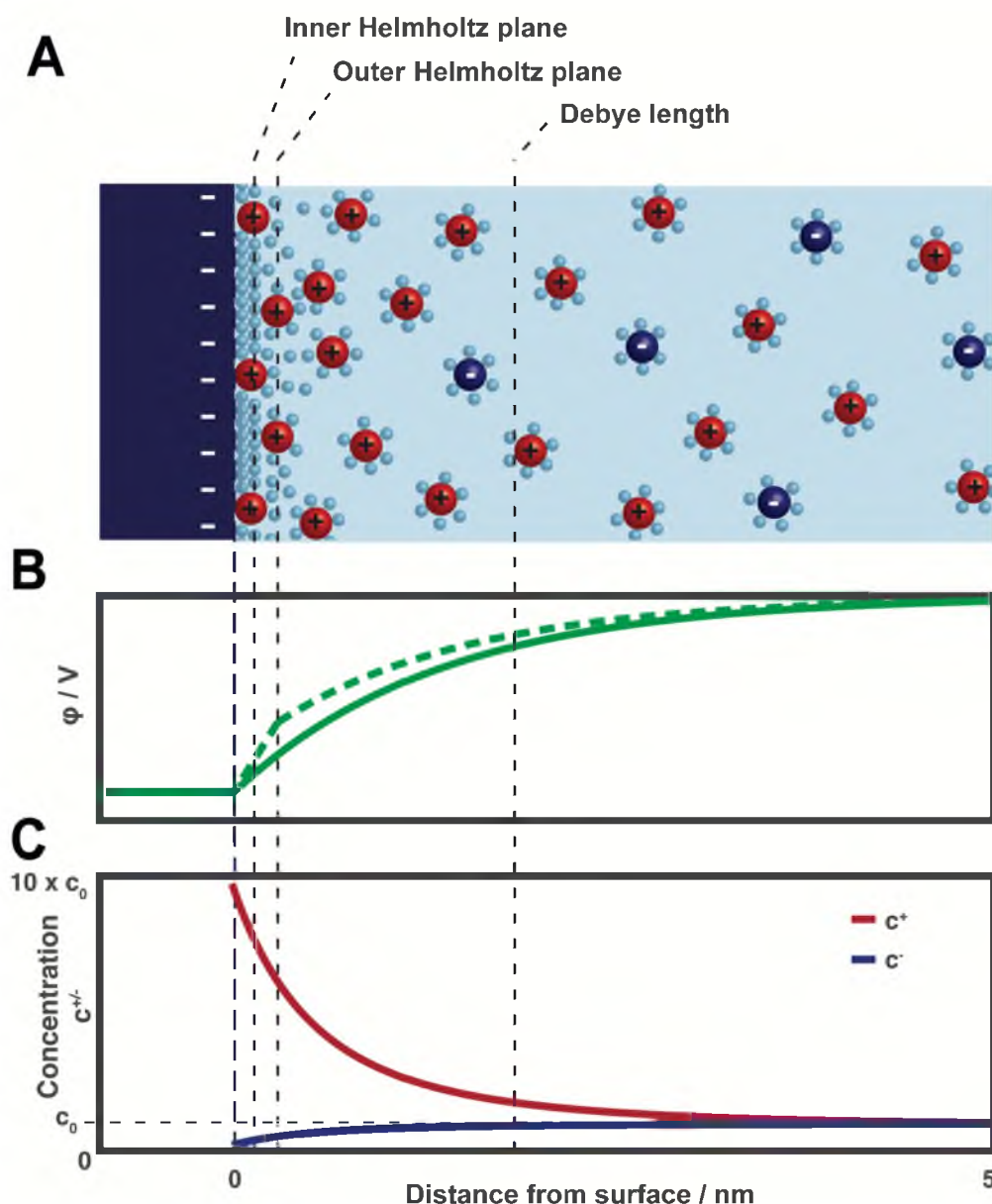


**Figure 1.1 Schematic of the double layer at a conductive interface.** The distribution of cations (red), anions (dark blue) and structured solvent (light blue spheres) at a negatively charged surface according to the Gouy-Chapman-Stern-Grahame model of the double layer. (B) The electric potential  $\phi$  described by the Poisson-Boltzmann distribution (Equation 1.2) causing an exponential decay of potential (green) and the model with the Stern layer considered causes a linear drop over this region (dashed). (C) The concentration profile of cations (red) and anions (blue) according to the Poisson-Boltzmann distribution (Equation 1.2), concentrations considering the Stern layer are not included as they depend on the specific surface interactions and are also therefore discontinuous.

### 1.2.4 The Gouy-Chapman Model

Gouy and Chapman introduced the implementation of Maxwell-Boltzmann statistics to account for the influence of thermal energy on the spatial distribution of each ion in proximity to the interface. Thus allowing calculation of the local charge density  $\rho$  (Equations 1.1a-c).

$$c^- = c_0 \cdot e^{\frac{ze\phi}{k_B T}} \quad (1.1a)$$

$$c^+ = c_0 \cdot e^{\frac{-ze\phi}{k_B T}} \quad (1.1b)$$

$$\rho = ze(c^+ - c^-) \quad (1.1c)$$

Where  $\phi$  is the electric potential defined as the work required to bring a charge from infinite distance to a given distance from the surface,  $c^-$  and  $c^+$  are the concentrations of anions and cations respectively, and  $c_0$  is the bulk concentration of the respective ion. The charge of each ion is defined as  $z$ , while  $e$  is the elementary charge,  $k_B$  is the Boltzman constant, and  $T$  is the absolute temperature. This defines the concentrations of ions in terms of the energy required to place them, which is provided by thermal equilibrium and the Coulomb forces acting according to the electric potential.<sup>33</sup> Gauss's law dictates the behaviour of the electric field  $\mathbf{E}$ , allowing description of the electrostatic potential in a medium with homogeneous dielectric permittivity by the Poisson equation (Equation 1.2).

$$-\nabla \cdot \mathbf{E} = \nabla^2 \phi = -\frac{\rho}{\varepsilon \varepsilon_0} \quad (1.2)$$

Where  $\nabla^2 \phi$  is the Laplacian of the electric potential ( $\nabla \cdot \nabla \phi$ ) which therefore defines the divergence of  $\mathbf{E}$ ,  $\varepsilon_0$  is vacuum dielectric permittivity, and  $\varepsilon$  is the relative permittivity of solution.

Combining Equations 1.1c and 1.2 yields the Poisson-Boltzmann distribution, as defined by Equation 1.3a, thus describing the spatial distribution of mobile charges normal to a surface. This must generally be solved numerically, however it can be accurately approximated at low potentials by the linearised Poisson-Boltzmann equation (Equation 1.3b) which can be formulated as  $\sinh(x) \approx x$  for small  $\phi$  through Taylor expansion. This allows solutions of the Poisson-Boltzmann equation to be solved analytically and leads to the formulation of the Debye parameter (Equation 1.3c).

$$\nabla^2 \phi = \frac{2ze\epsilon_0}{\epsilon\epsilon_0} \sinh\left(\frac{ze\phi}{k_B T}\right) \quad (1.3a)$$

$$\nabla^2 \phi = \frac{2ze\epsilon_0}{\epsilon\epsilon_0} \left(\frac{ze\phi}{k_B T}\right) = \kappa^2 \phi \quad (1.3b)$$

$$\kappa = \sqrt{\frac{2z^2 e \epsilon_0}{\epsilon\epsilon_0 k_B T}} \quad (1.3c)$$

The Debye length ( $\kappa^{-1}$ ) is a useful descriptor of the double layer structure and defines the distance from a surface at which the potential has decreased by a factor of  $e^{-1}$ . This is a convenient mathematical formulation which simplifies many calculations of the double layer properties and provides a simple descriptor of the effects of different solution parameters. For example, increasing bulk concentration or electrolyte valency compresses the double layer, with a proportionality of  $\sqrt{c_0}$  or  $z$ . However, as the definition of the Debye length is a constant fraction of the screening it does not change with surface charge. The link between these factors and the surface charge can be calculated through the Grahame equation (Equation 1.4) by taking the integral of the total mobile charge in the double layer which is screening the surface.<sup>32</sup>

$$\sigma = \sqrt{8c_0 \epsilon \epsilon_0 k_B N_a T} \sinh\left(\frac{ze\phi_0}{2k_B T}\right) \quad (1.4)$$

where all of the terms are the same as described previously, and  $N_a$  is Avogadro's constant.

The applicability of this model is limited by various assumptions contained within, principally that the thermal energy is much greater than that of the surface potential ( $k_B T \gg e\phi$ ), it is also bound by any assumptions of Maxwell-Boltzmann statistics. Concentrations must therefore remain low enough to prevent interactions between individual ions, there is not significant specific interaction with the surface, and each ion is affected only by the mean electric field of its neighbours. The concentrations and potentials proximal to the surface must also not become high enough to significantly alter the dielectric permittivity of the solution by excluding, confining, or disrupting the solvent. Nevertheless, Gouy-Chapman theory is generally applicable over a wide range of common systems, including many in physiological conditions, and adequately describes the double layer if experimental conditions are judiciously selected.<sup>34</sup>

It is possible to modify this theory to circumvent some of the limitations of the model with additional corrections or approximations surrounding features of a particular system. Corrections to the Gouy-Chapman model for varying dielectric

permittivity, concentration, and ion radius are being continually developed and applied.<sup>35–37</sup> Beyond the continuum models of the double layer, molecular modelling is providing increasingly valuable information, however computational limitations are still prohibitive towards accurate modelling of many systems.<sup>38,39</sup> Innovations in these techniques have allowed description of systems in which solvent and ion surface interactions are considered, providing fresh insights into the structure of the double layer at the molecular level.<sup>26,37,40,41</sup>

The Gouy-Chapman model of the double layer has been exploited to understand a wide range of systems and interfacial phenomena. It can be used to describe the potential and concentration distributions which form the basis of a huge number of modelling techniques from FEM simulations of interfaces to molecular dynamics.<sup>17,39,42,43</sup> Surface heterogeneities cause changes in the local structure of the double-layer, leading to changes in the local distribution of electrical potential and species.<sup>44,45</sup> This leads to gradients across the surface which drive transport phenomena, and also causes differences in the kinetics of interfacial processes through changes in the concentration and potential distributions or through specific interaction with chemical moieties at the surface. These local gradients in the electric field and species concentrations require a more generalised model to be formulated which describes reaction kinetics and mass transport in three dimensions.

### 1.2.5 Mass Transport

Mass transport is the movement of species in solutions according to diffusion, migration, and convection. The total flux of a species ( $J_i$ ) can be described by the Nernst-Planck equation in terms of these component fluxes (Equation 1.5):

$$J_i = -D_i \nabla c_i - z_i \frac{F}{RT} D_i c_i \nabla \phi + c_i u \quad (1.5a)$$

$$J_i = J_{i,d} + J_{i,m} + J_{i,u} \quad (1.5b)$$

where  $F$  is Faraday's constant and  $u$  is the solution velocity. For each species ( $i$ ),  $D_i$  is the diffusion coefficient,  $c_i$  is the concentration and  $z_i$  is the charge number. The first term ( $J_{i,d}$ ) describes the diffusive flux derived from Fick's law, encompassing mass transport due to concentration gradients and diffusion. Migration is governed by  $J_{i,m}$ , this describes flux due to the force exerted upon an ion by the electric field with respect to its mobility in the solution. In many electrochemical systems  $J_{i,d}$  is the dominant term as electrolyte concentrations are usually selected to be high enough to

prevent Ohmic drop due to solution resistance. This causes the potential gradient to be confined mainly to the electrode-solution interface as determined by double layer theory.

The Nernst-Planck equation is linked to Gouy-Chapman theory through the Einstein relation (Equation 1.6), which can be derived from the Boltzmann distribution and describes the diffusion coefficient of a species in terms of the ion mobility ( $\mu_i$ ),  $k_B$ ,  $T$ , and charge ( $q_i$ ).<sup>46,47</sup>

$$D_i = \frac{\mu_i k_B T}{q_i} \quad (1.6)$$

This means that the interfacial ion concentrations described by Boltzmann statistics in Gouy-Chapman theory can also be described by coupling the Poisson and Nernst-Planck equations. This is a common method for numerical analyses of systems in which transport and local concentrations are important, thereby allowing systems to be described in which fluxes occur, for example due to mixing of solutions in Chapter 2 or localised reactions as in Chapters 2 and 3.

The final term of the Nernst-Planck equation ( $J_{i,u}$ ) describes convective flux caused by the movement of the fluid itself. This flow velocity field can take many forms in electrochemical experiments including pressure driven flow,<sup>48</sup> density driven flow,<sup>49</sup> shear flow,<sup>50</sup> and electroosmotic flow (EOF).<sup>51</sup>

### 1.2.6 Electroosmotic Flow

In many permutations of the SICM set-up, EOF is a dominant transport mechanism and must also be incorporated into models of the system by coupling the movement of species to the fluid flow. The vector field for the flow of a system can be described by the Navier-Stokes equations, in the case of most experimental set-ups the incompressible Navier-Stokes equation (Equation 1.7) is the most appropriate. This requires that the liquid is Newtonian in nature, the Reynolds number is sufficiently low to minimise turbulence, and that the density of the fluid is constant, or at least that differences in density are negligible. These assumptions are reasonable in aqueous systems with no measurable temperature gradients, where density and viscosity are constant and viscous forces outweigh inertial forces. The incompressible Navier-Stokes equation is given by Equation 1.7a and is solved alongside the continuity equation which enforces conservation of mass (Equation 1.7b):



$$u \nabla u = \frac{1}{\rho} (-\nabla p + \mu \nabla^2 u + g) \quad (1.7a)$$

$$\nabla \cdot u = 0 \quad (1.7b)$$

where  $\rho$  is the density of the solution,  $\mu$  is the viscosity, and  $p$  is pressure. The first term of this equation gives the flow velocity due to pressure gradients, the second term accounts for the momentum spread due to viscosity and the surrounding flow velocities, while the final term defines volume forces which can drive flow. The final term ( $g$ ) is important in the coupling of the Navier-Stokes equations to the transport and electric field described above in order to drive EOF, the principle flow type in nanofluidic systems such as SICM.

EOF arises due to the flux of ions in solution exerting viscous forces upon the fluid in the direction of their movement, in many systems this force is not significant because this force is equalised by the migration of cations and anions in opposite directions.<sup>52</sup> However, the existence of a charged surface causes an accumulation of counterions as described by double layer theory and an exclusion of ions of the opposite charge. An extrinsic electric field tangential to the double layer is also required to induce migration of the ions in the diffuse part of double layer in the corresponding direction. This local imbalance of mobile charges within the double layer causes net flux in one direction, thereby driving flow, this force is described by Equation 1.8 in terms of the net charge ( $\sum_i z_i c_i$ ), electric field ( $\nabla \phi$ ) and Faraday's constant ( $F$ ).

$$g = -F(\sum_i z_i c_i) \nabla \phi \quad (1.8)$$

EOF is of relevance in SICM because at glass-aqueous interfaces, the silanol groups on the surface of the glass are partially or fully dissociated depending upon the solution pH (pK<sub>a</sub> 5-8), resulting in a net negative surface charge. There is therefore an imbalance of mobile charges within the double layer in favour of anions, meaning that in most SICM configurations, electroosmotic flow will generally be driven towards the cathode (Figure 1.2). There is also a significant electric field parallel to the pipette wall to drive flow, this is due to potential drop caused by the high resistance provided by the constriction of the nanopipette.

The flow profile within the double layer is more complex than described so far due to the complex transport properties within the double layer itself and the actual mobility of ions and solution within the double layer is poorly understood.<sup>53,54</sup> However, it is generally agreed that there is a critical distance from the surface at

which both ions and fluid become mobile, known as the slipping plane. This plane marks the start of the diffuse layer and it is usually assumed to be the limit of the Stern layer, within which motion is essentially prohibited due to the ordered structure of the solvent and the Coulombic interactions with the surface. In simulations this effect is usually enforced by imposing a no-slip boundary condition upon the flow velocity field. Flow is therefore driven by the motion of ions outside of the slipping plane, resulting in a plug flow profile within a channel. However, this is also dependent upon other geometric and electrostatic effects and can instead result in extremely complex flow phenomena. The effects of these phenomena are currently of interest in nano-scale systems, where due to the relatively large size of the double layer when compared to the channel radius, EOF can have large effects upon system behaviour.<sup>55–59</sup> The emergence of complex flow phenomena in SICM is therefore an area of active research and is examined in Chapter 2.

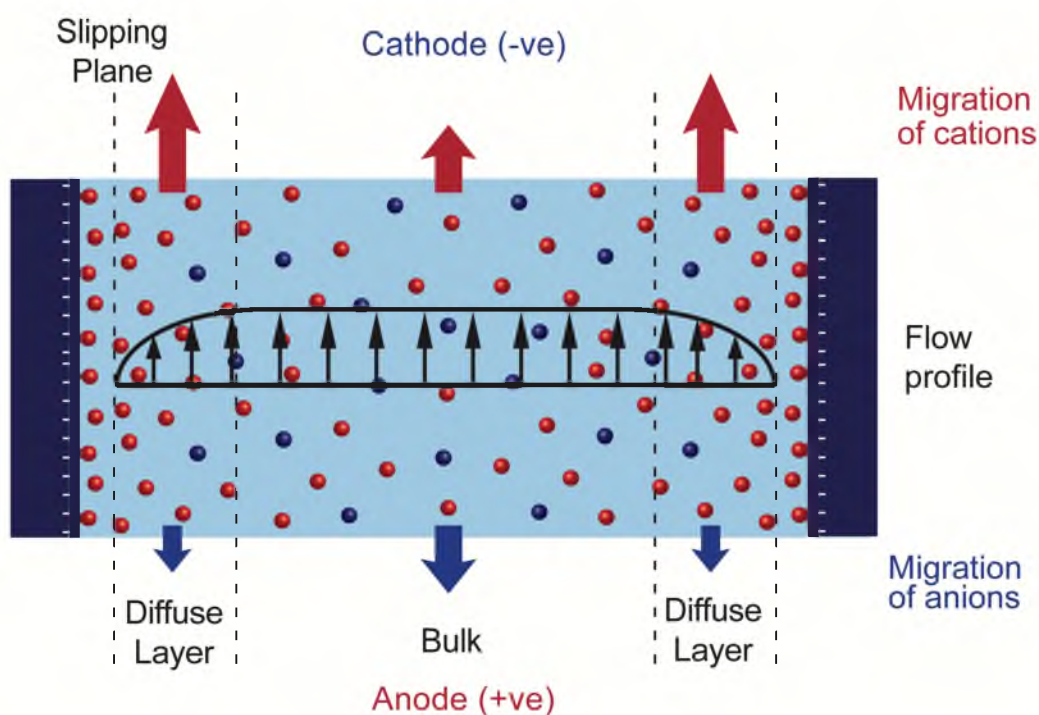


**Figure 1.2 Schematic of the EOF and ion distribution in a negatively charged channel.** The electrical double layer formed at the walls consists of a stagnant layer and diffuse layer, separated by the slipping plane. An electric field tangential to the double layer causes migration of mobile ions in the diffuse layer and bulk domains. The dominance of cation migration in the diffuse layer generates EOF through forces exerted upon the solvent by net ion movement. This typically generates a plug flow

profile due to the friction at the slipping plane reducing flow velocity at the edges, while the centre of the channel is relatively unimpeded.

### **1.2.7 Electrohydrodynamics**

The fully coupled system of the Poisson, Nernst-Planck, and Navier-Stokes equations provides a full description of the electrokinetic phenomena observed in many electrochemically and physiologically relevant systems. The caveats for applying this description to a system are that the charges and concentrations remain low enough to maintain the assumptions of a dilute system, and that there the temperature and viscosity remain constant. Numerical solutions to these equations can be used to describe and quantify the phenomena which arise in electrohydrodynamic systems such as in SICM.<sup>56,60</sup> A common method for this is FEM simulation which allows accurate representation of the geometry of a system while calculating numerical solutions to these equations across the represented space.<sup>34</sup> The details of method and its application in SICM is described in more detail in Section 1.5.3.

Description of experimental systems with this system of equations allows us to calculate the properties of the interface which give rise to the experimental response observed. In Chapters 2 and 3, this allows us to calculate the flux of a species which has been loaded into a nanopipette and delivered to a surface. This allows us to investigate the transport properties of the system and quantitatively manipulate the transport of the species in order to probe the reactions and processes occurring at the interface. This also allow subtle perturbations to be applied to the interfaces examined in Chapter 3, providing the opportunity to probe the structure and properties of the interface itself. The application of this methodology to complex real-world systems requires that the systems themselves are accurately described and incorporated into the model, therefore it is necessary to understand the mechanisms driving reactions at electrodes (Chapter 2) and complex biomaterials (Chapters 3 and 4). This allows us to elucidate the interplay between the transport mechanisms and surface processes at such interfaces and determine the array of responses arising from individual sites and entities at the nanoscale.

### 1.3 Processes at Active Surfaces

#### 1.3.1 Reactions at Electrodes

Electrodes are integral components of scanning electrochemical probe microscopies (SEPMs); in SICM they are used to drive ionic currents and in the case of scanning electrochemical microscopy (SECM) they are used for direct feedback from faradaic processes. Electrodes are also interesting substrates for SEPM and in the wider literature due to their broad applications including sensing,<sup>61,62</sup> industrial reactors,<sup>63,64</sup> energy storage,<sup>65</sup> and catalysis.<sup>66</sup> Electrode-solution interfaces exhibit the same mechanics explored previously but also have the additional capability for electron transfer between the electrode material and species in solution, and the ability to poise the electrode at a given potential with respect to a reference electrode in solution.<sup>26</sup> In order for electron transfer to occur between solution phase species and the electrode material, the species must be in close proximity to the interface. There must also be sufficient driving force between the species and surface, defined by a difference in electric potential. The observed currents are therefore dependent upon the mass transfer to the electrode and the principles governing the rate of charge transfer at the interface.<sup>67</sup>

Figure 1.3 demonstrates relationship between the electrode and molecular potentials which govern these reactions. The electrons within a fully conductive electrode possess a continuum of energy states up to the Fermi level which can be raised or lowered in order to induce reduction or oxidation of the interfacial molecule. Reduction of a species will occur if the potential energy of the electrons within the material is great enough to occupy the lowest unoccupied molecular orbital (LUMO) of the molecule. Alternatively, oxidation will occur if the energy level within the electrode material is lower than that of the highest occupied molecular orbital (HOMO).

In the case of outer-sphere reactions the molecule does not have a strong interaction with the electrode surface but must be within distances where quantum tunnelling is possible.<sup>68</sup> This distance is typically less than 10 Å, however it is highly dependent upon the interfacial potential and the structure of the double layer.<sup>69</sup> Outer-sphere reactions include many metal complexes, also encompassing many proteins, and the kinetics for such reactions can be defined by Marcus theory (1956).<sup>70</sup> This theory accounts for the difference in time scales between electron transfer and nuclear

motion; the reorganisation of nuclear coordinates cannot happen on the timescale of electron transfer. The probability of electron transfer is therefore far greater when the nuclear coordinates of the reactant are in a position which they have in common with the product, this is known as the Franck-Condon principle.<sup>71</sup>

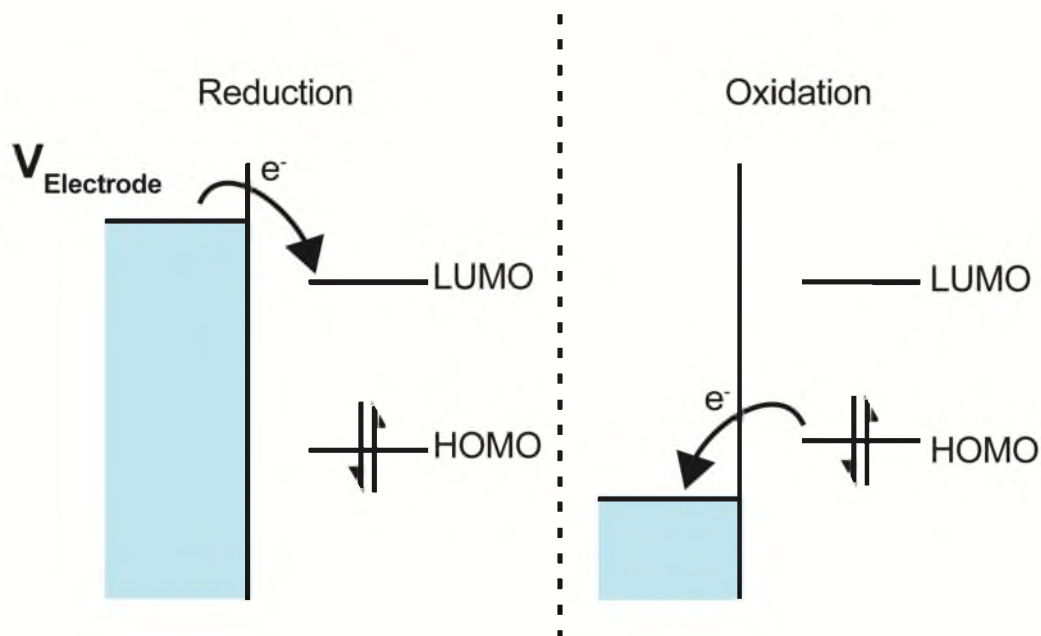


**Figure 1.3 Schematic of the electron transfer processes according to electrode potential.** Electrodes have a continuous band of electron energies which can be raised or lowered, known as the Fermi level. Raising the potential within the electrode sufficiently will drive electrons from the electrode into the LUMO of a solution phase species, reducing the molecule. Similarly, lowering the potential below that of the HOMO will cause oxidation of the solution phase species by driving electrons into the electrode. Note electrons need not be fully paired as displayed above.

These restrictions also apply to inner-sphere reactions which are defined by strong interactions with the surface through which charge transfer can occur, though these also have a dependency upon the factors controlling these interactions.<sup>72</sup> After electron transfer, the molecule is often in an intermediate state which must undergo further reactions to reach the thermodynamically favourable product. These reactions can be multi-step in both the electron transfer and chemical reactions which take place and are often dependent upon the local solution conditions to provide other species such as protons to react with. The properties of the interface can therefore have strong

effects upon the rate of charge transfer reactions by defining the transport to the surface, local surface concentrations of reactants, and local potential distribution.

### 1.3.2 Analytical Expressions for Charge Transfer

In cases where electron transfer is the rate limiting step, the kinetics are controlled by the interfacial potential and can be described empirically by the Butler-Volmer equation. To understand Butler-Volmer kinetics, we must first consider the potential of an electrode at equilibrium. A general charge transfer reaction can be described by:



Where  $O$  is the oxidised form of a species,  $R$  is the reduced form,  $e^-$  is an electron and the  $n$  is the number of electrons transferred in the reaction. The electrochemical potential ( $E$ ) of a reaction is defined by the Nernst equation (Equation 1.10) which describes the driving force of the reaction relative to the energy under standard conditions. This can be derived from the thermodynamic potential and the Gibbs free energy through the relationship between the two (1.9):

$$\Delta G = \Delta G^0 + RT \ln Q \quad (1.9a)$$

$$\Delta G = -nFE \quad (1.9b)$$

$$Q = \frac{[R]}{[O]} \quad (1.9c)$$

$$E = E_0 - \frac{RT}{nF} \ln \frac{R}{O} \quad (1.10)$$

where  $\Delta G$  is the Gibbs free energy,  $\Delta G^0$  is the Gibbs free energy under standard conditions,  $Q$  is the reaction quotient,  $E$  is the electrochemical potential,  $E_0$  is the electrochemical potential under standard conditions. This derivation is fundamental to electrochemistry as it links measurements with absolute thermodynamic parameters of the system. The definition of the concentration dependence of electrode potential is important in SICM where quasi-counter-reference electrodes (QRCEs) are used to apply potentials in the system (Section 1.5). The Nernst equation determines the equilibrium properties of the system, where there is no net current at the electrode, however where currents are being driven the system must be described kinetically.

The overall rate expression at an electrode can be written in terms of the net current ( $i_{net}$ ) which is the sum of the currents generated by the overall rate of the forwards  $k_f$  and backwards reactions  $k_r$  at an electrode of area  $A$ :

$$i_{net} = i_f + i_r = -FAk_f[O] + FAk_r[R] \quad (1.11)$$

where the reaction is a simple first order reaction, the rates can be assumed to take an Arrhenius form in which the difference in Gibbs free energy is defined by the overpotential ( $\eta$ ). This demonstrates an exponential dependence of each rate upon overpotential:

$$\eta = E_{electrode} - E_{eq} \quad (1.12a)$$

$$k_f = k^0 e^{-\alpha \frac{nF\eta}{RT}} \quad (1.12b)$$

$$k_r = k^0 e^{(1-\alpha) \frac{nF\eta}{RT}} \quad (1.12c)$$

where  $k^0$  is the standard rate constant and  $\alpha$  is the charge transfer coefficient, a measure of the energy difference between products and reactants generally assumed to be 0.5. Through substitution into Equation 1.11, the full Butler-Volmer relationship defining the current density can be derived:

$$i_{net} = nAFk^0 \cdot \left( [R]e^{\frac{(1-\alpha)nF\eta}{RT}} - [O]e^{-\frac{\alpha nF\eta}{RT}} \right) \quad (1.13)$$

These relationships are used in bulk measurements of electrochemical systems to relate experimental currents to the surface kinetics and transport properties of the system. They can also be used to derive further relationships between the system properties and the current response for more complex systems such as the Levich equation for rotating-disk electrodes,<sup>50</sup> steady state currents for ultramicroelectrode (UME) geometries,<sup>73</sup> or linked to electrohydrodynamic descriptions of the system. This is important in Chapter 2, where Butler-Volmer kinetics are used to describe the localised current at a UME during controlled delivery by SICM.

### 1.3.3 Ultramicroelectrodes

UMEs are electrodes which possess a critical dimension smaller than that of the diffusion layer generated at steady state, generally agreed to be less than  $25 \mu\text{m}$ .<sup>5</sup> There are a range of geometries used for UMEs but the most common are disk electrodes which have been produced at nanometer sizes. The advantages of using a UME are the lower non-faradaic currents, decreased susceptibility to Ohmic drop, and high mass transport. This is due to smaller electrode area, lower currents, and changing the diffusion profile from the mostly planar diffusion of a macro-electrode to the radial or hemispherical diffusion of a UME (Figure 1.4).<sup>74</sup>

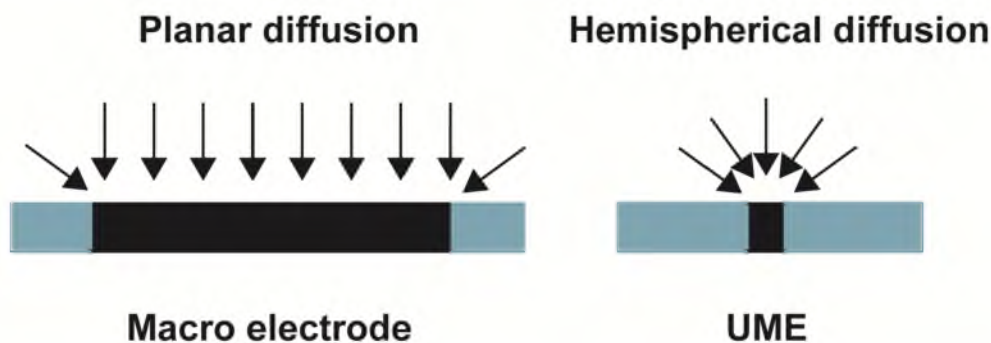


**Figure 1.4 Diffusion profile at a macro electrode and a UME.**

As discussed above, the current response of an electrode is described by the Butler-Volmer equation (Equation 1.15), with increasing overpotential a limiting case can be reached where the electron transfer reaction is faster than the mass transport to the surface.<sup>75</sup> The system then reaches a steady state with a constant limiting current ( $i_{lim}$ ) and the reaction is considered transport limited, as opposed to one limited by surface kinetics.<sup>73</sup> In the case of a macro-electrode with mostly planar diffusion, the Butler-Volmer equation reduces to a form which is dependent upon the size of the diffusion layer ( $\delta$ ):<sup>76</sup>

$$i_{lim} = \frac{nAFDc_0}{\delta} \quad (1.14)$$

At a UME,  $i_{lim}$  can be described by geometry dependent analytical expressions in terms of the bulk concentration ( $c_0$ ), the diffusion coefficient of the species ( $D$ ), the number of electrons transferred ( $n$ ), and Faraday's constant ( $F$ ).<sup>73</sup> For a planar disc electrode this uses the radius of the electroactive area ( $r_{UME}$ ) and is defined as:<sup>77</sup>

$$i_{lim} = 4nFDc_0r_{UME} \quad (1.15)$$

The fast transport to UMEs and low background charging currents mean that they are useful for accessing information about fast kinetic reactions which are inaccessible to larger electrodes that reach steady state at much larger overpotentials.<sup>73</sup> UMEs are therefore used where fast, sensitive and robust responses are required, such as SECM, with a broad range of applications,<sup>78</sup> and are often used the investigation of cellular signalling and metabolism.<sup>79,80</sup> Thus, UME behaviour is an important field of investigation as the accurate determination of the response of a UME underpins many measurements (see Section 1.5.1), this is investigated in Chapter 2.<sup>81</sup>



### 1.3.4 Bulk Investigations of Electrodes

The interfacial processes and double layer structure have been shown to be important to electrode activity, especially as electrodes approach the nanoscale.<sup>82,83</sup> Many electrodes are heterogeneous surfaces due to the presence of different crystal faces, grain boundaries, nanostructures, or surface terminations. Seemingly homogeneous electrode surfaces can also have heterogeneities due to defects, edge effects, or heterogeneities at smaller scales.<sup>6,66</sup> Differences between these sites with regard to surface termination and conductivity of the electrode material contribute to the overall response of an electrode by affecting the local double layer structure and available chemical groups.<sup>25,84,85</sup> This causes differences in the capacitive and faradaic responses which must be considered when using electrodes that can have nanoscale heterogeneities, particularly when looking at localised events such as nanoparticle impacts or vesicle measurements.<sup>86–89</sup> Understanding the effects of these factors upon double layer structure and surface kinetics is key to designing more accurate electrochemical sensors, and more efficient materials for batteries and catalysts.<sup>90,91</sup>

Bulk electrochemical experiments take the form of amperometric or potentiometric measurements in which the total current or average potential over an electrode is measured. The kinetics at individual sites contribute to the ensemble response of measurements such as cyclic voltammetry (CV) in which the potential dependence of electrochemical processes are observed.<sup>92</sup> Different sites will have a different current-potential ( $i$ - $V$ ) dependence and the overall peak observed in a CV will be a sum of the peaks at different sites, thereby obscuring the underlying processes. Bulk measurements have been made for the ensemble response of electrodes such as the carbon fibre UMEs investigated in Chapter 2,<sup>25</sup> and for measurements of crystal dissolution kinetics such as dental enamel used in Chapter 3.<sup>93,94</sup>

### 1.3.5 Soft Interfaces

Surfaces which are permeable to ions and solvent present a particularly complex challenge for determining the properties of the interface. The structure and response of the interface in this case is dependent upon potentials, ion transport, charge distribution, and flow within the material.<sup>95</sup> Materials which display behaviour of this kind include many biological materials and the polyelectrolyte gels upon which cells

and microbes are cultured (as considered in Chapter 4).<sup>96,97</sup> These considerations are also necessary at other porous materials such as the polymeric matrices of pharmaceutical formulations, or porous membranes.<sup>98,99</sup> There are a number of methodologies used to approximate the response of such materials.<sup>100</sup>

The fixed charges of a permeable polyelectrolyte layer contribute to the charge density ( $\rho$ ) contained within the Poisson equation (Equation 1.3a), which can therefore be used to describe the potentials which arise in these systems. The bulk material potential can be described with respect to the potential in bulk solution by the Donnan potential.<sup>101</sup> This arises as a sum of the Nernst potentials for each charged species due to the ratio of the concentration within the material compared to that in bulk solution.

However, when ionic currents are being driven within the material the transport properties within the material must also be considered in order to calculate the resulting ionic fluxes. The properties which affect transport are generally caused by the tortuosity of the path between two points giving the effective diffusion coefficient within a material due to the increased distance travelled.<sup>102</sup> However, charged nanoscale channels can introduce added complications as the double layer is highly overlapping and the diameter of a hydrated ion is approximately 10% of the channel diameter in the systems considered herein.<sup>103,104</sup> These effects cause increased anion exclusion and surface conductivity as the double layers of each side of the channel overlap significantly.<sup>95</sup> This is therefore dependent upon the charge of the channel walls and the same factors which contribute to the Debye parameter (Equation 1.3c), effects similar to this are discussed in section 1.5.3.2.

Flow within a porous material is also altered for similar reasons to diffusive flux, with an additional increase in internal fluid stresses due to the confinement within channels. Therefore there is a decreased flow velocity, this is described by the Brinkman form of Darcy's law, which modifies the Navier-Stokes equations with the material properties of permeability to correct for the accessible volume and the effects of confinement upon internal stress:

$$u \nabla u = \frac{1}{\rho} \left( -\nabla p + \frac{\mu}{K} \nabla^2 u - F(\sum_i z_i c_i) \nabla \phi \right) \quad (1.16)$$

where  $K$  is the material permeability to flow.

### 1.3.6 Electrohydrodynamics of Living Cells

The interface at living cells is comprised of a complex soft interface with additional fluxes of charged and neutral species caused by the metabolic and homeostatic processes occurring within the cell.<sup>105–107</sup> A cell interface is comprised of an insulating lipid bilayer with limited permeability to ions provided by protein channels, flux of these ions is carefully controlled for internal osmoregulation of the cell. These protein channels can be affected by pressure and voltage changes, even causing depolarisation of the cell membrane potential and large fluxes of ions across the membrane.<sup>108</sup> Prokaryotes also generate a proton gradient across the cell membrane which is used for generation of ATP. The flux of metabolites in either direction is also carefully controlled and can generate a total ionic flux in either direction.<sup>109</sup> The membrane will also have other proteins and carbohydrates associated with it, generating permeable charged polyelectrolyte layers which are described above. Due to the range of factors affecting the structure and fluxes at cellular interface living cells form especially challenging substrates to interrogate.

Analysis of the electrohydrodynamics across entire cells and averaged over populations has been performed, however cells display a high degree of heterogeneity across individual cell membranes and throughout cellular populations.<sup>110,111</sup> The main way in which this is performed is by applying an alternating voltage across a population of cells in suspension and using dynamic light scattering to monitor the resulting motion.<sup>112</sup> This information can be used with various approximations to calculate the charge and flow properties of the soft interface at cell surfaces. The potential, resistance, and capacitance of the cell membrane can also be measured through patch-clamp techniques, however this requires a seal to be formed at a small portion of the cell membrane and doesn't allow measurement of the highly permeable portions of the cell envelope external to the membrane.<sup>113,114</sup> The concentration and fluxes of metabolites can also be measured through electrochemical means using UMEs.<sup>80</sup> Microiontophoretic techniques are also important for investigation of cellular responses to chemical stimuli and can be used to measure the response of cells to controlled delivery of drugs or other species.<sup>115</sup> These have been used to extensively investigate cellular signalling among other processes, and this delivery methodology has been well characterised experimentally and through simulation.<sup>116–119</sup>

Bacterial cells are particularly interesting due to their diversity and the complexity of their external interface.<sup>106</sup> This is due to the intricate integration of their metabolism with their cell envelope and their capacity to modify their external environment through secreted substances.<sup>120,121</sup> These factors are important for the design of antimicrobial interfaces,<sup>122,123</sup> investigation of bacterial communities,<sup>124</sup> and antibiotic resistance.<sup>125,126</sup> Chapter 4 exploits the difference between gram-positive and gram-negative cell envelopes to ascertain the effects of the above properties on the SICM response and use SICM functional mapping to begin building models of the bacterial cell envelope.

## 1.4 Techniques for *in situ* Functional Mapping

Investigating the characteristics and activity of a surface requires techniques which are extremely sensitive to variation in the properties of the interface. Across a wide range of fields it is becoming increasingly appreciated that to comprehensively understand bulk or population characteristics, the function of constituent sites and individual entities must be considered.<sup>2,3</sup> The value of single entity functional imaging has been demonstrated in catalysis,<sup>66,127</sup> corrosion,<sup>128</sup> crystallization,<sup>8</sup> and across various aspects of biology,<sup>79,87,129</sup> where various microscopies lend themselves to this aim<sup>130</sup> and are generally split into three categories; optical microscopy, electron microscopy, and scanning probe microscopy (SPM), each containing an abundance of techniques with individual advantages and disadvantages.

### 1.4.1 Optical Microscopy

Optical microscopes were the first to be developed in the early 1600's using visible light and now extend to include fluorescent microscopy,<sup>131</sup> spectroscopies,<sup>132</sup> and X-ray microscopy.<sup>133</sup> The resolution of optical microscopy is defined the Abbe diffraction limit (Equation 1.17):

$$r = \frac{\lambda}{2NA} \quad (1.17)$$

Where  $r$  is the minimum resolvable distance between two points, and  $NA$  is the numerical aperture usually with a value of 1.4, giving a best possible lateral resolution on the order of a few hundred nanometres depending upon the wavelength used.<sup>134,135</sup> This allows visualisation at length scales which are useful for many applications in which processes can be directly observed but is otherwise information poor. One

method of circumventing the diffraction limit is using high frequency light such as UV or X-rays, with tens of nanometres resolution demonstrated.<sup>133</sup> However, damage to the sample due to the high energies of incident radiation is generally a concern.

Combining microscopy and spectroscopy, by measuring the spectrum of scattered or transmitted light, allows far more information to be gathered about the properties of a surface.<sup>132</sup> A common example of this is Raman microscopy which uses the Raman shift from laser light inelastically scattered by the sample to report upon the vibration states of the irradiated molecules.<sup>132,136</sup> This allows highly specific characterisation of a surface while providing high information density however it is inherently insensitive and complex mixtures can prove difficult to analyse. Surface enhanced Raman spectroscopy (SERS) is one method to overcome this barrier, enhancing the Raman signal by interaction with induced plasmons on nanostructured metals to provide selectivity and sensitivity capable of single molecule detection.<sup>137</sup> A related technique is surface plasmon resonance (SPR), which has been used for mapping of structural changes in cells and surface binding phenomena.<sup>138–140</sup> However, these techniques are only able to access the interface between the sample and the polarisable dielectric material (generally a noble metal).

Fluorescence microscopy can be considered a special form of spectroscopic microscopy which excites and detects a small band of wavelengths. This technique generally requires tagging or staining of the sample with a fluorescent marker protein or dye. Selectivity is provided by irradiating and detecting at the specific excitation and emission wavelengths of these markers.<sup>135</sup> Functional properties structures and surfaces can be investigated by selecting marker dyes with specific binding or the ability to report characteristics such as pH.<sup>141</sup> The wide variety of available markers allows investigation of a range of functional properties, however dyes can significantly perturb the system being investigated, are often cytotoxic, and have limited specificity.<sup>142</sup> Fluorescent tagging of proteins is also labour intensive and can alter or inhibit protein function. While optical microscopy is well suited to fragile and live samples, the high intensity of excitation light can cause photodamage which can be particularly problematic in long confocal scanning regimes.<sup>142</sup> Fluorescent microscopy is generally diffraction limited, however super-resolution microscopies which ‘break’ the diffraction limit have been advent.<sup>134,143</sup> These methods generally employ sophisticated and complex fluorophores, computational procedures, or

detection methods.<sup>135</sup> Overall, optical microscopy is generally well suited to *in situ* functional imaging if suitable fluorophores are available or the system in question does not require resolution below that of a few hundred nanometres.

#### **1.4.2 Electron Microscopy**

Electron microscopy allows far higher resolution compared to optical microscopy due to the smaller wavelength of electrons which is around 2 pm depending on acceleration voltage of the electron beam (30 kV to 500 kV).<sup>144</sup> Scanning electron microscopy (SEM) scans the electron beam over the surface of a sample and detects secondary or backscattered electrons from the surface. SEM resolution is highly system and sample dependent, highly conductive samples permit higher acceleration voltages and therefore resolution on the scale of nanometres. On the other hand, insulating samples may require sputtering with a conductive layer to prevent charging and allow any imaging at all. TEM lacks the requirement for conductivity because the sample must be thin enough (< 500 nm) for the electron beam to pass through.<sup>145</sup> Cryo-TEM allows imaging at a similar resolution of soft samples and interfaces and has been used to image both sample and solution structure.<sup>146</sup> Atomic resolution is possible with scanning transmission electron microscopy (STEM) which scans the TEM electron beam over the sample.<sup>147</sup> Samples must generally be robust to high vacuum as ambient, *in situ*, or liquid EM require more complex configurations. Limited resolution can also be achieved for organic samples as beam damage occurs at higher magnifications.<sup>144</sup> Electron microscopy provides high resolution information about interfaces but any functional information must be inferred from structure.

#### **1.4.3 Scanning Probe Microscopy**

SPMs are not limited by diffraction as they use various probes controlled by piezoelectric positioning systems to interrogate the surface. The first SPM developed was scanning tunnelling microscopy (STM) in 1981,<sup>148</sup> closely followed by atomic force microscopy (AFM) in 1986,<sup>149</sup> and the first scanning electrochemical probe microscopy (SEPM) was scanning electrochemical microscopy (SECM) which was developed in the late 1980s.<sup>78,150–153</sup>

#### 1.4.3.1 Scanning Tunnelling Microscopy

STM uses a conducting tip to measure the topography of a conductive substrate by applying a bias between the two which causes a current to be passed once the tip is within electron tunnelling distance of the substrate.<sup>154</sup> The main requirement of STM is therefore that the substrate is conductive, however it can be used to report the local of conductivity.<sup>155,156</sup> These systems capable of resolving individual atoms and bonds, as the main limit on the resolution is the radius of curvature at the end of the tip. STM has been used to image bond rotations<sup>157</sup> and is capable of ‘video-rate’ time resolution.<sup>158</sup> Metallic probes are usually used however the highest resolution techniques functionalise the apex of the tip with molecules such as carbon monoxide.<sup>159</sup> STM is usually operated under ultra-high vacuum however it can be used in other media such as air and water, though with some sacrifice in resolution.<sup>160</sup>

#### 1.4.3.2 Atomic Force Microscopy

AFM similarly maps the topography of samples however it can be used for insulating substrates. A laser is used to measure the deflection of a cantilever which is generally brought into contact with the surface, thereby measuring the forces generated. Non-contact mapping can also be achieved by oscillation of the probe and measurement of the change in frequency as the tip approaches the surface.<sup>161</sup> AFM can therefore be applied to a wide variety of substrates *in situ*, including soft samples for which the mechanical properties can also be mapped.<sup>162</sup> The resolution of AFM approaches atomic level under ultra-high vacuum but is otherwise sample dependent due to molecular motions in other media and therefore on the scale of nanometres.<sup>163</sup>

Two common forms of functional mapping techniques based upon AFM are electrostatic force microscopy (EFM) and Kelvin probe force microscopy (KPFM). The most common form of EFM operates much like non-contact AFM, however a potential bias is applied between the tip and the sample while the cantilever is oscillated at its resonant frequency. The electrostatic forces between the tip and sample affect the oscillation of the cantilever in terms of phase or frequency throughout approach to the surface.<sup>164</sup> Given knowledge of the work functions of both the tip and substrate, this information can be used to calculate the local surface charge however this interpretation is a major challenge in many systems.<sup>165</sup> The major limitation of this method is that the sample must be in a highly resistive media to prevent faradaic

reactions and formation of a double layer at the tip and surface, therefore physiological conditions are not possible. However, this does allow use of the technique in air and deionised water, and it has been used to measure the nanoscale electrical properties of bacteria,<sup>166</sup> graphene,<sup>167</sup> ionic transport,<sup>168</sup> and photovoltaic dynamics.<sup>169</sup>

KPFM is capable of reporting similar information to EFM by applying an alternating voltage to the probe at the resonance frequency of the probe, with a direct voltage offset.<sup>170</sup> This forms a capacitor between the probe and substrate, much like with EFM, with the direct current (DC) component reporting topography and the alternating current (AC) component relating to capacitance and therefore surface potential. As a conductive substrate is required, KPFM has been used largely for characterising the work function of electrodes and semiconductors, however it has had limited use upon biological molecules.<sup>171–173</sup>

#### **1.4.3.3 Scanning Electrochemical Probe Microscopy**

SEPMs use an electrochemical signal to interrogate a surface; SECM uses a UME as a probe to provide feedback,<sup>78</sup> while SICM and scanning electrochemical cell microscopy (SECCM) use an open channel in the form of a nanopipette.<sup>6,174,175</sup> Electrochemical probes such as these have a far wider scope for functional mapping in comparison to other SPMs, allowing analysis of dynamic properties of the surface such as electrochemical activity,<sup>176</sup> transport,<sup>177</sup> reactivity,<sup>178</sup> and stability.<sup>179</sup>

SECM is the most common technique employed for this purpose, using amperometric or sometimes potentiometric feedback to report local transport and electrochemical properties.<sup>180,181</sup> It requires the sample to be immersed in electrolyte solution, allowing a potential bias to be applied (or measured in the case of potentiometric SECM) between the UME probe and a QRCE. This is used to drive faradaic reactions at the surface through oxidation or reduction of an electroactive molecule which may be present in solution or generated by the substrate surface, depending upon the feedback mechanism.

Approaching the UME to an inert substrate will cause a decrease in the current due to hinderance of transport to the electrode surface, causing a drop in current and allowing the surface to be detected. In cases where the substrate is reactive towards the electroactive reporter molecule or if transport is occurring into or out of the substrate, the consequential local changes in concentration can be detected. SECM is



therefore sensitive to a wide range of surface processes, including conductivity, reactivity, topography, permeability, and porosity.<sup>180</sup> This causes a convolution between interfacial processes and tip-substrate separation which usually requires numerical simulation to access the contributing factors.<sup>180</sup> The resolution of SECM is also typically on the scale of microns as fabrication of nanoelectrodes is difficult and time consuming, however recent progress in this area has allowed nanoscale imaging with SECM.<sup>79,109,18210,183</sup> SECM has been used extensively for the measurement of cellular metabolites and signalling molecules,<sup>80</sup> and has also been used to generate protons at an enamel surface to induce dissolution which can be quantified by subsequent measurement of the etch pit.<sup>184</sup>

Open channel techniques such as SICM and SECCM utilise nanopipettes which are simple to fabricate using a laser pulling system. The pulling parameters such as heat, pulling time, and speed can be tuned to produce a nanopipette of the desired dimensions.<sup>185,186</sup> These techniques also require electrolyte solution as they rely upon the ionic current being passed between two QRCEs, however no electroactive mediator is required. SECCM can be used in single or dual barrel mode,<sup>128,187</sup> and avoids immersing the entire sample in electrolyte, instead using a droplet of electrolyte delivered via the nanopipette to create a confined electrochemical cell within which the surface is interrogated.<sup>6,175</sup> This is beneficial for large conductive samples which in SICM would cause parasitic currents to overwhelm the ionic current response, a processes limited by permitting electrochemical measurements only in the wetted area. The response and resolution of SECCM is therefore dependent upon the surface wetting properties which must be carefully considered when designing experiments.<sup>176</sup> SECCM has been used for a range of substrates, in dual barrel mode for insulating substrates, or single barrel mode where a potential bias can be applied to very small areas of the substrate. However, this means that SECCM does require that the rest of the interface is dry or protected by an immiscible fluid and is therefore generally unsuitable for biological systems.

Single barrel SECCM has been used to examine surface heterogeneities across a range of electroactive substrates with applications in batteries,<sup>92</sup> corrosion<sup>128</sup> and catalysis.<sup>188</sup> This allows elucidation of the amperometric and voltammetric response of individual entities and sites by performing traditional electrochemical experiments like CV or galvanostatic methods on isolated areas of the surface.<sup>92,176,189</sup> Double barrel

SECCM can be used for nanoscale delivery of species to a surface and the two barrels can be loaded with different solutions. This method has been used to deliver species for nanoscale surface patterning<sup>190</sup> and has also been used for crystal dissolution studies in a similar manner to SECM by delivering an acidic solution to an enamel substrate (*vide supra*).<sup>179</sup>

SEPMs are extremely versatile in the potential applications to measure processes at the interface and access surficial information at the nanoscale *in situ*. SICM is the main technique used in this work because of its potential for accessing electrochemical dynamics and physical properties *in situ* for aqueous interfaces and physiological conditions (*vide infra*).

#### **1.4.4 Multi-Microscopy Methods**

The most powerful investigations into surface properties have been performed using multi-microscopy techniques to access complementary information about a substrate, often providing the ability to link structure and function.<sup>6</sup> The versatility of scanning probe techniques facilitates development of hybrid methods through employment of probes which can simultaneously act as various combinations of SEPMs, AFM, and STM. Examples of this are SECM-STM,<sup>191</sup> SICM-SECM,<sup>192</sup> AFM-SECM,<sup>193</sup> and AFM-SICM,<sup>194</sup> in these methods one technique is often used for accurate topographical feedback while the other provides the capacity for functional mapping. These can also be combined with spectroscopic microscopy for example in the case of tip enhanced Raman spectroscopy, or through correlative multi-microscopy by analysing the same sample on multiple or integrated platforms.<sup>130,195</sup>

### **1.5 Scanning Ion Conductance Microscopy**

#### **1.5.1 Technique Fundamentals**

SICM uses changes in the ionic current driven through a nanopipette as feedback for pipette-substrate separation in order to build a topographical map of a substrate immersed in electrolyte solution (Figure 1.5). The technique was first developed in 1989 by Hansma *et al.* for the topographical imaging of insulating surfaces.<sup>196</sup> Korchev *et al.* (1997) introduced important theoretical considerations of the feedback response which improved the robustness of the technique and allowed the application of SICM to living cells.<sup>197</sup> Development of more robust scanning protocols have aided in

improving the resolution and expanding the application of SICM to a more diverse range of substrates.<sup>198,199</sup> Meanwhile, increased understanding of the ion current response has facilitated the use of SICM for functional imaging, allowing extraction of information about the processes and properties at the substrate interface.<sup>34,60,200</sup>

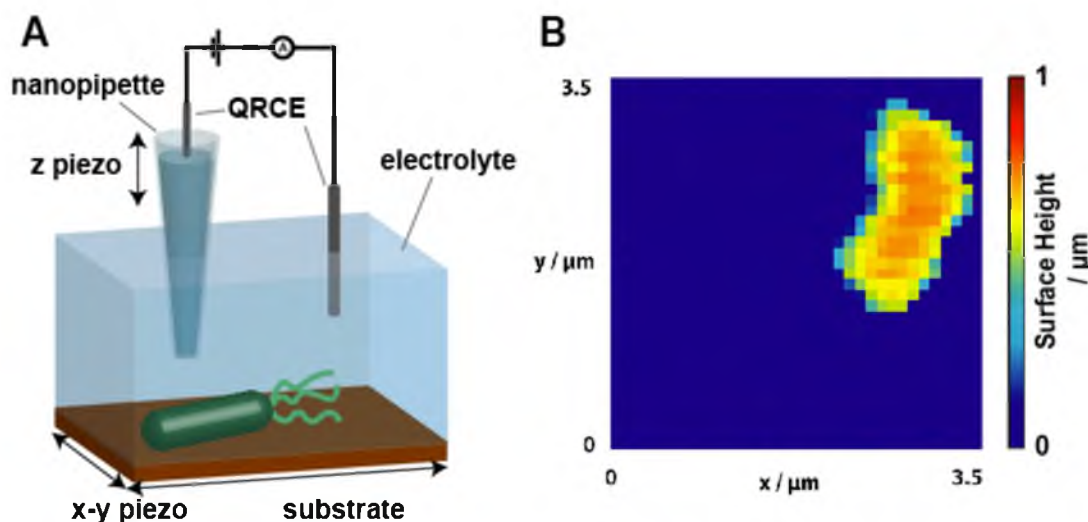


**Figure 1.5 Schematic of a standard SICM experimental configuration and example topography.** (A) The standard SICM set up in which a bias is applied between two QRCEs in electrolyte solution, one of which is within a nanopipette, using the ionic current driven through the nanopipette for positional feedback (a schematic of a bacteria is used to represent the substrate). (B) An example of a topographic image obtained through SICM topographical mapping of *Bacillus subtilis* (taken from Chapter 4).

The probe utilised in conventional SICM experiments comprises of a single barrelled borosilicate or quartz pipette with a typical aperture diameter of around 200 nm, though this can range from 5 nm to 2  $\mu\text{m}$ .<sup>201</sup> The resolution of SICM is calculated to be between 2/3 and 3/2 times the pipette diameter, the discrepancy between these values is likely due to differences in the height and geometry of the features for which resolving power was calculated.<sup>202,203</sup> Therefore the maximum resolution of SICM is less than 10 nm and it has been used to effectively resolve individual proteins with experimentally estimated resolution of 3-6 nm.<sup>204</sup> The pipette is usually filled with the same electrolyte solution in which the substrate is immersed, however this is not a strict requirement as differential concentrations and solvents have been used.<sup>56,205</sup> An ionic current is generated through the pipette channel by applying a potential bias

between two QRCEs; one placed in the bulk electrolyte solution and the other confined within the nanopipette. The constriction at the orifice of the pipette limits the ionic flux through the system, generating a resistance on the scale of  $G\Omega$  which dominates the ion current response.<sup>200</sup> Consequently, the technique is particularly sensitive to the local ionic conductivity and resistance in the region around the pipette orifice.

The probe position relative to the sample is controlled by a three-dimensional piezoelectric positioning system which controls vertical (z) and horizontal (x-y) translation of the probe and/or sample with sub-nm precision. This allows translation of the pipette towards the surface, increasing the gap resistance as a function of tip-substrate separation therefore the increasing the system resistance as defined by Equation 1.17.<sup>197</sup>

$$i = \frac{V}{R_p + R_g(d)} \quad (1.17)$$

where  $i$  is the ionic current,  $V$  is the voltage between the two QRCEs,  $R_p$  is the pore resistance, and  $R_g$  is the gap resistance as a function of distance  $d$ . When the gap resistance is on a similar order of magnitude to the access resistance of the nanopipette, it causes a detectable decrease in the ionic current which can be used as positional feedback for distance from the substrate. This occurs at distances which are similar to the inner diameter of the pipette orifice, providing a feedback mechanism which prevents the probe from touching the surface. However, complexities can occur within the feedback response due to phenomena such as surface charge or interfacial ion fluxes which affect the local ionic conductivity at the pipette orifice.<sup>206</sup> With careful selection of experimental parameters, the contribution from these effects can be minimised and even exploited to provide further information about the interface in the form of functional imaging. The lack of surface contact makes SICM an ideal non-invasive imaging technique for soft samples such as biological samples, and with careful experimental design the dependency of the ionic current of surface phenomena can be exploited to provide new avenues for information.

### 1.5.2 Feedback Types and Scanning Regimes

The scanning protocol used in SICM can be altered in several ways to suit the sample and experimental requirements. Constant-distance mode was the first scanning protocol used in SICM (Figure 1.6A), whereby the tip is first approached to the surface until a desired change in ion current is observed (usually 1-2% that of the bulk

current).<sup>174</sup> This current magnitude is maintained throughout the scan by adjusting the z-height of the probe accordingly as the tip is translated across the surface, maintaining a constant tip-substrate separation. This method provides continuous surface information and is the fastest scanning method as it maintains surface engagement throughout the scan, which is often performed in a raster pattern but can also be performed in harmonic scan patterns such as spirals which reduce the limitations imposed by x-y piezo feedback times and momentum.<sup>178,207</sup> However steep changes in the surface topography can cause contact which jeopardises the probe integrity and can cause damage to the sample.<sup>197,207</sup>

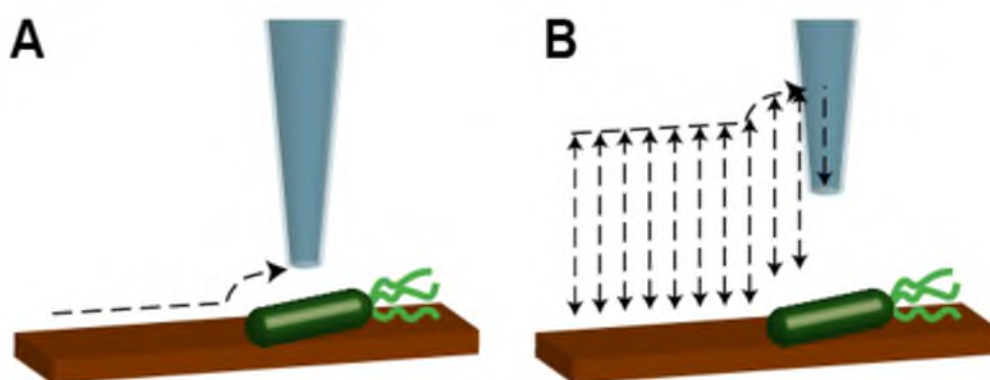


**Figure 1.6 Main scanning procedures of SICM.** (A) Constant-distance mode in which the same tip-substrate separation is maintained while the probe is scanned over the surface. (B) One possible configuration of scan-hopping mode in which the probe is retracted a set distance from the previously obtained approach distance before lateral translation.

The scan-hopping procedure offers the greatest robustness to steep changes in surface height and is the primary technique used in this work (Chapters 2 and 4). In this case the tip is again approached to the surface using the change in ionic current as feedback but in this case the tip is retracted into the bulk electrolyte before x-y translation and the procedure repeated at each pixel (Figure 1.6B). In this manner a topography map of the surface can be constructed from pixels which are point measurements of the surface. The retract distance required depends upon the how precipitous the sample is but for most measurements<sup>208</sup> greater than 1-2  $\mu\text{m}$  from the surface is considered bulk. This greatly reduces the probability of contact with the

surface as the probe generally approaches from a direction perpendicular to the surface. Drift in the ionic current can be accounted for by normalising the currents at each pixel to the corresponding bulk measurement, ensuring that changes in current during the approach at each pixel are predominantly due to proportional changes in  $R_g$ . The hopping protocols also allow greater experimental complexity as, after approaching to the set tip-substrate separation, the voltage can be modified to provide information for functional mapping.<sup>34</sup> This protocol is slower than the constant-distance method, however ongoing developments in the protocol and instrumentation are closing the gap to allow robust high-speed SICM.<sup>209–212</sup>

So far, the protocols described have concerned the DC mode of feedback which uses the unprocessed ion current under a regime where the potential between the QRCEs is held constant and the probe is translated at linearly in the z-axis. This is the most conventional SICM feedback type as it is the simplest to implement and provides the fastest response time to changes in resistance at the tip orifice and therefore the fastest scan rate. However, the parameters must be judiciously selected to minimise contribution of surface properties such as surface charge to the feedback signal which can alter the approach distance. For this reason, electrolyte concentrations are usually kept relatively high (>50 mM) and applied biases low (<100 mV).<sup>208</sup> It is also prone to drift which can compromise the scan, and changes in DC can be sensitive to surface phenomena. It can therefore be advantageous to employ more complex feedback types which can be combined with both scanning protocols to minimise these issues.

Distance modulated (DM-SICM) and bias modulated SICM (BM-SICM) introduce an AC component to the otherwise DC ion current signal. DM-SICM holds a constant potential while applying a sinusoidal perturbation to the z-height of the tip with an amplitude 10-20% of the nanopipette diameter and a frequency of several hundred Hz.<sup>213</sup> When the tip is in the bulk environment there is no AC component to the signal, however as tip-substrate separation is decreased, the differential gap resistance between the heights within a single period of probe oscillation introduces an AC component to the current. The amplitude of the AC component is extracted at the same frequency as the oscillation and used as feedback for tip-substrate separation, increasing upon approach to the surface. This minimises the effect of current drift over the course of a scan as the AC amplitude is only dependent upon the current change

within a single period of oscillation. DM-SICM is therefore extremely useful for constant-distance scanning protocols which are susceptible to DC drift and maintains accurate tip-substrate separation even with changing local ionic conductivity due to dynamic interfacial processes (Chapter 3).

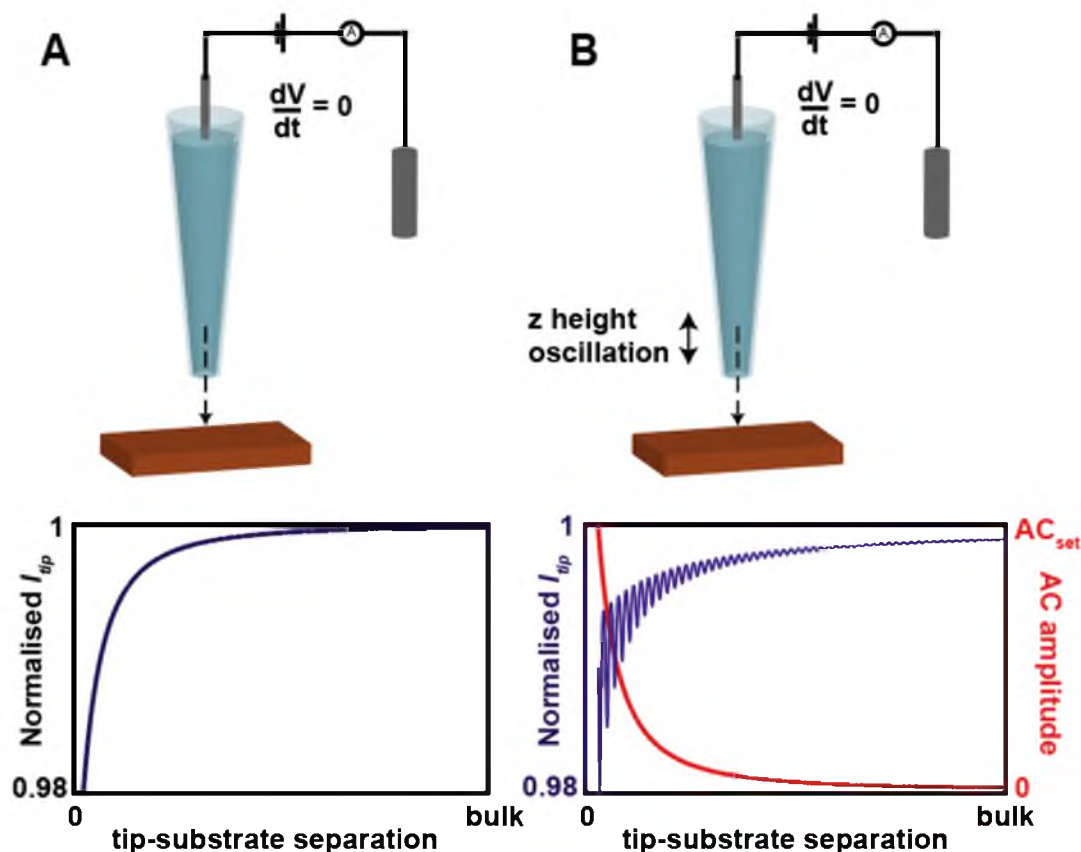


**Figure 1.7 Diagram of SICM feedback regimes used herein.** (A) DC feedback where the voltage between the two QRCEs is maintained constant and the probe is translated monotonically towards the surface, resulting in a decrease in normalised current with decreasing tip-substrate separation. (B) DM-SICM in which a sinusoidal oscillation is applied to the z-height of the probe, resulting in an AC component within the normalised current due to the oscillating resistance, the amplitude of this AC component is used for feedback.

BM-SICM is not utilised within this work, however it is an important feedback type which has been developed to ensure minimal perturbation of the substrate.<sup>214</sup> In this feedback mode, the sinusoidal perturbation is applied instead to the bias between the two QRCEs to directly generate an AC feedback signal. The monitored output in this case is the AC phase which is extremely sensitive to changes in the capacitance

of the system and therefore proximity to the substrate double-layer. This has the advantage of applying no net bias to the system, allowing the surface to remain almost completely unperturbed by the measurement. Furthermore, the range of frequencies which can be applied are far wider and the system has the potential to provide similar information to electrochemical impedance spectroscopy from which a full equivalence circuit of a system can be calculated.<sup>5,214</sup>

Each of these techniques has its own advantages or disadvantages with regard to speed, precision, robustness, and sample perturbation. The scan hopping protocol with DC feedback is employed in Chapters 2 and 4 because it allows the greatest flexibility for changing the bias at the substrate surface for functional mapping and controlled delivery of species from the pipette. A distance modulated procedure is used in Chapter 3 as it provides precise and continuous positional feedback, while the AC component of the signal is more robust to changes in local ionic conductivity (*vide infra*).

### **1.5.3 Quantifying the SICM Response with FEM**

#### **1.5.3.1 Modelling of SICM Systems**

The SICM ion current response for the described scanning procedures is a convolution of a number of different factors which can only be understood with theoretical considerations of the underlying mechanisms. A number of analytical expressions have been determined which relate the ionic current to the tip-substrate separation as a function of nanopipette semi-angle and the diameter of the opening.<sup>215</sup> However, this has limitations, and the inner and outer geometry of glass of the tens to hundreds of microns into the pipette has been shown to affect the SICM response.<sup>200</sup> These expressions also cannot incorporate the details of more the complex systems which require consideration of local ion distributions.

Discretisation methods allow description of these inhomogeneities by building a representation of the geometry of the system. At discrete points across this geometry, a system of partial differential equations which describe the physicochemical phenomena can be solved. In the case of SICM this is the Poisson-Nernst-Planck system, which may also be coupled to the Navier-Stokes equations to incorporate the effects of fluid flow. It is also possible to include descriptions of processes or reactions at surfaces or in solution, allowing simulation of a wide range of systems. This makes



discretisation methods extremely valuable in understanding the ionic current response in electrochemical systems such as SICM.<sup>60</sup> FEM simulations are the most widely applied as the system of equations and boundary conditions is easily formulated and commercially available programs such as COMSOL Multiphysics (used herein) can be employed. Finite volume method simulations and finite difference method simulations have also been employed for similar systems, however they are less numerically stable and have more geometric constraints.<sup>216</sup>

FEM simulations allow accurate representation of the pipette geometry and have proven efficacy in the modelling of accurate current-voltage ( $i$ - $V$ ) responses of nanopipettes. Through measurement of the pipette using TEM (Figure 1.8A), accurate geometries of nanopipettes can be obtained at nanometre scale resolution and replicated in an FEM model.<sup>200</sup> The geometry of the nanopipette is one of the most important factors determining the SICM response because it defines the resistance to ionic flux through the pipette. Once the geometry is built the simulation domain is meshed, a process in which the domain is represented by interlinked nodes at which the system of partial differential equations describing the physics of the system is solved (Figure 1.8B).

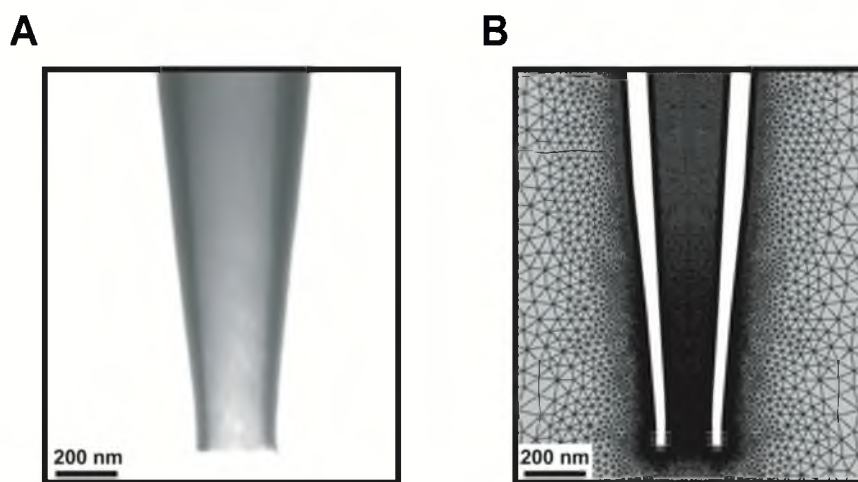


**Figure 1.8 TEM of a typical nanopipette used in SICM experiments with the COMSOL simulation domain built from it.**

Boundary conditions must also be selected to enforce the voltages applied during the experiment, the fluid conditions at surfaces or openings, surface charge,

and species fluxes. Numerical solutions to these equations can be obtained using a number of methods but often the damped Newton-Raphson method is common for steady-state simulations and backwards differentiation formula for time-dependent simulations.<sup>217</sup> Interpretation of these simulations requires careful inspection to ensure physically realistic solutions, however they are capable of providing insights into the mechanisms underlying complex measurements such as SICM and calculation of quantifiable surface properties.

### 1.5.3.2 Ion Current Rectification

The  $i$ - $V$  response of a nanopipette is a convolution of several physical factors which define a potential dependent resistance to the ionic current through the pipette. Imbalances in the mobility of ions through a nanopipette or conical nanopore cause a characteristic curvature in the  $i$ - $V$  response, or rectification. The most important factors are the wall charge, pore geometry, and ion distribution. The double layer formed at the negatively charged glass walls causes an enrichment of cations within the channel and larger volume through which they can travel, while the same effects causes a relative exclusion of anions. This reduces the relative resistance within the pore when the QRCE within the pipette is poised at negative biases when current is largely carried by the inwards flux of cations, causing an enhanced ion current. At positive tip QRCE biases, the increased access resistance to anions travelling into the pipette causes a reduced ion current. The pore radius to Debye length ratio ( $\kappa^{-1}r$ ) is therefore important, as the double layer must encompass a significant volume of the pore for the effect to be prevalent.<sup>218</sup> This effect dominates the current response to such a large degree because the access resistance of the pipette is the largest source of resistance in the system. Overlap between the double layers either side of the channel will also enhance the effect, therefore any factors which affect the Debye length will have an impact upon the nanopipette response. The cone angle of the pore also has a strong effect upon this as it defines the length of the channel through which these effects take place.

Many SICM systems can be accurately described by the Poisson-Nernst-Planck system of equations (Equations 1.3a and 1.5) coupled to the Navier-Stokes equation (Equation 1.7), as these govern the aforementioned processes (*vide supra*). FEM simulations can therefore be employed to accurately describe the geometric and

physical effects in SICM systems. They have also been valuable in understanding the driving forces and interactions between factors which determine ion-current rectification including wall charge,<sup>200</sup> pipette geometry,<sup>219</sup> pore length,<sup>220</sup> pressure,<sup>221</sup> electrolyte concentration,<sup>222</sup> ionic gradients,<sup>223</sup> potential scan rate,<sup>224</sup> and solution viscosity.<sup>225</sup>

### 1.5.3.3 Electroosmotic Flow in SICM

Description of the SICM system using FEM with incorporation of the Navier-Stokes equation allows assessment of the flow phenomena which may occur and could affect the system properties. Generally EOF does not have a significant effect upon the ionic current response in SICM as ion transport is dominated by migration,<sup>226,227</sup> however it can be significant in some configurations especially when used to control the flux of neutral species.<sup>56,57,117</sup>

EOF in a nanopipette has a complex behaviour due to effects of the changes in channel width upon pressure and electric field. In SICM the channel takes the shape of a conical frustrum with varying cone angle, this causes non-linearity in the electric field tangential to the wall driving EOF.<sup>219</sup> At the same time, the nature of incompressible flow (Equation 1.7) in a conical system dictates that the total flow velocity across the channel is maintained throughout the entire length. This is a manifestation of Bernoulli's principle, which causes a drop in pressure with an increase in velocity where flow is constricted, and an increase in pressure with a decrease in velocity where channels expand.<sup>228</sup> Combined with the EOF driven at the channel walls this results in complex flow phenomena which are only just being described.<sup>51,55,227</sup>

Factors which affect the ionic migration and contribute to ICR also affect EOF,<sup>51,229</sup> therefore causing flow rectification which allows the use of nanopipettes as fluidic diodes.<sup>230–232</sup> Wall charge is the main underlying cause of EOF and alteration of the wall charge has been used to control and reverse EOF in nanopipettes.<sup>233,234</sup> Electrolyte concentration also has a large effect because of the relationship with the size of the diffuse layer, reducing the electrolyte concentration increases the Debye length and increases flow rate where there is overlap between the double layers either side of the channel.<sup>218</sup> Other aspects of an SICM system that have been explored in terms of flow are concentration imbalance,<sup>55,56</sup> pressure,<sup>221,235</sup> and nano-biopsy.<sup>79,236,237</sup>

## 1.6 SICM Functional Mapping

In recent years, SICM protocols have been adapted to allow mapping of the processes at interfaces and provide information about properties beyond that of surface topography. SICM has the ability to access information about any processes which affect the transport properties and local ion conductance at the tip interface. It can also be applied in a wide range of conditions, allowing *in situ* functional mapping of catalysts and biological substrates. The power of SICM to access this information has been displayed since its inception, with the first paper mapping transport through 800 nm membrane pores.<sup>196</sup> Since then, the sensitivity of SICM to changes in the local ionic conductivity has been used to map transport such as that through individual ion channels in living cells,<sup>129</sup> and reactivity through the electrochemical flux at nanoparticles.<sup>178</sup>

Manipulating the potential bias between the QRCEs has allowed precise control over the sensitivity of the ion current to interfacial properties and has also facilitated controlled delivery of species with SICM.<sup>81,238</sup> Figure 1.9 shows the scanning regimes utilised for these methodologies, where a hopping regime is used to approach the surface at the approach potential ( $V_a$ ), after which the probe remains at the surface and the potential is pulsed ( $V_p$ ) and the current monitored to product an  $i-t$  curve, alternatively the potential can be scanned over a range ( $V_{iv}$ ) to produce  $i-V$  curves. The probe is then retracted and the procedure repeated in bulk in order to normalise the current and account for drift.<sup>6</sup>

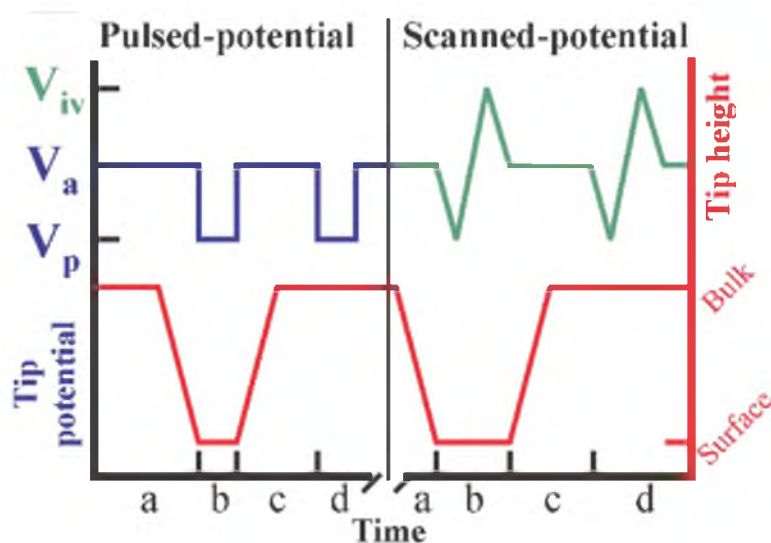


Figure 1.9 SICM functional mapping potential control regimes.

Comprehensive simulation of the pipette response allows the surface properties to be investigated as any further changes to the ionic current at the surface are due to interaction with the substrate. Careful selection of approach parameters can be used to determine tip-substrate separation independent of substrate properties.<sup>208</sup> The *i-V* or *i-t* curves can then be simulated with a range of interfacial properties to calculate which substrate properties give rise to the experimental response. Through this protocol the underlying surface properties and processes can be extracted.

### 1.6.1 Ion Flux Quantification

SICM functional mapping is particularly powerful when applied to the detection of local ion fluxes at surfaces. These methodologies have been used to monitor nanoscale variations in fluxes from individual catalytic nanoparticles,<sup>178,239</sup> synthetic nanopore membranes,<sup>240</sup> and individual nanopores in cell membranes.<sup>129</sup> Potential control methodologies have also been extended to control of the flux of species contained within the nanopipette, through migration in the case of charged species or by controlling EOF in the case of neutral species.<sup>116,118,241</sup> These methodologies have been adapted from microiontophoresis techniques which control delivery of species from a micropipette or nanopipette through the application of pressure or voltage.<sup>115</sup> This allows controlled delivery of such as drugs or other molecules to a cell, usually at the scale of individual cells. These methods have been integrated with SICM methodologies for combined delivery and mapping, and the smaller channel size of SICM probes allow EOF to be exploited to control delivery of neutral species.<sup>57</sup> This was first demonstrated by the SICM mapping of cells with the simultaneous localised delivery of capsaicin, and combined with fluorescence microscopy for quantification of the cellular response.<sup>57,238</sup> This has been applied to the delivery of DNA,<sup>242</sup> proteins,<sup>243</sup> fluorophores,<sup>244</sup> and other small molecules,<sup>238</sup> combined with multi-microscopy methods and FEM simulations to quantify delivery.<sup>57</sup> Delivery methodologies have proven powerful in quantification of the localised uptake and response of cells to neurotransmitters and drugs, recently this has been extended to mapping nanoscale electrochemical activity of electrodes.<sup>81</sup>

The ability to perform controlled delivery of a species to an electrode with nanoscale precision is an incredibly powerful technique for probing the structure of and interface. Bulk techniques such as chronoamperometry require the changing of

electrode potential to induce charge transfer between the electrode and species in solution. This causes a large capacitive spike in the current as the double layer is established and mobile ions rearrange to counteract the surface potential, obscuring the initial faradaic current. Controlled delivery to an already poised electrode allows the charge transfer at that particular potential to be accurately assessed at the nanoscale in a system which is already at equilibrium. This allows quantification of local surface kinetics and interactions of the delivered species with the already established double layer. This is particularly important as electrodes become smaller and these effects become more prominent,<sup>182</sup> and electrocatalysts incorporate nanostructured materials.<sup>4,90</sup> It is also important to understand these heterogeneities in terms of the electrode response to allow further analysis, especially in the case of individual events.<sup>86,245</sup>

These methods are utilized in Chapters 2 and 3 to examine the underlying mechanisms of delivery and to understand reaction kinetics at a dissolving surface. The same effects are also considered in Chapter 4 where the complex interface of the bacterial cell envelope is investigated.

### 1.6.2 Charge Mapping

The sensitivity of SICM to different interfacial properties can also be controlled through the potential program applied during scanning. Substrate surface charge has emerged as an important and influential factor in defining the SICM response at a substrate, causing a phenomena known as surface induced rectification.<sup>232,246</sup> This phenomenon has been used to map the surface charge at lipid membranes,<sup>247</sup> hair follicles,<sup>248</sup> polymer layers,<sup>249,250</sup> and living cells.<sup>208,251</sup> At low biases the ion-current response is insensitive to the substrate charge and the response is instead dominated by the system resistance, allowing accurate approach to the surface. High biases confer ion-current sensitivity to the surface charge and therefore the potential upon reaching the surface is either swept or pulsed to higher potentials, generating  $i$ - $V$  or  $i$ - $t$  curves.<sup>208,247,249,250</sup> The current during this period is then analysed to infer relative surface charge measurements,<sup>247</sup> or FEM simulations are performed to calculate the substrate charge underlying the response.<sup>208</sup>

The underlying mechanisms of this technique are generally attributed to formation of a perm-selective channel similar to the ICR described previously,

however there is also a contribution from a very small depolarisation of surface potential which causes a flux of counterions from the surface.<sup>208</sup> Due to the high concentrations of counterions in the double layer of even a moderately charged surface, this flux is large enough to detect in the ion current, these mechanisms are discussed in Chapter 4 where they underpin the nanoscale electrochemical characterisation of the bacterial cell envelope.

### **1.6.3 Functional Mapping of Complex Surfaces**

As described above nanoscale *in situ* functional mapping has been used in a wide range of areas to elucidate the mechanisms underlying processes at heterogeneous surfaces. Nanoscale surface heterogeneities cause a convoluted overall response of many real-world interfaces, requiring nanoscale functional mapping to fully understand the underlying mechanisms. The complex properties and processes at complex surfaces such as electrodes, polycrystalline biomaterials, and living interfaces require special considerations for nanoscale functional mapping, as shown herein. These interfaces offer the opportunity to further develop the accuracy of SICM functional mapping and to extend complexity of questions which the technique is able to explore. In doing so we access important information about transport from nanopipettes, phenomena occurring at complex surfaces, and properties of living cells.

## 1.7 References

- 1 J. Lyklema, *Fundamentals of interface and colloid science. Volume 2: Solid-liquid interfaces.*, Academic Press, Cambridge, 1995, vol. 2.
- 2 M. A. Edwards, D. A. Robinson, H. Ren, C. G. Cheyne, C. S. Tan and H. S. White, *Faraday Discuss.*, 2018, **210**, 9–28.
- 3 L. A. Baker, *J. Am. Chem. Soc.*, 2018, **46**, 15549–15559.
- 4 C. L. Bentley, M. Kang and P. R. Unwin, *J. Am. Chem. Soc.*, 2018, **141**, 2179–2193.
- 5 A. J. Bard and L. R. Faulkner, *Electrochemical Methods: Fundamentals and Applications*, Wiley, New York, 2nd edn., 2001, vol. 2.
- 6 C. L. Bentley, J. Edmondson, G. N. Meloni, D. Perry, V. Shkirskiy and P. R. Unwin, *Anal. Chem.*, 2019, **91**, 84–108.
- 7 S. Muto, J. Rusz, K. Tatsumi, R. Adam, S. Arai, V. Kocovski, P. M. Oppeneer, D. E. Bürgler and C. M. Schneider, *Nat. Commun.*, 2014, **5**, 1–7.
- 8 J. Vandiver, D. Dean, N. Patel, W. Bonfield and C. Ortiz, *Biomaterials*, 2005, **26**, 271–283.
- 9 P. F. Rottmann and K. J. Hemker, *Mater. Res. Lett.*, 2018, **6**, 249–254.
- 10 F. P. Filice, M. S. M. Li and Z. Ding, *Adv. Theory Simulations*, 2019, **2**, 1800124.
- 11 J. Lü, J. Yang, M. Dong and O. Sahin, *Nanoscale*, 2014, **6**, 7604–7608.
- 12 L. C. Kam, *J. Struct. Biol.*, 2009, **168**, 3–10.
- 13 D. Hebenstreit, *Biology (Basel)*, 2012, **1**, 658–667.
- 14 F. P. Filice and Z. Ding, *Analyst*, 2019, **144**, 738–752.
- 15 P. Actis, M. M. Maalouf, H. J. Kim, A. Lohith, B. Viložny, R. A. Seger and N. Pourmand, *ACS Nano*, 2014, **8**, 546–553.
- 16 R. Parsons, *Chem. Rev.*, 1990, **90**, 813–826.
- 17 P. Attard, *Curr. Opin. Colloid Interface Sci.*, 2001, **6**, 366–371.
- 18 D. Leckband and J. Israelachvili, *Q. Rev. Biophys.*, 2001, **34**, 105–267.
- 19 Y. Wang, Y. Song and Y. Xia, *Chem. Soc. Rev.*, 2016, **45**, 5925–5950.
- 20 S. Chen, Y. Liu and J. Chen, *Chem. Soc. Rev.*, 2014, **43**, 5372–86.
- 21 M. Dunwell, Y. Yan and B. Xu, *Curr. Opin. Chem. Eng.*, 2018, **20**, 151–158.
- 22 R. R. Netz and D. Andelman, *Phys. Rep.*, 2003, **380**, 1–95.
- 23 J. M. Kinsella and A. Ivanisevic, *Nat. Nanotechnol.*, 2007, **2**, 596–597.



- 24 S. Ohki and H. Ohshima, in *Electrical Double Layers in Biology*, Springer US, New York, 2012, pp. 1–16.
- 25 P. N. Bartlett, R. C. Alkire and J. Lipkowski, *Electrochemistry of Carbon Electrodes*, Wiley-VCH Verlag GmbH & Co. KGaA, Weinheim, Germany, 2015.
- 26 A. Groß and S. Sakong, *Curr. Opin. Electrochem.*, 2019, **14**, 1–6.
- 27 H. Helmholtz, *Ann. der Phys. und Chemie*, 1879, **243**, 337–382.
- 28 O. Stern, *Zeitschrift für Elektrochemie und Angew. Phys. Chemie*, 1924, **30**, 508–516.
- 29 M. Gouy, *J. Phys. Théorique Appliquée*, 1910, **9**, 457–468.
- 30 D. L. Chapman, *London, Edinburgh, Dublin Philos. Mag. J. Sci.*, 1913, **25**, 475–481.
- 31 S. Levine and E. Matijević, *J. Colloid Interface Sci.*, 1967, **23**, 188–199.
- 32 D. C. Grahame, *Chem. Rev.*, 1947, **41**, 441–501.
- 33 F. Leroy, *Molecular Driving Forces: Statistical Thermodynamics in Biology, Chemistry, Physics, and Nanoscience*, Garland Science, New York, 2002, vol. 2.
- 34 A. Page, D. Perry and P. R. Unwin, *Proc. R. Soc. A*, 2017, **473**, 1–34.
- 35 L. Pilon, H. Wang and A. d’Entremont, *J. Electrochem. Soc.*, 2015, **162**, A5158–A5178.
- 36 R. Sundararaman and K. Schwarz, *J. Chem. Phys.*, 2017, **146**, 084111.
- 37 J. J. Howard, J. S. Perkyns and B. M. Pettitt, *J. Phys. Chem. B*, 2010, **114**, 6074–6083.
- 38 D. A. Welch, B. L. Mehdi, H. J. Hatchell, R. Faller, J. E. Evans and N. D. Browning, *Adv. Struct. Chem. Imaging*, 2015, **1**, 1.
- 39 A. Voukadinova, M. Valiskó and D. Gillespie, *Phys. Rev. E*, 2018, **98**, 012116.
- 40 R. Burt, G. Birkett and X. S. Zhao, *Phys. Chem. Chem. Phys.*, 2014, **16**, 6519.
- 41 D. Henderson and D. Boda, *Phys. Chem. Chem. Phys.*, 2009, **11**, 3822.
- 42 J. J. López-García, J. Horno and C. Grosse, *Langmuir*, 2011, **27**, 13970–13974.
- 43 T. Z. Lwin, R. Zhou and R. Luo, *J. Chem. Phys.*, 2006, **124**, 034902.
- 44 J. Drelich and Y. U. Wang, *Adv. Colloid Interface Sci.*, 2011, **165**, 91–101.
- 45 C. Tian, Y. Xu, D. Nordlund, F. Lin, J. Liu, Z. Sun, Y. Liu and M. Doeff, *Joule*, 2018, **2**, 464–477.

- 46 A. Einstein, *Ann. Phys.*, 1905, **322**, 549–560.
- 47 R. Kubo, *Reports Prog. Phys.*, 1966, **29**, 306.
- 48 R. G. Compton, A. C. Fisher and G. P. Tyley, *J. Appl. Electrochem.*, 1991, **21**, 2–5.
- 49 J. K. Novev and R. G. Compton, *Phys. Chem. Chem. Phys.*, 2017, **19**, 12759–12775.
- 50 J. Nikolic, E. Expósito, J. Iniesta, J. González-Garcia and V. Montiel, *J. Chem. Educ.*, 2000, **77**, 1191.
- 51 W.-J. Lan, M. A. Edwards, L. Luo, R. T. Perera, X. Wu, C. R. Martin and H. S. White, *Acc. Chem. Res.*, 2016, **49**, 2605–2613.
- 52 C. Y. Lim, A. E. Lim and Y. C. Lam, *Sci. Rep.*, 2016, **6**, 22329.
- 53 C. S. Mangelsdorf and L. R. White, *J. Chem. Soc. Faraday Trans.*, 1990, **86**, 2859.
- 54 C. E. McNamee, *Adv. Colloid Interface Sci.*, 2019, **266**, 21–33.
- 55 J. Rabinowitz, M. A. Edwards, E. Whittier, K. Jayant and K. L. Shepard, *J. Phys. Chem. A*, 2019, **123**, 8285–8293.
- 56 D. Perry, A. Page, B. Chen, B. G. Frenguelli and P. R. Unwin, *Anal. Chem.*, 2017, **89**, 12458–12465.
- 57 B. Babakinejad, P. Jönsson, A. López Córdoba, P. Actis, P. Novak, Y. Takahashi, A. Shevchuk, U. Anand, P. Anand, A. Drews, A. Ferrer-Montiel, D. Klenerman and Y. E. Korchev, *Anal. Chem.*, 2013, **85**, 9333–9342.
- 58 D. A. Lazarchik and K. B. Frazier, *Gen. Dent.*, 2009, **57**, 151–156.
- 59 D. G. Haywood, A. Saha-Shah, L. A. Baker and S. C. Jacobson, *Anal. Chem.*, 2015, **87**, 172–187.
- 60 M. A. Edwards, C. G. Williams, A. L. Whitworth and P. R. Unwin, *Anal. Chem.*, 2009, **81**, 4482–4492.
- 61 Z. Tavakolian-Ardakani, O. Hosu, C. Cristea, M. Mazloum-Ardakani and G. Marrazza, *Sensors (Basel)*, 2019, **19**, 2037.
- 62 D. W. Kimmel, G. LeBlanc, M. E. Meschievitz and D. E. Cliffel, *Anal. Chem.*, 2012, **84**, 685–707.
- 63 C. A. Martínez-Huitle, M. A. Rodrigo, I. Sirés and O. Scialdone, *Chem. Rev.*, 2015, **115**, 13362–13407.
- 64 F. C. Walsh and C. Ponce de León, *Electrochim. Acta*, 2018, **280**, 121–148.

- 65 E. E. Miller, Y. Hua and F. H. Tezel, *J. Energy Storage*, 2018, **20**, 30–40.
- 66 C. L. Bentley, M. Kang and P. R. Unwin, *J. Am. Chem. Soc.*, 2017, **139**, 16813–16821.
- 67 N. N. Elgrishi, K. J. Rountree, B. D. McCarthy, E. S. Rountree, T. T. Eisenhart and J. L. Dempsey, *J. Chem. Educ.*, 2017, **95**, 197–206.
- 68 T. Albrecht, *Nat. Commun.*, 2012, **3**, 829.
- 69 F. C. Simeone, D. M. Kolb, S. Venkatachalam and T. Jacob, *Surf. Sci.*, 2008, **602**, 1401–1407.
- 70 R. A. Marcus, *J. Chem. Phys.*, 1956, **24**, 966–978.
- 71 W. F. Libby, *J. Chem. Phys.*, 1963, **38**, 420–425.
- 72 N. S. Hush, *Trans. Faraday Soc.*, 1961, **57**, 557.
- 73 C. G. G. Zoski, *Electroanalysis*, 2002, **14**, 1041–1051.
- 74 R. M. Wightman, *Anal. Chem.*, 1981, **53**, 1125A–1134A.
- 75 J. Heinze, *Angew. Chemie Int. Ed. English*, 1993, **32**, 1268–1288.
- 76 A. Hickling and W. H. Wilson, *Nature*, 1948, **162**, 489–490.
- 77 K. T. Kawagoe, J. B. Zimmerman and R. M. Wightman, *J. Neurosci. Methods*, 1993, **48**, 225–240.
- 78 R. C. Engstrom and C. M. Pharr, *Anal. Chem.*, 1989, **61**, 1099–1104.
- 79 P. Actis, S. Tokar, J. Clausmeyer, B. Babakinejad, S. Mikhaleva, R. Cornut, Y. Takahashi, A. López Córdoba, P. Novak, A. I. Shevchuck, J. A. Dougan, S. G. Kazarian, P. V. Gorelkin, A. S. Erofeev, I. V. Yaminsky, P. R. Unwin, W. Schuhmann, D. Klenerman, D. A. Rusakov, E. V. Sviderskaya and Y. E. Korchev, *ACS Nano*, 2014, **8**, 875–884.
- 80 L. Huang, Z. Li, Y. Lou, F. Cao, D. Zhang and X. Li, *Mater. (Basel, Switzerland)*, 2018, **11**, 1996–1944.
- 81 B. Chen, D. Perry, A. Page, M. Kang and P. R. Unwin, *Anal. Chem.*, 2019, **91**, 2516–2524.
- 82 S. Y. Tan, J. Zhang, A. M. Bond, J. V. Macpherson and P. R. Unwin, *Anal. Chem.*, 2016, **88**, 3272–3280.
- 83 T. Kai, C. G. Zoski and A. J. Bard, *Chem. Commun.*, 2018, **54**, 1934–1947.
- 84 B. A. Newcomb, *Compos. Part A Appl. Sci. Manuf.*, 2016, **91**, 262–282.
- 85 P. Daubinger, J. Kieninger, T. Unmüssig and G. A. Urban, *Phys. Chem. Chem. Phys.*, 2014, **16**, 8392–8399.

- 86 D. J. Watson, R. R. Gummi, J. B. Papke and A. B. Harkins , *Electroanalysis*, 2011, **23**, 2757–2763.
- 87 M. M. P. Da Silva Neves and D. Martín-Yerga, *Biosensors*, 2018, **8**, 100.
- 88 S. Tan, P. R. Unwin, J. V. Macpherson, J. Zhang and A. M. Bond, *Anal. Chem.*, 2017, **89**, 2830–2837.
- 89 J. Ustarroz, M. Kang, E. Bullions and P. R. Unwin, *Chem. Sci.*, 2017, **8**, 1841–1853.
- 90 P. Grosse, D. Gao, F. Scholten, I. Sinev, H. Mistry and B. Roldan Cuenya, *Angew. Chemie - Int. Ed.*, 2018, **57**, 6192–6197.
- 91 S. M. Oja, Y. Fan, C. M. Armstrong, P. Defnet and B. Zhang, *Anal. Chem.*, 2016, 88.
- 92 B. Tao, L. C. Yule, E. Daviddi, C. L. Bentley and P. R. Unwin, *Angew. Chemie - Int. Ed.*, 2019, **58**, 4606–4611.
- 93 W. White and G. H. Nancollas, *J. Dent. Res.*, 1977, **56**, 524–530.
- 94 H. G. Linge and G. H. Nancollas, *Calcif. Tissue Res.*, 1973, **12**, 193–208.
- 95 R. B. Schoch, J. Han and P. Renaud, *Rev. Mod. Phys.*, 2008, **80**, 839–883.
- 96 T. R. Farhat and J. B. Schlenoff, *Langmuir*, 2001, **17**, 1184–1192.
- 97 H. J. Kwon, Y. Osada and J. P. Gong, *Polym. J.*, 2006, **38**, 1211–1219.
- 98 S. Mafé, J. A. Manzanares and P. Ramirez, *Phys. Chem. Chem. Phys.*, 2003, **5**, 376–383.
- 99 C.-H. Chou, J.-P. Hsu, C.-C. Kuo, H. Ohshima, S. Tseng and R. M. Wu, *Colloids Surfaces B Biointerfaces*, 2012, **93**, 154–160.
- 100 R. Zimmermann, C. Werner and J. F. L. Duval, *Polymers (Basel)*, 2016, **8**, 7.
- 101 F. G. Donnan, *Chem. Rev.*, 1924, **1**, 73–90.
- 102 L. Shen and Z. Chen, *Chem. Eng. Sci.*, 2007, **62**, 3748–3755.
- 103 J. Cervera, P. Ramírez, J. A. Manzanares and S. Mafé, *Microfluid. Nanofluidics*, 2010, **9**, 41–53.
- 104 P. Demchick and A. L. Koch, *J. Bacteriol.*, 1996, **178**, 768–773.
- 105 E. N. Schaumann and B. Tian, *Small Methods*, 2020, **4**, 1900868.
- 106 T. J. Silhavy, D. Kahne and S. Walker, *Cold Spring Harb. Perspect. Biol.*, 2010, **2**, 414.
- 107 N. K. Sarangi, K. G. Ayappa and J. K. Basu, *Sci. Rep.*, 2017, **7**, 11173.
- 108 M. B. Jackson and M. B. Jackson, *Mol. Cell. Biophys.*, 2010, 339–366.

- 109 J. Clausmeyer and W. Schuhmann, *TrAC - Trends Anal. Chem.*, 2016, **79**, 46–59.
- 110 J. F. L. Duval and F. Gaboriaud, *Curr. Opin. Colloid Interface Sci.*, 2010, **15**, 184–195.
- 111 J. Cervera, J. A. Manzanares and S. Mafe, *J. Phys. Chem. B*, 2015, **119**, 2968–2978.
- 112 A. J. De Kerchove and M. Elimelech, *Langmuir*, 2005, **21**, 6462–6472.
- 113 I. Szabó, V. Petronilli and M. Zoratti, *A patch-clamp study of Bacillus subtilis*, 1992, vol. 1112.
- 114 B. Martinac, M. Buechner, A. H. Delcour, J. Adler and C. Kung, *Proc. Natl. Acad. Sci. U. S. A.*, 1987, **84**, 2297–2301.
- 115 T. P. Hicks, *Prog. Neurobiol.*, 1984, **22**, 185–240.
- 116 N. R. Herr, B. M. Kile, R. M. Carelli and R. M. Wightman, *Anal. Chem.*, 2008, **80**, 8635–8641.
- 117 D. C. Kirkpatrick, L. R. Walton, M. A. Edwards and R. M. Wightman, *Analyst*, 2016, **141**, 1930–1938.
- 118 D. C. Kirkpatrick, M. A. Edwards, P. A. Flowers and R. M. Wightman, *Anal. Chem.*, 2014, **86**, 9909–9916.
- 119 Y. Guy, A. H. Faraji, C. A. Gavigan, T. G. Strein and S. G. Weber, *Anal. Chem.*, 2012, **84**, 2179–87.
- 120 Y. Xiao, E. Zhang, J. Zhang, Y. Dai, Z. Yang, H. E. M. Christensen, J. Ulstrup and F. Zhao, *Sci. Adv.*, 2017, **3**, e1700623.
- 121 J. Wingender, T. R. Neu and H.-C. Flemming, in *Microbial Extracellular Polymeric Substances*, Springer Berlin Heidelberg, Berlin, Heidelberg, 1999, pp. 1–19.
- 122 B. Gottenbos, D. W. Grijpma, H. C. van der Mei, J. Feijen and H. J. Busscher, *J. Antimicrob. Chemother.*, **48**, 7–13.
- 123 K. Colville, N. Tompkins, A. D. Rutenberg and M. H. Jericho, *Langmuir*, 2010, **26**, 2639–2644.
- 124 M. Schwab, C. Bergonzi, J. Sakkos, C. Staley, Q. Zhang, M. J. Sadowsky, A. Aksan and M. Elias, *Front. Microbiol.*, 2019, **10**, 611.
- 125 M. Beeby, J. C. Gumbart, B. Roux and G. J. Jensen, *Mol. Microbiol.*, 2013, **88**, 664–72.

- 126 A. J. Park, J. P. Okhovat and J. Kim, *Clin. Basic Immunodermatology Second Ed.*, 2017, 81–95.
- 127 Y. Liang, J. H. K. Pfisterer, D. McLaughlin, C. Csoklich, L. Seidl, A. S. Bandarenka and O. Schneider, *Small Methods*, 2019, **3**, 1800387.
- 128 L. C. Yule, C. L. Bentley, G. West, B. A. Shollock and P. R. Unwin, *Electrochim. Acta*, 2019, **298**, 80–88.
- 129 Y. E. Korchev, Y. A. Negulyaev, C. R. W. Edwards, I. Vodyanoy and M. J. Lab, *Nat. Cell Biol.*, 2000, **2**, 616–619.
- 130 A. Belianinov, A. V. Ievlev, M. Lorenz, N. Borodinov, B. Doughty, S. V. Kalinin, F. M. Fernández and O. S. Ovchinnikova, *ACS Nano*, 2018, **12**, 11798–11818.
- 131 K. Thorn, *Mol. Biol. Cell*, 2016, **27**, 219–22.
- 132 A. Rzhetskii, *Biosensors*, 2019, **9**, 25.
- 133 Y. Yamamoto and K. Shinohara, *Anat. Rec.*, 2002, **269**, 217–223.
- 134 S. So, M. Kim, D. Lee, D. M. Nguyen and J. Rho, *Appl. Spectrosc. Rev.*, 2018, **53**, 290–312.
- 135 M. J. Sanderson, I. Smith, I. Parker and M. D. Bootman, *Cold Spring Harb. Protoc.*, 2014, **2014**, pdb.top071795.
- 136 L. Opilik, T. Schmid and R. Zenobi, *Annu. Rev. Anal. Chem.*, 2013, **6**, 379–398.
- 137 R. Zhang, Y. Zhang, Z. C. Dong, S. Jiang, C. Zhang, L. G. Chen, L. Zhang, Y. Liao, J. Aizpurua, Y. Luo, J. L. Yang and J. G. Hou, *Nature*, 2013, **498**, 82–86.
- 138 R. Robelek and J. Wegener, *Biosens. Bioelectron.*, 2010, **25**, 1221–1224.
- 139 J.-S. Maltais, J.-B. Denault, L. Gendron and M. Grandbois, *Apoptosis*, 2012, **17**, 916–925.
- 140 C. L. Howe, K. F. Webb, S. A. Abayzeed, D. J. Anderson, C. Denning and N. A. Russell, *J. Phys. D. Appl. Phys.*, 2019, **52**, 104001.
- 141 L. Ma, Q. Ouyang, G. C. Werthmann, H. M. Thompson and E. M. Morrow, *Front. Cell Dev. Biol.*, 2017, **5**, 71.
- 142 A. Ettinger and T. Wittmann, *Methods Cell Biol.*, 2014, **123**, 77.
- 143 *Editorial: Beyond the diffraction limit*, Nature Publishing Group, 2009, vol. 3.
- 144 N. de Jonge and F. M. Ross, *Nat. Nanotechnol.*, 2011, **6**, 695–704.
- 145 D. J. Barber, *Opt. Acta Int. J. Opt.*, 1984, **31**, 848–848.

- 146 M. J. Zachman, E. Asenath-Smith, L. A. Estroff and L. F. Kourkoutis, *Microsc. Microanal.*, 2016, **22**, 1338–1349.
- 147 J. J. Bozzola and L. D. Russell, *Electron Microscopy: Principles and Techniques for Biologists.*, Jones & Bartlett Pub, Burlington, 1999.
- 148 G. Binnig, H. Rohrer, C. Gerber and E. Weibel, *Phys. Rev. Lett.*, 1982, **49**, 57–61.
- 149 G. Binnig, C. F. Quate and C. Gerber, *Phys. Rev. Lett.*, 1986, **56**, 930–933.
- 150 A. J. Bard, F. R. F. Fan, J. Kwak and O. Lev, *Anal. Chem.*, 1989, **61**, 132–138.
- 151 H. Y. Liu, F. R. F. Fan, C. W. Lin and A. J. Bard, *J. Am. Chem. Soc.*, 1986, **108**, 3838–3839.
- 152 N. X. West and A. Joiner, *J. Dent.*, 2014, **42**, S2–S11.
- 153 R. C. Engstrom, M. Weber, D. J. Wunder, R. Burgess and S. Winquist, *Anal. Chem.*, 1986, **58**, 844–848.
- 154 J. A. Stroscio and W. J. Kaiser, *Scanning tunneling microscopy*, Academic Press, New York, 1st edn., 1993.
- 155 H.-J. Gao and L. Gao, *Prog. Surf. Sci.*, 2010, **85**, 28–91.
- 156 A. M. Moore and P. S. Weiss, *Annu. Rev. Anal. Chem.*, 2008, **1**, 857–882.
- 157 T. Waldmann, J. Klein, H. E. Hoster and R. J. Behm, *ChemPhysChem*, 2013, **14**, 162–169.
- 158 G. Schitter and M. J. Rost, *Mater. Today*, 2008, **11**, 40–48.
- 159 A. Gustafsson, N. Okabayashi, A. Peronio, F. J. Giessibl and M. Paulsson, *Phys. Rev. B*, 2017, **96**, 085415.
- 160 G. Serrano, B. Bonanni, T. Kosmala, M. Di Giovannantonio, U. Diebold, K. Wandelt and C. Goletti, *Beilstein J. Nanotechnol.*, 2015, **6**, 438–443.
- 161 P. C. Braga and D. Ricci, *Atomic Force Microscopy*, Humana Press, New Jersey, 2003, vol. 242.
- 162 P. K. Viji Babu, C. Rianna, U. Mirastschijski and M. Radmacher, *Sci. Rep.*, 2019, **9**, 12317.
- 163 F. J. Giessibl, *Rev. Mod. Phys.*, 2003, **75**, 949–983.
- 164 S. Xu and M. F. Arnsdorf, *Proc. Natl. Acad. Sci. U. S. A.*, 1995, **92**, 10384–8.
- 165 L. N. Kantorovich, A. I. Livshits and M. Stoneham, *J. Phys. Condens. Matter*, 2000, **12**, 795–814.
- 166 D. Esteban-Ferrer, M. A. Edwards, L. Fumagalli, A. Juárez and G. Gomila,

- 2019, **13**, 9.
- 167 T. Burnett, R. Yakimova and O. Kazakova, *Nano Lett.*, 2011, **11**, 2324–2328.
  - 168 A. Mascaro, Y. Miyahara, T. Enright, O. E. Dagdeviren and P. Grütter, *Beilstein J. Nanotechnol.*, 2019, **10**, 617–633.
  - 169 K. Araki, Y. Ie, Y. Aso, H. Ohoyama and T. Matsumoto, *Commun. Phys.*, 2019, **2**, 10.
  - 170 M. Nonnenmacher, M. P. O’Boyle and H. K. Wickramasinghe, *Appl. Phys. Lett.*, 1991, **58**, 2921–2923.
  - 171 W. Melitz, J. Shen, A. C. Kummel and S. Lee, *Surf. Sci. Rep.*, 2011, **66**, 1–27.
  - 172 N. G. Clack, K. Salaita and J. T. Groves, *Nat. Biotechnol.*, 2008, **26**, 825–830.
  - 173 E. Finot, Y. Leonenko, B. Moores, L. Eng, M. Amrein and Z. Leonenko, *Langmuir*, 2010, **26**, 1929–1935.
  - 174 C.-C. Chen, Y. Zhou and L. A. Baker, *Annu. Rev. Anal. Chem.*, 2012, **5**, 207–228.
  - 175 N. Ebejer, A. G. Güell, S. C. S. Lai, K. McKelvey, M. E. Snowden and P. R. Unwin, *Annu. Rev. Anal. Chem.*, 2013, **6**, 329–351.
  - 176 E. Daviddi, K. L. Gonos, A. W. Colburn, C. L. Bentley and P. R. Unwin, *Anal. Chem.*, 2019, **91**, 9229–9237.
  - 177 M. Gonsalves, A. L. Barker, J. V. Macpherson, P. R. Unwin, D. O’Hare and C. P. Winlove, *Biophys. J.*, 2000, **78**, 1578–1588.
  - 178 D. Momotenko, K. McKelvey, M. Kang, G. N. Meloni and P. R. Unwin, *Anal. Chem.*, 2016, **88**, 2838–2846.
  - 179 A. S. Parker, R. Al Botros, S. L. Kinnear, M. E. Snowden, K. McKelvey, A. T. Ashcroft, M. Carvell, A. Joiner, M. Peruffo, C. Philpotts and P. R. Unwin, *J. Colloid Interface Sci.*, 2016, **476**, 94–102.
  - 180 M. A. Edwards, S. Martin, A. L. Whitworth, J. V Macpherson and P. R. Unwin, *Physiol. Meas.*, 2006, **27**, R63–R108.
  - 181 B. R. Horrocks, M. V. Mirkin, D. T. Pierce, A. J. Bard, G. Nagy and K. Toth, *Anal. Chem.*, 1993, **65**, 1213–1224.
  - 182 Y.-L. Ying, Z. Ding, D. Zhan and Y.-T. Long, *Chem. Sci.*, 2017, **8**, 3338–3348.
  - 183 F. Conzuelo, A. Schulte and W. Schuhmann, *Proceedings. Math. Phys. Eng. Sci.*, 2018, **474**, 20180409.
  - 184 C. A. McGeouch, M. A. Edwards, M. M. Mbogoro, C. Parkinson and P. R.



- Unwin, *Anal. Chem.*, 2010, **82**, 9322–9328.
- 185 C. A. Morris, A. K. Friedman and L. A. Baker, *Analyst*, 2010, **135**, 2190–2202.
- 186 S. Zhang, M. Li, B. Su and Y. Shao, *Annu. Rev. Anal. Chem.*, 2018, **11**, 265–286.
- 187 C. L. Bentley, M. Kang and P. R. Unwin, *Curr. Opin. Electrochem.*, 2017, **6**, 23–30.
- 188 B. Tao, P. R. Unwin and C. L. Bentley, *J. Phys. Chem. C*, 2020, **124**, 789–798.
- 189 E. Daviddi, Z. Chen, B. Beam Massani, J. Lee, C. L. Bentley, P. R. Unwin and E. L. Ratcliff, *ACS Nano*, 2019, **13**, 13271–13284.
- 190 E. E. Oseland, Z. J. Ayres, A. Basile, D. M. Haddleton, P. Wilson and P. R. Unwin, *Chem. Commun.*, 2016, **52**, 9929–9932.
- 191 F.-F. Wang, W. Wang, X. He, L. Han, J.-Z. Zhou, Z.-Q. Tian, Z.-W. Tian and D. Zhan, *Sci. China Chem.*, 2017, **60**, 649–655.
- 192 A. Page, M. Kang, A. Armitstead, D. Perry and P. R. Unwin, *Anal. Chem.*, 2017, **89**, 3021–3028.
- 193 M. R. Nellist, Y. Chen, A. Mark, S. Gödrich, C. Stelling, J. Jiang, R. Poddar, C. Li, R. Kumar, G. Papastavrou, M. Retsch, B. S. Brunschwig, Z. Huang, C. Xiang and S. W. Boettcher, *Nanotechnology*, 2017, **28**, 095711.
- 194 L. Dorwling-Carter, M. Aramesh, H. Han, T. Zambelli and D. Momotenko, *Anal. Chem.*, 2018, **90**, 11453–11460.
- 195 F. M. Maddar, R. A. Lazenby, A. N. Patel and P. R. Unwin, *Phys. Chem. Chem. Phys.*, 2016, **18**, 26404–26411.
- 196 P. K. Hansma, B. Drake, O. Marti, S. A. C. Gould and C. B. Prater, *Science*, 1989, **243**, 641–643.
- 197 Y. E. Korchev, C. L. Bashford, M. Milovanovic, I. Vodyanoy and M. J. Lab, *Scanning ion conductance microscopy of living cells*, 1997, vol. 73.
- 198 P. Novak, C. Li, A. I. Shevchuk, R. Stepanyan, M. Caldwell, S. Hughes, T. G. Smart, J. Gorelik, V. P. Ostanin, M. J. Lab, G. W. J. Moss, G. I. Frolenkov, D. Klenerman and Y. E. Korchev, *Nat. Methods*, 2009, **6**, 279–281.
- 199 S. A. Mann, G. Hoffmann, A. Hengstenberg, W. Schuhmann and I. D. Dietzel, *J. Neurosci. Methods*, 2002, **116**, 113–117.
- 200 D. Perry, D. Momotenko, R. A. Lazenby, M. Kang and P. R. Unwin, *Anal. Chem.*, 2016, **88**, 5523–5530.

- 201 N. Schierbaum, M. Hack, O. Betz and T. E. Schäffer, *Anal. Chem.*, 2018, **90**, 5048–5054.
- 202 J. Rheinlaender and T. E. Schäffer, *J. Appl. Phys.*, 2009, **105**, 094905.
- 203 A. E. Weber and L. A. Baker, *J. Electrochem. Soc.*, 2014, **161**, H924–H929.
- 204 A. I. Shevchuk, G. I. Frolenkov, D. Sánchez, P. S. James, N. Freedman, M. J. Lab, R. Jones, D. Klenerman and Y. E. Korchev, *Angew. Chemie - Int. Ed.*, 2006, **45**, 2212–2216.
- 205 M. Choi and L. A. Baker, *Anal. Chem.*, 2018, **90**, 11797–11801.
- 206 R. W. Clarke, A. Zhukov, O. Richards, N. Johnson, V. Ostanin and D. Klenerman, *J. Am. Chem. Soc.*, 2013, **135**, 322–329.
- 207 D. Momotenko, J. C. Byers, K. McKelvey, M. Kang and P. R. Unwin, *ACS Nano*, 2015, **9**, 8942–8952.
- 208 A. Page, D. Perry, P. Young, D. A. Mitchell, B. G. Frenguelli and P. R. Unwin, *Anal. Chem.*, 2016, **88**, 10854–10859.
- 209 H. Ida, Y. Takahashi, A. Kumatani, H. Shiku and T. Matsue, *Anal. Chem.*, 2017, **89**, 6015–6020.
- 210 S. Simeonov and T. E. Schäffer, *Nanoscale*, 2019, **11**, 8579–8587.
- 211 S. Watanabe and T. Ando, *Appl. Phys. Lett.*, 2017, **111**, 113106.
- 212 A. C. Vélez-Ortega, O. Belov, P. Novak, S. A. Rawashdeh, G. P. Sinha, Y. E. Korchev and G. I. Frolenkov, *Biophys. J.*, 2014, **106**, 797a–798a.
- 213 C. Li, N. Johnson, V. Ostanin, A. Shevchuk, L. Ying, Y. Korchev and D. Klenerman, *Prog. Nat. Sci.*, 2008, **18**, 671–677.
- 214 K. McKelvey, D. Perry, J. C. Byers, A. W. Colburn and P. R. Unwin, *Anal. Chem.*, 2014, **86**, 14.
- 215 J. Rheinlaender, T. E. Schä and T. E. Schäffer, *Anal. Chem.*, 2017, **89**, 11875–11880.
- 216 L. I. Stephens and J. Mauzeroll, *J. Chem. Educ.*, 2019, **96**, 2217–2224.
- 217 T. Nann and J. Heinze, *Electrochem. commun.*, 1999, **1**, 289–294.
- 218 D. G. Haywood, Z. D. Harms and S. C. Jacobson, *Anal. Chem.*, 2014, **86**, 11174–11180.
- 219 D. Momotenko, F. Cortés-Salazar, J. Josserand, S. Liu, Y. Shao and H. H. Girault, *Phys. Chem. Chem. Phys.*, 2011, **13**, 5430–5440.
- 220 J. F. Pietschmann, M. T. Wolfram, M. Burger, C. Trautmann, G. Nguyen, M.

- Pevarnik, V. Bayer and Z. Siwy, *Phys. Chem. Chem. Phys.*, 2013, **15**, 16917–16926.
- 221 W.-J. Lan, D. A. Holden and H. S. White, *J. Am. Chem. Soc.*, 2011, **133**, 13300–13303.
- 222 C. Weit, A. J. Bard and S. W. Feldberg, *Anal. Chem.*, 1997, **69**, 4627–4633.
- 223 L. Cao, W. Guo, Y. Wang and L. Jiang, *Langmuir*, 2012, **28**, 2194–2199.
- 224 D. Momotenko and H. H. Girault, *J. Am. Chem. Soc.*, 2011, **133**, 14496–14499.
- 225 Y. Qiu, Z. S. Siwy and M. Wanunu, *Anal. Chem.*, 2019, **91**, 996–1004.
- 226 D. Perry, R. Al Botros, D. Momotenko, S. L. Kinnear and P. R. Unwin, *ACS Nano*, 2015, **9**, 7266–7276.
- 227 M. R. Powell, N. Sa, M. Davenport, K. Healy, I. Vlassioug, S. E. Létant, L. A. Baker and Z. S. Siwy, *J. Phys. Chem. C*, 2011, **115**, 8775–8783.
- 228 R. Singhal and M. Z. Ansari, *Procedia Technol.*, 2016, **23**, 447–453.
- 229 J. Experton, X. Wu and C. R. Martin, *Nanomaterials*, 2017, **7**, 445.
- 230 I. Vlassioug and Z. S. Siwy, *Nano Lett.*, 2007, **7**, 552–556.
- 231 M. Ali, S. Mafe, P. Ramirez, R. Neumann and W. Ensinger, *Langmuir*, 2009, **25**, 11993–11997.
- 232 N. Sa and L. A. Baker, *J. Am. Chem. Soc.*, 2011, **133**, 10398–10401.
- 233 W. Shi, N. Sa, R. Thakar and L. A. Baker, *Analyst*, 2015, **140**, 4835–4842.
- 234 M. Ali, P. Ramirez, S. Mafé, R. Neumann and W. Ensinger, *ACS Nano*, 2009, **3**, 603–608.
- 235 L. Luo, D. A. Holden and H. S. White, *ACS Nano*, 2014, **8**, 3023–3030.
- 236 P. Actis, *Small Methods*, 2018, **2**, 1700300.
- 237 E. N. Tóth, A. Lohith, M. Mondal, J. Guo, A. Fukamizu and N. Pourmand, *J. Biol. Chem.*, 2018, **293**, 4940–4951.
- 238 S. Schobesberger, P. Jönsson, A. Buzuk, Y. Korchev, J. Siggers and J. Gorelik, *Biophys. J.*, 2016, **110**, 141–146.
- 239 M. Kang, D. Perry, C. L. Bentley, G. West, A. Page and P. R. Unwin, *ACS Nano*, 2017, **11**, 9525–9535.
- 240 C. C. Chen, M. A. Derylo and L. A. Baker, *Anal. Chem.*, 2009, **81**, 4742–4751.
- 241 J. D. Piper, C. Li, C. J. Lo, R. Berry, Y. Korchev, L. Ying and D. Klenerman, *J. Am. Chem. Soc.*, 2008, **130**, 10386–10393.
- 242 A. P. Ivanov, P. Actis, P. Jönsson, D. Klenerman, Y. Korchev and J. B. Edel,

- ACS Nano*, 2015, **9**, 3587–3594.
- 243 A. Bruckbauer, L. Ying, A. M. Rothery, D. Zhou, A. I. Shevchuk, C. Abell, Y. E. Korchev and D. Klenerman, *J. Am. Chem. Soc.*, 2002, **124**, 8810–8811.
  - 244 A. Bruckbauer, P. James, D. Zhou, W. Y. Ji, D. Excell, Y. Korchev, R. Jones and D. Klenerman, *Biophys. J.*, 2007, **93**, 3120–3131.
  - 245 H. Fathali and A.-S. Cans, *Pflügers Arch. - Eur. J. Physiol.*, 2018, **470**, 125–134.
  - 246 L. Burkinshaw, R. Clarke, P. Novak, Y. Korchev and D. Klenerman, *Biophys. J.*, 2010, **98**, 395a.
  - 247 C. Zhu, L. Zhou, M. Choi and L. A. Baker, *ChemElectroChem*, 2018, **5**, 2986–2990.
  - 248 F. M. Maddar, D. Perry, R. Brooks, A. Page and P. R. Unwin, *Anal. Chem.*, 2019, **91**, 4632–4639.
  - 249 N. Sa, W. J. Lan, W. Shi and L. A. Baker, *ACS Nano*, 2013, **7**, 11272–11282.
  - 250 K. McKelvey, S. L. Kinnear, D. Perry, D. Momotenko and P. R. Unwin, *J. Am. Chem. Soc.*, 2014, **136**, 13735–13744.
  - 251 D. Perry, B. Paulose Nadappuram, D. Momotenko, P. D. Voyias, A. Page, G. Tripathi, B. G. Frenguelli and P. R. Unwin, *J. Am. Chem. Soc.*, 2016, **138**, 3152–3160.

## **2 Surface Effects on Electroosmotic Flow-Delivery of Neutral Molecules using Scanning Ion Conductance Microscopy (SICM)**

This chapter explores the ability of SICM for the controlled delivery of species to a substrate. The substrate used is a carbon fiber (CF) UME which is used to quantify the delivered hydroquinone (HQ) through oxidation. This allows the delivery conditions and the effects of the substrate properties to be examined in relation to the quantity of HQ delivered to the surface. FEM simulations are used to examine the underlying interactions involved in determining this response and further understanding of fundamental mechanisms underpinning SICM. The effects of substrate charge and reactivity upon the EOF profile at the substrate-probe interface are described. The effects of these mechanisms upon the flux of species from the nanopipette are investigated and can be used to inform parameterisation of future delivery experiments when delivering to complex active surfaces.

This chapter is in preparation to be submitted for publication. All experiments and simulations were performed by the author with advice from Dr. David Perry, with additional advice from Baoping Chen on experiments. The manuscript was written by the author.

## **2.1 Abstract**

SICM is a powerful and versatile technique which allows for the probing of interfacial properties and processes at a wide range of surfaces. The methodology discussed and developed herein builds on previous work that demonstrated how SICM could be used for the controlled delivery of charged species to an electroactive surface through the application of a driving delivery potential of suitable polarity. This work provides a comprehensive understanding of how, through tuning the SICM experimental design, neutral species can also be held or delivered from the nanopipette and examines the additional factors that must be considered in this case. Manipulation of the applied SICM bias provides control over the electroosmotic flow (EOF) through the nanopipette orifice which in turn allows neutral species to be delivered to surfaces in a controlled manner. The turnover of the species at an electroactive surface provides quantitative information on the rate of delivery from the nanopipette, whilst simultaneous measurements of the tip ionic current allows detection of the surface charge. By combining experimental results with finite element method (FEM) simulations it is possible to examine the transport mechanisms underpinning SICM. It is shown that EOF, and therefore species delivery, has a strong dependence upon the charge of the substrate surface. This effect must be accounted for to quantify the effects of the delivered species on the substrate.

## **2.2 Introduction**

SICM has transitioned beyond its original use as a powerful non-contact topographical imaging technique, becoming increasingly versatile in the wealth of information it can provide about interfaces.<sup>1,2</sup> SICM experiments utilize a nanopipette filled with electrolyte solution to probe an interface which is immersed in an electrolyte bath. Two quasi-reference counter electrodes (QRCEs) are used, one in the bulk electrolyte and the other within the nanopipette. A bias between the two QRCEs is applied to generate an ionic current through the nanopipette orifice. As the nanopipette approaches a surface, to distances on the scale of the orifice diameter, the ionic current generally decreases due to the increased gap resistance.<sup>3</sup> However, the ionic current is also influenced by properties and processes which change the local conductivity at the interface and variations in the SICM current can provide information on surface charge, interfacial reactions, and other processes.<sup>2,4-8</sup>

Localized delivery of molecules on the microscale and nanoscale using iontophoresis has a long history in the fields of neurobiology and cellular signalling, where it has become a powerful aspect of techniques for the elucidation of signalling pathways.<sup>9,10</sup> On the SICM instrumental platform, scanning regimes have been developed which enable the synchronous mapping of substrate topography together with the controlled delivery of species from the nanopipette tip.<sup>11–17</sup> The efflux of the delivered species is controlled *via* the bias between the two QRCEs with the resulting flux defined by the Nernst-Planck equation (Section 2.6.1, Equation 2.1) (Figure 2.1a). For charged molecules, ion migration is a significant factor controlling transport into, or out of, the nanopipette.<sup>15,17,18</sup>

As we explore in this paper, the transport of neutral molecules can be controlled by exploiting and modulating EOF, a phenomena that typically results from the increased concentration of cations in the double layer at the negatively charged walls of borosilicate and quartz nanopipettes in aqueous solutions (Figure 2.1b).<sup>18</sup> The imbalance of mobile charges, causes a net flux towards the cathode as the cations migrate, generating EOF and the consequent transport of neutral species in the direction of the fluid flow.<sup>18</sup>

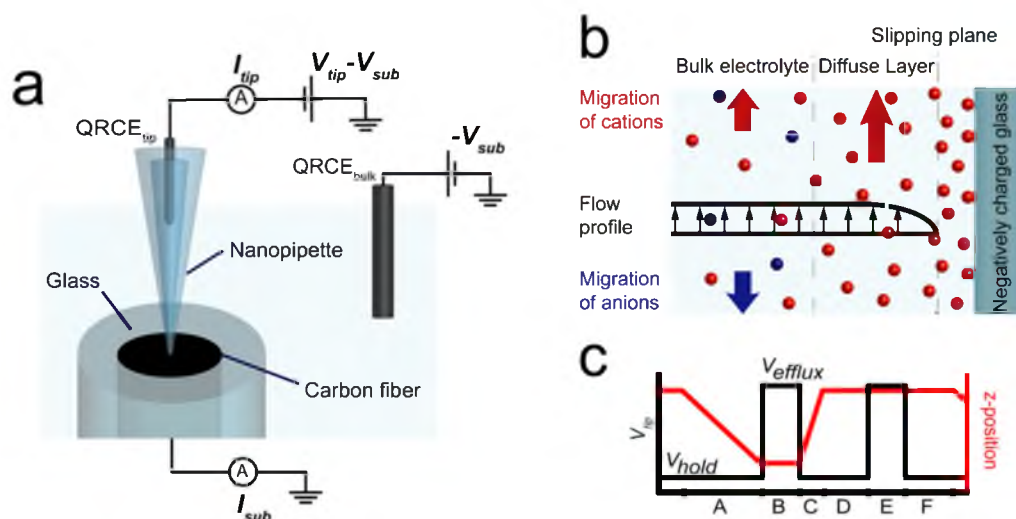


**Figure 2.1 SICM delivery methodology.** (a) Schematic of the experimental setup used for simultaneous mapping of substrate topography and electrochemical activity of neutral molecules delivered from the SICM nanopipette tip. (b) Diagram of the mechanism driving EOF in an SICM nanopipette tip, anions (blue) migrate towards

the anode (in this case QRCE2 in the tip), while cations (red) migrate towards the cathode (QRCE1 in the bulk solution). There is a net flow of the solvent and neutral species into the tip. (c) An outline of changes in the z-position (red) and tip potential ( $V_{tip}$ , black) at each pixel in the scan hopping regime implemented experimentally herein: (A) tip approaches the substrate with a potential applied to hold the neutral molecules (to be delivered) within the tip ( $V_{hold}$ ), (B) the potential is changed to expel the neutral analyte from the tip ( $V_{efflux}$ ), (C) the potential returns to  $V_{hold}$  as the tip is retracted from the surface into bulk solution, (D) the tip is held in bulk while the system re-equilibrates, (E) the pulse ( $V_{efflux}$ ) is repeated in bulk solution (to self-reference the current signal for comparison to that with the tip near the surface), (F) the potential is returned to  $V_{hold}$  and again re-equilibrated before subsequent translation to the next pixel in the image, where the process is repeated.

A number of factors have been explored and manipulated to influence delivery from nanopipettes, including the pipette wall charge,<sup>19</sup> pressure,<sup>13</sup> voltage,<sup>13,20,21</sup> and topographical effects.<sup>14</sup> Quantification has largely focussed on measurements in the microiontophoresis regime using fluorescence microscopy, biological response, electrochemical response, development of analytical expressions, and numerical simulations to assess delivery.<sup>12–17,19–22</sup> Delivery under the microiontophoresis regime has been well characterised through a combination of experiments and simulation.<sup>20,21</sup> Babakinejad *et al.* provided one of the first quantitative considerations of the SICM delivery regime, using the fluorescent response of a stimulated cell to quantify the response to the delivery of capsaicin with respect to the delivery potential.<sup>13</sup> A combination of FEM simulations and spatial measurements with a carbon nanoelectrode were used to define the distribution of species being delivered from the nanopipette. The same group used FEM simulations to examine the effects of substrate geometry upon delivered concentrations.<sup>14</sup> Shi *et al.* have also examined the effects of nanopipette wall charge upon holding and delivery efficacy through fluorescence measurements.<sup>19</sup> These methodologies allow mapping of cellular responses and therefore receptor and pore distributions.<sup>10</sup>



Recent work has shown that SICM can be used to simultaneously map the surface charge of a substrate while quantitatively delivering charged species from the tip.<sup>17</sup> Through FEM simulations it was observed that for the delivery of charged species from an SICM nanopipette to an ultramicroelectrode (UME) substrate, surface charge had a significant effect on the resulting nanopipette ionic current ( $I_{tip}$ ). Detailed consideration of the effects of surface charge and reactions upon transport to the surface is required for accurate determination of the local surface concentrations and therefore local reactivity. Neutral species are delivered mainly through EOF which is generated at charged surfaces, the surface charge is therefore intimately coupled to the quantity transported to the surface, an effect is examined. Heterogeneous charge has been reported at numerous interfaces, including those investigated through SICM charge mapping methodologies such as mammalian cells<sup>23</sup> and electrode surfaces.<sup>17</sup> Quantitative analysis of the systems response to delivered species requires accurate determination of the effects of surface charge upon SICM delivery methodologies.

Herein, we apply this platform to investigate the delivery of the neutral species hydroquinone (HQ) to a carbon fiber (CF) UME. This type of system is of interest, because the delivery of neutral species is strongly coupled to the surface charge of the substrate through EOF, a process which is intimately related to the properties of the nanopipette and electrolyte.<sup>24</sup> HQ delivery to the substrate was controlled by manipulating the strength and direction of EOF by altering the applied nanopipette tip bias, and the oxidation of HQ to benzoquinone (BQ) was driven at the CF UME. In unbuffered solutions, around pH 7.4, HQ undergoes a two-electron, two-proton oxidation which depends upon the local proton concentration.<sup>25</sup> In this case, the substrate was held at a high overpotential to account for the unbuffered solution, and thereby allow contribution of the resultant proton fluxes to  $I_{tip}$  to be assessed.  $I_{tip}$  and the substrate current  $I_{sub}$  (see Figure 2.1a) were recorded throughout and provided an extensive dataset that was used to quantitatively examine the role of EOF in SICM delivery.

## 2.3 Materials and Methods

### 2.3.1 Solutions

All chemicals were purchased from Sigma Aldrich and used as received. For all experiments 20 mM KCl (>99%) was used as the supporting electrolyte in both the nanopipette and bulk solution, but the nanopipette also contained 20 mM HQ (>99.5%). All solutions were prepared with Milli-Q reagent grade water (resistivity *ca.* 18.2 M $\Omega$  cm at 25 °C) and filtered through a 0.2  $\mu$ m filter (Minisart, cellulose acetate) prior to use.

### 2.3.2 Nanopipettes

Nanopipettes were pulled from borosilicate glass capillaries (o.d. 1.2 mm, i.d. 0.69 mm, Harvard Apparatus) to *ca.* 200 nm internal diameter at the tapered end, using a laser puller (P-2000, Sutter Instruments). Pulling parameters used were as follows: Line 1: Heat 330, Fil 3, Vel 30, Del 220, Pul -; Line 2: Heat 300, Fil 3, Vel 40, Del 180, Pul 120. A Zeiss Gemini 500 scanning electron microscope (SEM) equipped with scanning transmission electron microscopy mode (STEM), was used to characterize the nanopipette geometry for FEM simulations. A representative STEM image of a nanopipette is shown in Figure 2.2.



**Figure 2.2 Scanning transmission electron microscopy (STEM) image of a representative nanopipette.** Tip diameter of approximately 180 nm.

### 2.3.3 Quasi-Reference Counter Electrodes

Chloridized silver wires were used as QRCEs (Ag/AgCl, 20 mM KCl), one in the bulk electrolyte (QRCE<sub>bulk</sub>, Figure 1a) and a second placed inside the nanopipette (QRCE<sub>tip</sub>, Figure 1a). These electrodes are stable over long periods.<sup>26</sup> QRCE<sub>bulk</sub> was also used as the QRCE for controlling the substrate (CF-UME) bias. All potentials quoted in this paper are with respect to the potentials applied to QRCE<sub>bulk</sub>.

### 2.3.4 CF-UME Fabrication and Bulk HQ Voltammetry

Carbon fiber (CF) UMEs were fabricated according to established procedures with some modifications.<sup>17,27</sup> Conductive silver paint (186-3600, RS PRO) was used to connect a ~7  $\mu\text{m}$  diameter CF (XAS grade, Goodfellow) to a thin copper wire, this was inserted into the end of a pulled and sealed borosilicate glass capillary. A moderate vacuum was applied to using a vacuum pump (GLD-136C, ULVAC), and a seal between the glass and the CF formed by heating at approximately 85 °C. A larger copper wire was then inserted into the capillary and solder used to make an electrical contact to the thin copper wire. The UME surface was polished using a micropipette polishing wheel with a diamond particles pad (diameter 0.1  $\mu\text{m}$ , Buehler), followed by polishing by hand with an alumina slurry (diameter 0.05  $\mu\text{m}$ ) on a soft microfiber polishing pad (Buehler), and finally a soft microfiber polishing pad with water to produce the finished substrate surface.

### 2.3.5 Instrumentation

The nanopipette was mounted on a custom-designed holder and positioned above the substrate electrode using a mechanical micropositioner (Newport, M-461-XYZ-M) with the aid of a 3 MP digital camera (PixelLink, PL-B776U), equipped with a 6 $\times$  magnification lens. Coarse vertical movement of the nanopipette was achieved using a picomotor (Newport, 8303 Picomotor Actuator), and precise movement with a 38- $\mu\text{m}$ -range single-axis piezoelectric positioner (Physik Instruments, P-753.3CD). Precise lateral movement of the substrate was achieved using a two-axis piezoelectric positioner system (NanoBioS300, Mad City Labs Inc) with a range of 300  $\mu\text{m}$  on each axis. The system was installed on a vibration isolation platform (BM-8 Bench Top,

Minus K Technology). Currents were measured using home-built current–voltage converters. Instrumentation control and data collection were conducted using custom-written LabVIEW (2017, National Instruments) code through an FPGA card (7852R, National Instruments). Data were acquired at a rate of 516  $\mu$ s per data point (4  $\mu$ s sampling time and averaging of 129 sample points) for SICM mapping.

### 2.3.6 SICM Delivery and Sensing

The experimental setup has been discussed in previous work from our group and is summarised in Figure 2.1a.<sup>4,15,17,28</sup> Briefly, the QRCE in bulk solution (QRCE<sub>bulk</sub>, Figure 2.1a) was biased at a potential of  $-V_{sub}$  with respect to the substrate (working) electrode through a common ground and held constant throughout each experiment. The substrate current ( $I_{sub}$ ) was measured directly at the substrate. The ionic current ( $I_{tip}$ ) was generated by a bias of  $V_{tip}$  applied at QRCE<sub>tip</sub> with respect to QRCE<sub>bulk</sub>.

A hopping scan protocol was used in which the z-position and  $V_{tip}$  were controlled synchronously at each pixel with  $I_{tip}$  and  $I_{sub}$  measured continuously throughout (Figure 2.1c). (A) The nanopipette was translated towards the substrate surface at a rate of 3  $\mu$ m/s with QRCE<sub>tip</sub> poised at a negative potential ( $V_{hold} = -0.1, -0.2, \text{ or } -0.3$  V), generating EOF into the nanopipette (Figure 2.1b), so as to restrict the net diffusive flux of HQ from the tip, while also generating the ionic current used for tip positioning and feedback control. Upon reaching the feedback threshold (either 1.25% or 2% decrease from the bulk value of  $I_{tip}$ ) the nanopipette approach stopped, resulting in a precise working distance based upon FEM simulations (*vide infra*). (B)  $V_{tip}$  was then pulsed for 150 ms to  $V_{efflux}$ , which varied between the same value as  $V_{hold}$  and 0.4 V depending upon the experiment, causing the EOF to respond accordingly, promoting an increased efflux of HQ when the  $V_{tip}$  became more positive. (C) The tip potential was then stepped back to  $V_{hold}$  and the nanopipette retracted from the surface at 10  $\mu$ m/s into the bulk (10  $\mu$ m from the surface). A short pause (D) for 300 ms allowed re-equilibration with the bulk conditions. In experiments for which the normalized ionic current (normalized  $I_{tip}$ ) was measured, a second pulse identical to the first was performed (E), along with another pause (F) before x-y translation and

repeating the cycle at the next pixel. For experiments assessing holding potential efficacy (Figure 2.5) no bulk pulse was performed.

Topographical data were acquired from the z-position corresponding to closest approach of the nanopipette to the surface at each pixel. Throughout the entire procedure,  $V_{sub}$  was kept at a fixed value of 0.8 V to drive the transport-limited oxidation of 20 mM HQ on a 7  $\mu\text{m}$  CF electrode in 20 mM KCl (Figure 2.3).

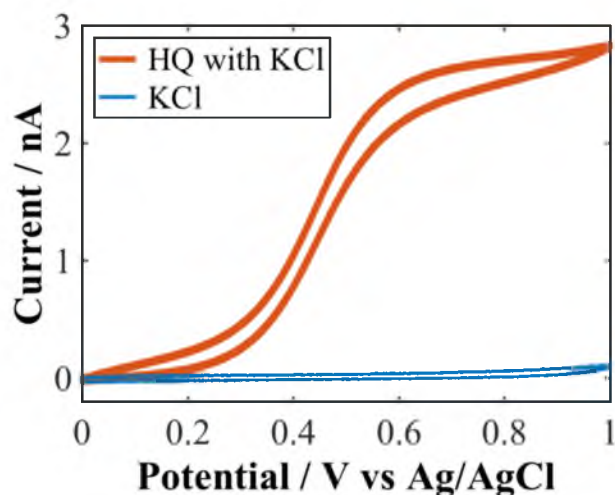


**Figure 2.3 HQ voltammetry on a CF UME.** 1 mM HQ with 20 mM KCl supporting electrolyte. The scan rate was 100 mV s<sup>-1</sup>.

### 2.3.7 FEM Simulations

Finite element method (FEM) simulations were constructed in COMSOL Multiphysics (v5.3a) as 2D axisymmetric domains, constructed using dimensions from STEM images of the nanopipettes. A schematic of the FEM simulation domain is shown in Figure 2.4. The electrostatics, transport of diluted species and laminar flow modules were used to model the experimental system. All boundaries not specifically labelled were set as no flux boundaries with no surface charges applied and a no-slip flow condition was applied to all boundaries except for the symmetry axis, B1, and B2. All potentials stated herein were applied to the upper boundary within the nanopipette, labelled B1, positioned 1 mm above the base of the nanopipette.

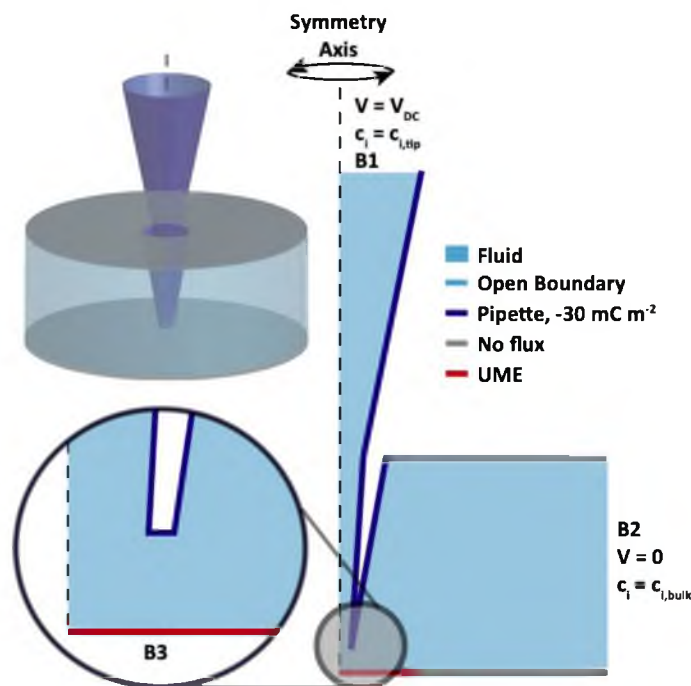


**Figure 2.4 Schematic (not to scale) of FEM simulation domain with the main boundaries labelled.**

Electrochemical flux conditions relating to HQ oxidation were applied to B3 and surface charge was applied at this locale. In simulations which considered delivery to the electrode, a sink boundary condition for the transport-limited oxidation of HQ was applied at B3 ( $[HQ] \cdot k_0$ , where  $k_0 = 100$  cm/s), reasonable for the high overpotentials applied. Integrating the flux across the electrode surface and multiplication by number of electrons transferred in HQ oxidation ( $n = 2$ ) gives  $I_{sub}$ . B2 was held at ground in all simulations whilst pipette boundaries (blue) had a surface charge density of  $-30$  mC/m<sup>2</sup> applied in all simulations, reasonable for borosilicate glass in aqueous solution under the conditions of our experiments.<sup>6</sup> The concentrations at B1 were set to  $[HQ] = 20$  mM,  $[K^+] = 20$  mM,  $[Cl^-] = 20$  mM, representing bulk solution in the nanopipette. At B2,  $[K^+] = 20$  mM,  $[Cl^-] = 20$  mM,  $[HQ] = 0$  mM conditions were maintained in all simulations, with the boundary positioned 1 mm away from the nanopipette opening laterally, sufficient to be considered bulk.

The system of differential equations was as follows. The flux  $J_i$  of each species  $i$ , was described by the Nernst-Planck equation:

$$J_i = -D_i \nabla c_i - z_i \frac{F}{RT} D_i c_i \nabla \phi + c_i u \quad (2.1)$$

and the Poisson equation defined the electric potential  $\phi$ :

$$\nabla^2 \phi = -\frac{F}{\epsilon \epsilon_0} \sum_i z_i c_i \quad (2.2)$$

where  $D_i$ ,  $z_i$  and  $c_i$  are the diffusion coefficients, charge number and concentrations of species  $i$  and  $u$  is the solution velocity described below (Equation 2.3).  $F$ ,  $R$  and  $T$  are the Faraday constant, gas constant and absolute temperature (298 K),  $\epsilon$  is the dielectric constant of the solution (78) and  $\epsilon_0$  ( $8.85 \times 10^{-12}$  F/m) is the vacuum permittivity. The diffusion coefficients at infinite dilution for  $K^+$  ( $1.96 \times 10^{-5}$  cm<sup>2</sup>/s),  $Cl^-$  ( $2.05 \times 10^{-5}$  cm<sup>2</sup>/s) and  $H^+$  ( $9.31 \times 10^{-5}$  cm<sup>2</sup>/s) were taken from the CRC handbook.<sup>29</sup> These values are reasonable because of the sufficiently dilute concentrations used and the self-referencing nature of experiments.<sup>2</sup> The diffusion coefficients for HQ and BQ were taken from literature values to be  $6.8 \times 10^{-5}$  cm<sup>2</sup>/s and  $6 \times 10^{-5}$  cm<sup>2</sup>/s, respectively.<sup>30</sup> The solution velocity was described by the incompressible Navier-Stokes equation with electroosmotic flow (EOF) incorporated, in which  $\rho$  is the solution density,  $\mu$  is the solution viscosity, and  $p$  is pressure (Equation 2.3):

$$u \nabla u = \frac{1}{\rho} (-\nabla p + \mu \nabla^2 u - F (\sum_i z_i c_i) \nabla \phi) \quad (2.3)$$

FEM simulation domains were constructed from geometries of nanopipettes measured with scanning transmission electron microscopy (STEM) (Figure 2.2). First the experimental working approach distance between the nanopipette and the surface was estimated by steady-state simulations with the boundary at the top of the pipette (Boundary B1, Figure 2.4) held at  $V_{hold}$ , the distances were taken from the distance at which the ionic current normalized to the bulk current reached the experimental approach set point; 75 nm for 1.25% (all voltages) and 30 nm for 2% (-200 mV only). Time dependent simulations of the 150 ms pulse were then performed by stepping the voltage to  $V_{efflux}$ , using the corresponding steady-state approach simulation as starting conditions for the simulation.

## 2.4 Results and Discussion

### 2.4.1 Preliminary Experiments

Delivery of BQ to Pt and CF UMEs was initially investigated, however this was not found to be quantitative for two reasons. Steady state BQ reduction on a CF UME occurs at approximately -0.5 V vs. Ag/AgCl, at this negative potential the oxygen reduction reaction generates ionic fluxes which prevents reliable approach of the nanopipette to the surface. Similar effects occur on Pt electrodes which are far more electrochemically active than CF, thus creating ionic fluxes which make approach in SICM difficult. At anodic potentials the solvent window on a CF UME is wider, therefore allowing more reliable approach to the surface when using DC-SICM feedback and allowing transport limited oxidation of HQ (Figure 2.3). These problems could be diminished by using more complex feedback types such as DM-SICM as shown in Chapter 3.

### 2.4.2 Efficacy of Hold Potentials

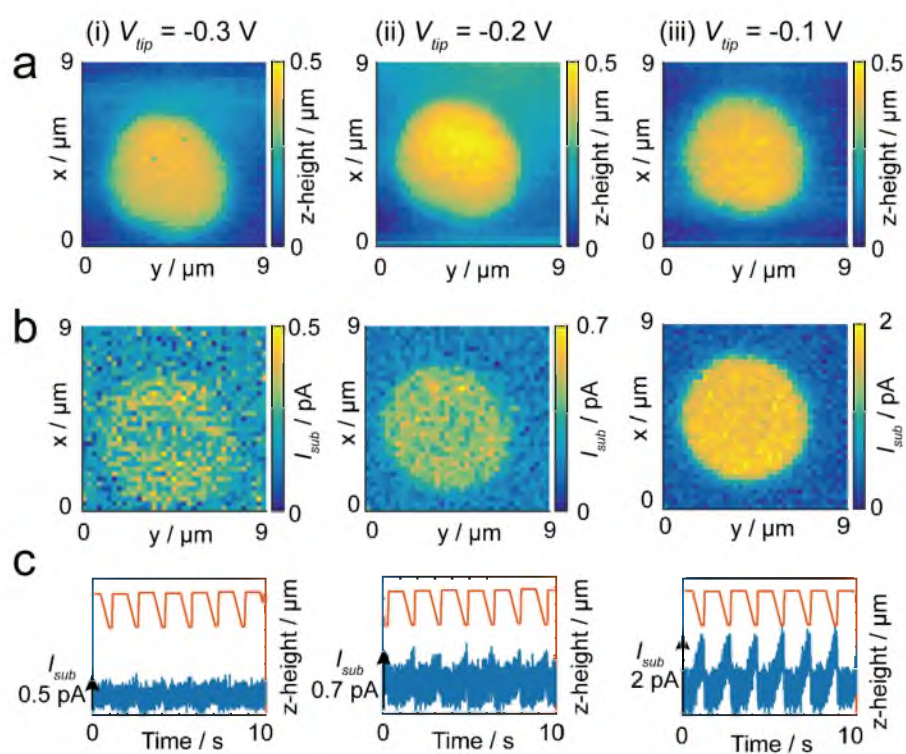
HQ was used in this study as a general model uncharged redox-active species, which has been employed previously as an EOF marker.<sup>21</sup> Oxidation of HQ occurs by a  $2e^-$ ,  $2H^+$  process in solutions with high proton availability (buffered or  $[H^+] > [HQ]$ ) and a  $2e^-$  process when  $[H^+] < [HQ]$ .<sup>25,31</sup>

We first consider the effect of  $V_{hold}$  on retaining HQ (20 mM) within the nanopipette. To this effect, the CF UME was immersed in the KCl solution and a constant bias of 0.8 V was applied, imposing a transport-limited regime as demonstrated by the cyclic voltammogram of a CF UME in 20 mM HQ with 20 mM KCl (Section 2.6.3, Figure 2.3). Initially, the efficacy of different holding potentials was examined, with delivery experiments performed while  $V_{tip}$  was set to  $V_{hold} = -0.1$ ,  $-0.2$ , and  $-0.3$  V and kept constant throughout (Figure 2.5). A feedback threshold of 1.25% and the resulting z-position at closest approach of the tip to the surface could be used to produce a topography map of the CF UME (Figure 2.5a). At each pixel the nanopipette paused at the distance defined by the feedback threshold for 150 ms, and  $V_{tip}$  bias continuously at  $V_{hold}$ , while the substrate current was recorded throughout. The



CF UME protrudes from the surrounding glass surface by a few hundred nm, due to differential polishing of the CF compared to the surrounding borosilicate glass.

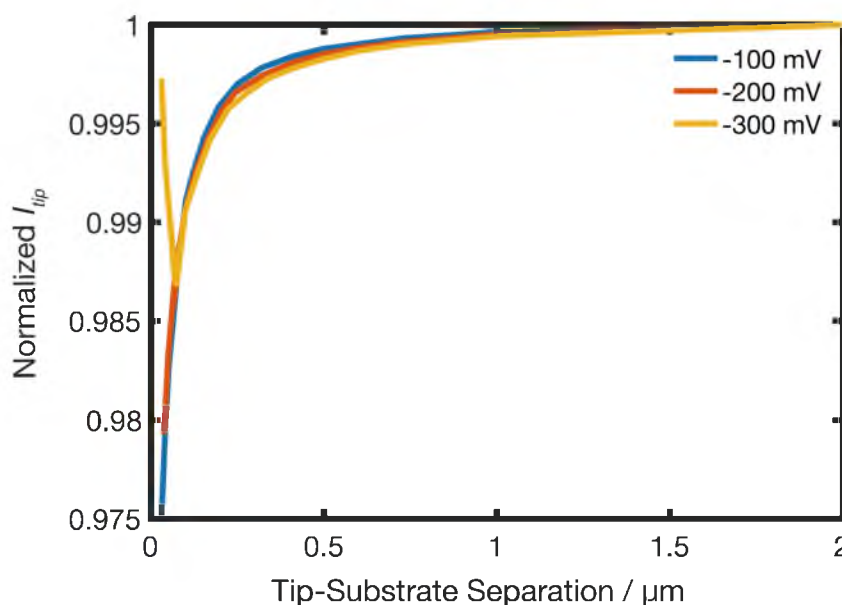
The  $I_{sub}$  map was obtained as the mean of substrate current over the final 10 ms of the pulse to reduce the contribution of noise, thus allowing the clear presentation of CF-UME reactivity maps. Increases in substrate current occur at pixels where the nanopipette is clearly positioned above the CF. The  $I_{sub}$ - $t$  transient (Figure 2.5c) increases over the duration of the approach of the nanopipette towards the substrate surface due to oxidation of HQ which is pulled from the nanopipette (akin to SECM induced transfer)<sup>32,33</sup> to an extent depending on the value of  $V_{hold}$ .



**Figure 2.5 Holding potential efficacy for delivery of HQ.** Series of simultaneously obtained (a) topography and (b)  $I_{sub}$  maps of a 7  $\mu\text{m}$  diameter CF-UME at  $V_{sub}$  of 0.8 V for the oxidation of HQ and three different  $V_{tip}$ .  $I_{sub}$ - $t$  (blue) and  $z$ -height (orange) transients recorded during the measurement of six pixels across the center of the UME are shown in (c).

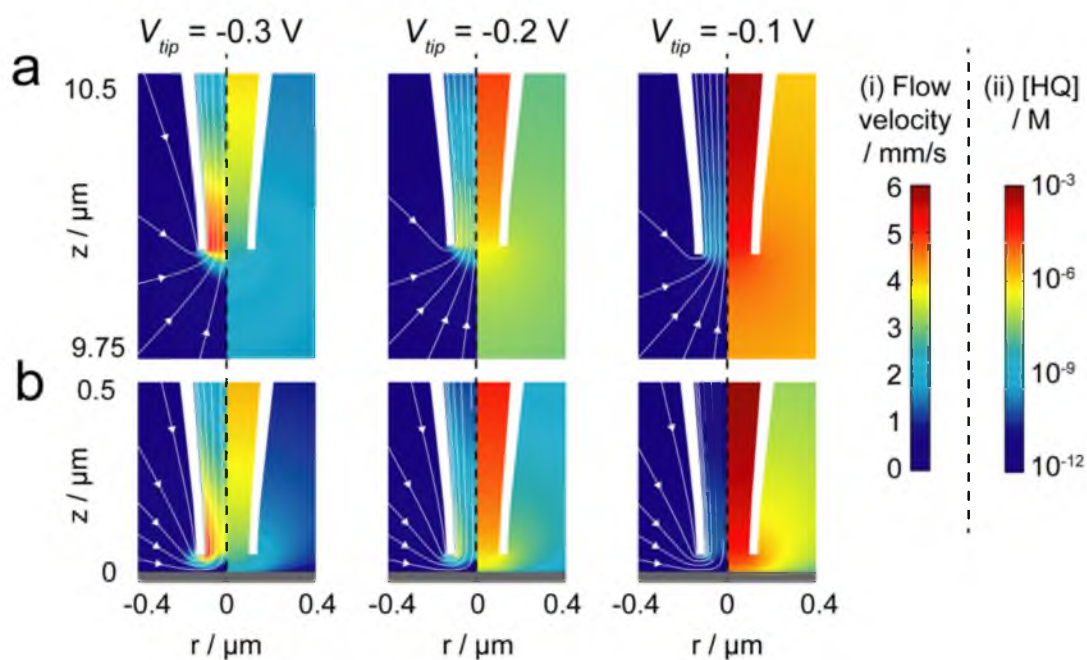
When  $V_{hold} = -0.1$  V there is a maximum current increase of approximately 2 pA at each pixel, as  $V_{hold}$  is increased in magnitude to -0.2 V and -0.3 V, there is a diminution in  $I_{sub}$  magnitude to  $\sim 0.7$  pA and  $\sim 0.5$  pA, respectively. It is clear from these experiments that the efflux of HQ from the tip is reduced by the application of a negative  $V_{hold}$  potential, but is still just detectable. FEM simulations were employed to provide deeper understanding of the underlying processes.

The approach distance was first estimated by performing steady-state simulations with the nanopipette positioned at varying heights above the UME for each  $V_{hold}$ . The approach distance was  $\sim 75$  nm for all three cases at the feedback threshold applied of 1.25% (Figure 2.6). It should be noted that for simplicity an uncharged substrate surface was assumed, but we note that (extreme) charged surfaces may affect the tip current.<sup>6,7,34</sup> The small feedback threshold was chosen to minimize such effects.<sup>4,17</sup>



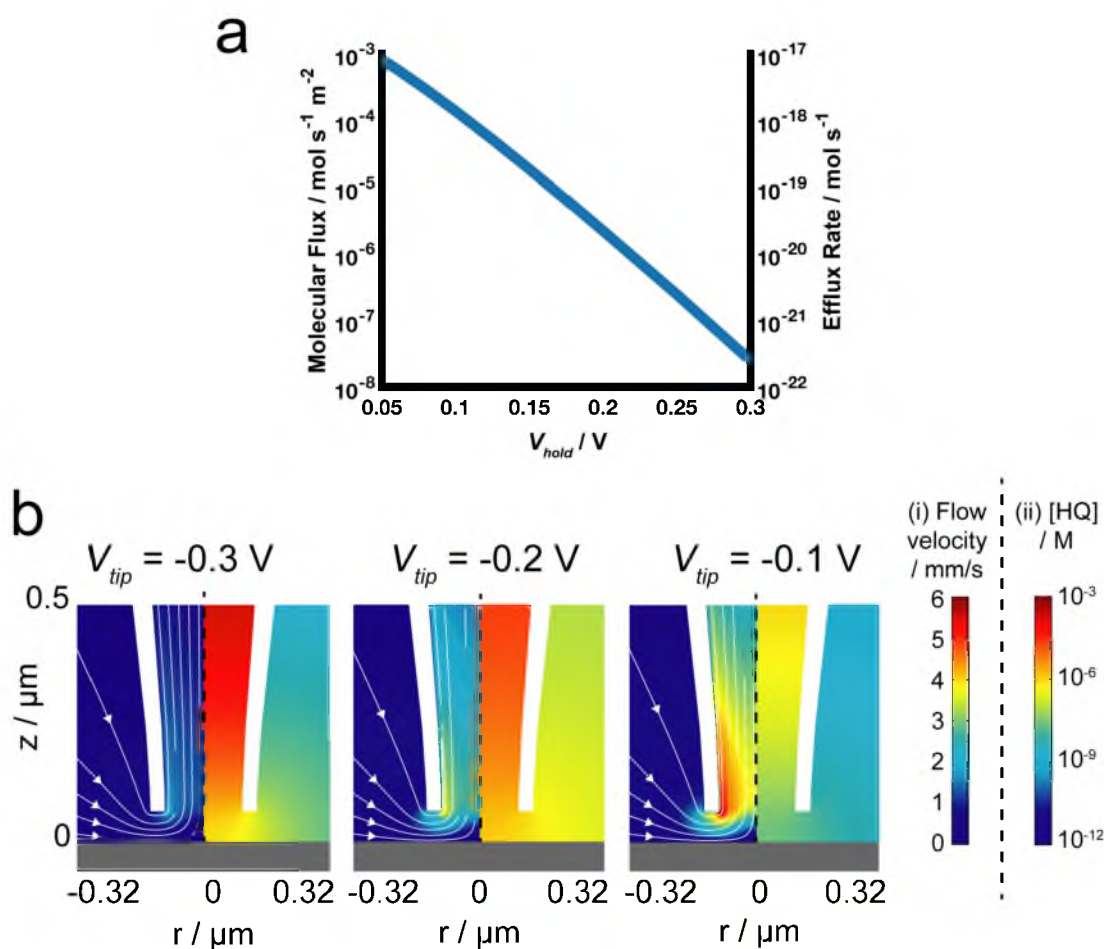
**Figure 2.6 Simulated approach curves of a nanopipette at hold biases.** Simulated approach curves for the three experimental cases of  $V_{hold} = -100$  mV (blue),  $-200$  mV (orange),  $-300$  mV (yellow), with 20 mM HQ in the tip and 20 mM KCl in tip and bulk. These yielded approach distances of 75 nm for 1.25% approach threshold in all cases, and 30 nm for 2% approach threshold for  $-200$  mV.

Figure 2.7 demonstrates the efficacy of the experimental  $V_{hold}$  in retaining HQ within the nanopipette, while the nanopipette was positioned in bulk solution. It can be seen that the rate of EOF into the tip orifice when  $V_{hold} = -0.1$  V is approximately 2 mm/s (Figure 2.7a(i)), resulting in [HQ] *ca.* 1000  $\mu$ M at a location 500 nm up the tip, in the range 10-100  $\mu$ M at the orifice, and *ca.* 1  $\mu$ M in the surrounding solution (within a 250 nm radial distance from the orifice) (Figure 2.7a(ii), -0.1 V). The concentrations observed when  $V_{hold} = -0.2$  V are approximately 2 orders of magnitude lower and for  $V_{hold} = -0.3$  V approximately 3 orders of magnitude lower than those at -0.1 V (Figure 2.7a(ii)). This trend is a result of the fluid velocity into the tip increasing to around 3-4 mm/s ( $V_{hold} = -0.2$  V) and 5-6 mm/s ( $V_{hold} = -0.3$  V) across the nanopipette orifice (Figure 2.7a(i)).



**Figure 2.7 FEM simulations of hold biases.** (a) In bulk (10  $\mu$ m from substrate) and (b) 75 nm from a UME substrate, with HQ released from the nanopipette oxidized at a transport-limited rate at the UME ( $V_{sub} = 0.8$  V). For each of the hold biases, namely  $V_{tip} = -0.3$  V,  $-0.2$  V and  $-0.1$  V, profiles of (i) the fluid velocity and (ii) [HQ] are shown. Note that the scales for [HQ] are displayed logarithmically between 1 mM and 1 pM.

The simulated efflux of HQ from the nanopipette orifice as a function of  $V_{hold}$  is shown in Figure 2.8a (distance from the end of the nanopipette to the substrate was 10  $\mu\text{m}$ ), indicating a semi-logarithmic dependence of efflux rate on potential. Similar effects are seen when the nanopipette is approached to an electrochemically active surface (Figure 2.7b) or an electrochemically inert surface (Figure 2.8b), however the flow development is inhibited in the center of the channel, allowing HQ flux to a confined area.



**Figure 2.8 FEM simulations of hold biases in bulk and at an inert surface.** (a) Simulated efflux rates of HQ across the nanopipette orifice at different holding potentials, presented terms of molecular flux ( $\text{mol s}^{-1} \text{m}^{-2}$ ) and total rate of efflux ( $\text{mol s}^{-1}$ ). (b) FEM simulations of the nanopipette under approached conditions (75 nm from

substrate) to the substrate with boundary no flux of HQ. For each of the hold biases -0.3, -0.2, -0.1 V, profiles of (i) the fluid velocity magnitude and (ii) HQ concentration are shown. Note that the scales for [HQ] are displayed logarithmically between 1 mM and 1 pM.

The flow profiles under these conditions (Figure 2.9) deviate from the typical plug-like flow profiles expected for EOF in a straight channel where  $\kappa r \approx 44$  (where  $\kappa$  is the Debye–Hückel parameter;  $2.14 \text{ nm}^{-1}$  for 20 mM monovalent electrolyte, and  $r$  is the pore radius of 93.5 nm).<sup>35–37</sup> This is a consequence of the conical geometry of the nanopipette; when EOF is directed into the nanopipette, the increased cross-sectional area causes a decrease in fluid velocity. EOF near the wall is driven by the mobile charge in the diffuse layer and the electric field parallel to the wall,<sup>18</sup> which also becomes less intense with distance into the nanopipette, but with a different functional dependence on distance along the nanopipette axis to that of the fluid velocity, due to the ion accumulation profile within the tip of the pipette.<sup>38–40</sup> Similar effects occur with flow driven out of the nanopipette (positive tip bias), where the increasing constriction as the flow approaches the nanopipette orifice causes increased back pressure, with ion depletion at the nanopipette end affecting the local ionic strength and electric field (*vide infra*). These mechanisms are especially effective when the tip is close to the surface, enhancing the constriction effects upon flow (Figure 2.7b).

$I_{sub}$  was calculated from the FEM simulations by setting a sink boundary condition for the transport-limited oxidation of HQ and integrating the flux across the electrode surface, multiplied by number of electrons transferred in HQ oxidation (see Section 2.6.1). For  $V_{hold} = -0.1 \text{ V}$ , the calculated (2.25 pA) and experimental ( $\approx 2 \text{ pA}$ )  $I_{sub}$  values were in agreement. However, at higher  $V_{hold}$ ,  $I_{sub}$  was underestimated in the simulations to surfaces with neutral charge, predicting values an order of magnitude lower than those observed experimentally (e.g. when  $V_{hold} = -0.2 \text{ V}$ ,  $I_{sub} \approx 700 \text{ fA}$ , simulated  $I_{sub} = 60 \text{ fA}$ ). This indicates that the simple model (particularly the assumption of an uncharged surface) does not fully account for all experimental factors; further simulations were required to account for this (*vide infra*).

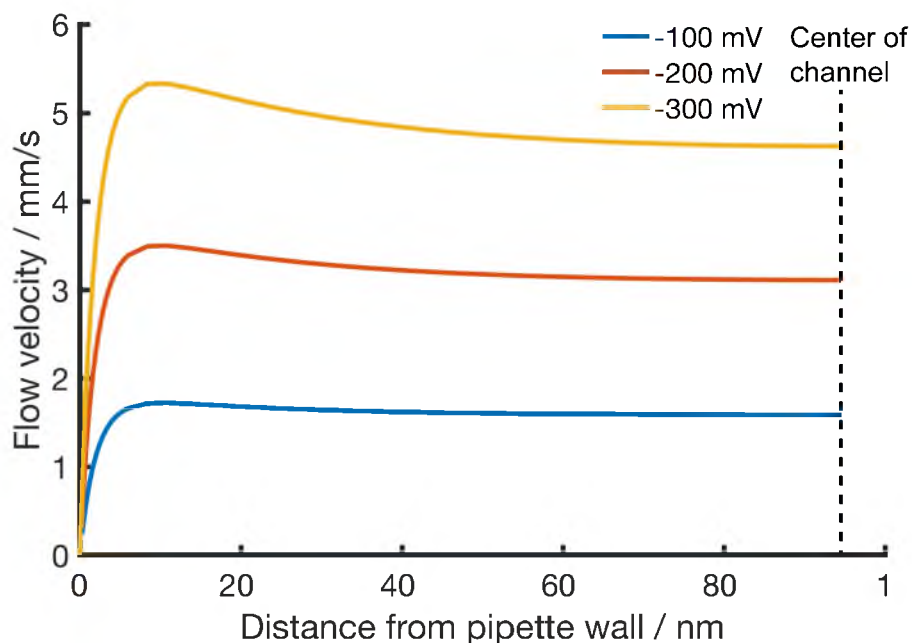


**Figure 2.9 Simulated flow profiles at hold potentials.** Simulated flow profiles across the radius (50 nm from pipette orifice) of a nanopipette in bulk solution (10  $\mu\text{m}$  from a surface) with 20 mM KCl bulk electrolyte during delivery of HQ. Three  $V_{\text{hold}}$  are applied corresponding to experimental conditions.

Flow velocity magnitudes at the tip orifice are similar when the nanopipette is in bulk solution and close to a substrate surface (Figure 2.7). This is similar to the ionic current in typical SICM practice, whereby a small decrease (1 – 2%) between the ionic current in bulk and near-surface is usually set for imaging.<sup>3,41,42</sup> Evidently, at such distances, the flow is also only slightly affected. HQ concentrations at the end of the nanopipette are also similar when the nanopipette is in bulk and near an active surface, highlighting the efficiency with which HQ can be retained in the nanopipette (Figure 2.7). Based on these results, subsequent measurements in this work used  $V_{\text{hold}} = -0.2$  V. This was a compromise between an applied potential where [HQ] could be retained in the nanopipette, with only small leakage, but the holding potential was not so large in magnitude that surface charge effects would be more prominent in the nanopipette response.<sup>5-7,34</sup>

To explain differences in  $I_{sub}$  between the simple model outlined and experiments (*vide supra*), FEM simulations were performed with varying substrate charges with  $V_{hold} = 0.2$  V and the tip-substrate separation set to be 75 nm (Figure 2.10). Even at this relatively large distance from the surface, it is evident from Figure 2.10a that flow velocity into the tip is increased when above surfaces with a moderate negative charge ( $-20$  mC/m<sup>2</sup>) (Figure 4a(i)) and decreased at positively charged surfaces ( $+20$  mC/m<sup>2</sup>) (Figure 2.10a(ii)). At negatively charged surfaces, the increased flow in the channel formed between the nanopipette wall and the surface results in a more developed flow profile across the pipette diameter and therefore a reduced substrate current;  $\sim 60\%$  of  $I_{sub}$  at a neutral surface (Figure 2.10c). Conversely, a positively charged surface restricts flow in this channel due to the direction of net ionic flux being reversed within the double layer of the substrate in comparison to that generated by the negative charged walls of the nanopipette, resulting in diminished flow across the center of the pipette and increasing  $I_{sub}$  by  $\sim 65\%$  compared to a neutral surface (Figure 2.10c). This phenomenon not only affects the concentration of species delivered directly to an electrochemically active surface, which consumes the delivered species, but also the amount that diffuses into bulk when the nanopipette is at an inert surface (Figure 2.10b). The concentrations in proximity to the delivery area in Figure 2.10b indicate that the holding bias is more effective at negatively charged surfaces than positive ones.



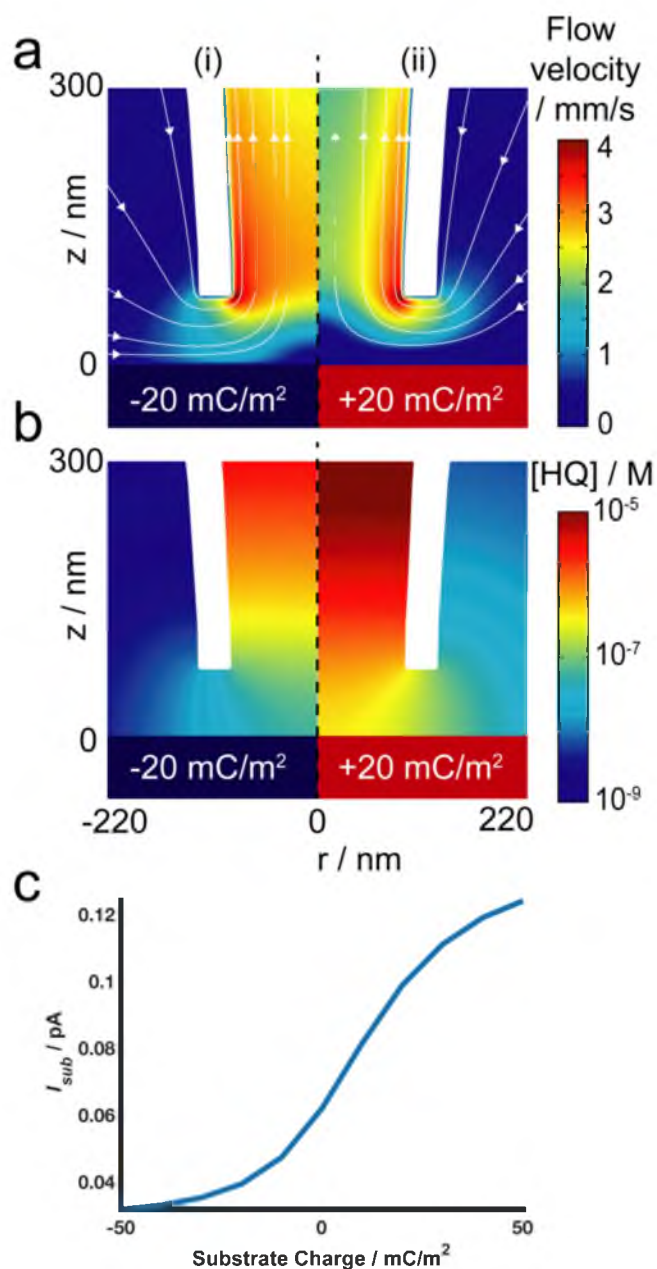


**Figure 2.10 Steady-state simulations of hold biases at approached distances.** (a) Flow velocity and (b) HQ concentration profiles when  $V_{\text{hold}} = -0.2 \text{ V}$ , at the interface of a nanopipette 75 nm from the surface of an electrochemically inactive substrate (no flux boundary condition). Different charges are applied to the in a moderate charge range; (i)  $-20$  and (ii)  $+20 \text{ mC/m}^2$ . (b) Substrate currents ( $I_{\text{sub}}$ ) from simulations at a surface with variable charge, which oxidizes HQ at a transport limited rate.



### 2.4.3 Delivery with $V_{\text{efflux}}$

We now consider imaging experiments in which the tip potential was pulsed to  $V_{\text{efflux}}$  for 150 ms upon reaching the approach threshold (Figure 2.1c). Representative results are shown in Figure 2.11 for  $V_{\text{efflux}} = 0.4$  V for the substrate topography, tip current and substrate current, with  $V_{\text{efflux}} = 0.2$  V and 0.05 V shown in Figure 2.12. Under these conditions (transport-limited oxidation) it has been shown by Chen *et al.*<sup>17</sup> that for ions delivered mainly through migration,  $I_{\text{sub}}$  is independent of surface charge, while  $I_{\text{tip}}$  is dominated by surface charge effects, allowing simultaneous reactivity and surface charge mapping from these 2 quantities that are recorded synchronously. In contrast, control of neutral species delivery is dependent entirely on the generation of EOF.

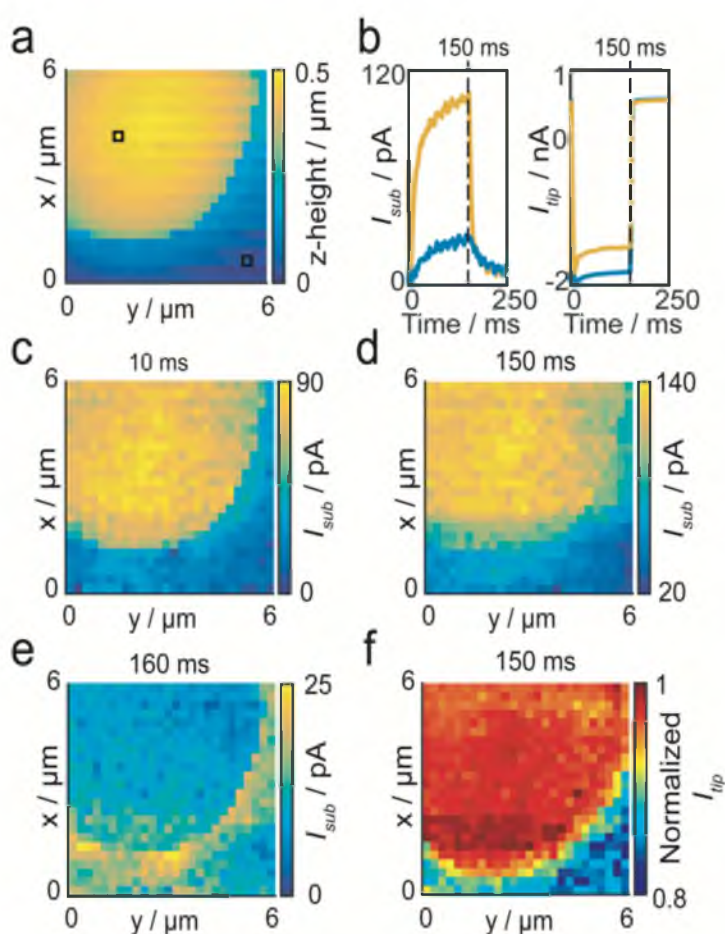


**Figure 2.11 Functional mapping of HQ oxidation on a 7  $\mu\text{m}$  CF-UME.** Functional mapping of HQ oxidation on a 7  $\mu\text{m}$  diameter CF-UME when  $V_{\text{efflux}} = 0.4$  V for 150 ms. The (a) topography is obtained simultaneously with currents recorded continuously to provide  $I_{\text{sub}}$  and  $I_{\text{tip}}$ , (b) presented at selected pixels (black bordered on

topography) during and after the delivery pulse, with one pixel at the CF-UME (yellow) and over glass (blue). This allows mapping of substrate current at selected times, for example; (c) during the delivery pulse (10 ms), (d) at the end of the pulse (150 ms), and (e) 10 ms after the pulse (160 ms), alongside (f) normalized  $I_{tip}$  (at 150 ms).

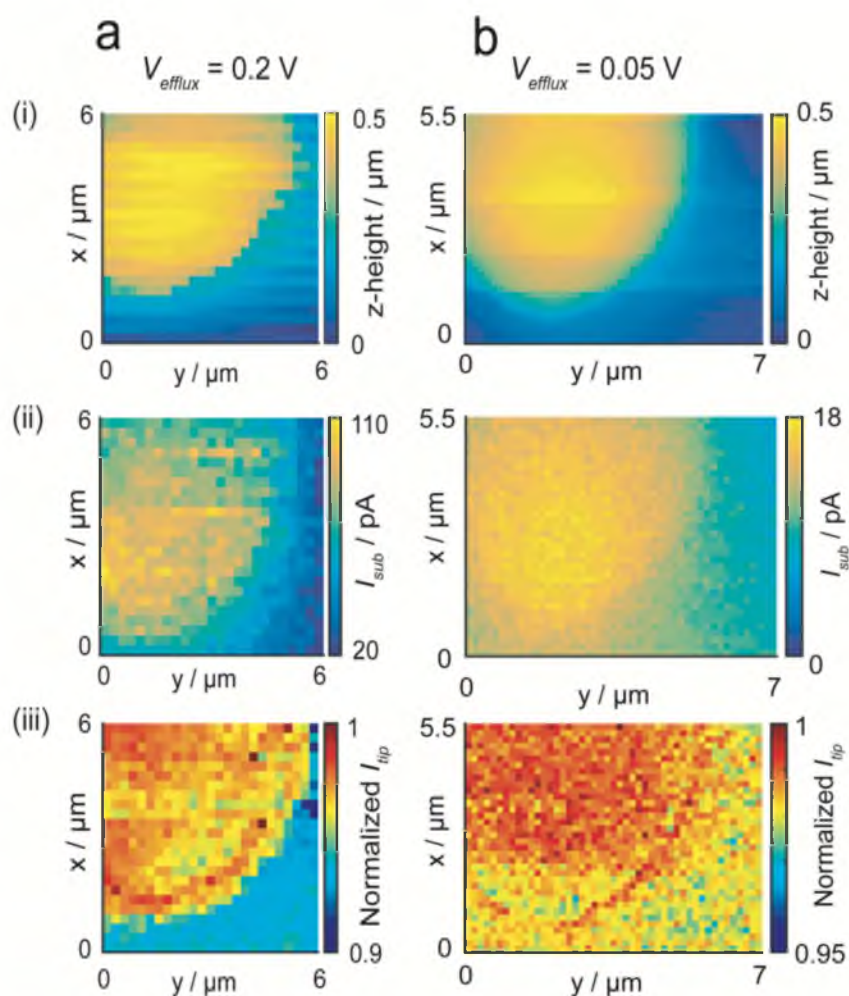


**Figure 2.12 Simultaneously obtained maps of SICM HQ delivery.** HQ oxidation at a  $7 \mu\text{m}$  diameter CF-UME when (a)  $V_{efflux} = 0.2 \text{ V}$  and (b)  $V_{efflux} = 0.05 \text{ V}$ , giving the (i) topography, (ii)  $I_{sub}$ , and (iii) normalized  $I_{tip}$ .

Figure 2.11b to Figure 2.11d show an appreciable substrate current when the efflux pulse is performed over both the CF-UME and the glass (by comparison to the topography maps of the UME substrate in Figure 2.11a). The current is highest when the nanopipette is over the UME and then monotonically decreases in magnitude as the nanopipette moves away laterally from the active part of the UME over the glass, indicating significant diffusional broadening in the delivery of HQ from the nanopipette to the UME, which acts as a strong sink. Figure 2.11b clearly shows the difference in slope and magnitude of  $I_{sub}$  during the efflux pulse at the CF and glass, the slower response time indicating the time taken for transport of HQ from the delivery site to electrochemically active sites. When the nanopipette is over the UME, some heterogeneities are evident in the maps of  $I_{sub}$ . This can be attributed to heterogeneities in the local delivery process (induced, for example by variations in surface charge), rather than the local activity of the part of the electrode under the tip, because if the nanopipette were over a relatively inactive part of the surface, for example, HQ could easily diffuse to a nearby active site.

The density of information provided by this method is demonstrated by further analysis of  $I_{sub}$  (Figure 2.13 and Figure 2.14), as properties of  $I_{sub}$  response such as rate of current increase at a given time, half-rise time, and fall time can provide insight into the transport and kinetic properties. The differences in transport mechanisms are also apparent from the difference between the relatively homogeneous initial response over the UME at 10 ms (Figure 2.11c, Figure 2.13b, Figure 2.14b) and the lower relative  $I_{sub}$  near the edge of the UME in comparison to the center at 150 ms (Figure 2.11d, Figure 2.13c, Figure 2.14c). Furthermore, the initial rate of current increase at 2 ms (Figure 2.13g, Figure 2.14g) exhibits only minor heterogeneity over the electrochemically active areas suggesting that, at this resolution, the electrochemical response of the substrate to HQ is relatively homogeneous at a time when the delivery is localised as wider transport effects are not yet significant.

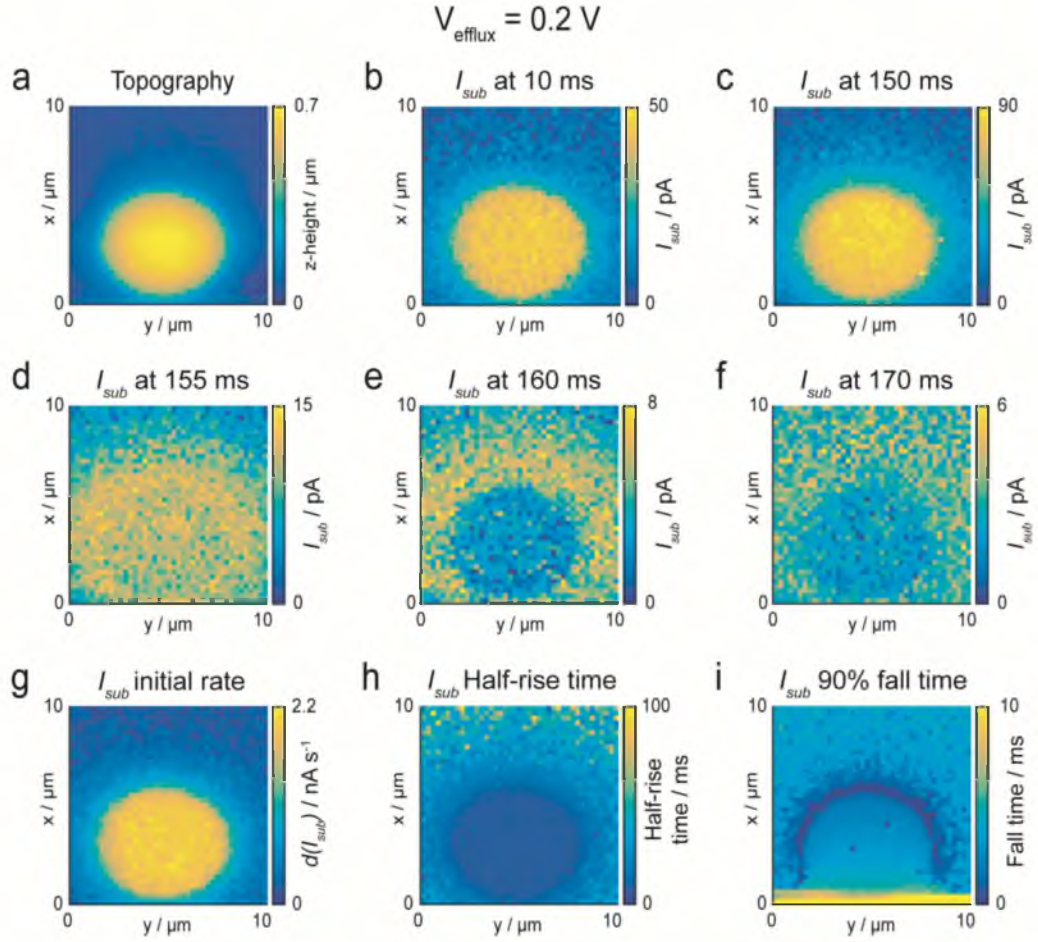


**Figure 2.13 Analysis of substrate currents during HQ delivery when  $V_{\text{efflux}} = 0.2 \text{ V}$ .** Simultaneously obtained maps of SICM HQ delivery and oxidation at a  $7 \mu\text{m}$  diameter CF-UME when  $V_{\text{efflux}} = 0.2 \text{ V}$ , giving the (a) topography,  $I_{\text{sub}}$  at (b) 10 ms, (c) 150 ms (end of efflux pulse), (d) 155 ms (5 ms after the efflux pulse), (e) 160 ms, and (f) 170 ms. Alongside (g) the rate of  $I_{\text{sub}}$  increase at 2 ms, (h) half-rise time, and (i) fall time (to 90% of the maximum current). The fall time is extremely sensitive to small changes in  $I_{\text{sub}}$ , causing a discrepancy first few lines of the scan due to pA scale drift as the UME current is settling.



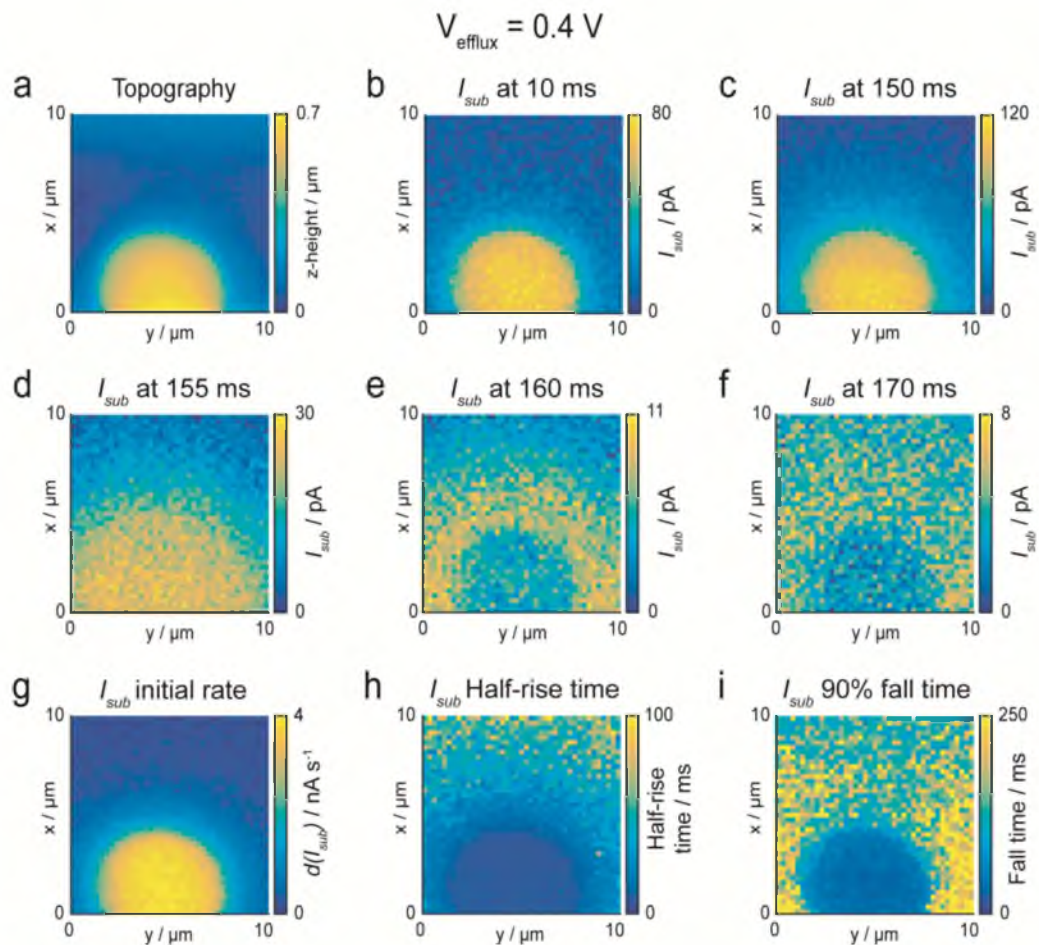


**Figure 2.14 Analysis of substrate currents during HQ delivery when  $V_{\text{efflux}} = 0.4 \text{ V}$ .** Simultaneously obtained maps of SICM HQ delivery and oxidation at a  $7 \mu\text{m}$  diameter CF-UME when  $V_{\text{efflux}} = 0.4 \text{ V}$ , giving the (a) topography,  $I_{\text{sub}}$  at (b) 10 ms, (c) 150 ms (end of efflux pulse), (d) 155 ms (5 ms after the efflux pulse), (e) 160 ms, and (f) 170 ms. Alongside (g) the rate of  $I_{\text{sub}}$  increase at 2 ms, (h) half-rise time, and (i) fall time (to 90% of the maximum current).

The half-rise time (Figure 2.13h, Figure 2.14h) is small and relatively homogeneous over the electrochemically active area (9 ms and 7 ms, though further discrimination could be achieved through higher sampling rates), however this can increase to 100 ms at  $5 \mu\text{m}$  from the CF edge due to the time taken for HQ transport to electrochemically active sites. The half-rise time above the glass is also far more

heterogeneous, indicating that the quantity of HQ delivered to the surface depends upon local surface properties other than electrochemical activity.

Diffusional broadening is evident from Figure 2.11e, where  $I_{sub}$  is higher 10 ms after the end of the efflux pulse over the adjacent glass than over the UME, and is clearly demonstrated by wider area scans in Figure 2.13 and Figure 2.14. This can be quantified as the fall time which shows that  $I_{sub}$  persists for longer periods when HQ is delivered to the glass, however there is a marked difference between the fall time of  $V_{efflux} = 0.2$  V and 0.4 V, with clear edge effects when smaller quantities of HQ are delivered ( $V_{efflux} = 0.2$  V, Figure 2.13i) which are not apparent at higher  $V_{efflux}$  ( $V_{efflux} = 0.4$  V, Figure 2.14) where the response will be broadened over a greater area. The decrease in fall time at the edge can be attributed to a greater electrochemical area as the CF is not perfectly coplanar with the glass, thereby providing a larger electrochemically active area for oxidation of HQ. However, normalised  $I_{tip}$  in higher resolution scans indicate some difference in surface properties at these areas; Figure 2.11f shows areas of higher  $I_{tip}$  response near the edge of the CF and in the center, which are more visible in Figure 2.12 where lower  $V_{efflux}$  pulses are presented. It should be noted that for these experiments a 2% approach threshold was used for nanopipette positioning, which would bring the nanopipette closer to the surface (30 nm calculated by FEM simulation (Figure 2.15)) where surface charge effects are known to be significant.<sup>5-7,34</sup>

Differences between scans at the same delivery potential are likely due to the effects of pipette geometry upon approach and delivery.<sup>43</sup> Overall the extensive information contained within these data demonstrate that delivery parameters can be tuned to access different information about the system, revealing that  $I_{sub}$  and  $I_{tip}$  exhibit significant spatial heterogeneity which is not only dependent upon the electrochemical activity of the substrate. Possible explanations for these heterogeneities are differing electrochemical surface activity, surface charge effects due to the structure of the CF, and proton generation as part of the HQ oxidation process. To fully understand the underlying processes, and evaluate the contributions from these respective factors, FEM simulations are necessary.

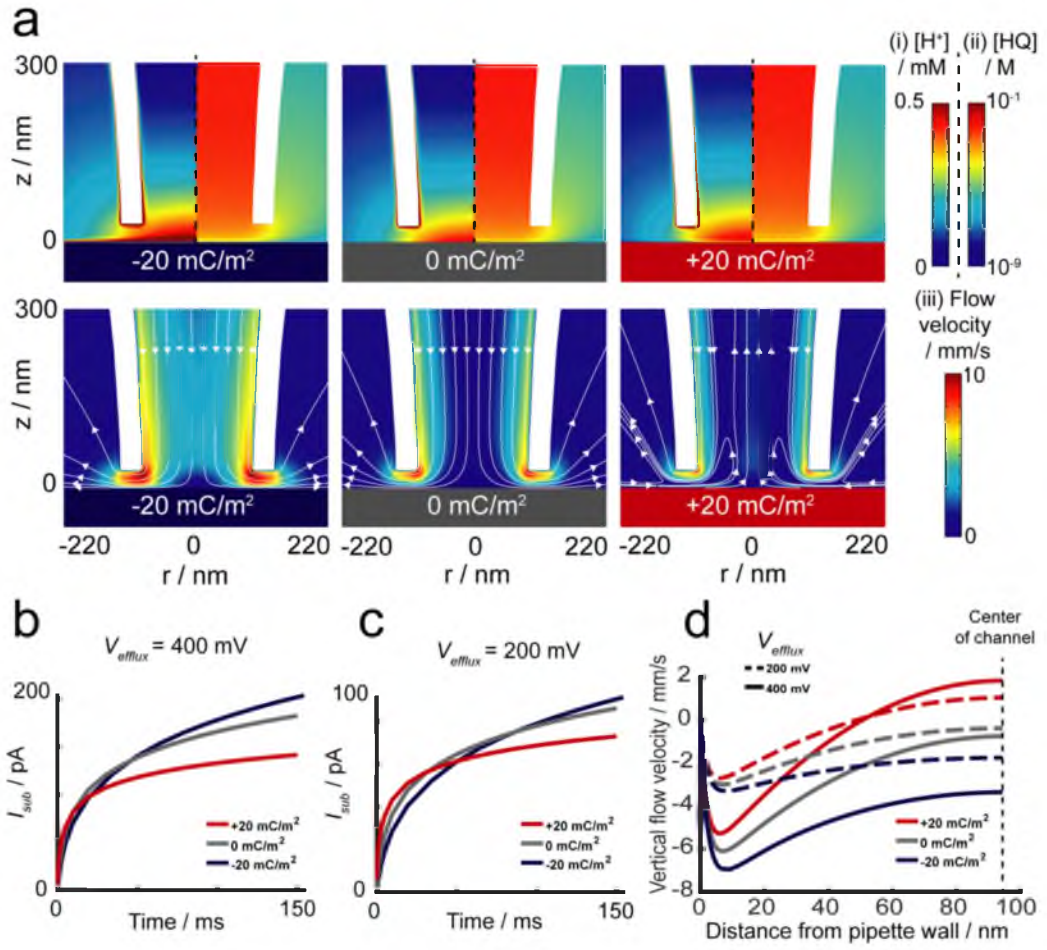
Simulations were performed with  $V_{efflux} = 0.05$  V, 0.2 V, and 0.4 V and the tip-substrate separation either 75 nm (1.25% approach threshold, as used in Figure 2.13,  $V_{efflux} = 0.05$  V) or 30 nm (2% threshold, as used in the experiment for Figure 2.11). At 75 nm both  $I_{tip}$  and  $I_{sub}$  were insensitive to proton flux and only  $I_{tip}$  had sensitivity to surface charge (Table 2.1), indicating that at a sufficient distance delivery was independent of surface charge. At a tip-substrate separation of 30 nm, proton generation does not contribute significantly to the ionic currents, shown by the similarity in  $I_{tip}$  between the simulated cases of delivery to an electrochemically active and electrochemically inert surfaces (Table 2.1). Figure 2.15a(i) indicates that the small effect of proton generation on  $I_{tip}$  is likely due to the low concentrations generated; approximately 0.5 mM in comparison to the 20 mM background electrolyte plus effects from charged substrate surfaces.

Figure 2.15b and Figure 2.15c demonstrate the effect of varied substrate surface charge on  $I_{sub}$ . A marked decrease in  $I_{sub}$  at positive surface charges and an increase at negative surface charges is predicted. The underlying cause of this is demonstrated by the EOF velocity profiles in Figure 2.15a. The flow velocity magnitude (Figure 2.15a(iii)) shows surface charge effects similar to those influencing the hold potential efficacy (Figure 2.10), however the comparatively high  $V_{efflux}$  and closer approach distance leads to a more pronounced effect. To understand the details of delivery to a charged surface we must also consider Figure 2.15d; the flow profile within the pipette, in which the z-component of the flow is plotted for the pipette radius from 50 nm above the pipette orifice. These plots show that the flow out of the pipette (efflux flow) at the negative (blue) and neutral (grey) surfaces is developed across the entire channel, though the efflux flow at the neutral surface dissipates to less than 1 mm/s towards the center of the channel. This is as a result of flow effects explored previously (*vide supra*) with additional back pressure due to the gap resistance, the stagnant zone caused by redirection of the vertical flow laterally at the surface, and no-slip condition on the surface (Figure 2.15a(iii)). In the case of the negative surface this is counteracted by additional efflux flow generation by the negatively charged substrate.

**Table 2.1 Simulated delivery currents under different conditions.** Simulated currents for the delivery of HQ to a 7  $\mu\text{m}$  diameter CF-UME ( $I_{\text{sub}}$  and  $I_{\text{tip}}$ ) or an electrochemically inert surface ( $I_{\text{tip}}$  (inert)). These currents demonstrate that at 75 nm delivery of neutral species can be achieved with relative independence from substrate charge effects, while at 30 nm, the quantity of neutral species delivered is highly dependent upon the charge of the substrate. Simulations of substrate currents at an electrochemically active surface in the absence of proton generation were identical to those including proton generation.

Tip-Substrate Separation	75 nm			30 nm			10 $\mu\text{m}$
Surface Charge / $\text{mC}/\text{m}^2$	-20	0	20	-20	0	20	0
$V_{\text{efflux}} = 50 \text{ mV}$							
$I_{\text{sub}} / \text{pA}$	25	24	24	35	27	26	5
$I_{\text{tip}} / \text{pA}$	-214	-214	-215	-209	-210	-210	-217
$I_{\text{tip}} / \text{pA}$ (inert)	-215	-215	-215	-209	-210	-211	-217
$V_{\text{efflux}} = 200 \text{ mV}$							
$I_{\text{sub}} / \text{pA}$	91	92	92	90	91	73	19
$I_{\text{tip}} / \text{pA}$	-834	-834	-835	-808	-807	-813	-846
$I_{\text{tip}} / \text{pA}$ (inert)	-833	-833	-833	-804	-811	-816	-846
$V_{\text{efflux}} = 400 \text{ mV}$							
$I_{\text{sub}} / \text{pA}$	210	209	207	202	204	142	45
$I_{\text{tip}} / \text{pA}$	-1621	-1623	-1628	-1554	-1553	-1558	-1653
$I_{\text{tip}} / \text{pA}$ (inert)	-1619	-1622	-1626	-1534	-1551	-1583	-1653





**Figure 2.15 FEM simulations of HQ delivery to a 7  $\mu\text{m}$  CF-UME 30 nm from the pipette orifice.** Simulations where  $V_{\text{efflux}} = 0.4 \text{ V}$ , at surfaces of charges (red) +20  $\text{mC/m}^2$ , (grey) 0  $\text{mC/m}^2$ , (blue) -20  $\text{mC/m}^2$ , were used to generate profiles (a) of (i) proton concentration, (ii) HQ concentration (displayed as  $\log_{10}([\text{HQ}])$ ), (iii) flow velocity magnitude. Simulated  $I_{\text{sub}}$  response when (a)  $V_{\text{efflux}} = 0.4 \text{ V}$  and (b)  $V_{\text{efflux}} = 0.2 \text{ V}$  for delivery to a substrate with different surface charges (same color key as (a)). (d) The vertical ( $z$ -axis) component of the simulated flow velocity across the nanopipette radius (from 0 to 98.5 nm, starting at the nanopipette wall) 50 nm above the pipette opening for  $V_{\text{efflux}} = 0.4 \text{ V}$  (solid) and  $V_{\text{efflux}} = 0.2 \text{ V}$  (dashed), surface charge colors the same key as (a).

The case for a positively charged surface is more complex; the flow velocity appears to dissipate more quickly but increases again in the center of the channel. The flow generated in proximity to a positively charged surface (red) acts in two distinct ways; efflux flow is still generated at the pipette wall, however, at the center of the pipette the flow has been completely reversed, at increasing intensity with higher applied potentials (Figure 2.15d). The flow originates at the substrate surface (Figure 2.16) where the anions forming the substrate double layer migrate into the pipette with sufficient flux to generate  $\sim 2$  mm/s EOF into the pipette. This can also be seen as the flow magnitude extending from the substrate beneath the glass towards the center of the channel and then upwards (Figure 2.15c(iii)).

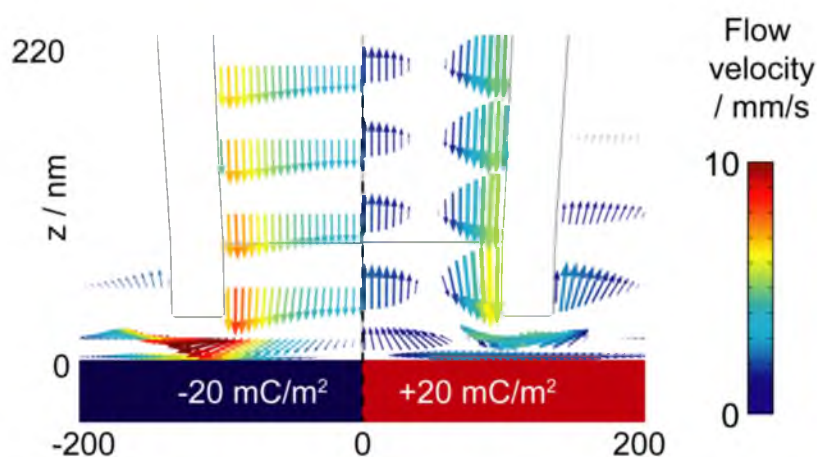


**Figure 2.16 Phase portraits of flow during HQ delivery.** Simulated flow profiles for HQ delivery from a nanopipette at  $V_{efflux} = 0.4$  V, nanopipette is placed 30 nm from negatively charged ( $-20$  mC/m<sup>2</sup>, left) and positively charged ( $+20$  mC/m<sup>2</sup>, right) surfaces. Flow arrows are on a  $\log_{10}$  scale with each of the two separate simulations having a different scaling factor applied to allow visualization, arrows are colored by flow velocity which is the same in both sides of the plot.

The surface induced flow inversion described has not been previously demonstrated, however it was suggested by Clarke *et al.* that flow separation could occur in negatively charged borosilicate capillaries at sufficiently positively charged surfaces.<sup>24</sup> The described flow inversion effect is similar to flow profiles generated by nanopore diodes with heterogeneous charge,<sup>44</sup> and similar effects have been observed

within conical nanopores with  $\kappa r \approx 1.7$ ,<sup>45</sup> though the underlying causes were not thoroughly explored. There has also been recent interest in similar phenomena caused by large gradients in ionic conductivity.<sup>46</sup>

This surface charge dependence for neutral species delivery will have large effects when delivering to biological samples such as living cells, which can have highly localized and heterogeneous surface charge distributions.<sup>6</sup> Transport into the tip has also previously been suggested to affect long term stability of nanopipette currents when a hold potential is applied, an effect which would be compounded by this transport into the pipette at the surface even when delivering species.<sup>21</sup> However, we observe stable currents over multiple scans by allowing equilibration of the nanopipette in bulk conditions between pixels.

## **2.5 Conclusions**

Building upon previous work, we show that careful control of the applied potentials in SICM, can be used to deliver neutral species and simultaneously acquire information on the charge of the surface. However, this study indicates that delivery of neutral species requires careful consideration of approach and delivery parameters. Approaching the surface closely allows simultaneous acquisition of surface charge data but delivered concentrations also depend on the surface charge, whereas at greater tip-substrate distances consistent, but less localized, delivery can be achieved. The effects of surface charge on EOF have a significant impact on the delivery of neutral species using SICM and must be controlled, or evaluated with detailed simulations, for truly quantitative delivery. FEM models have been used to elucidate the complex interplay of surface processes and their contributions to detected currents. The complex flow profile induced by proximity to charged surfaces is previously unreported in SICM and is likely present in many pulsed-SICM measurements. This work adds to the growing understanding of factors at work in the increasingly diverse range of SICM methodologies, for which comprehensive models are required to allow quantification.

## 2.6 References

- 1 P. K. Hansma, B. Drake, O. Marti, S. A. C. Gould and C. B. Prater, *Science*, 1989, **243**, 641–643.
- 2 A. Page, D. Perry and P. R. Unwin, *Proc. R. Soc. A*, 2017, **473**, 1–34.
- 3 P. Novak, C. Li, A. I. Shevchuk, R. Stepanyan, M. Caldwell, S. Hughes, T. G. Smart, J. Gorelik, V. P. Ostanin, M. J. Lab, G. W. J. Moss, G. I. Frolenkov, D. Klenerman and Y. E. Korchev, *Nat. Methods*, 2009, **6**, 279–281.
- 4 M. Kang, D. Perry, C. L. Bentley, G. West, A. Page and P. R. Unwin, *ACS Nano*, 2017, **11**, 9525–9535.
- 5 N. Sa, W. J. Lan, W. Shi and L. A. Baker, *ACS Nano*, 2013, **7**, 11272–11282.
- 6 A. Page, D. Perry, P. Young, D. A. Mitchell, B. G. Frenguelli and P. R. Unwin, *Anal. Chem.*, 2016, **88**, 10854–10859.
- 7 C. Zhu, L. Zhou, M. Choi and L. A. Baker, *ChemElectroChem*, 2018, **5**, 2986–2990.
- 8 A. P. Ivanov, P. Actis, P. Jönsson, D. Klenerman, Y. Korchev and J. B. Edel, *ACS Nano*, 2015, **9**, 3587–3594.
- 9 D. R. Curtis, *Electrophysiol. Methods*, 1964, 144–190.
- 10 T. P. Hicks, *Prog. Neurobiol.*, 1984, **22**, 185–240.
- 11 A. Bruckbauer, P. James, D. Zhou, W. Y. Ji, D. Excell, Y. Korchev, R. Jones and D. Klenerman, *Biophys. J.*, 2007, **93**, 3120–3131.
- 12 J. D. Piper, C. Li, C. J. Lo, R. Berry, Y. Korchev, L. Ying and D. Klenerman, *J. Am. Chem. Soc.*, 2008, **130**, 10386–10393.
- 13 B. Babakinejad, P. Jönsson, A. López Córdoba, P. Actis, P. Novak, Y. Takahashi, A. Shevchuk, U. Anand, P. Anand, A. Drews, A. Ferrer-Montiel, D. Klenerman and Y. E. Korchev, *Anal. Chem.*, 2013, **85**, 9333–9342.
- 14 S. Schobesberger, P. Jönsson, A. Buzuk, Y. Korchev, J. Siggers and J. Gorelik, *Biophys. J.*, 2016, **110**, 141–146.
- 15 D. Perry, A. Page, B. Chen, B. G. Frenguelli and P. R. Unwin, *Anal. Chem.*, 2017, **89**, 12458–12465.

- 16 A. Page, M. Kang, A. Armitstead, D. Perry and P. R. Unwin, *Anal. Chem.*, 2017, **89**, 3021–3028.
- 17 B. Chen, D. Perry, A. Page, M. Kang and P. R. Unwin, *Anal. Chem.*, 2019, **91**, 2516–2524.
- 18 A. V. Delgado, F. González-Caballero, R. J. Hunter, L. K. Koopal and J. Lyklema, *Pure Appl. Chem.*, 2005, **77**, 1753–1805.
- 19 W. Shi, N. Sa, R. Thakar and L. A. Baker, *Analyst*, 2015, **140**, 4835–4842.
- 20 D. C. Kirkpatrick, M. A. Edwards, P. A. Flowers and R. M. Wightman, *Anal. Chem.*, 2014, **86**, 9909–9916.
- 21 D. C. Kirkpatrick, L. R. Walton, M. A. Edwards and R. M. Wightman, *Analyst*, 2016, **141**, 1930–1938.
- 22 N. R. Herr, B. M. Kile, R. M. Carelli and R. M. Wightman, *Anal. Chem.*, 2008, **80**, 8635–8641.
- 23 D. Perry, B. Paulose Nadappuram, D. Momotenko, P. D. Voyias, A. Page, G. Tripathi, B. G. Frenguelli and P. R. Unwin, *J. Am. Chem. Soc.*, 2016, **138**, 3152–3160.
- 24 R. W. Clarke, A. Zhukov, O. Richards, N. Johnson, V. Ostanin and D. Klenerman, *J. Am. Chem. Soc.*, 2013, **135**, 322–329.
- 25 M. Quan, D. Sanchez, M. F. Wasylkiw and D. K. Smith, 2007, **129**, 12847–12856.
- 26 C. L. Bentley, D. Perry and P. R. Unwin, *Anal. Chem.*, 2018, **90**, 7700–7707.
- 27 K. T. Kawagoe, J. B. Zimmerman and R. M. Wightman, *J. Neurosci. Methods*, 1993, **48**, 225–240.
- 28 D. Momotenko, K. McKelvey, M. Kang, G. N. Meloni and P. R. Unwin, *Anal. Chem.*, 2016, **88**, 2838–2846.
- 29 J. R. Rumble, D. R. Lide and T. J. Bruno, *CRC handbook of chemistry and physics 98th edition*, CRC Press, Cleveland, 2017.
- 30 J. H. Bae, Y.-R. Kim, R. S. Kim and T. D. Chung, *Phys. Chem. Chem. Phys.*, 2013, **15**, 10645–10653.
- 31 P. S. Guin, S. Das and P. C. Mandal, *Int. J. Electrochem.*, 2011, **2011**, 1–22.
- 32 A. L. Barker, J. V Macpherson, C. J. Slevin and P. R. Unwin, *J. Phys. Chem.*

- B*, 1998, **102**, 1586–1598.
- 33 M. Gonsalves, A. L. Barker, J. V. Macpherson, P. R. Unwin, D. O'Hare and C. P. Winlove, *Biophys. J.*, 2000, **78**, 1578–1588.
  - 34 K. McKelvey, S. L. Kinnear, D. Perry, D. Momotenko and P. R. Unwin, *J. Am. Chem. Soc.*, 2014, **136**, 13735–13744.
  - 35 D. G. Haywood, Z. D. Harms and S. C. Jacobson, *Anal. Chem.*, 2014, **86**, 11174–11180.
  - 36 D. G. Haywood, A. Saha-Shah, L. A. Baker and S. C. Jacobson, *Anal. Chem.*, 2015, **87**, 172–187.
  - 37 W.-J. Lan, M. A. Edwards, L. Luo, R. T. Perera, X. Wu, C. R. Martin and H. S. White, *Acc. Chem. Res.*, 2016, **49**, 2605–2613.
  - 38 D. Momotenko, F. Cortés-Salazar, J. Josserand, S. Liu, Y. Shao and H. H. Girault, *Phys. Chem. Chem. Phys.*, 2011, **13**, 5430–5440.
  - 39 C. Kubeil and A. Bund, *J. Phys. Chem. C*, 2011, **115**, 7866–7873.
  - 40 L. Luo, D. A. Holden and H. S. White, *ACS Nano*, 2014, **8**, 3023–3030.
  - 41 M. J. Lab, A. Bhargava, P. T. Wright and J. Gorelik, *Am J Physiol Hear. Circ Physiol*, 2013, **304**, H1–H11.
  - 42 J. Rheinlaender and T. E. Schäffer, *J. Appl. Phys*, 2009, **105**, 94905.
  - 43 D. Perry, D. Momotenko, R. A. Lazenby, M. Kang and P. R. Unwin, *Anal. Chem.*, 2016, **88**, 5523–5530.
  - 44 H. Daiguji, Y. Oka and K. Shirono, *Nano Lett.*, 2005, **5**, 2274–2280.
  - 45 M. R. Powell, N. Sa, M. Davenport, K. Healy, I. Vlassiuk, S. E. Létant, L. A. Baker and Z. S. Siwy, *J. Phys. Chem. C*, 2011, **115**, 8775–8783.
  - 46 J. Rabinowitz, M. A. Edwards, E. Whittier, K. Jayant and K. L. Shepard, *J. Phys. Chem. A*, 2019, **123**, 8285–8293.

### **3 Scanning Ion Conductance Microscopy Potential Controlled Acid Delivery: A Tool to Assess Dental Corrosion**

This chapter continues the development of delivery methodologies in SICM by combining this with the ability to simultaneously track and quantify surface etching in real time. This is applied to an enamel substrate, a complex biological matrix mainly comprised of crystalline hydroxyapatite. Controlled delivery of protons by controlling the applied potential induces surface etching which is tracked through DM-SICM and quantified. FEM simulations are used to examine the accuracy of this method and the mechanisms underpinning surface tracking under situations which are actively generating ionic fluxes. DM-SICM is shown to be robust to the ionic fluxes from the surface, allowing quantitative assessment of surface treatments by determining the effect upon the effective heterogeneous rate constant through FEM.

This chapter is in preparation to be submitted for publication. The experiments presented herein were performed by Bryn Jones. Simulations and data analysis were performed by the author and the manuscript was prepared by the author in collaboration with Bryn Jones.

### **3.1 Abstract**

Scanning ion conductance microscopy (SICM) is a non-contact scanning probe microscopy that is increasingly being used for functional mapping of surfaces. We exploit established delivery methodologies for the controlled delivery of acid from the SICM nanopipette to an enamel substrate to induce dissolution. Combining this methodology with distance modulated procedures we are able to monitor and measure the controlled dissolution of the substrate in real time. Coupled with finite element method (FEM) simulations we quantify delivered proton concentrations to access the heterogeneous rate constant of the reaction. Quantitative analysis of dissolution rates through FEM allows direct comparison of the effects of protective and weakening surface treatments. This work presents SICM as a powerful technique for assessing erosion rates and as a versatile screening system for protective and harmful materials in relation to enamel acid dissolution. We directly demonstrate the ability of the technique to obtain robust statistics regarding the susceptibility of a surface to acid attack and present a new method of quantifying erosive damage from extremely mild acidic challenges whilst returning robust nanoscale measurements. We expand the technique further by including analysis of a salivary pellicle and present the opportunity that arises for combined topographical mapping and potentiometric acid delivery with the same nanopipette. This work contributes to the emergence of SICM as a tool for direct surface dissolution measurements and gives emphasis to the use of SICM for further understanding the dissolution kinetics of early stage dental erosion.

### **3.2 Introduction**

Dental erosion is a wide spread and prolific cause of tooth loss throughout the globe. Defined as the irreversible loss of dental hard tissues without the action of microorganisms,<sup>1</sup> it indiscriminately affects all social demographics and age groups,<sup>2-4</sup> often becoming a problem in otherwise healthy individuals through dietary acid exposure.<sup>5</sup> Understanding acid induced enamel dissolution is therefore instrumental to engineering methods to prohibit it.<sup>6</sup> Techniques that can probe and quantify acid erosion are of considerable value to the field of dental science<sup>7-9</sup> and have applications in metal corrosion,<sup>10,11</sup> analysis of coatings and paints,<sup>12</sup> the earth sciences,<sup>13</sup> pharmaceuticals<sup>14</sup> and chemistry.<sup>6,15</sup>

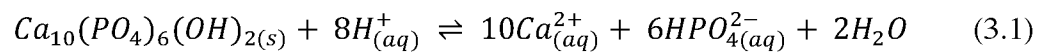


SICM is a non-contact imaging technique in the Scanning Probe Microscopy (SPM) family which uses a glass or quartz nanopipette to obtain topographical information about a surface.<sup>16–18</sup> This is achieved through applying a potential bias between a quasi-reference counter electrode (QRCE) inside the nanopipette and a second positioned in the bulk solution that bathes the substrate. This generates an ionic current which can be used to position the probe near a surface of interest either directly,<sup>19</sup> or through using AC feedback techniques for enhanced stability to changes in the ionic current.<sup>20,21</sup> The resolution is limited by the nanopipette aperture size with the smallest recorded resolution estimated at 6 nm using a pipette aperture of 10 nm.<sup>22</sup> Quantitative electrochemical information about the local ion concentration in the vicinity of the probe opening can be attained through careful selection of the voltage applied and analysis of the generated current.<sup>23</sup> Surface charge mapping<sup>24–28</sup> and controlled delivery of electroactive species<sup>29</sup> have demonstrated that careful design of SICM experiments can further expand the scope of this versatile imaging technique.<sup>18,30</sup>

Herein we position SICM as a tool for quantifying nanoscale corrosive damage through using the SICM bias to deliver protons from a reservoir in the probe to the enamel surface, whilst employing distance (z position) modulated feedback to track the induced surface dissolution, providing *in situ* etch pit depth measurements. By controlling the bias of the nanopipette relative to bulk, protons within the probe can either be retained or expelled into the local environment depending on the polarity and magnitude of the bias. In this work it is demonstrated that employing SICM for potential controlled acid delivery with surface tracking in close proximity to a surface, it is possible to induce and track localised surface erosion in the footprint of the probe. The capability of SICM to provide information on the susceptibility of a surface to acid attack is evaluated together with further investigation into whether applied surface treatments can be quantifiably assessed at the nanoscale. Through FEM simulation, quantified dissolution kinetics can be calculated from the pit formation rates. This information is of particular significance in the field of dental science where greater understanding of the dissolution kinetics may lead to preventative treatments for acid erosion.

Enamel is a complex biomineral matrix comprised primarily of HAP crystals and forming the outer protective layer of teeth.<sup>31,32</sup> It resists the physical and erosive

wear associated with mastication due to its extreme hardness and durability offered in part by its complex microstructure.<sup>33</sup> This consists of tightly packed and organised hydroxyapatite (HAP) nanocrystals, approximately 70 nm in size, arranged into 4-8 µm wide hexagonal rods that run deep into the tooth, perpendicular to the dentine-enamel junction.<sup>34</sup> These function as supporting bars within the structure and enhance the tensile properties of the material. Once formed, enamel can only regenerate through remineralisation pathways in the oral cavity which are pH dependant,<sup>35</sup> slow<sup>36</sup> and often insufficient at countering erosive processes.<sup>37</sup> Subsequently this can make enamel loss through chemical erosion permanent.<sup>38</sup> The proton induced dissolution of HAP can be approximated by Equation 3.1.<sup>39</sup>



As enamel is 90% HAP by weight this is the primary process of acid induced dissolution.<sup>40</sup> Protons react with HAP and produce free calcium ions, solvated phosphates and water.

The principal electrochemical methods to study dissolution of enamel involve the use of rotating disc electrodes (RDEs) to employ a regime of well defined mass transport.<sup>41-43</sup> Although these methods allow the surface kinetics to be investigated they are restricted to bulk measurements, making the study of transient surface treatments difficult. These techniques measure the average response of the surface, obscuring the activity of individual sites, while they allow the overall rate constants to be determined it is not possible to accurately assess the underlying mechanisms. This is especially important considering the heterogeneous nature of complex biomaterials such as enamel, with some areas primarily comprised of HAP and others mainly consisting of proteins. Nanoscale measurements are possible through multiple SEM images of a treated area, however the mass transport is often ill defined and the experiments require the enamel to be exposed to solutions for a long period of time and limited options exist for directly monitoring topography changes.<sup>44,45</sup>

Previous studies which have employed SPMs for dissolution measurements have relied on using subsequent different techniques to first induce surface dissolution, either with scanning electrochemical microscopy (SECM)<sup>46</sup> or scanning electrochemical cell microscopy (SECCM),<sup>6</sup> and then measuring the resulting etch pit formation. The SECM method used a Pt ultramicroelectrode for the localised production of protons, followed by interferometry for measuring etch pit formation,

while SECCM was used to deliver a defined quantity of acidic media which formed an etch pit that was measured with AFM. Both methods use FEM simulations to extract the effective heterogeneous rate constant, however they are unable to do so in real-time and dissolution continues to occur between proton delivery and measurement of the etch pit dimensions.

The approach used herein allows nanoscale measurements of surface processes as they happen, inducing the enamel dissolution and providing a simultaneous topographic assessment consecutively with SICM. As the technique requires electrolyte, but is not limited to identical bulk and probe solutions,<sup>47</sup> different conditions could be used, *e.g.* simulated sea water as bulk solution for metal corrosion experiments. The feedback methodology used herein allows for etching rates to be calculated as experiments progress and keeps experimental times short. 36 etch pits are produced on a surface in tens of minutes and good statistics are obtained. 30 nm probes were used allowing for nanoscale precision and analysis of features on the 100 nm scale. This could allow for the identification of highly resolved surface heterogeneities.

A common method of protecting enamel from acid dissolution is fluoridation. The exposure to fluoride results in a layer of fluoridated HAP being formed, which has a higher acid resistance than sound enamel due to the relative difficulty of removing the surface bound fluoride by protonation, in comparison to OH groups.<sup>48,49</sup> The human mouth has natural defence mechanisms against acid erosion. The salivary pellicle, a thin film of glycoproteins present on all oral cavity surfaces has a well-documented role in enamel protection although there is still much to learn about the mechanism behind the protection offered.<sup>50–54</sup> Using SICM, as described above, to acid challenge samples that have either been treated with fluoride or which have a pellicle layer, allow the protective benefits to be quantified and assessed through the study of the etch pits generated using SICM, comparing treated and untreated regions.

Finally, the effect of a corrosive wash, simulating an acidic challenge by exposing sound and fluoride treated enamel to a citric acid rinse is considered. Citric acid, a known dietary acid contributor to dental erosion, weakens the HAP lattice by inducing mild dissolution through the pathway outlined in Equation 3.1 but also through calcium stripping *via* citrate ligand chelation.<sup>44,55–57</sup> A deliberately mild challenge of 1% citric acid for 30 seconds was chosen to demonstrate the ability to

quantitatively detect early stage dental erosion.<sup>45</sup> The detection of statistical differences with low level exposures to these treatments is a step forward in dental erosion analysis, measuring nanoscale surface damage that was previously undetectable without SICM surface tracking and proton delivery.

These examples serve to highlight the wide applicability of SICM for addressing key questions in the field of dental science, and should serve as a powerful technique for benchmarking the protective benefits of novel treatments. More generally the work demonstrates the versatility of SICM as a multi-faceted tool for probing biological systems beyond topography.

### **3.3 Materials and Methods**

#### **3.3.1 Solutions**

Milli-Q reagent grade water (resistivity *ca.* 18.2 M $\Omega$  cm at 25 °C) was used in the preparation of all solutions. 50 mM potassium chloride (Sigma-Aldrich) was used as bulk electrolyte for all SICM experiments. The acid etching solution in the nanopipette was 20 mM hydrochloric acid (Sigma-Aldrich) with 50 mM potassium chloride supporting electrolyte. HCl was used as a biologically relevant monoprotic acid which also enabled the modelling procedure described below to be simplified. The citric acid solution (1% w/w, Fischer scientific, pH 3.6) The fluoride treatment solution was 1450 ppm sodium fluoride (Fischer scientific).

#### **3.3.2 Substrates**

Bovine enamel blocks (4x4 mm, ~1.5 mm thickness, Intertek, Wirral, UK) were hand polished with diamond polish sprays (Kemet ltd) and polishing pads (Buehler), working down through the following grain sizes: 3  $\mu$ m, 1  $\mu$ m, 0.5  $\mu$ m, 0.25  $\mu$ m and 0.1  $\mu$ m. A 50 nm diamond lapping compound (Buehler) for use with silk polishing pads (Struers) was used for the final polish. Samples were thoroughly rinsed between grain sizes and sonicated for 2 minutes (Decon F5200b) after the final polish. Samples were mounted onto glass petri dishes (4 cm diameter, WilcoWells) using a small amount of nail polish which was allowed to set for 1 hour.

### 3.3.3 Fluoride and citric acid treatments

Figure 3.1 gives the full details of the multistep process used for the fluoride and citric acid study. In summary, a section of the enamel block is masked off to protect it from a fluoride treatment. The fluoride and non-fluoride sections are then analysed using SICM. A citric acid treatment is then administered, and the sample sections reanalysed in a different area to that previously measured, giving an insight into the protection benefit offered by fluoride against a citric acid exposure.

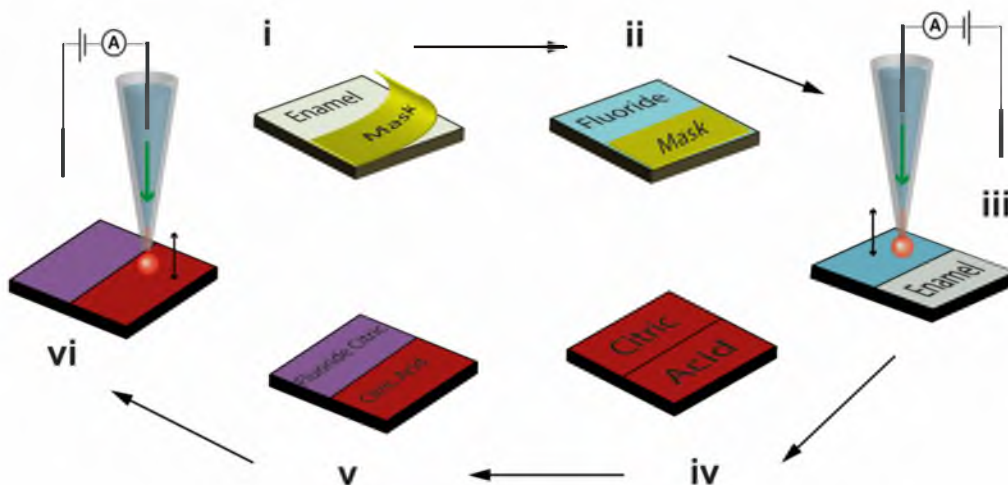


**Figure 3.1 Procedure for experimental surface treatments.** Experimental treatment process. **i.** Polished enamel block is half masked with Kapton tape. **ii.** The Unmasked enamel is then treated with 1450 ppm sodium fluoride solution for 30 minutes at 37 °C. **iii.** Mask is removed, sample thoroughly rinsed and SICM etch pit analysis undertaken on both sides of sample. **iv.** The electrolyte is then removed and the entire sample is exposed to a 1% citric acid solution for 30 s. **v.** The sample is then thoroughly rinsed and the electrolyte replaced. **vi.** SICM etch pit analysis is then repeated for the fluoride treated citric acid exposed enamel and citric acid exposed enamel, taking care that this second SICM analysis is performed far away from the initial region studied.

### 3.3.4 Kapton tape control

A control study was run to ensure the Kapton tape was not adversely affecting the results by leaving any residue. The sample was prepared identically to those used in

a-c of the multistep process in Figure 3.1, except 37 °C deionized water was used in place of the 30-minute sodium fluoride exposure. The taped and un-taped sides of the sample were then compared and were not found to be significantly different (Section 3.7.1).

### **3.3.5 Pellicle layer deposition**

To establish a pellicle layer, the sample was incubated in 5 ml of whole clarified saliva for 30 minutes at 37°C. The saliva was collected from volunteers at Unilever Port Sunlight research facility and sterilised on site. Studies have shown this is long enough for salivary proteins to adhere to an enamel surface and create a film that acts as a natural protective barrier.<sup>58</sup> After incubation the sample was thoroughly rinsed and reanalysed.

### **3.3.6 Statistical analysis**

Statistical analysis was performed in RStudio 1.2.1335, R version 3.4.2. All datasets were tested for normality using the Shapiro-Wilk test, yielding significant values ( $p < 0.05$ ) for several datasets, therefore non-parametric statistical tests are used throughout analysis. Individual experiments are summarized using the median as a measure of central tendency and the first and third quartiles (Q1 and Q3, respectively) as measures of spread, allowing comparison of skew between each group. The mean of medians is used with the standard error of the mean to convey sample variability. Wilcoxon rank-sum tests were used for comparisons between two groups and Kruskal-Wallis tests for multiple groups, the Bonferroni correction is also applied wherever multiple comparisons are employed.

### **3.3.7 SICM methodology**

30 nm diameter SICM nanopipettes were pulled from quartz capillaries (o.d. 1 mm, i.d. 0.5 mm, Sutter Instruments, QF100-50-10) using a laser puller (P-2000, Sutter Instruments; pulling parameters: Line 1: Heat 750, Fil 4, Vel 30, Del 150, Pul 80; Line 2: Heat 650, Fil 4, Vel 40, Del 135, Pul 150). The inner diameter of the probe was measured using a Zeiss Gemini 500 SEM (operating in scanning transmission electron microscopy mode) and for these pulling parameters was found to consistently be 30 nm  $\pm$  10% (Section 3.7.1, Figure 3.4). Two Ag/AgCl QRCEs were used, one in the

nanopipette and a second in bulk solution and were fabricated by electrolysis of silver wire in saturated potassium chloride solution.

The basic instrumentation setup has been described in detail previously.<sup>26,27,59</sup> Briefly, the nanopipette probes were mounted on a mechanical micro-positioner (Newport, M-461-XYZ-M) for coarse probe positioning over a sample. The fine horizontal movement of the probe was controlled using a two-axis piezoelectric positioning system with a range of 30  $\mu\text{m}$  (Physik Instrumente, model P-733.2 XY nanopositioner), while vertical movement was controlled using a single axis piezoelectric positioning stage of range 15  $\mu\text{m}$  (Physik Instrumente, model P-753.1 LISA). The piezoelectric positioners were mounted inside a faraday cage, built on an air pressurised optical table (Newport, RS 2000) to avoid mechanical vibrations, which incorporated acoustic insulation. Vacuum insulating panels (Kevothermal) and aluminium heat sinks (aimed to reduce thermal fluctuations and drift of the piezoelectric positioners) were also used. The stage housing the piezo was mounted on a vibration isolation platform (Minus K) also incorporated within the faraday cage. The electrometer and current–voltage converter used were bespoke, both made in-house, while user control of probe position, voltage output, and data collection was *via* custom-made programs in LabVIEW (2017, National Instruments) through a field programmable graphics array (FPGA) card (7852R, National Instruments).

The nanopipette filled with low pH electrolyte solution described above was brought into close proximity to the mounted enamel surface with manual micrometre (M-461 series, Newport) and the aid of a camera (Pixel link with Edmund Optics lens, 6.0x magnification, 65 mm focal length). The bulk electrolyte solution was then added and the tip approached to the surface with the piezoelectric positioner while using DC feedback. Once surface is located, an oscillation of 10 nm was applied to the z-position of the tip at a frequency of 210 Hz using an external lock-in amplifier (SR830DSP, Stanford Research Systems) and the resulting AC current used to provide a stable feedback signal for throughout the approach and etch pit generation. LabVIEW software for controlled surface delivery in patterned arrays was used to carry out 36 dissolution measurements in a confined area. The probe position, AC current, and DC current were recorded and monitored simultaneously throughout.

To quantify the extent of the erosive damage caused by the proton attack, the depth of the etch pits is measured *in situ*. By applying a physical oscillation to the

probe in the  $z$  direction, an AC component is introduced into the ion current. This modulated AC signal originates from any change in the ion current over the course of an oscillation, which is usually only significant when the probe is brought into close proximity of a surface. In essence, when in bulk solution there is negligible change in the current from peak to trough (*i.e.*, AC signal is zero), as the system resistance remains constant. However, when the oscillating probe is at a distance from the surface with a similar size to the diameter of the nanopipette pore, there is an appreciable AC component as the tip-surface distance is modulated. This is due to the restricted ion flow resulting from the increased access resistance when the tip is closer to the substrate *i.e.* at the bottom of the  $z$ -height oscillation.

The direct current (DC) component of the ion current is sensitive to both the access resistance (tip-substrate distance) and local ionic environment (*i.e.* induced by surface charge or chemical reactions). This is especially important when attempting to measure a dissolution process which generates a local flux of ions from the target surface, and therefore may affect the DC component of the ion current. The AC amplitude is far less susceptible to changes in the local ionic environment at the surface because it is calculated over the period of an oscillation throughout which the local concentrations do not change appreciably (*vide infra*). Employing an AC feedback condition by applying a small sinusoidal perturbation to the height of the probe therefore allows accurate determination of the tip-substrate separation.

During the approach, the probe is biased at -100 mV which causes migration of protons up the nanopipette, counteracting the concentration gradient, and minimizing proton efflux from the tip (Figure 3.2A LHS.) Upon detection of the surface, the probe QRCE is then biased positively relative to bulk (100 mV in most cases herein, Figure 3.2A RHS), the protons are thereby expelled, inducing a dissolution reaction and etch pit formation at the enamel surface. As the pit forms a constant  $d$  value will be maintained by moving the probe closer to the sample and into the etch pit. As a result, the  $z$  height measured during the 10 second dissolution (proton delivery) pulse is an accurate measure of the depth of the etch pit, and the change in  $z$  is proportional to the rate of dissolution (or the rate of pit formation).

Through utilisation of a scan hopping regime, it is possible to generate and record multiple etch pits on a sample in a discrete area. Once a pit is made, the probe is retracted from the surface ( $\sim 2\text{ }\mu\text{m}$ ) and translated in the  $x$ - $y$  plane to begin the next



approach. A separation distance of 3  $\mu\text{m}$  between approaches was chosen, as the diameter of each pit being sub 1  $\mu\text{m}$ . From this a 6 x 6 array of etch pits was generated which can be adjusted along with the delivery time to provide a balance between statistically significant numbers of etches per array and an acceptable experiment duration of ~30 minutes.

With a polished enamel surface (roughness < 10 nm) repeatability is good, however etch pit failures do occur. Due to small surface defects or variations in the current attributed to minor blocking events at the nanopipette opening, etching may not occur in a uniform manner. This is evident from a 20 nm retract from the approach distance due to the change in current with the change to delivery potential. At this distance, surface sensitivity can be lost and the tip does not re-engage tracking of the surface, shown by the maintenance of this retracted height throughout the pulse. Figure 3.2C provides an example of such an event. All such traces are counted as false engagements and are thus excluded from analysis.

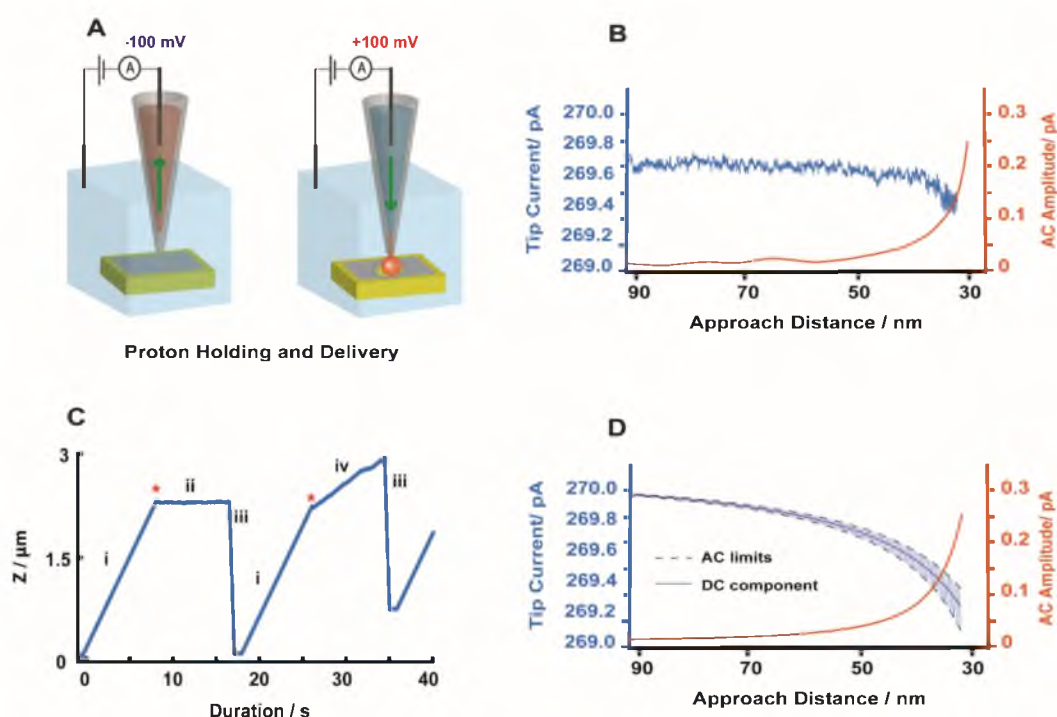


**Figure 3.2 SICM procedure.** (A) Infographic depicting proton holding (LHS) and delivery (RHS) with a nanopipette. When a positive bias is applied to the working electrode the protons are driven out of the nanopipette and react with the enamel in

the footprint of the probe, generating an etch pit. (B) Experimental AC and DC approach curves, raw experimental data showing the change in DC (blue) and AC (red) feedback currents when the nanopipette is translated towards a dental enamel surface. Approach distance calculated with FEM simulation. As separation distance decreases, DC also decreases and AC increases to the approach threshold of 0.25 pA. Either of these can be used for positional feedback. (C) Two Z profiles from which the etch pit depths are calculated, first trace being a false engagement and second a valid etch trace i. Approach to the surface at holding potential. ii. Delivery during a false engagement, note minimal penetration to the surface. iii. Retracting away from the surface at holding potential. iv. Delivery to the surface during a valid etch pit formation resulting in a constant etching rate. \* Denotes the point the probe engages the surface in each trace. In the first trace it is clear no etching occurs as the surface is not engaged. (D) Calculated approach curves from the FEM model. The DC (blue) has the AC amplitude of the oscillation superimposed over it. The AC amplitude (red) increases at close separation distances.

### **3.4 Theory and Simulations**

#### **3.4.1 FEM Model**

FEM simulations were constructed in COMSOL Multiphysics (v5.4) to extract the effective rate of reaction for acid induced enamel erosion. The system was simulated using 2D axisymmetric model (Figure 3.3A), with the nanopipette geometry built from representative scanning transmission electron micrographs (STEM) of experimental nanopipettes (a representative STEM image is presented in Figure 3.4).<sup>60</sup> The radius of the pipette opening was measured as 15 nm and the height of the simulation domain of the nanopipette was chosen sufficiently large enough to not affect the results of the simulation (650  $\mu\text{m}$ ), likewise the outer boundaries (Figure 3.3A, Boundary B2) were sufficiently far away to be considered bulk (100  $\mu\text{m}$ ).

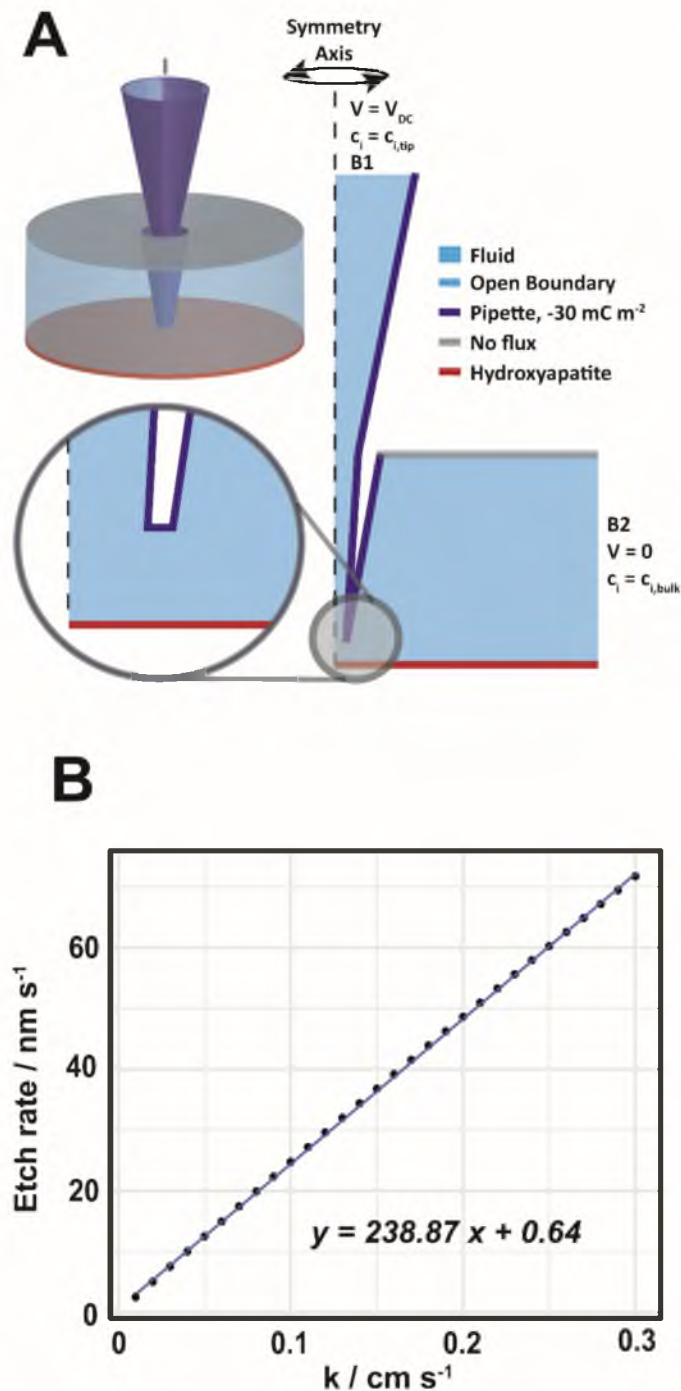


**Figure 3.3 Schematic and results from FEM simulations.** (A) Schematic (not to scale) of the FEM simulation domain for SICM tracked etching of enamel substrates (red). Nernst-Planck, Poisson and Navier-Stokes equations (Equations. 3.2-3.4) are solved throughout the simulation domain as described in the main text. Boundaries were prescribed as labelled, with B1 and B2 as open boundaries for fluid with set concentrations and voltages. Dashed line shows the 2D axisymmetric axis. All other boundaries are no-slip fluid boundaries, with charge of  $-30 \text{ mC m}^{-2}$  in the case of the

pipette (purple) and 0 mC m<sup>-2</sup> for all other boundaries. (B) Calibration plot of kinetic rate constant ( $k_0$ ) against etching rate during proton delivery, as calculated through steady state simulations, allowing effective rate constant to be calculated.



**Figure 3.4 Scanning transmission electron microscopy (STEM) image of a representative nanopipette.** Pore diameter of approximately 30 nm.

Transport of dissolved species were described by the Nernst-Planck equation (Equation. 3.2):

$$J_i = -D_i \nabla c_i - z_i \frac{F}{RT} D_i c_i \nabla \phi + c_i u \quad (3.2)$$

where  $F$ ,  $R$  and  $T$  are the Faraday constant, gas constant and absolute temperature (298 K), and  $D_i$ ,  $z_i$  and  $c_i$  are the diffusion coefficients, charge number and concentrations of species  $i$  (Table 3.1). This is coupled to the Poisson equation (Equation. 3.3) to describe the electric potential ( $\phi$ ), and the Navier-Stokes equation (Equation 3.4) to describe solution velocity ( $u$ ) accounting for movement due to electroosmotic flow.

$$\nabla^2 \phi = -\frac{F}{\epsilon \epsilon_0} \sum_i z_i c_i \quad (3.3)$$

$$u \nabla u = \frac{1}{\rho} (-\nabla p + \mu \nabla^2 u - F (\sum_i z_i c_i) \nabla \phi) \quad (3.4)$$

At the enamel/solution interface (red boundary) the dissolution of HAP is modelled through the reaction described in Equation 3.1, where the inward flux of dissolution

products is defined by the heterogeneous reaction rate ( $k_0$ ), local proton activity  $\{H^+\}$ , and unit vector normal to the boundary ( $n$ ):

$$-n \cdot N_{Ca^{2+}} = k_0 \cdot \{H^+\} \cdot \left(\frac{10}{8}\right) \quad (3.5a)$$

$$-n \cdot N_{HPO_4^{2-}} = k_0 \cdot \{H^+\} \cdot \left(\frac{6}{8}\right) \quad (3.5b)$$

$$-n \cdot N_{H^+} = -k_0 \cdot \{H^+\} \quad (3.5c)$$

Throughout the simulation domain, species equilibrium was controlled by a set of reactions which were defined as follows:

$$H_3PO_4 \rightleftharpoons H^+ + H_2PO_4^- \quad K_{a1}^+ = \frac{\{H_2PO_4^-\}\{H^+\}}{\{H_3PO_4\}} \quad (3.6a)$$

$$H_2PO_4^- \rightleftharpoons H^+ + HPO_4^{2-} \quad K_{a2}^+ = \frac{\{HPO_4^{2-}\}\{H^+\}}{\{H_2PO_4^-\}} \quad (3.6b)$$

$$H_2O \rightleftharpoons H^+ + OH^- \quad K_w = \frac{\{OH^-\}\{H^+\}}{55.5 \text{ M}} \quad (3.6c)$$

where  $K_{a1}^+$ ,  $K_{a2}^+$  and  $K_w$  are the dissociation constants. The local activity ( $a_i$ ) of each ion (Equation 3.7) is calculated through the Truesdell-Jones equation (Equation 3.7b) from Debye-Hückel theory:

$$a_i = \gamma_i \frac{c_i}{c_0} \quad (3.7a)$$

$$\log_{10} \gamma_i = -Az_i^2 \left( \frac{\sqrt{I}}{1+\sqrt{I}} + BI \right) \quad (3.7b)$$

$$I = \frac{1}{2} \sum_{i=1}^n c_i z_i^2 \quad (3.7c)$$

where local  $\gamma_i$  is the activity coefficient of each ion, A and B are empirical parameters with values of 0.5 and 0.2 respectively and  $I$  is the local ionic strength (Equation 3.8). All electric potentials were applied to the upper nanopipette boundary (B1) at which concentrations were maintained corresponding to those of the acid filled pipette; ( $[K^+] = 50 \text{ mM}$ ,  $[Cl^-] = 70 \text{ mM}$ ,  $[H^+] = 20 \text{ mM}$ ) with the concentration of phosphate species set to 0 mM and  $[OH^-]$  set by the resulting pH of 1.70. At the bulk boundary (B2), electric ground ( $V = 0$ ) was applied alongside bulk concentrations ( $[K^+] = 50 \text{ mM}$ ,  $[Cl^-] = 50 \text{ mM}$ ,  $[H_3PO_4] = [HPO_4^{2-}] = 0 \text{ mM}$ ), where  $[H^+]$  and  $[OH^-]$  were defined by the solution pH of 6.8. Each of these boundaries (B1 and B2) was also defined as an open fluid boundary, while a no-slip condition was enforced at all remaining boundaries. Surface charge was only applied to the walls of the pipette ( $-30 \text{ mC m}^{-2}$ ), resulting in electroosmotically driven flow. The transport properties of simulated species used in Equations 3.2-3.9 are presented in Table 3.1.

**Table 3.1 Table of species properties used in FEM.** Diffusion coefficients and charges of species used in FEM simulations, obtained from the CRC handbook.<sup>61</sup>

Species	Diffusion Coefficient ( $D$ ) / $\text{cm}^2 \text{s}^{-1}$	Charge ( $z$ )
$\text{H}^+$	$9.311 \times 10^{-5}$	1
$\text{OH}^-$	$5.273 \times 10^{-5}$	-1
$\text{HPO}_4^{2-}$	$0.759 \times 10^{-5}$	-2
$\text{H}_2\text{PO}_4^-$	$0.959 \times 10^{-5}$	-1
$\text{H}_3\text{PO}_4$	$0.882 \times 10^{-5}$	0
$\text{Ca}^{2+}$	$0.792 \times 10^{-5}$	+2

### 3.4.2 Simulation Methodology and Validation

The approach was first simulated with the holding bias of -100 mV as a steady state simulation, corresponding to the DC component from which the AC amplitude was calculated from the DC amplitude of a 10 nm peak to peak oscillation of the tip. For visualisation of the approach characteristics, the DC approach was fitted with an accepted semi-empirical formula<sup>62</sup> and the distance modulated current calculated as a sum of the DC component and AC perturbation (Figure 3.2D). The AC amplitude approach set point of 0.25 pA was calculated as a tip-substrate separation of 36.5 nm, at this point the proton flux is low with a surface pH of 5, marginally more acidic than the accepted critical pH of 5.5,<sup>41</sup> indicating that the holding potential is effective and the substrate is relatively stable throughout the approach.

Acid delivery was simulated as a steady state simulation with +100 mV bias applied at the top of the pipette, the AC amplitude set point of 0.25 pA is maintained and the calculated tip-substrate separation is 39 nm as the centre of the of  $\pm 5$  nm oscillation. Simulations at  $39 \pm 5$  nm indicate that the AC amplitude is insensitive to changes in surficial fluxes across the range of  $k_0$ , thereby maintaining a constant tip-substrate separation independent of local surface dissolution (Section 3.7.2, Figure 3.5). These simulations also show that over a full period of oscillation, the resulting tip-substrate separation causes very small differences in estimates of  $k_0$ , with only 2%

deviation between the peak (44 nm) and trough (34 nm) of the perturbation (Figure 3.6). Steady state simulations are therefore considered reasonable because the surface tracking is able to maintain a constant tip-substrate separation and the etching rate is independent of the sinusoidal perturbation in tip-substrate separation. Additionally, the etching rates (up to 70 nm s<sup>-1</sup>) are slow in comparison to the time required to reach steady state (10's of ms), particularly considering that there will be additional mixing induced by pipette oscillation. Etching rates were calculated from the depth of HAP removed in the region underneath the pipette, using the molar volume of HAP ( $V_m = 3147.4 \text{ mol m}^{-3}$ ) (Equation 3.9):

$$K_{etch} = \frac{-k_0 \cdot \{H^+\}}{\frac{1}{8}V_m} \quad (9)$$

While enamel is not pure HAP, estimates suggest that 90% of the content comprises of individual HAP crystals which are 75 nm in diameter.<sup>63</sup> Thus the scale of the tip diameter (30 nm) and associated SICM resolution are smaller than the scale of HAP crystals and enamel heterogeneities (*vide infra*).<sup>31</sup> By applying different  $k_0$  values in the simulations, a calibration between etching rate and effective rate constant ( $k_{eff}$ ) can be obtained (Figure 3.3B), the high degree of linearity in this plot indicates that the mass transfer of protons to the surface is sufficiently high to ensure that the reaction is kinetically limited even at high reaction rates. As such, the fully surface limited regime generated by SICM delivery techniques ensures experimental values are a direct measurement of surface kinetics, demonstrating ability to specifically probe even very fast interfacial processes.

FEM simulations were performed to assess the accuracy and validity of steady state models during the delivery pulse, the deviation in AC over the range of  $k_0$  corresponding to experimental  $K_{etch}$  was assessed (Figure 3.5), as was the effect of the sinusoidal perturbation in z-height upon  $K_{etch}$  (Figure 3.6). Figure 3.5 shows that the ionic fluxes from the surface induce deviation in the AC of only -0.05 pA compared to an inert substrate (0.25 pA). FEM simulations indicate that this causes a maximum change in tip-substrate separation of approximately -0.25 nm. This minor change is not expected to significantly affect  $k_{eff}$  calculated from experimental  $K_{etch}$ .

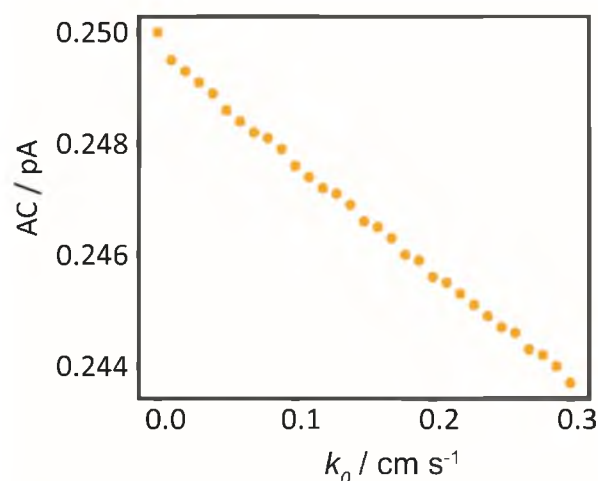


**Figure 3.5 AC amplitude at different rate constants.** FEM simulation of AC during SICM proton delivery at across the range of  $k_0$  corresponding to the experimental  $K_{etch}$  at 39 nm tip-substrate separation  $\pm 5$  nm sinusoidal oscillation.

To assess whether the applied oscillation affects the etching rate to a significant degree  $k_0$  was estimated for the extremes of the oscillation. Figure 3.6A presents simulated  $K_{etch}$  as a function of  $k_0$  for the peak (44 nm) and trough (34 nm) of the  $\pm 5$  nm sinusoidal perturbation of the tip-substrate separation. The steady state simulations presented in the main text assume that the center of this oscillation (39 nm) is representative of the entire period of oscillation. The requirement of this assumption is that  $K_{etch}$  varies linearly with tip-substrate separation, thereby allowing the mean height to be representative of the mean  $K_{etch}$ . However, if there is a significant skew in acid delivery between the maxima and minima, the response will be incorrectly calculated due to non-linearity of the dissolution response between the highest point (delivering less acid, overestimating surface kinetics) and the lowest point (delivering more acid, underestimating surface kinetics). The maximum deviation from the mean height estimate will be caused by the two extremes of the oscillation (44 nm and 34 nm), therefore the mean  $K_{etch}$  of these two tip-substrate separations represents the largest possible deviations from this assumption. Figure 3.6B shows the difference between the  $K_{etch}$  calculated at the mean height and calculated as the mean of the  $K_{etch}$  from both extremes in height. This indicates a maximum systematic underestimation of 1.7-1.8% of  $K_{etch}$  over the range of  $k_0$ , which would lead to a similar magnitude in overestimation of  $k_{eff}$ . These data show that the increase in accuracy from simulating



the entire period of oscillation are insufficient for the computational cost and that simulation error is well within sample deviation.

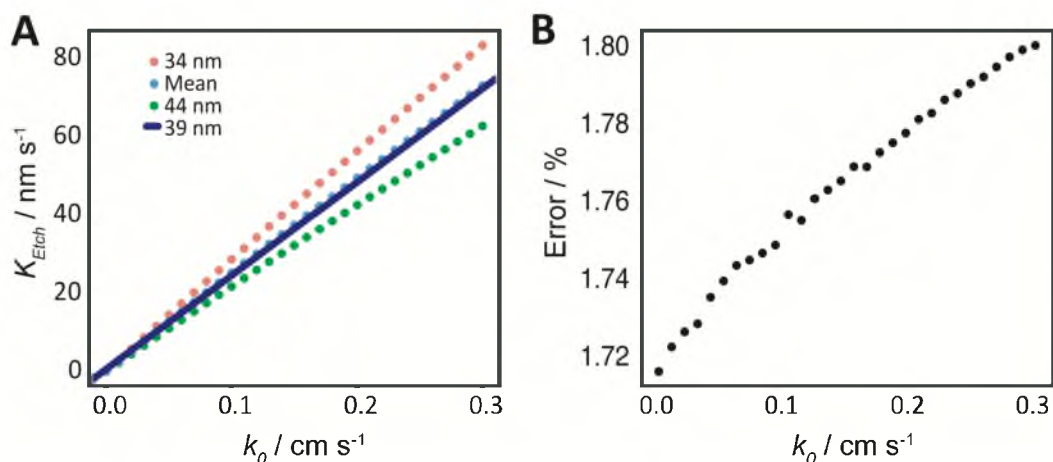


**Figure 3.6 FEM simulations of the relationship between the etching rate and  $k_0$ .**

(A) Simulated  $K_{Etch}$  for the peak (44 nm, orange) and trough (34 nm, green) of the oscillation for distance modulated surface tracking during the proton delivery pulse. The etching rate calculated from the mean  $K_{Etch}$  of the peak and trough within one period of oscillation (light blue) shows the maximum deviation from the etching rate calibration line calculated by steady state simulations at the center of the oscillating tip-substrate separation (39 nm, dark blue). (B) shows the percentage difference between the two estimations is 1.7-1.8% within the relevant range of  $k_0$ .

### 3.5 Results and discussion

#### 3.5.1 Parameter testing

Initial experiments to validate the procedure and to establish a suitable holding potential as well as delivery potential were undertaken. Figure 3.7 shows the etch pit z traces at different potentials over 30 seconds. For all positive potentials the same etching trace was observed demonstrating that over this range of potentials the reaction is surface kinetically limited. Increasing the flux of protons into the reaction space does not increase the etch pit depth meaning the size of the etch pit generated is dependent on the erosive properties of the surface and not any migration, diffusion or delivery based limitations. It can be seen that at -100 mV a minimal amount of etching occurs. The protons are largely retained by the bias at this potential, and the minor z change that does occur may be down to piezo drift or a negligible amount of proton leakage. This makes -100 mV a good choice for a holding potential.

Applying a bias of -50 mV only partially retains the protons in the nanopipette and an etch pit is formed, albeit at a slower rate. This is due to the migrative flux induced by the electric field being unable to completely counteract the diffusive proton flux out of the nanopipette at this potential. The flux of species out of the probe, due to the concentration gradient from inside to outside of the nanopipette, overcomes the holding potential and etching occurs. 100 mV was used as a delivery potential over a 10 second duration for all experiments. Keeping the experimental duration low but obtaining a statistically relevant number of etch traces (36) was prioritised. Other delivery conditions and array sizes can easily be studied with this system.

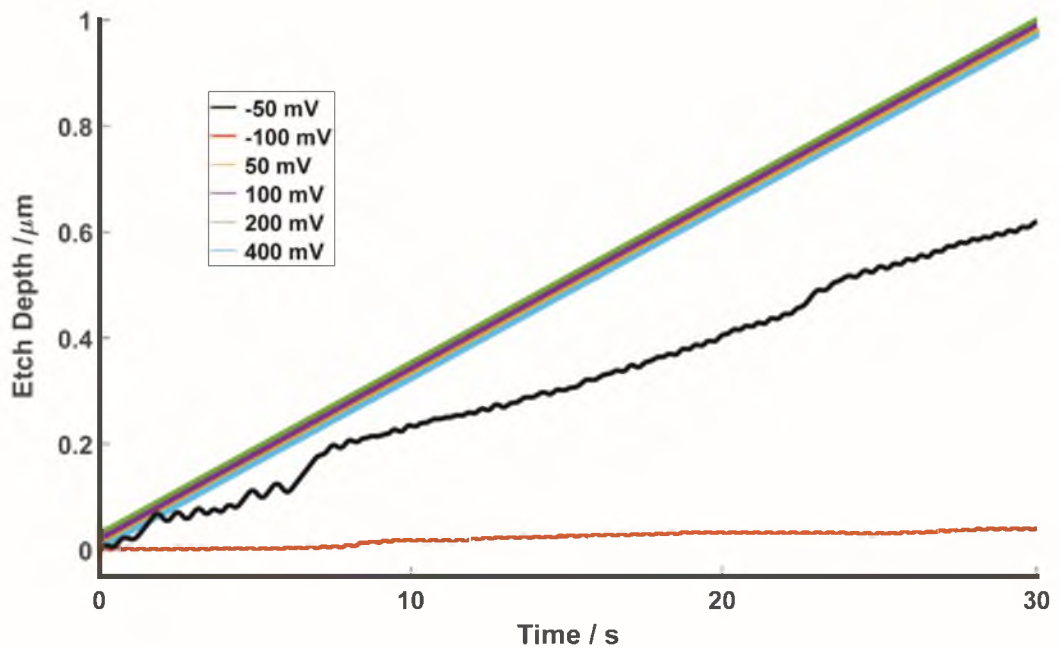


**Figure 3.7 Etching depth vs. time for different delivery biases.**

### 3.5.2 Probe and sample variability.

To ensure consistency between etch arrays, a 30 nm nanopipette was used to make 3 identical arrays of 36 pits on the same enamel sample. A Kruskal-Wallis test showed no statistically significant difference between the arrays ( $\chi^2 = 3.261$ ,  $p = 0.196$ ) with median etch depths of 594 nm (Q1 = 534 nm, Q3 = 653 nm), 610 nm (Q1 = 534 nm, Q3 = 667 nm), and 532 nm (Q1 = 456, Q3 = 673). To test inter-probe variation, 3 different probes were used on discrete areas of the same sample and also lack statistically significant differences ( $\chi^2 = 0.506$ ,  $p = 0.777$ ), with median etch depths

of 610 nm (Q1 = 539 nm, Q3 = 693 nm), 598 nm (Q1 = 522 nm, Q3 = 702 nm) and 633 nm (Q1 = 541 nm, Q3 = 714 nm). This indicates that there is experimental consistency between experiments using different tips and between repeated tests of the same sample, with variation due to spatial heterogeneity. It is notable that mean etch pit depths of the two enamel blocks in this section are different. This was seen throughout the experiments and reflects the heterogeneous nature of organic dental samples.

### **3.5.3 Taped enamel Vs sound enamel**

To ensure any residue that may be left after using Kapton tape as a protective covering does not adversely affect the experiment, a control was run. The control follows the same procedure but administers 37 °C distilled water to the sample rather than a fluoride solution. 106 measurements were taken on the un-taped sound enamel and 81 on the taped enamel, with means of 558 nm (Q1 = 496 nm, Q3 = 646 nm) and 569 nm (Q1 = 485, Q3 = 631), respectively. Using a Wilcoxon rank-sum test  $p = 0.912$ , indicating no significant difference between the taped and un-taped enamel.

### **3.5.4 Citric acid and fluoride treatments**

To investigate whether the technique has the potential to be used as a screening test for enamel repair and protection assays a multiple treatment study was undertaken.  $N = 5$  enamel blocks were polished down to a 50 nm finish with diamond lapping suspension. Each sample was masked with Kapton tape so that half of the enamel surface was covered and protected. The samples were exposed to 1450 ppm sodium fluoride solution for 30 minutes at 37 °C, thus exposing one half of the sample to fluoride. Once completed, the samples were thoroughly rinsed, and the protective tape removed. Each sample was then subsequently tested with SICM. 6x6 arrays were made on the untreated side of the enamel and then the fluoride treated. The electrolyte solution was then removed, and the probe retracted to the maximum distance from the surface (~1 cm) before the entire sample was exposed to a 30 second 1% citric acid wash. The sample was rinsed thoroughly, the electrolyte replaced, and the probe returned to the surface. Being sure to avoid the original etching areas, the samples were then re-measured with the SICM etching protocol on both the sound enamel and fluoride treated regions. This gives results from each sample reflecting the sound,

fluoride treated, citric acid treated and fluoride followed by citric acid treated enamel. These experiments allow for the investigation of inter-sample variability, fluoride protection benefits for sound enamel, quantification of the weakness caused by citric acid exposure and an assessment of the protective benefit offered by fluoride against citric acid erosion (Figure 3.8).

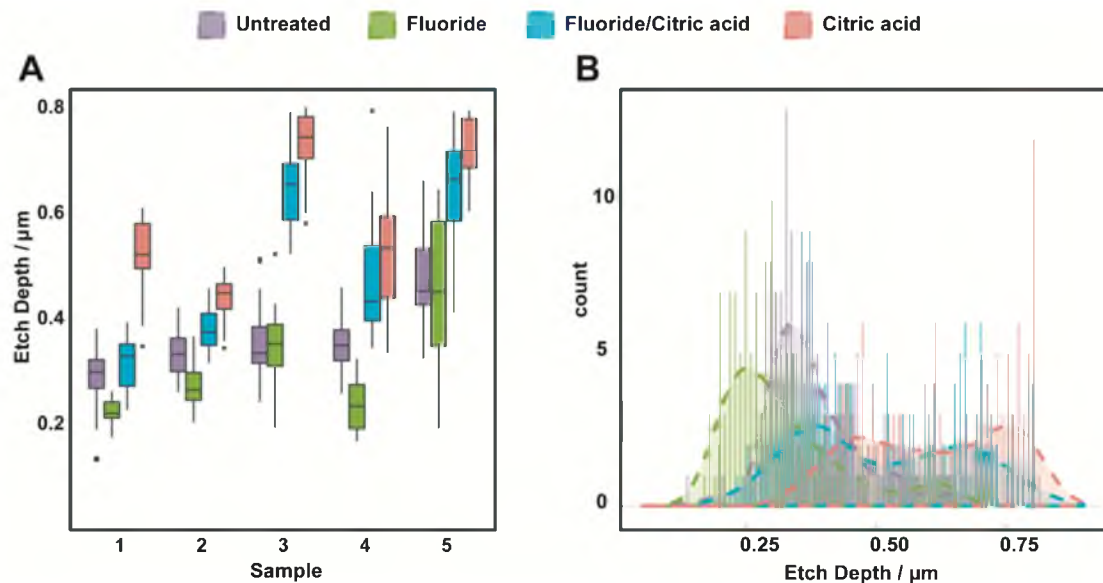


**Figure 3.8 Summary figures of recorded etch depths.** (A) Box plot of etch pit depth for untreated, fluoride treated, fluoride then citric acid and citric acid treated enamel across the 5 samples. Median is central black line, extents of boxes are first and third quartile, black lines are range of data (within 1.5 times the interquartile range) and dots are outliers from this range. (B) A histogram showing the spread of all results for sound, fluoride treated, fluoride then citric acid treated, and citric acid treated enamel, with overlaid kernel density estimates. General trends can be distinguished, primarily fluoride decreasing etch pit depth compared to sound enamel and citric acid exposure greatly increasing etch pit depth.

Table 3.2 provides a summary of the mean etch pit depths which are also displayed in Figure 3.8 alongside aggregated treatment distributions. The etch pit depths, in conjunction with FEM modelling, allow for the dissolution rate and calcium release rate from the surface to be calculated. Using the calibration plot in Figure 3.3 the experimental etch depths can be converted to etching and calcium dissolution rates. The calculated rates are shown in Table 3.2, along with the mean depth value for each etch pit array on each sample.

**Table 3.2 Summary table of etch pit depth and FEM calculated dissolution rates.**

The combined mean of the median etch rates for each condition is shown with the standard error of the mean to indicate sample variation. The mean of medians is used to calculate  $k_{eff}$  through the calibration in Figure 3.3B and also converted to surficial

	Untreated Enamel	Fluoride	Fluoride / Citric Acid	Citric Acid
Mean of median etch rate (nm s <sup>-1</sup> )	36.0 ± 2.6	31.1 ± 4.3	49.8 ± 7.0	60.0 ± 5.85
$k_{eff}$ / cm s <sup>-1</sup>	0.148 ± 0.008	0.128 ± 0.015	0.206 ± 0.027	0.249 ± 0.022
$j_{Ca^{2+}} \times 10^{-5}$ / mol m <sup>-2</sup> s <sup>-1</sup>	1.7 ± 0.2	1.5 ± 0.2	2.4 ± 0.3	2.9 ± 0.3

calcium flux ( $j_{Ca^{2+}}$ ).

Differences between treatments were significant when analysed by Kruskal-Wallis test ( $\chi^2 = 247.91$ ,  $p < 2.2 \times 10^{-16}$ ) and analysis by pairwise Wilcoxon rank-sum test also indicates that each treatment is significantly different from each of the others ( $p < 0.05$ , Section 3.7.3 Table 3.3). This allows analysis of general trends within the data, however the standard error of the means is large and there are also significant differences across the samples ( $\chi^2 = 162.23$ ,  $p < 2.2 \times 10^{-16}$ ), with individual sample distributions shown in Figure 3.9. Comparing the means reported in Table 3.2 it is evident that fluoridation of the enamel leads to a decrease in the etch pit depth and citric acid exposure causes an increase,

Figure 3.8B also demonstrates the spatial heterogeneity observed over the samples with regards to the sample response.

**Table 3.3 Pairwise analysis of aggregated data.** Calculated *p*-values from pairwise analysis of aggregate data by the Wilcoxon rank-sum test with Bonferroni adjustment. Ratios of median etch pit depths demonstrate protective effect of fluoride vs. sound enamel (0.863), weakening effect of citric acid vs. sound enamel (1.667), and weakening effect of citric acid treatment to fluoride exposed enamel (0.83).

	Citric acid	Fluoride	Fluoride/Citric acid
Fluoride	$< 2 \times 10^{-16}$	-	-
Fluoride/Citric acid	$2.8 \times 10^{-7}$	$< 2 \times 10^{-16}$	-
Untreated	$< 2 \times 10^{-16}$	$3.1 \times 10^{-7}$	$6.1 \times 10^{-13}$

The relatively brief citric acid treatment has a strong weakening effect upon enamel, increasing etching rates under subsequent acid delivery by 1.67 times. This is caused by a sustained increase in etching rate over the 10 seconds of the experiment (representative etching traces are shown in Figure 3.2C and Figure 3.7), suggesting that citric acid is able to permeate more than 500 nm into the enamel surface where it is at sufficiently high concentration to cause significant weakening of the enamel. This weakening occurs through two mechanisms; simple acid attack which dissolves the enamel and increases the porosity of the surface, and chelation of  $\text{Ca}^{2+}$  which leaves less stable HAP.<sup>44,55,57</sup>

Fluoride etch depths are 0.86 those of sound enamel, indicating a strong protective effect of fluoride from acid attack, suggesting that fluoride is also able to permeate into the enamel. While it is known that fluoroapatite is more resistant to acid dissolution than HAP, the penetration depth of fluoride ions into the enamel layer is debated, with some reports suggesting only 10s of nanometres being substituted.<sup>64</sup> This debate could be addressed through employing SICM and longer delivery times in future work. If there exists a surface layer of the HAP that has been substituted for fluoroapatite rather than a bulk change in the material, there should be a point at which the gradient of the etching curve begins to change with the rate of dissolution

increasing when moving from the fluoroapatite to HAP region. However, many estimates consider enamel as a perfect crystalline HAP surface, while in reality enamel is a heterogeneous biomaterial made up of small HAP crystals in a biopolymer matrix and could therefore allow deeper permeation, especially as the samples have been cut and may experience cracking. Interestingly, where the citric acid treatment is preceded by fluoride there is a similar reduction in etch rates (0.83 that of citric acid only) to those observed when citric acid is not applied (0.86). This suggests that fluoride does not provide extra protection against citric acid attack and possible chelation of calcium compared to general protection against acid attack.<sup>63</sup>

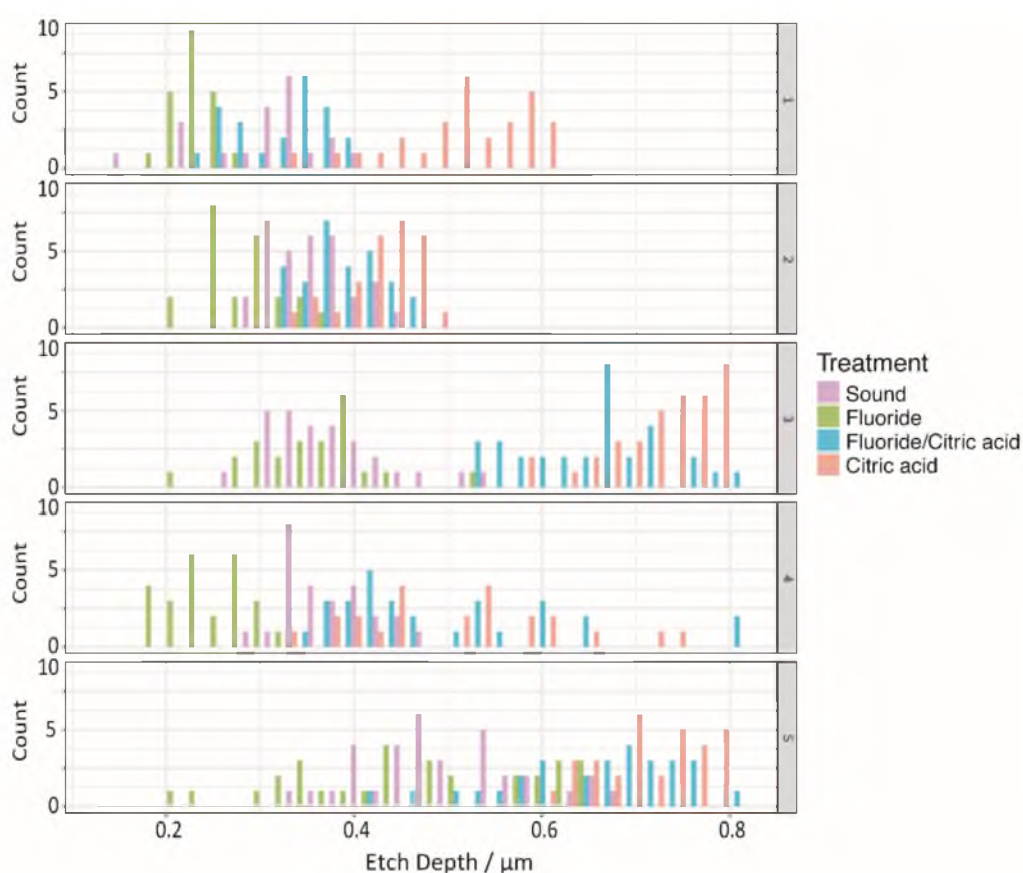


**Figure 3.9 Individual sample distributions for etch pit depth.** Distribution of etch pit depths generated through SICM proton delivery and surface tracking for 5 separate enamel samples with various surface treatments; (pink) sound enamel, (green) 30 minute exposure to fluoride (1450 ppm), (red) 30 s exposure to citric acid (1%), and (blue) exposure to fluoride followed by citric acid.

FEM simulations of the acid delivery conditions show that the concentration of protons at the surface results in a pH of 2.8 at areas proximal to the probe (Figure 3.10), this corresponds to a moderate to strong acid attack treatment, comparable to exposure to stomach acid.<sup>65,66</sup> The average effective rate constants for each treatment are shown, with sound enamel calculated to be  $0.15 \text{ cm s}^{-1}$ , comparable to literature values and previous research from this group.<sup>6,46</sup> As the reaction has been shown to be almost entirely surface limited, there is a linear relationship between etching rate and effective kinetic rate constant. The shape of etch pits is also shown for each treatment mean as the etching rate, as the pH decreases to bulk (pH 6.8) across the surface, the etching rate decreases accordingly.

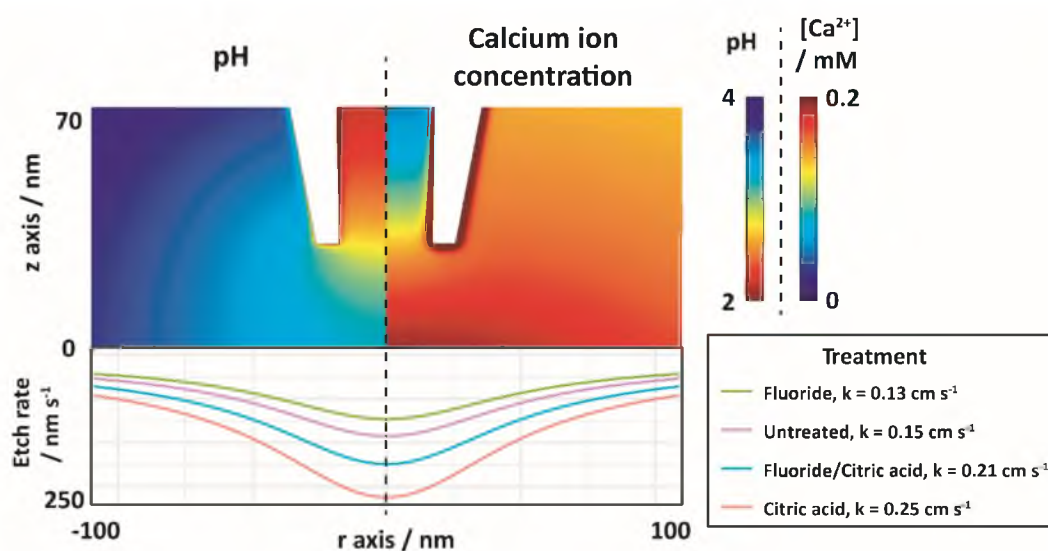


**Figure 3.10 FEM simulation of the SICM proton delivery and surface tracking process on enamel with various surface treatments.** Steady state simulation of pH distribution created by controlled proton flux from the pipette in proximity to the surface are shown for  $k = 0.15 \text{ cm s}^{-1}$  (left), with the corresponding concentrations of  $\text{Ca}^{2+}$  due to dissolution flux (right). Surface etching rates are shown across the surface (bottom) for rates of interest from Table 3.1.



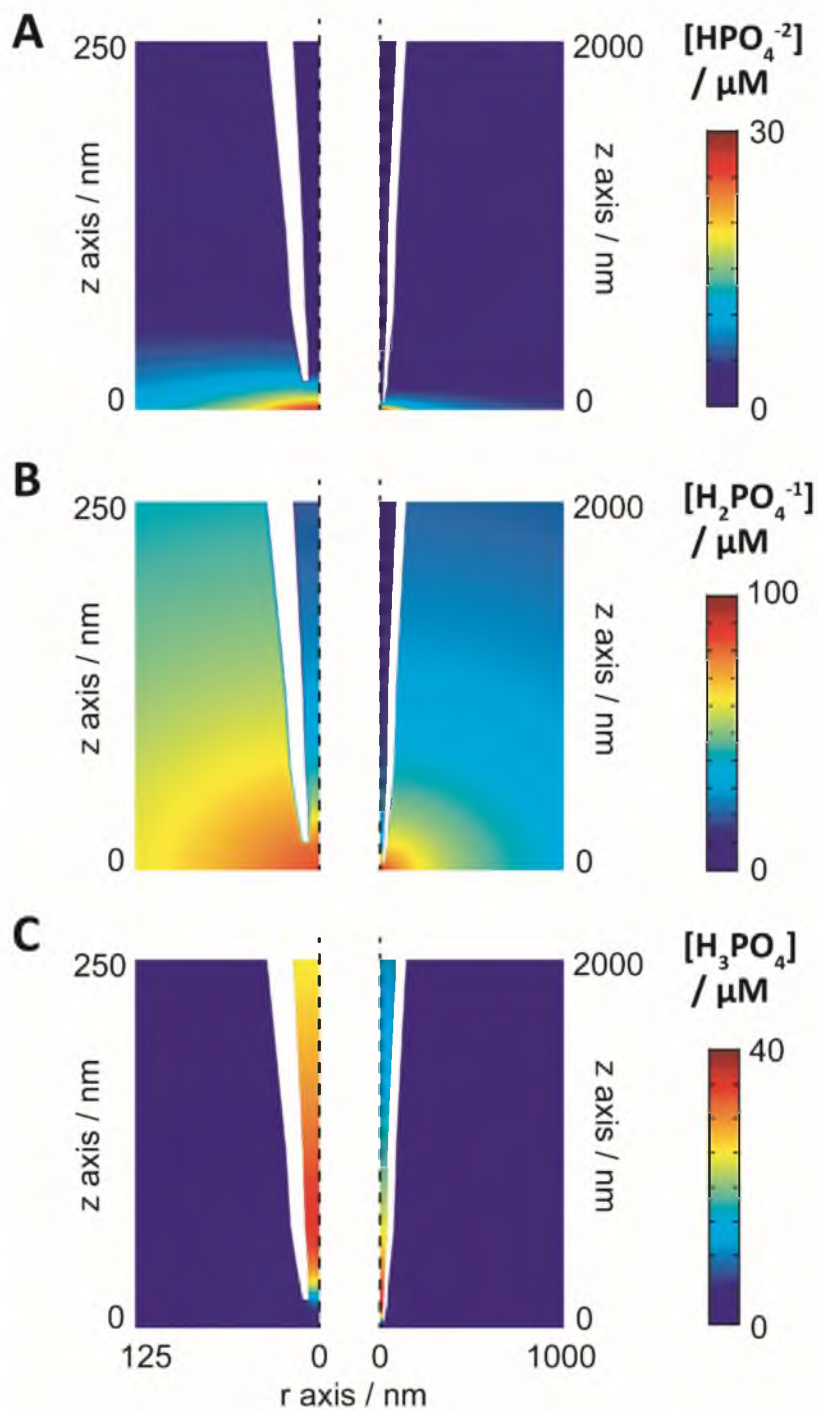


**Figure 3.11 FEM simulations of species distributions.** Distribution of phosphate species in steady state FEM simulations of SICM proton delivery. (A)  $\text{HPO}_4^{2-}$  is produced by acid induced dissolution of HAP at the substrate surface, this is quickly protonated to (B)  $\text{H}_2\text{PO}_4^-$  which mainly diffuses into bulk but also migrates into the tip where it is again protonated to (C)  $\text{H}_3\text{PO}_4$  which is only present in the first few microns of the pipette.

The rate constant for fluoride treated enamel is less well represented in the literature due to the increased number of factors involved which define the ratio of fluoride substitution. The effective rate constant from this work is ( $0.15 \text{ cm s}^{-1}$ ), this is far higher than that of fluoroapatite, which is estimated to be an order of magnitude lower than HAP,<sup>67</sup> and suggests that a small proportion of fluoroapatite is incorporated into the enamel. The flux of calcium from the surface is also shown (capped at 0.2 mM as it is concentrated within the double layer of the glass), with it shown to be excluded from the nanopipette due to the applied bias. The phosphate products however, form more complex spatial distributions.  $\text{H}_3\text{PO}_4$  is localised only within the last 2.5-3.5  $\mu\text{m}$  of the nanopipette (Figure 3.11) due to flux of phosphate products from the surface and the local pH gradient within the tip, generating spatially confined speciation which may be of interest to crystallisation studies.

For each sample, differences in the magnitude of response to citric acid and fluoride treatments were apparent (Figure 3.5), therefore a more detailed analysis was performed on each sample individually. The differences between treatments are once again significant for all samples as shown by the Kruskal-Wallis ( $p < 0.05$ , Table 3.3), however not all treatments are significantly different for each sample individually (

Table 3.4). Figure 7 demonstrates the effect of each treatment when compared with the sound enamel along with the  $p$ -value for each comparison.

The citric acid treatment shows a consistently significant weakening effect on the enamel, however both fluoride treatments show varied sample dependent protection efficacies. Fluoride treatment alone always reduces mean pit depth, however in two cases (3 and 5) these effects are small and the arrays not significantly different compared to the sound enamel. The effect of fluoride pre-treatment upon citric acid weakening is also complex, sample 1 demonstrates the strongest fluoride protection response in both cases (Figure 3.12), while samples 3 and 5 reflect poor response to fluoride overall. On the other hand, samples 2 and 4 are protected well against induced acid dissolution alone but poorly against the citric acid treatment.

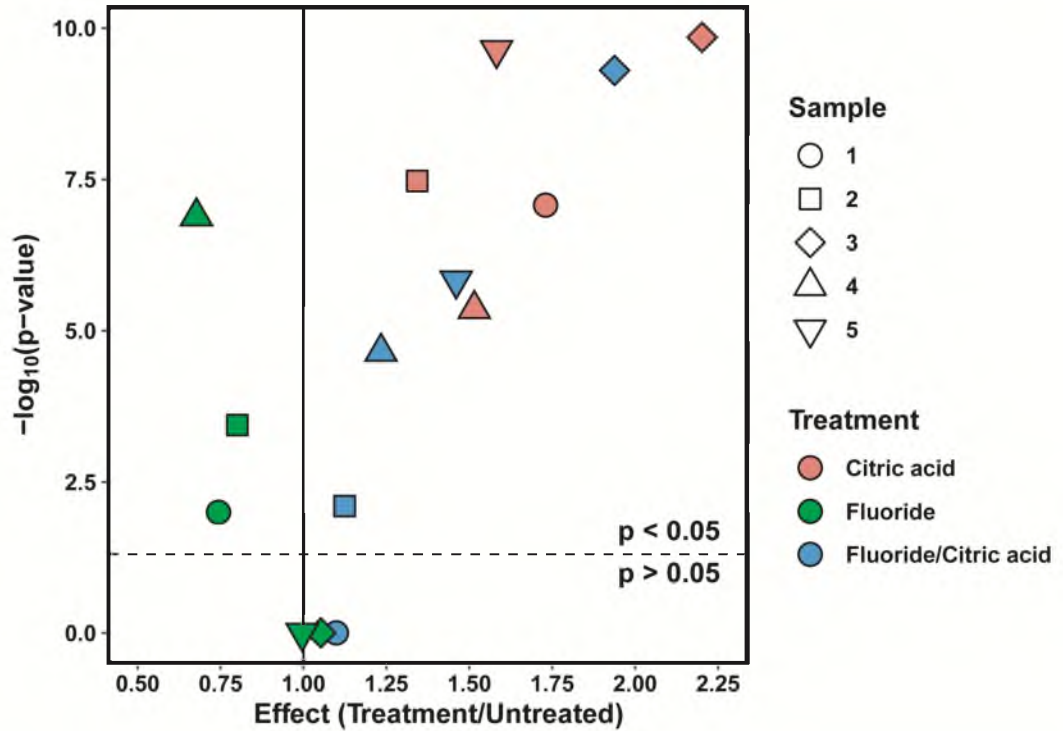


**Figure 3.12 Volcano plot of all treatments for each enamel sample.** For each sample (represented by different shapes) the ratio between median etch depth of sound enamel and each treatment (shape colour) is shown against the  $p$ -value comparing the treated array with the sound enamel, as determined by Wilcoxon ranked-sum tests with Bonferroni correction. The dashed line indicates the significance threshold of  $p = 0.05$  and the solid line shows the sound enamel. Treatments to the right of the vertical black line indicate an increased rate of etching compared to the corresponding untreated enamel sample, while treatments to the left of the same line indicate a relative decrease in etching rate. Treatments above the dashed line have statistically significant effects compared to untreated enamel.

**Table 3.4 Pairwise analysis of treatments from individual samples.** Calculated *p*-values from pairwise analysis of 5 individual samples by the Wilcoxon rank-sum test with Bonferroni adjustment.

Sample 1	Citric acid	Fluoride	Fluoride/Citric acid
Fluoride	$1.40 \times 10^{-8}$	-	-
Fluoride/Citric acid	$2.20 \times 10^{-12}$	$2.30 \times 10^{-6}$	-
Untreated	$3.40 \times 10^{-8}$	0.004	1
Sample 2	Citric acid	Fluoride	Fluoride/Citric acid
Fluoride	$1.20 \times 10^{-8}$	-	-
Fluoride/Citric acid	$3.30 \times 10^{-5}$	$9.60 \times 10^{-8}$	-
Untreated	$1.30 \times 10^{-8}$	0.00014	0.00315
Sample 3	Citric acid	Fluoride	Fluoride/Citric acid
Fluoride	$7.80 \times 10^{-10}$	-	-
Fluoride/Citric acid	$8.50 \times 10^{-6}$	$6.40 \times 10^{-15}$	-
Untreated	$5.70 \times 10^{-11}$	1	$2.00 \times 10^{-10}$
Sample 4	Citric acid	Fluoride	Fluoride/Citric acid
Fluoride	$1.90 \times 10^{-8}$	-	-
Fluoride/Citric acid	0.72	$2.00 \times 10^{-9}$	-
Untreated	$1.70 \times 10^{-6}$	$5.20 \times 10^{-8}$	$8.90 \times 10^{-6}$
Sample 5	Citric acid	Fluoride	Fluoride/Citric acid
Fluoride	$3.80 \times 10^{-10}$	-	-
Fluoride/Citric acid	0.0042	$3.80 \times 10^{-6}$	-
Untreated	$9.20 \times 10^{-11}$	1	$5.90 \times 10^{-7}$

There is also large within-sample variation, and it appears that there are often 2 distributions within each sample, suggesting 2 distinct surface environments with overlapping distributions (Figure 3.9). More samples would be needed across the sample surface to confirm this. The presence of 2 distributions may be due to the length scale on which SICM induced dissolution operates; the pipette diameter is much smaller (30 nm) than the 200-400 nm estimates of the size of inter-rod regions within

the enamel lattice, with the etch pits generated being on a similar scale.<sup>34</sup> It is possible that these 2 distributions correspond with inter-rod and central region enamel, with a more defined study being needed to confirm this.

These data suggest that there are properties of the different samples and different sites which make fluoride treatments more or less effective. A likely explanation for this is differences in composition or porosity which affect permeation into the sample, where some sites are only protected by fluoride at the surface. However, the same samples would therefore be expected to be least affected by citric acid exposure and this is not the case, suggesting that there are more factors influencing the sample response. These factors are difficult to standardise due to differences in the samples cut direction and depth leading to varying contribution from inter-rod and central regions, along with variability between individual donors. However, these spatial and sample variations would be completely inaccessible with other methods and SICM as a tool for inducing acid dissolution offers new opportunities to probe and understand enamel erosion and crystal stability as a whole.

### **3.5.5 Pellicle layer SICM enamel dissolution with topographical images.**

After completing an array, it is possible to run a topographical map without changing the probe or disturbing the sample, if the bias employed is negative and large enough (-100 mV) to retain the protons. The option to visualise the etch pits with a topographical map is a powerful tool when investigating surface modifications and treatments. Figure 3.13 compares the topography of etch pit arrays on a bovine enamel sample, with and without a salivary pellicle present. The protection benefit to the surface is evident in the reduction of the depth and width of the etch pits. The median depth of the pits without pellicle layer is 377 nm (Q1 = 352 nm, Q3 = 412 nm) and with pellicle present 284 nm (Q1 = 252 nm, Q3 = 331 nm), with statistically significant difference between the groups ( $p = 1.13 \times 10^{-23}$ ,  $n=31$ ).

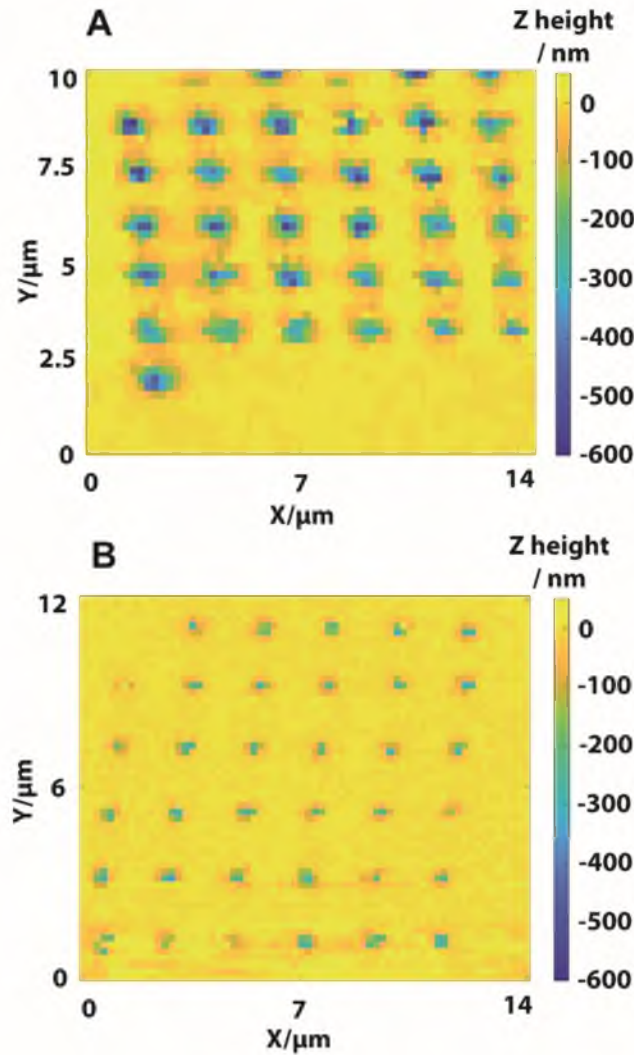


**Figure 3.13 SICM topography images of etch pit arrays on a) sound bovine enamel and b) with adhered pellicle layer.** Pellicle generated by 30 minute incubation in whole human saliva at 37 °C. Protective benefit of pellicle visualised by a reduction in etch pit size and depth. The median etch depth of 377 nm for the pellicle free sample corresponds to a  $k_{eff}$  of 0.155 cm s<sup>-1</sup> and the pellicle coated samples average depth of 284 nm corresponds to a  $k_{eff}$  of 0.116 cm s<sup>-1</sup>.

The 93 nm difference in etching depth is greater than the predicted maximum pellicle layer thickness of 40 nm.<sup>53</sup> This shows that the protective benefit of the pellicle against acid erosion is not solely sacrificial, *i.e.* the proteins and make-up of the layer inhibit the dissolution, potentially through a buffering effect that keeps the local pH higher.<sup>68</sup> However this would also be observed to some degree if the enamel was

significantly damaged by polishing that the pellicle layer could form within the resulting cracks. These images help to visualise the significant reduction in erosion offered by the pellicle layer. An exact measurement in the etch pit width is hindered by the resolution provided by the 200 nm hopping distance used, however the depths are consistent with the obtained pit depths from the acid delivery experiments.

These data show that the technique is adaptable and, for future studies on dental substrates the system, can be made more representative of real-world conditions by adding factors such as a pellicle layer. Going forward SICM can be utilised to further enhance the effectiveness of *in-vitro* studies and help bridge the knowledge gap with *in-vivo* counterparts by simulating conditions within the body as accurately as possible.

### 3.6 Conclusions

The work presented here positions SICM, combined with FEM modelling, as a powerful tool to both induce dissolution and simultaneously quantify the dissolution rates of enamel at the nanoscale. This novel approach utilises distance modulated AC currents to track surface topography changes that occur during dissolution driven by the controlled SICM bias. Quantification of small changes in dissolution susceptibility imparted by mild treatments similar to real world conditions demonstrates this technique as a powerful tool. With improved resolution and carefully controlled delivery this could open up the possibility of exploring surface heterogeneities such as comparing the dissolution rates of the inter-rod regions of enamel with the bulk. Combined with correlative microscopy, this would allow the differences in the underlying mechanisms at different sites to be examined.

FEM simulation allows conversion of the experimental etch pit depth data into effective heterogeneous reaction rates, providing relevant quantitative kinetic information about a complex interface. This work focusses on dental protective coatings and their relative susceptibility to acid attack, however this technique is widely applicable and could provide a wealth of information about additives, protective coatings and oxide layers on surfaces required to be corrosion resistant.

The protective influence of a fluoride treatment against HCl induced dissolution upon tooth enamel was quantified and shown to be significant. Citric acid

exposure weakened the surface, leading to enhanced dissolution rates of the surface when exposed to a further HCl attack. Future work could utilise this platform and longer delivery times to address important questions as how deep such treatments penetrate the surface. The presence of a pellicle layer also was shown to protect the surface, as reported in literature, and its inclusion offers promise of improving the relevance of future *in vitro* dental studies, with SICM experiments amenable to a range of biologically relevant conditions.

SICM is an incredibly versatile technique for the study of different interfaces owing to the wide range of conditions in which it can be employed and the high degree of potential control it allows. As this work demonstrates, through careful experimental design and choice of parameters and conditions used, a whole range of questions surrounding interesting and important interfacial chemistries can be addressed at the nanoscale.



### 3.7 References

- 1 T. Imfeld, *Eur J Oral Sci*, 1996, **104**, 151–155.
- 2 Y. H. Al-Dlaigan, L. Shaw and a J. Smith, *Br. Dent. J.*, 2002, **192**, 526–530.
- 3 N. J. Kassebaum, E. Bernabé, M. Dahiya, B. Bhandari, C. J. L. Murray and W. Marcenes, *J. Dent. Res.*, 2015, **94**, 650–658.
- 4 J. E. Frencken, P. Sharma, L. Stenhouse, D. Green, D. Lavery and T. Dietrich, *J. Clin. Periodontol.*, 2017, **44**, S94–S105.
- 5 A. Lussi, T. Jaeggi and D. Zero, *Caries Res.*, 2004, **38**, 34–44.
- 6 A. S. Parker, R. Al Botros, S. L. Kinnear, M. E. Snowden, K. McKelvey, A. T. Ashcroft, M. Carvell, A. Joiner, M. Peruffo, C. Philpotts and P. R. Unwin, *J. Colloid Interface Sci.*, 2016, **476**, 94–102.
- 7 S. V Dorozhkin, *World J. Methodol.*, 2012, **2**, 1.
- 8 M. E. Barbour and J. S. Rees, *J. Dent.*, 2004, **32**, 591–602.
- 9 R. P. r. Shellis, J. D. B. Featherstone and A. Lussi, *Erosive Tooth Wear From Diagnosis to Ther.*, 2012, **20**, 163–179.
- 10 L. C. Yule, C. L. Bentley, G. West, B. A. Shollock and P. R. Unwin, *Electrochim. Acta*, 2019, **298**, 80–88.
- 11 E. S. M. Sherif, R. M. Erasmus and J. D. Comins, *J. Colloid Interface Sci.*, 2007, **309**, 470–477.
- 12 V. B. Møller, K. Dam-Johansen, S. M. Frankær and S. Kiil, *J. Coatings Technol. Res.*, 2017, **14**, 279–306.
- 13 J. C. Orr, V. J. Fabry, O. Aumont, L. Bopp, S. C. Doney, R. A. Feely, A. Gnanadesikan, N. Gruber, A. Ishida, F. Joos, R. M. Key, K. Lindsay, E. Maier-Reimer, R. Matear, P. Monfray, A. Mouchet, R. G. Najjar, G. K. Plattner, K. B. Rodgers, C. L. Sabine, J. L. Sarmiento, R. Schlitzer, R. D. Slater, I. J. Totterdell, M. F. Weirig, Y. Yamanaka and A. Yool, *Nature*, 2005, **437**, 681–686.
- 14 L. J. De Cock, S. De Koker, B. G. De Geest, J. Grooten, C. Vervaet, J. P. Remon, G. B. Sukhorukov and M. N. Antipina, *Angew. Chemie - Int. Ed.*, 2010, **49**, 6954–6973.
- 15 M. Adobes-Vidal, H. Pearce and P. R. Unwin, *Phys. Chem. Chem. Phys.*, 2017, **19**, 17827–17833.
- 16 P. K. Hansma, B. Drake, O. Marti, S. A. C. Gould and C. B. Prater, *Science (80-. )*, 1989, **243**, 641–643.

- 17 C.-C. Chen, Y. Zhou and L. A. Baker, *Annu. Rev. Anal. Chem.*, 2012, **5**, 207–228.
- 18 I. T. Selezov, Y. G. Kryvonos and I. S. Gandzha, *Found. Eng. Mech.*, 2018, **50**, 1–24.
- 19 P. Novak, C. Li, A. I. Shevchuk, R. Stepanyan, M. Caldwell, S. Hughes, T. G. Smart, J. Gorelik, V. P. Ostanin, M. J. Lab, G. W. J. Moss, G. I. Frolenkov, D. Klenerman and Y. E. Korchev, *Nat. Methods*, 2009, **6**, 279–281.
- 20 K. McKelvey, D. Perry, J. C. Byers, A. W. Colburn and P. R. Unwin, *Anal. Chem.*, 2014, **86**, 14.
- 21 M. Böcker, B. Anczykowski, J. Wegener and T. E. Schäffer, *Nanotechnology*, , DOI:10.1088/0957-4484/18/14/145505.
- 22 R. A. Lazenby and R. J. White, *Chemosensors*, , DOI:10.3390/chemosensors6020024.
- 23 D. Momotenko, K. McKelvey, M. Kang, G. N. Meloni and P. R. Unwin, *Anal. Chem.*, 2016, **88**, 2838–2846.
- 24 F. M. Maddar, D. Perry, R. Brooks, A. Page and P. R. Unwin, *Anal. Chem.*, 2019, **91**, 4632–4639.
- 25 D. Perry, R. Al Botros, D. Momotenko, S. L. Kinnear and P. R. Unwin, *ACS Nano*, 2015, **9**, 7266–7276.
- 26 A. Page, D. Perry, P. Young, D. A. Mitchell, B. G. Frenguelli and P. R. Unwin, *Anal. Chem.*, 2016, **88**, 10854–10859.
- 27 D. Perry, B. Paulose Nadappuram, D. Momotenko, P. D. Voyias, A. Page, G. Tripathi, B. G. Frenguelli and P. R. Unwin, *J. Am. Chem. Soc.*, 2016, **138**, 3152–3160.
- 28 K. McKelvey, S. L. Kinnear, D. Perry, D. Momotenko and P. R. Unwin, *J. Am. Chem. Soc.*, 2014, **136**, 13735–13744.
- 29 B. Chen, D. Perry, A. Page, M. Kang and P. R. Unwin, *Anal. Chem.*, 2019, **91**, 2516–2524.
- 30 C. L. Bentley, J. Edmondson, G. N. Meloni, D. Perry, V. Shkirskiy and P. R. Unwin, *Anal. Chem.*, 2019, **91**, 84–108.
- 31 A. G. Fincham, J. Moradian-Oldak and J. P. Simmer, *J. Struct. Biol.*, 1999, **126**, 270–299.
- 32 C. Robinson, S. Connell, J. Kirkham, R. Shore and A. Smith, *J. Mater. Chem.*,

- 2004, **14**, 2242–2248.
- 33 H. Eimar, E. Ghadimi, B. Marelli, H. Vali, S. N. Nazhat, W. M. Amin, J. Torres, O. Ciobanu, R. F. Albuquerque Junior and F. Tamimi, *Acta Biomater.*, 2012, **8**, 3400–3410.
  - 34 S. Habeliz, S. J. Marshall, G. W. M. Jr, M. Balooch, S. Habelitz, S. J. Marshall, G. W. M. Jr and M. Balooch, *Arch. Oral Biol.*, 2001, **46**, 173–183.
  - 35 L. F. Francisconi, H. M. Honório, D. Rios, A. C. Magalhães, M. A. A. M. Machado and M. A. R. Buzalaf, *Oper. Dent.*, 2008, **33**, 203–208.
  - 36 T. T. Thuy, H. Nakagaki, K. Kato, P. A. Hung, J. Inukai, S. Tsuboi, H. Nakagaki, M. N. Hirose, S. Igarashi and C. Robinson, *Arch. Oral Biol.*, 2008, **53**, 1017–1022.
  - 37 N. X. West and A. Joiner, *J. Dent.*, 2014, **42**, S2–S11.
  - 38 A. Lussi and T. Jaeggi, *Clin. Oral Investig.*, 2008, **12**, 5–13.
  - 39 J. A. Gray, *J. Dent. Res.*, 1962, **41**, 633–645.
  - 40 H. Warshawsky, *Anat. Rec.*, 1989, **224**, 242–262.
  - 41 H. G. Linge and G. H. Nancollas, *Calcif. Tissue Res.*, 1973, **12**, 193–208.
  - 42 M. S. wu, W. I. Higuchi, J. L. Fox and M. Friedman, *J. Dent. Res.*, 1976, **55**, 496–505.
  - 43 W. White and G. H. Nancollas, *J. Dent. Res.*, 1977, **56**, 524–530.
  - 44 N. X. West, A. Maxwell, J. A. Hughes, D. M. Parker, R. G. Newcombe and M. Addy, *J. Dent.*, 1998, **26**, 329–335.
  - 45 Z. J. Cheng, X. M. Wang, F. Z. Cui, J. Ge and J. X. Yan, *Biomed. Mater.*, , DOI:10.1088/1748-6041/4/1/015020.
  - 46 C. A. McGeouch, M. A. Edwards, M. M. Mbogoro, C. Parkinson and P. R. Unwin, *Anal. Chem.*, 2010, **82**, 9322–9328.
  - 47 D. Perry, A. Page, B. Chen, B. G. Frenguelli and P. R. Unwin, *Anal. Chem.*, 2017, **89**, 12458–12465.
  - 48 J. D. B. Featherstone, *Community Dent. Oral Epidemiol.*, 1999, **27**, 31–40.
  - 49 W. I. Higuchi, S. C. Valvani and J. J. Hefferren, *Arch. Oral Biol.*, 1974, **19**, 737–746.
  - 50 Y. F. Zhang, D. Y. Li, J. X. Yu and H. T. He, *J. Dent.*, 2016, **55**, 99–104.
  - 51 A. Wiegand, A. Rosemann, M. Hoch, S. Barke, M. Dakna and P. Kanzow, *Caries Res.*, , DOI:10.1159/000500046.

- 52 J. H. Meurman and R. M. Frank, *Caries Res.*, 1991, **25**, 1–6.
- 53 M. Hannig and C. Hannig, in *Monographs in Oral Science*, 2014, vol. 25, pp. 206–214.
- 54 M. B. Kautsky and J. D. B. Featherstone, *Caries Res.*, 1993, **27**, 373–377.
- 55 B. Me, P. Dm, A. Gc, J. Kd, M. E. Barbour, M. David, G. C. Allen and D. Klaus, *Eur. J. Oral Sci.*, 2003, **111**, 258–262.
- 56 M. Eisenburger, R. P. Shellis and M. Addy, *Caries Res.*, 2004, **38**, 67–74.
- 57 Y. Yoshida, B. Van Meerbeek, Y. Nakayama, M. Yoshioka, J. Snauwaert, Y. Abe, P. Lambrechts, G. Vanherle and M. Okazaki, *J. Dent. Res.*, 2001, **80**, 1565–1569.
- 58 Y. F. Zhang, J. Zheng, L. Zheng and Z. R. Zhou, *J. Mech. Behav. Biomed. Mater.*, 2015, **42**, 257–266.
- 59 M. Kang, D. Perry, C. L. Bentley, G. West, A. Page and P. R. Unwin, *ACS Nano*, 2017, **11**, 9525–9535.
- 60 D. Perry, D. Momotenko, R. A. Lazenby, M. Kang and P. R. Unwin, *Anal. Chem.*, 2016, **88**, 5523–5530.
- 61 J. R. Rumble, D. R. Lide and T. J. Bruno, *CRC handbook of chemistry and physics 98th edition*, CRC Press, Cleveland, 2017.
- 62 J. Rheinlaender and T. E. Schäffer, *Anal. Chem.*, 2017, **89**, 11875–11880.
- 63 R. Shellis, J. Featherstone and A. Lussi, in *Monogr Oral Sci*, 2012, vol. 25, pp. 163–179.
- 64 N. H. de Leeuw, *J. Phys. Chem. B*, 2004, **108**, 1809–1811.
- 65 D. A. Lazarchik and K. B. Frazier, *Gen. Dent.*, 2009, **57**, 151–156.
- 66 L. Shaw and a J. Smith, *Br. Dent. J.*, 1999, **186**, 115–8.
- 67 K. O. Aileen Chin and G. H. Nancollas, *Langmuir*, 1991, **7**, 2175–2179.
- 68 A. T. Hara and D. T. Zero, in *Monographs in Oral Science*, 2014, vol. 25, pp. 197–205.

## **4 Nanoscale analysis of live bacteria using Scanning Ion Conductance Microscopy: towards bioelectrical models of the bacterial cell envelope**

This chapter continues the application of various SICM functional mapping methodologies to complex substrates. Pulsed-potential SICM and scanned-potential SICM are used to interrogate gram-positive and gram-negative bacteria and FEM simulations are used to deconvolute the mechanisms underpinning their bioelectrical response. The wealth of information obtainable from this combined methodology allows verification of models of the bacterial cell envelope and investigation into the effects that functional SICM mapping techniques have upon the substrates. FEM simulations are used to show that the gram-negative response is likely to be dominated by surface charge. The gram-positive response is complex and requires further consideration to be explained.

This chapter is in preparation to be submitted for publication. Experiments in this chapter were performed by Kelsey Cremin with help and preliminary experiments performed by Bryn Jones. The author has also performed similar experiments which are not included in this work. Simulations were primarily performed by the author with assistance from Kelsey Cremin. The manuscript was prepared by the author in collaboration with Gabriel Meloni, Kelsey Cremin, and Bryn Jones.

#### 4.1 Abstract

Functional mapping with scanning ion conductance microscopy (SICM) has been used to investigate the nanoscale charge properties and ion flux behaviour of a wide range of surfaces including live mammalian and plant cells. There is an increasing interest in bacteria as single entities within a population or community and the bioelectrical properties of bacteria underpin their interactions with the environment and each other. SICM was used herein to investigate the bioelectrical properties of two bacterial strains, a gram-negative *Escherichia coli* and a gram-positive *Bacillus subtilis*. Finite element method (FEM) simulations were employed to understand the contribution of fixed charges in the bacterial cell envelope to the bioelectrical response. Through this method, we demonstrate the challenges surrounding understanding the complex charge of gram-positive structures. This alludes to as yet unreported descriptors of the bacterial cell wall pertinent to fully understanding the charge environment, where the demonstrated capabilities of SICM to make sub-cellular measurements are set to perform a key role.

#### 4.2 Introduction

SICM is unique in the ability to perform nanoscale functional mapping of live biological substrates *in situ* to simultaneously provide an abundance of information about the surface topography,<sup>1,2</sup> interfacial properties,<sup>3</sup> and dynamic processes.<sup>4-10</sup> In particular, developments in SICM scanning procedures and finite element method (FEM) simulation have allowed SICM to be employed as a quantitative tool for surface charge mapping,<sup>11,12</sup> reaction mapping,<sup>13</sup> and controlled delivery of analytes to samples.<sup>14-16</sup> Combined with the robust topographical feedback, this places SICM as one of the most powerful and versatile tools for probing living systems.

SICM utilizes a glass or quartz nanopipette filled with an electrolyte solution to probe a substrate which is immersed in an electrolyte bath. A bias is applied between a quasi-reference counter electrode (QRCE) inserted into the nanopipette and a second placed in the bulk solution, this drives an ionic current through the pipette which is highly sensitive to tip-substrate separation and local ionic conductivity, allowing synchronous acquisition of topography and functional surface maps.<sup>17-22</sup> As the composition of the electrolyte solutions do not need to be the same, SICM can be used to probe living systems *in situ*, even in low ionic strength media.<sup>23</sup>

SICM methodologies have been applied to a wide range of complex systems providing information on nanoscale heterogeneities which contribute to a wide array of biological and interfacial processes. Surface charge mapping in particular has been used for mammalian cells,<sup>19</sup> complex biomaterials,<sup>24</sup> and ultra-micro electrodes.<sup>14</sup> Critical information about the surface charge distribution and dynamic processes that potentially occur at the interface of the sample and solution can be acquired by employing different potential scanning protocols.<sup>5,17,25,26</sup> The properties which define the bioelectrical response of cells are the local distribution of charges at the cellular interface and the fluxes of ions between the cell and the local microenvironment for metabolism and signalling.

Heterogeneities in charge distribution are known to play a role in crystal nucleation and growth,<sup>27</sup> biofilm formation,<sup>28</sup> cellular uptake,<sup>29</sup> differentiation (*e.g.* persister cells and biofilm forming cells),<sup>30</sup> and the antimicrobial resistance of bacteria.<sup>31–34</sup> Often these charge density heterogeneities are subtle, difficult to quantify and difficult to visualise, with only a handful of techniques able to probe them.<sup>35–37</sup> SICM is one of few techniques able to make non-invasive measurements of cells within their individual microenvironments with sub-diffraction resolution.<sup>38</sup> To date, most applications of SICM have focussed on mammalian cells,<sup>19,39–41</sup> with little work on investigating microbial substrates.

Single entity measurements have become increasingly important within biology,<sup>42,43</sup> catalysis,<sup>44</sup> and materials science,<sup>45</sup> as individual responses provide considerably more information than bulk measurements of the same ensembles and populations. Measurements of cellular heterogeneity are increasingly important for the study of bacterial populations, particularly that of bacterial communities which modify their environment and communicate between members of the quorum.<sup>46</sup> It has been previously shown that individual cellular responses show high heterogeneity even between genetically similar cells kept under seemingly identical conditions, thus stressing the importance of the feedback between the individual cells and their microenvironments.<sup>47</sup> Understanding the cause of variation across a population, and therefore the ensemble behaviour, is dependent upon understanding the contributions of heterogeneities in cellular microenvironments, genetic/phenotypic variation, and metabolic state.<sup>48</sup> These factors shape efforts to utilise and influence bacterial populations, such as in developing antifouling surfaces,<sup>49</sup> fighting antibiotic

resistance,<sup>33</sup> and building microbial fuel cells.<sup>42</sup> As a result, a wide range of fields have developed of single cell methods including cell sorting,<sup>50,51</sup> cell-scale *-omics* methods,<sup>52,53</sup> along with an array of fluorescence microscopy based and spectroscopic techniques.<sup>43,54</sup>

The environmental interface of individual bacterial cells is defined by the structure of their bacterial cell envelopes, which influence cellular processes including cellular uptake,<sup>29</sup> growth,<sup>55</sup> and cell adherence to substrates.<sup>19,56</sup> Bacterial cell envelopes are broadly classified into two polyphyletic groups; gram-positive and gram-negative (Figure 4.1), each arising from structural differences which underpin interactions with the environment.<sup>57–59</sup> Previous zeta-potential and electrophoretic measurements have shown that both gram-positive and gram-negative bacteria present a net negative charge, however the magnitude of the charge varies between the two groups and between specific species.<sup>60–63</sup> It has also been indicated that the surface charge is influenced by physical conditions such as growth medium,<sup>64</sup> age,<sup>65</sup> and surface structural features relating to differences across strains.<sup>65–67</sup>

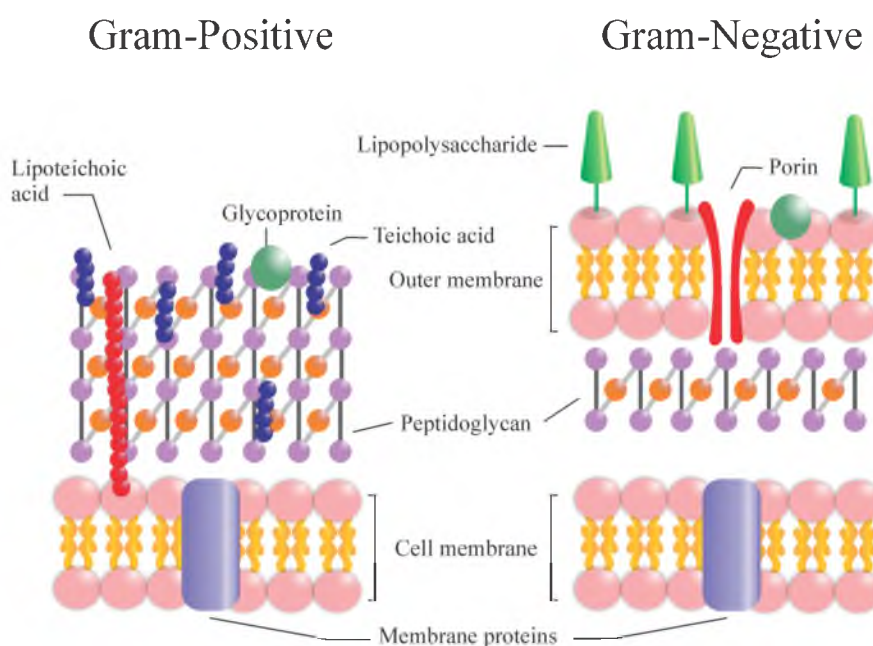


**Figure 4.1 Illustration of a simplified bacteria cell envelope.** The ultrastructure and principal components of gram-positive and gram-negative bacterial cell envelopes.



The charge properties of the bacterial cell envelope have been measured through a number of means, early work was done in the lab of Johannes Lyklema upon isolated cell walls to estimate the average charge density in the gram-positive and gram-negative cell walls.<sup>62,68,69</sup> Electrohydrodynamic considerations of the bacterial cell envelope have been developed which parameterise the charge and flow properties of the cell envelope through a softness parameter which can be determined through electrokinetic measurements of populations of cells in suspension.<sup>70,71</sup> These methods describe the average response of a population for measurements which are also averaged over the accessible volume of cell envelope, therefore it is difficult to infer detailed information from these measurements.<sup>72,73</sup> The charge properties of the bacterial cell envelope are mechanisms through which biofilms can form<sup>56</sup> and antimicrobial resistance can occur.<sup>34,67</sup> To fully understand these mechanisms and further research into combating these issues, it is necessary to understand the origin and distribution of the charge properties in the bacterial cell envelope. This is also important for the understanding of physiological processes such as cellular uptake and metabolism<sup>37</sup> and cell signalling.<sup>37</sup>

Herein, we apply SICM functional mapping methodologies to live bacterial cells to study two different bacterial species, gram-positive *Bacillus subtilis* and gram-negative *Escherchia coli*. Using two distinct potential scan protocols (pulsed-potential SICM and scanned-potential SICM) we investigate and report the nanoscale bioelectrical response at the cell interface. This allows us to further understand the local bioelectrical response of the cell envelope of live bacterial cells and the underlying contribution from the cell wall charge in each species. FEM simulations were used to build a more comprehensive picture of the properties and mechanisms influencing the interfacial electrical response of bacteria. This, in turn, will enable future analyses that can link diverse cellular behaviours to electrical responses within the cell-microenvironment interface.

## **4.3 Methods**

### **4.3.1 Chemicals**

All reagents were from analytical grade and used without further purification. Deionized water (Milli-Q, resistivity *ca.* 18.2 M $\Omega$  cm at 25 °C) was used in the preparation of all solutions. 50 mM potassium chloride, buffered at pH 7.0 with

tris(hydroxymethyl)aminomethane (both from Sigma-Aldrich) was used as supporting electrolyte for all the SICM experiments. Low melting point agarose (Cleaver Scientific, CSL-LMA100), poly-L-lysine (Sigma Aldrich) and Cell-Tak (Corning) were used as adherent substrates for the both bacterium species.

#### 4.3.2 Nanopipettes fabrication and characterization

Nanopipettes were pulled from borosilicate glass capillaries (o.d. 1.2 mm, i.d. 0.69 mm, Harvard Apparatus) using a laser puller (P-2000, Sutter Instruments: pulling parameters 200 nm pipettes: Line 1: Heat 330, Fil 3, Vel 30, Del 220, Pul -; Line 2: Heat 300, Fil 3, Vel 40, Del 180, Pul120. Pulled pipettes were characterized regarding their inner radius and overall probe geometry by SEM using a Zeiss Gemini 500 SEM (operating in scanning transmission electron microscopy (STEM) mode). A representative STEM image is presented in Figure 4.2.

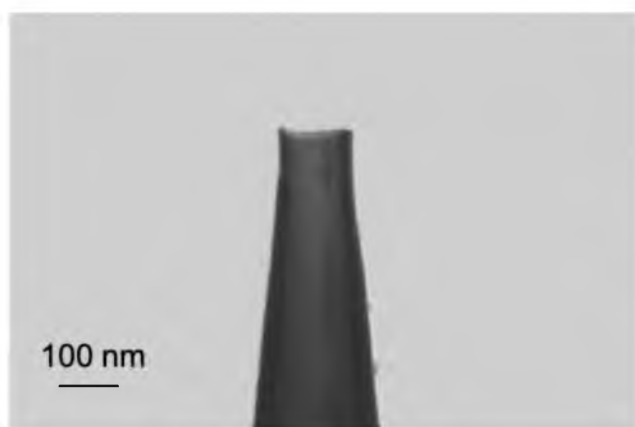


**Figure 4.2 STEM images of a typical nanopipette used herein.** Pore diameter approximately 180 nm.

#### 4.3.3 Instrumentation.

The basic instrumentation setup has been described in detail previously.<sup>11</sup> Briefly, the lateral movement of the probe was controlled using a two-axis piezoelectric positioning system with a range of 300  $\mu\text{m}$  (Nano- BioS300, Mad City Laboratories, Inc.), while movement normal to the substrate was controlled using a single axis piezoelectric positioning stage with a range of 38  $\mu\text{m}$  (P-753-3CD, Physik Intrumente). All electrochemical measurements were performed using in-house built instrumentation controlled *via* a custom-made LabVIEW interface (2016, National

Instruments) through an FPGA card (7852R, National Instruments). The instrumental setup is vibration and thermal insulated, and all measurements are performed inside a faraday cage to mitigate interference. An integrated Zeiss Axiovert inverted microscope was used for coarse positioning of the nanopipettes over the bacterial substrate and collection of optical images.

#### **4.3.4 Bacterial Strains**

Wildtype *E. coli* K12 was used in this study, originally obtained DSMZ. Due to issues during SICM scans caused by the mobility of the *B. subtilis*, a *B. subtilis* NCIB 3610 mutant strain with deleted *hag* genes was used instead. The strain (denoted as DS1677) was obtained from Munehiro Asally, University of Warwick, and is referenced in Mukherjee *et al.* (2013).<sup>74</sup> The  $\Delta hag$  mutation prevents production of flagellin which is a key subunit for the polymerisation that forms bacterial flagella. Therefore, species depleted in flagellin have limited flagella, resulting in reduced motility. For the application of SICM, the limited motility enabled the adhesives to hold the bacteria stationary across the SICM scan.

A mutant strain of *B. subtilis* NCIB 3610 without the *eps* operon was also investigated. The *eps* operon is responsible for the biosynthesis of an exopolysaccharide that binds chains of cells together in bundles and forms a major constituent of the extracellular polymeric substances (EPS) secreted by the cell. Strains depleted in these genes therefore do not produce this exopolysaccharide. Further details of this strain formation can be found in Kearns *et al.* (2005).<sup>75</sup> Wildtype *B. subtilis* NCIB 3610 strains were also studied for use in SICM, where there was no notable disparity in local charge values compared to the mutant *hag* resistant strain. However, the higher motility of this strain compromises the imaging quality in comparison to the *hag*-deplete strains used herein.

#### **4.3.5 Bacterial cultures**

*B. subtilis* NCIB 3610 -  $\Delta hag$ , *B. subtilis* NCIB 3610 -  $\Delta eps$ , and *E. coli* K12 (wild type, obtained from DSMZ) were cultured in a modified M9 media containing 0.4% w/v glucose and full media composition in 4.3.6). Bacteria were taken from freezer stocks (50% glycerol, -80 °C) and grown in 40 mL volumes of media, occupying 100

mL sterile Erlenmeyer flasks. The cultures were grown overnight prior to SICM measurements on a shaking incubator at 37 °C and 150 rpm.

#### 4.3.6 Bacterial Culturing in M9m

Modified M9 media (M9m) used for bacterial culturing was based on established minimal media and adapted for growing a range of bacteria of interest, including the *E. coli* and *B. subtilis* used in this work.<sup>76</sup> The media is also adapted to render it suitable for use as an electrolyte for scanning the bacteria. Listed in Table 4.1 are the final components included in 1L of the full M9 media with glucose as a carbon source. Tables 4.1-4.4 provide the composition of each individual component, used as purchased from Fisher Scientific. All media were adjusted to pH 7, autoclaved, and used within a week of formation.

**Table 4.1 Full M9m media components.**

	Details explained in	Components added to 1L
5x M9 minimal salts	Table 4.2	200 mL
1 M MgSO <sub>4</sub> •7H <sub>2</sub> O	-	2 mL
Carbon source (0.4% w/v)	-	20 mL
1 M CaCl <sub>2</sub>	-	100 µL
10 mM FeCl <sub>3</sub> •6H <sub>2</sub> O	-	1 mL
1000x Trace metal solution	Table 4.3	1 mL
5-vitamin solution	Table 4.4	1 mL

**Table 4.2 Quantities and concentrations for M9m minimal salts.**

	Components added for stock solution 1L	Concentration in 1L stock (mM)	Concentration in 1L final full M9 media (mM)
Na <sub>2</sub> HPO <sub>4</sub> •7H <sub>2</sub> O	64 g	238 mM	47.6 mM
KH <sub>2</sub> PO <sub>4</sub>	15 g	110 mM	22 mM
NaCl	2.5 g	43 mM	8.6 mM
NH <sub>4</sub> Cl	5 g	93 mM	18.6 mM

**Table 4.3 Quantities and concentrations for 1000x Trace metal solution.**

	<b>Components added to 1L stock solution</b>	<b>Concentration in 1L stock (mM)</b>	<b>Concentration in 1L final full M9 media (μM)</b>
CuCl <sub>2</sub> •2H <sub>2</sub> O	5.455 mg	0.032 mM	0.032 μM
ZnSO <sub>4</sub> •7H <sub>2</sub> O	219.968 mg	0.765 mM	0.765 μM
CoCl <sub>2</sub>	21.436 mg	0.169 mM	0.169 μM
Na <sub>2</sub> MoO <sub>4</sub> •2H <sub>2</sub> O	399.218 mg	1.650 mM	1.650 μM
H <sub>3</sub> BO <sub>3</sub>	2862.729 mg	46.300 mM	46.300 μM
NiCl <sub>2</sub> •6H <sub>2</sub> O	998.382 mg	4.200 mM	4.200 μM
Na <sub>2</sub> WO <sub>4</sub> •4H <sub>2</sub> O	80.154 mg	0.243 mM	0.243 μM
Na <sub>2</sub> SeO <sub>3</sub> •5H <sub>2</sub> O	59.966 mg	0.228 mM	0.228 μM

**Table 4.4 Quantities and concentrations for 5-vitamin solution.**

	<b>Components added to 100 mL stock solution</b>	<b>Concentration in 100mL stock (mM)</b>	<b>Concentration in 1L final full M9 media (μM)</b>
Biotin	2 mg	0.082 mM	0.082 μM
Pyridoxine hydrochloride	10 mg	0.486 mM	0.486 μM
Thiamin hydrochloride	5 mg	0.148 mM	0.148 μM
Riboflavin	5 mg	0.133 mM	0.133 μM
Nicotonic acid	5 mg	0.406 mM	0.406 μM

#### 4.3.7 Bacterial Substrates

For SICM scanning, adhesive layers of poly-L-lysine (PLL), Cell-Tak, or thin (< 0.5 mm) agarose gels were deposited on the glass surface of a 50 mm glass bottomed dish (WillCo Wells, USA, HBST-5040). All adhesion methods were able to anchor and restrict inherent bacterial movement, whilst not inhibiting culture survival, and further details of the adhesion procedures and viability tests can be found in Section 4.3.11.

For all adhesion methods and bacterium species, a 100  $\mu$ L aliquot of an overnight culture (optical density at 600 nm  $\sim$ 0.45) was drop cast to the substrate. The sample is then left for 30 minutes at room temperature to adhere.

During the optimisation stages of the experimental methodology, several adhesives were investigated for their ability to retain bacteria to the cover glass bottomed sample dishes across the SICM experiment. Those used in the scans included herein are described below.

**Agarose:** As the agarose layer is transparent and thin, visualisation of the bacteria using the inverted microscope was possible, facilitating positioning of the tip over areas of interest. Based on the agarose pads method by Young *et al.* (2011),<sup>77</sup> agarose solutions were made using 0.8% (w/v) Cleaver Scientific low melt agarose (CSL-LMA100) in artificial seawater media (ASWm) basal salts and 50 mM sodium acetate (as described in Zerfaß *et al.* (2018)).<sup>78</sup> The solution was autoclaved for 30 minutes to melt the agarose whilst maintaining sterility. At 80 °C the agarose solution flask was transferred to a water bath at 50 °C to keep the agarose liquefied.

For sterility, the agarose layers were prepared inside a laminar flow hood. 450  $\mu$ L of agarose solution was pipetted in an outwards expanding spiral from the centre of a 50 mm cover glass bottomed dishes (WillCo Wells, USA, HBST-5040, glass thickness approximately 170  $\mu$ m), the dish was rotated to evenly spread the agarose then placed in the laminar flow hood until set, creating a uniform layer. From the volume of agarose added to the dish, the agarose layer thickness is calculated to be approximately 0.25 mm. Solidified agarose plates were sealed and refrigerated until use for up to one week.

Prior to scanning, 100  $\mu$ L of an overnight culture (optical density at 600 nm  $\sim$ 0.3) is pipetted dropwise across the agarose layer and rotated to evenly spread. The sample is then left for 30 minutes at room temperature. Following this, the dish is placed into an incubator at 37 °C for 30 minutes to dehydrate the agarose and evaporate any residual liquid.

Whilst it is possible to adapt this method to incorporate other media instead of the ASWm, due to the transparency and minimal crystallisation and clouding, the ASWm pads had the best optical properties to permit experimental set-up.

**Poly-L- lysine:** PLL has minimal effect on bacterial viability if the substance is adhered to a substrate, and not free in solution where it is known for its antimicrobial properties. In order to adhere bacteria using PLL, 50 mm cover glass bottomed dishes (glass thickness approximately 170  $\mu\text{m}$ ) were coated in 500  $\mu\text{L}$  of 0.01% poly-L-lysine (Sigma Aldrich, sterile-filtered) for 15 seconds. The PLL solution was then extracted via pipette and the dish washed with 5 applications of 1 mL DI water, this leaves behind a nm thin surface layer of PLL. An overnight bacteria culture (50  $\mu\text{L}$ , OD<sub>600</sub> approximately 0.8) was added to the dish, which was rotated to evenly coat the surface. The sample was then allowed to incubate for 30 minutes at room temperature. The dish was then washed with 3 applications of 1 mL DI water to remove un-adhered bacteria.

**Corning® Cell-Tak™:** Cell-Tak was used in accordance with the adsorption method provided in the instructions for use provided by Corning (Catalog 354240, 354241). Cell-Tak was purchased at 2.36 mg/mL concentration, in acetic acid, where 200  $\mu\text{L}$  of formalised Cell-Tak adhesive was prepared per each 50 mm glass bottomed dish used.

For coating each sample dish 7  $\mu\text{L}$  of Cell-Tak was added to 193  $\mu\text{L}$  of sterile 100 mM sodium bicarbonate solution; adjusted to pH 8 with 5% acetic acid, and vortexed for 10 seconds. The solution was then immediately added to the centre of the dish and spread to cover approximately two thirds of the dish base. The dish was then placed in a 30 °C incubator for 20 minutes. Following this the dish was washed with MilliQ water to remove of residual sodium bicarbonate, and 50  $\mu\text{L}$  of an overnight bacterial culture (OD<sub>600</sub> approximately 0.8) was added to the middle of the dish and swirled to cover the Cell-Tak layer. The sample was then left for 30 minutes allowing adherence prior to SICM. Adhesion appeared to reduce over time, however was sufficient for up to 8 hours.

#### **4.3.8 Electron microscopy of bacteria**

Bacterial cultures were grown overnight from freezer stocks in M9m media, added to carbon-laced copper TEM grids, and then imaged using a Zeiss Supra 55VP. For Cryo-TEM, samples were grown overnight from freezer stocks in M9m media, 4  $\mu\text{L}$  were then sampled onto lacey carbon films on copper TEM grids, and immediately frozen in liquid ethane using a Leica EM GP cryo plunge freezer. Imaging was performed using a Jeol 2100 TEM with a field electron gun operating at 200 kV.

#### 4.3.9 Fluorescence microscopy

EPS was stained with Alexa Fluor 594 (Concanavalin A, Thermo Fisher Scientific, Catalog number: C11253). As Alexa Fluor 594 stains the EPS and the bacteria, a second stain of SYBR Green ( $\times 10,000$  in DMSO, Thermo Fisher Scientific, Catalog number: S7585) was also used which would only stain the bacteria, therefore allowing distinction between the bacteria and the EPS.

Cultures of *B. subtilis* ( $\Delta hag$ ) were grown in M9m overnight as described in Methods. To 1 mL of bacterial culture, 100  $\mu$ L of absolute methanol was added and allowed 15 minutes to permeabilise and fix the sample. To this sample, 1  $\mu$ L of a  $\times 1,000$  in DMSO solution of SYBR Green was added for 5 minutes. The sample was then centrifuged (5 minutes,  $5000\times g$ ) and the supernatant was replaced with fresh M9m media, this was repeated a total of three times. The sample was then stained with Alexa Fluor 594, giving a total concentration of 100  $\mu$ g/mL. The sample was vortex briefly and then added to a WillCo well plates treated with PLL, such as described in SI-3. The plates were allowed to incubate for 2 hours at 30 °C. For a control sample, media without bacteria was treated and stained with both dyes and applied to a PLL-coated plate in the same way as described for bacterial samples. The fluorescence response was then recorded and this was used to determine any background fluorescence which could not be attributed to the bacterial activity.

An Andor/Nikon Spinning Disk Confocal Laser Microscope confocal spinning disk microscope was used for imaging, courtesy of the Warwick Integrative Synthetic Biology (WISB) platform. This system used a EMCCD 1k x 1k pixel camera. Temperature was controlled to 30 °C using an OKOlabs Caged incubator. Alexa Fluor 594 was observed using a 561 nm laser excitation (50 mW laser, 20% power), with emission through a Alex568-TRITC filter. The SYBR Green was observed using 488 nm laser excitation (50 mW laser, 10% power), and observed emission with a GFP/FITC filter.



#### 4.3.10 SICM Scanning Regime.

The full details of SICM charge mapping have been described in detail elsewhere.<sup>11,12,19,20</sup> Briefly, the nanopipette is approached towards the surface with a small applied bias between the internal and bulk QRCEs (Figure 4.3A), typically 50 mV, where the ionic current response is insensitive to surface charge (Figure 2B a). When a set current threshold (usually 2% change in current magnitude) is reached, the tip bias is either pulsed to -500 mV or scanned from -500 mV to 500 mV, depending if a pulsed-potential or scanned-potential programs is employed (Figure 4.3B b). The corresponding ionic current response is measured for the duration of the potential pulse or scan and the nanopipette is then retracted 2  $\mu\text{m}$  into the bulk solution, held at 50 mV, and the same potential pulse or scan program is repeated at the bulk (Figure 4.3B c to d). This allows for each surface current measurement to be normalized against a bulk measurement.

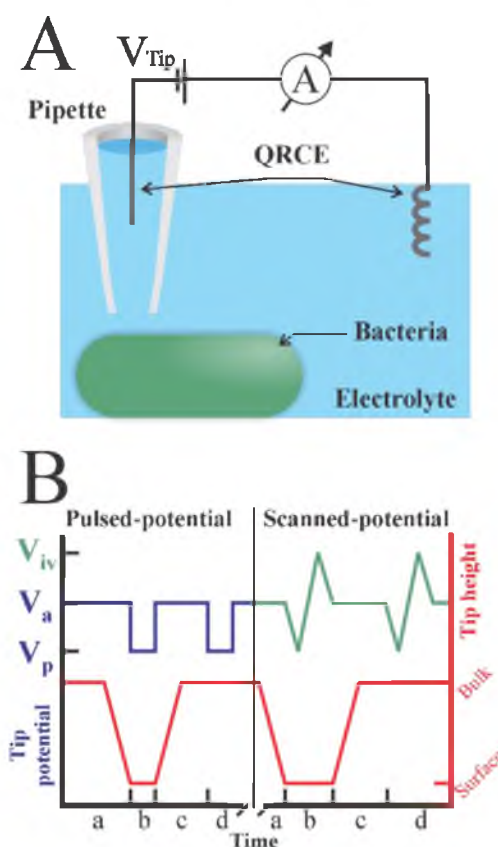


**Figure 4.3 Details of the SICM scanning regimes.** (A) SICM schematic depicting a nanopipette probe submerged in electrolyte and connected by two QRCE's. (B) An infographic to show probe vertical motion alongside changing on potential for both pulsed and scanned potential programs.

The probe is then laterally translated by a set distance and re-approached, starting the process over again. This procedure is repeated at every pixel of the electrochemical map. As the *z* height at each approach is also recorded, a topographical map is synchronously acquired. The nanopipette current response during the potential programs (pulse or potential sweep) gives a direct measurement of the local ionic conductivity in proximity to the nanopipette, be that at the surface or in bulk.<sup>12</sup> At the surface previous work has shown through a combination of experiments and FEM simulations, that the nanopipette is sensitive to the composition of the double layer without directly probing it.<sup>11</sup>

#### **4.3.11 Growth and viability of bacterial strains**

After the SICM experiment, bacteria were streaked from the experimental substrate onto LB-agarose plates and aliquots from the bath were also plated onto LB-agarose, with blank media and seed cultures as controls.

Growth studies were performed to ensure that the cells were in a healthy growth stage during the SICM experiment. Growth was measured in a 96 well plate (Falcon 96 Well Cell Culture plate, sterile (Corning, UK, #353072)) where the absorbance at 600 nm over time was used to examine the growth of culture, where increased absorbance is indicative of bacterial growth, as is standard procedure for growth studies. The optical density at 600 nm (OD<sub>600</sub>) was measured using a BMG Clariostar plate (BMG Labtech), set at 37 °C with a double orbital shaking at 150 rpm, measurements of growth were recorded once every 10 minutes for 2000 minutes.

200 µL of M9m was added to each well, to which 2 µL from a dense bacterial culture was added at the start of measurement. Along with replicates of each bacterial strains (*B.subtilis* ΔhAg, *B.subtilis* Δeps, *E.coli* WT), a control series of M9m was included for background subtraction.

The growth curves for the three bacterial strains are shown below (Figure 4.4), included is the M9m control to demonstrate the stability across the course of the experiment. Cultures are grown overnight from freezer stocks, therefore using the growth curve at approximately 15 hours (900 minutes), the *E.coli* would be in an early stationary phase, and the *B.subtilis* strains would both have passed the exponential growth phase and entered a lagging stationary phase.

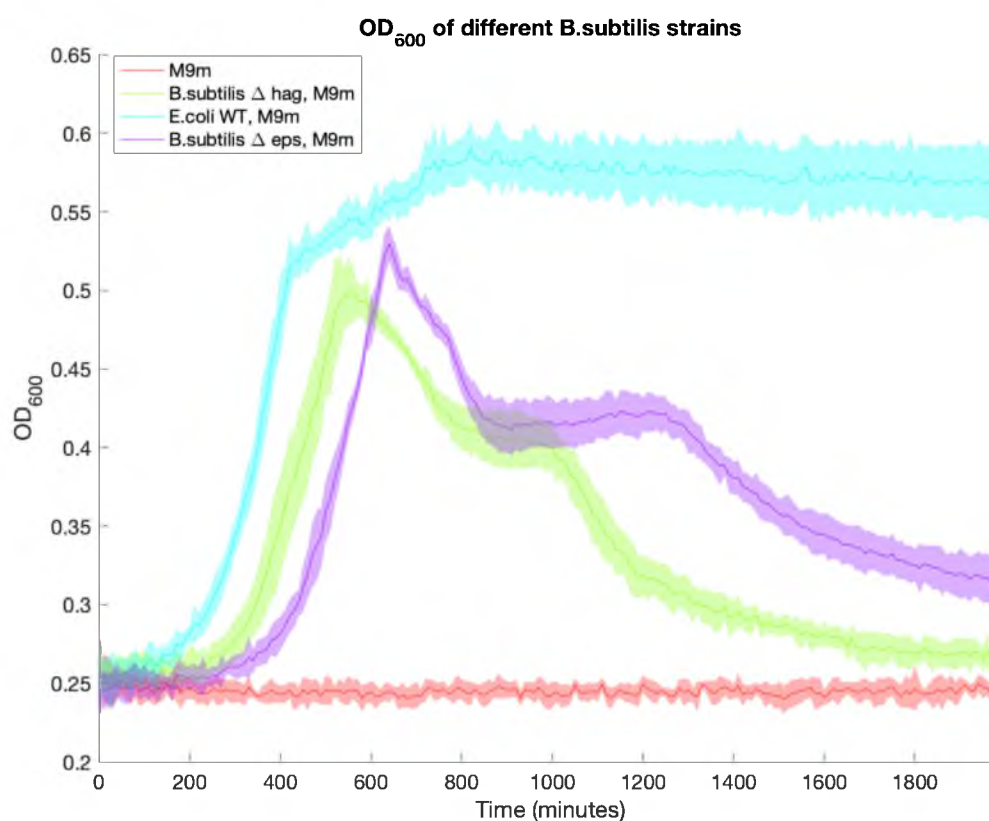


**Figure 4.4 Mean optical density growth curves.** Mean optical density at 600 nm ( $OD_{600}$ ) of different bacterial strains as grown in M9m media, and measured by plate reader. Standard deviation of 8 samples is shown by shading, measured across 2000 minutes, one measurement every 10 minutes.

In order to determine if there are viable cells left in the sample dishes of bacteria samples following a day of SICM experiments, surface swabs and liquid aliquots from SICM samples were spread on Lysogeny broth (LB) agar plates and left for 36 hours at 37°C. This was initially performed to allow colony counting of viable cells between different strains and electrolytes (*i.e.* 50 mM KCl or M9m). However, all the samples grew to a density where colony counting was not possible and whilst this showed growth of bacteria in KCl samples, it was not a quantitative assessment of the differences in viability between the SICM samples with KCl and M9m media in the place of electrolyte. These samples were compared to equivalently treated samples of cell free media to serve as a control, in these samples there was no observed bacterial growth as expected, demonstrating the bacterial growth was not caused by a lab or experiment contamination.

Whilst the LB plates show that there are viable cells following the SICM experiment using KCl and M9m as an electrolyte, it does not indicate the percentage of cell death or survival. To try to obtain quantitative observations of the growth of bacteria exposed to KCl, a plate reader experiment was set up in which bacteria samples were exposed to 50 mM KCl for 8 hours (the total standard length of SICM experiments), where recovery growth for bacteria placed back in M9m was recorded over time and compared to cultures not incubated in KCl.

Cultures of *B.subtilis*  $\Delta$ hag, *B.subtilis*  $\Delta$ eps, and *E.coli* WT were grown overnight in M9m at 37°C. 1 mL samples of each culture were centrifuged for 5 minutes at 5000 rpm to sediment the cells, where the supernatant was then removed and replaced with 1 mL of a 50 mM KCl solution buffered to pH 7 with tris(hydroxymethyl)aminomethane. The cells were resuspended and left in the microbial flow hood at room temperature for 8 hours, a similar maximum length of time to a day of SICM experiments. A control condition was included where sedimented cells were instead suspended in fresh M9m, in attempts to determine if the centrifugation process affected the cell viability following incubation.

After incubating for 8 hours, the cultures were again centrifuged for 5 minutes at 5000 rpm and resuspended in 10 mL of fresh M9m. The 10-fold dilution of cells in media was used to ensure that a representative proportion of the incubated cells enter to growth plates, therefore more clearly highlighting difference between KCl-incubated and M9m-incubated cells.

8 replicates of 200  $\mu$ L samples from each condition were added to a transparent 96 well plate (Falcon 96 Well Cell Culture plate, sterile (Corning, UK, #353072)), along with a condition of M9m for background subtraction. The optical density at 600 nm ( $OD_{600}$ ) was measured using a BMG Clariostar plate, set at 37°C with a double orbital shaking at 150 rpm, measurements of growth were recorded once every 10 minutes for 2000 minutes. The results of the growth study are shown in Figure 4.5.

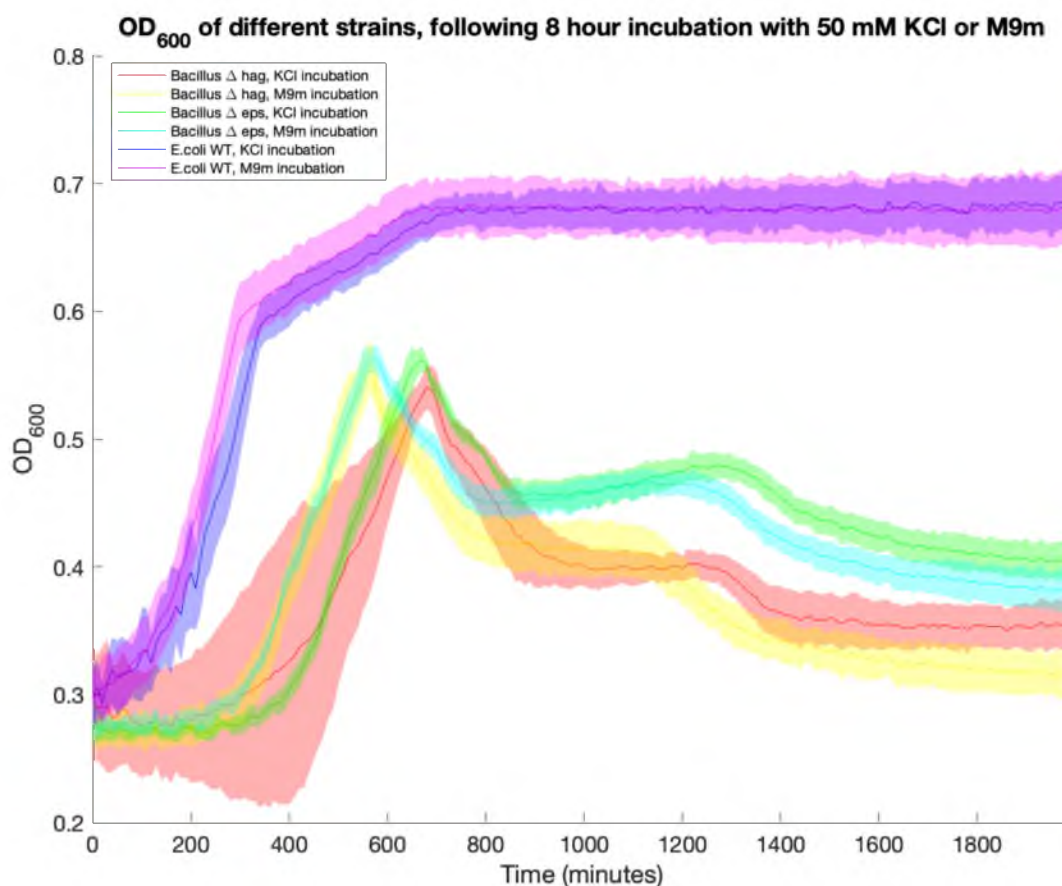


**Figure 4.5 Growth of bacterial strains in the presence of KCl.** Mean optical density at 600 nm (OD<sub>600</sub>) of different bacterial strains as grown in M9m media, following incubation of either KCl or M9m. Standard deviation is shown by the shading, measured across 2000 minutes, one measurement every 10 minutes (mean of 8 repeats with standard deviation at each time point).

The *B.subtilis* strains incubated in KCl show a delayed exponential growth curve until they reach maximum absorbance. This would imply that either the initial viable cell concentration is lower in the KCl condition at the initiation of the plate reader recording, which could indicate cell death in KCl, or a delay in recovery into exponential growth following KCl incubation. It is noted that the cells in 50 mM KCl are expected not to grow as the solution lacks a carbon source or other nutrients, therefore the incubation in M9m could have increased cell growth going into the plate reader, even at room temperature. If the M9m-incubated condition has a higher initial viable cell concentration then it would be expected that the peak of the exponential growth stage would be reached sooner. There is also a slight delay in the exponential

growth in *E.coli*, however as the bacterial species is faster growing the delay is less prominent.

Overall these results do show a difference in growth between the KCl- and M9m- incubated condition across all strains, however exponential growth still peaks within a similar time frame following inoculation. This implies that similar numbers of cells are still viable following KCl incubation compared to M9, suggesting that the bacteria are generally still viable during an SICM scan. Whilst it is not possible to ensure that individually scanned bacteria are alive, the culture as a whole is viable and recovers following the SICM experiment.

#### **4.4 FEM Simulations and Model Parameterisation**

FEM simulations were constructed in COMSOL Multiphysics (v5.4) as 2D axisymmetric domains, constructed using dimensions from STEM images of the nanopipettes with the physics described using the Transport of Diluted Species, Laminar Flow and Electrostatics modules. Briefly, *E. coli* were simulated as a non-porous insulating charged surface to describe the interface with the outer membrane. *B. subtilis* were simulated with a charge density applied to a volume which describes the permeable and charged cell wall. The SICM scanning procedure was simulated in full, with the approach simulated by steady-state simulation of different tip-substrate separations with the approach bias applied (50 mV), followed by time-dependent simulations of the potential pulse or potential scanning regime at the calculated approach height and bulk retract height.

##### **4.4.1 General Details and *E. coli* Model**

A schematic of the FEM simulation domain is shown in Figure 4.6. The electrostatics, transport of diluted species and laminar flow modules were used to model the experimental system. All boundaries not specifically labelled (grey) were set as no flux boundaries with no surface charges applied, and a no-slip flow condition was applied these boundaries and the pipette walls (blue). The pipette walls (blue) had a surface charge density of  $-30 \text{ mC/m}^2$  applied in all simulations, reasonable for borosilicate glass in aqueous solution under the conditions of our experiments.<sup>79</sup> All potentials stated herein were applied to the upper boundary within the nanopipette (B1), positioned 1 mm above the base of the nanopipette, whilst B2 was held at ground. The concentrations at B1 and B2 were set to  $[\text{K}^+] = 50 \text{ mM}$ ,  $[\text{Cl}^-] = 50 \text{ mM}$ ,

representing bulk solution in the nanopipette and bath. B2 was positioned 1 mm away from the nanopipette opening laterally, sufficient to be considered bulk. The substrate was defined differently depending upon whether it is modelling of the gram-negative (Figure 4.6A) or gram-positive (Figure 4.6B) cell envelope.

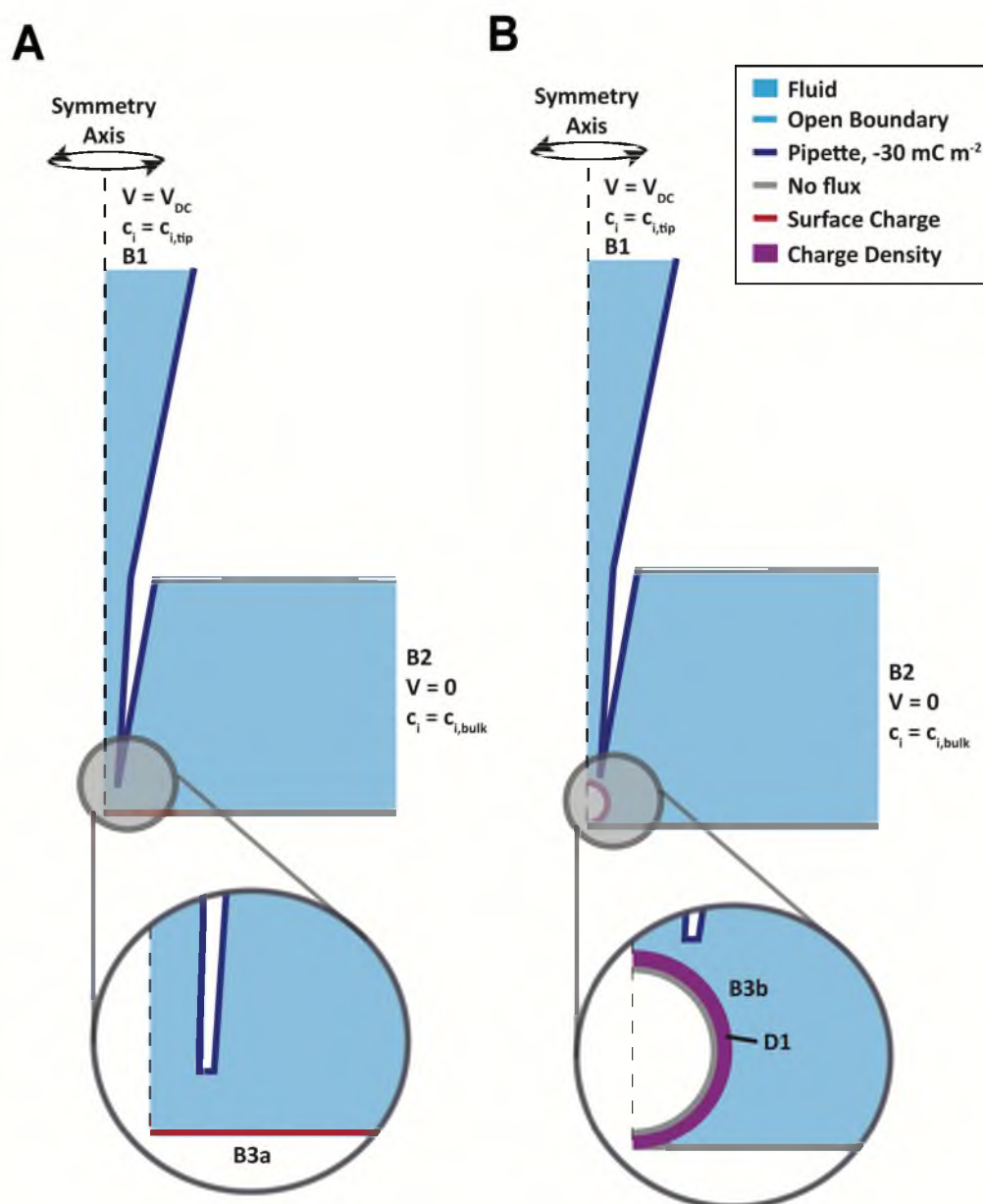


**Figure 4.6 Schematic (not to scale) of FEM simulation domain.**

Figure 4.6A depicts the simulations used to describe the *E. coli* case, where the substrate is treated as an impermeable charged insulator, therefore B3a (red) is set to a no-flux condition with varied surface charge. The system describing the gram-

negative simulations was defined the following differential equations. The flux  $J_i$  of each species  $i$ , was described by the Nernst-Planck equation:

$$J_i = -D_i \nabla c_i - z_i \frac{F}{RT} D_i c_i \nabla \phi + c_i u \quad (4.1)$$

and the Poisson equation defined the electric potential  $\phi$ :

$$\nabla^2 \phi = -\frac{F}{\varepsilon \varepsilon_0} \sum_i z_i c_i \quad (4.2)$$

where  $D_i$ ,  $z_i$  and  $c_i$  are the diffusion coefficients, charge number and concentrations of species  $i$  and  $u$  is the solution velocity described below (Equation 4.3).  $F$ ,  $R$  and  $T$  are the Faraday constant, gas constant and absolute temperature (298 K),  $\varepsilon$  is the dielectric constant of the solution (78) and  $\varepsilon_0$  ( $8.85 \times 10^{-12}$  F/m) is the vacuum permittivity. The diffusion coefficients at infinite dilution for  $K^+$  ( $1.96 \times 10^{-5}$  cm<sup>2</sup>/s) and  $Cl^-$  ( $2.05 \times 10^{-5}$  cm<sup>2</sup>/s) were taken from the CRC handbook. These values are reasonable because of the sufficiently dilute concentrations used and the self-referencing nature of experiments.<sup>80</sup> The solution velocity was described by the incompressible Navier-Stokes equation with electroosmotic flow (EOF) incorporated (Equation 4.3):

$$u \nabla u = \frac{1}{\rho} (-\nabla p + \mu \nabla^2 u - F (\sum_i z_i c_i) \nabla \phi) \quad (4.3)$$

#### 4.4.2 B. Subtilis Model

The simulations for the gram-positive cell envelope of *B. Subtilis* were defined in a similar way with some exceptions (Figure 4.6B). Instead of an insulating charged surface, the substrate is defined as a permeable domain (D1 - purple) with a concentration of fixed stationary negative charge ( $\rho_f$ ). The thickness of the cell wall was estimated from cryo-TEM images (Section 4.12.8) and literature values.<sup>81</sup>

Therefore a thickness of 34 nm was used but a range of values from 30-70 nm were explored to examine the effects of the thickness of the cell wall. This domain is bounded by an uncharged boundary below (grey) and a permeable interface above (B3b) at which the chloride permeability was varied in order to assess the effect of anion exclusion from the cell wall. The inclusion of a domain representing a periplasmic space with the same physics as bulk was also examined, this was introduced beneath the cell wall domain (replacing the no-flux boundary) and had variable electrolyte concentration within. Two geometric configurations were used for initial parameter testing; a flat cell wall domain and a sphere with diameter 1  $\mu$ m as



shown in Figure 4.6B. The response of each were found to be similar, the glass-wall approach distance and normalised currents were similar in each. However the sphere model gave slightly higher responses which were closer to experimentally determined currents and was considered to be more representative of the experimental conditions.

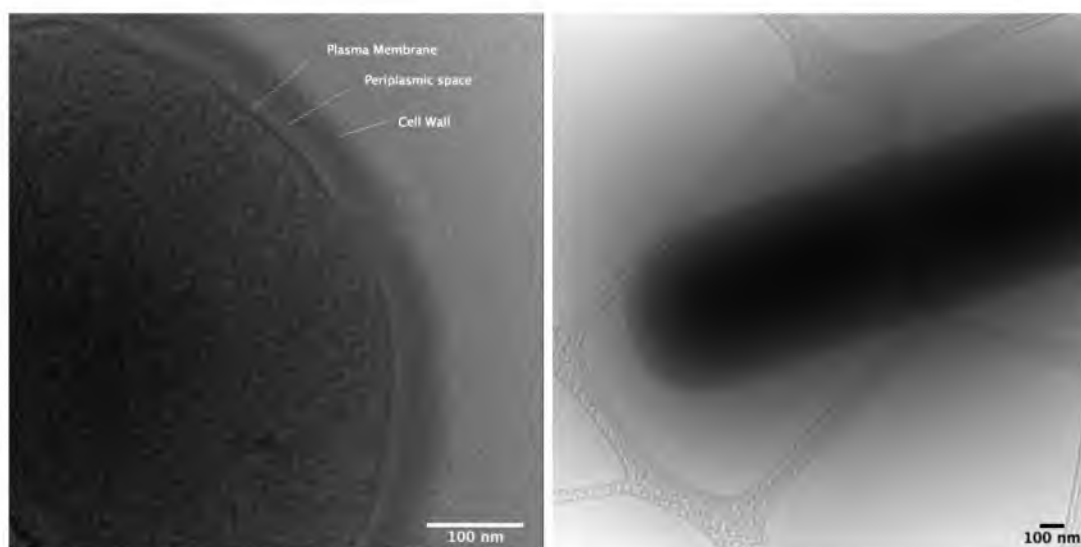


**Figure 4.7 Cryo-TEM of *B. subtilis*.**

**Table 4.5 Parameters measured from Cryo-TEM images.** Measurements of 12 cells, taken at 3 different points for each cell, these were used to parameterise FEM simulations.

Cell Structure	Range (nm)	Mean (nm)	STD (nm)
Whole Cell Wall	51-61	54.8	3.2
Cell Wall	31-40	34.0	3.2
Periplasmic space	12-16	14.6	1.4
Periplasmic membrane	7-10	8.3	1.2

The Poisson equation (Equation 4.2) is still used to describe the potential, however the total charge incorporates the stationary fixed charge within the volume of the cell wall ( $\rho_f$ ).

$$\nabla^2 \phi = -\frac{1}{\epsilon \epsilon_0} (\rho_f + F(\sum_i z_i c_i)) \quad (4.4)$$

This model of the gram-positive cell wall as a soft polyelectrolyte layer is well established in literature and has previously been used to calculate the Donnan potential within the cell wall for various species. is similar to previous considerations of interfaces in electrophoretic measurements.<sup>72,82</sup> The charge density of the *B. subtilis* cell wall has been calculated previously using electrokinetic theory, providing charge concentration values ( $\rho_f/F$ ) of approximately 15-25 mM.<sup>83</sup> However this is highly dependent upon strain, electrolyte composition, substrate, and pH so a wider range of charges were examined.<sup>63</sup> Varying the relative dielectric permittivity  $\epsilon$  of the cell wall from 78 to 20 (taken from literature electrostatic force microscopy measurements)<sup>84</sup> was found to have no effect upon approach or normalised currents.

The transport in all domains was described by the Nernst-Planck equation, however within the cell wall domain (D1) the effective diffusion coefficients were varied to be assess the effect of the tortuosity of the cell wall. The mobility of ions within the cell wall was again defined by the Nernst-Planck equation however mobility of each ion was considered within the cell wall by using an effective diffusion coefficient ( $D_{eff}$ ). Alteration of the diffusion coefficient in polyelectrolyte layers is due to the tortuosity of the channels which form the free space of the layer or interaction with the cell walls.  $D_{eff}$  was calculated as a product of the diffusion coefficient in ideal solutions (D) and a factor representing mobility within the wall ( $\mu_{wall}$ ). This factor can be estimated by the Renkin equation<sup>85</sup> based upon the pore size of the *B. subtilis* cell wall (2.12 nm)<sup>86</sup> and the hydrodynamic radius of ions.<sup>87</sup> This gives probable values for  $\mu_{wall}$  in the range of 0.5 to 0.75, however a wider range was explored.

The permeability of anions in the cell wall was found to be an important factor in simulations and the approach threshold of 2% was unobtainable with a fully permeable model of the cell wall for reasonable values of  $\rho_f$  and  $\mu_{wall}$ , including full contact between the cell wall and nanopipette. While approach was possible with specific combinations of anion permeability and charge, applying the potential pulse at these heights did not replicate experimental currents. Therefore it is assumed that an anion permeable cell wall model does not provide a realistic representation. This is

considered reasonable because anions would be more effectively excluded from the cell wall than by simply solving the Poisson equation as the reduction of accessible volume will create channels with high stationary negative charge and effective anion exclusion is predicted in the literature.<sup>62</sup> Therefore the exterior of the cell wall, boundary B3b, was set to be impermeable to chloride and  $\mu_{\text{wall}}$  was only applied to potassium.

Electroosmotic flow is not incorporated into these simulations for a number of reasons. Previous work on charge mapping simulations in have shown that EOF has a negligible effect upon the simulated normalised current due to the self-referencing nature of the experiment.<sup>18</sup> Furthermore, the flow properties within the cell wall are usually described by the Brinkman equation:<sup>82</sup>

$$u \nabla u = \frac{1}{\rho} \left( -\nabla p + \frac{\mu}{K} \nabla^2 u - F(\sum_i z_i c_i) \nabla \phi \right) \quad (4.5)$$

where  $K$  is a permeability coefficient which represents the increase in stress due to confinement, tortuosity, and interactions with the channel walls and is on the scale of  $10^{-17}$  for the bacterial cell wall.<sup>63,70</sup> This indicates that fluid flow is severely inhibited within the cell wall and therefore is not expected to significantly contribute to the ionic current response in SICM modalities.

First the experimental working approach distance between the nanopipette and the surface was estimated by steady-state simulations with the boundary at the top of the pipette (Boundary B1, Figure 4.6) held at  $V_{\text{hold}}$ , the distances were taken from the distance at which the ionic current normalized to the bulk current reached the experimental approach set point of a 2% decrease from bulk current. Approach curves for the *E. coli* are presented alongside the corresponding images, approach height was approximately 30 nm. Figure 4.8 shows the approach curve for simulations of *B. subtilis*, with a calculated approach height of 20 nm independent of  $\rho_f$  and  $\mu_{\text{wall}}$ , this corresponds to a glass-substrate separation of approximately 40 nm due to the curvature of the bacterium.

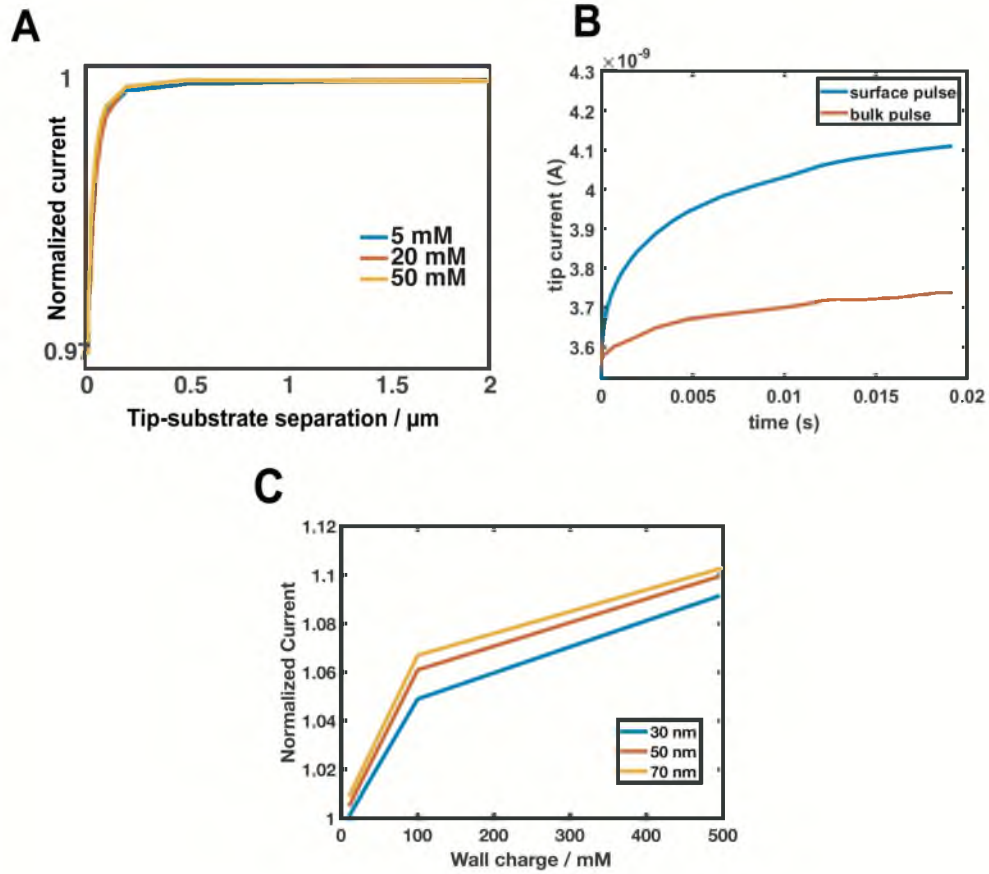


**Figure 4.8 FEM simulations for functional mapping of *B. subtilis*.** (A) Simulated approaches to gram-positive cell walls of various charge density. (B) Example simulated pulses of -500 mV at a wall with 100 mM charge density. (C) The effect of cell wall thickness on simulated normalised currents.

Time dependent simulations of the 20 ms pulse were then performed by stepping the voltage to  $V_{pulse}$ , using the corresponding steady-state approach simulation as starting conditions for the simulation. The same procedure was performed at the bulk retract height and the surface current normalised to the bulk current (Figure 4.6A). For *E. coli* scans the surface charge was then varied to form a calibration plot for surface charge against normalised current at 20 ms which was then used to calibrate each image. For *B. subtilis*, the parameters explored were  $\rho_f$ ,  $\mu_{wall}$ , membrane thickness, and the effect of the periplasmic space. The periplasmic space was added as a domain with various configurations underneath the cell wall domain (D1), the space charge density and electrolyte composition were the same as bulk and

the interface between the two was modelled as both permeable and impermeable to anions. Little is known about the periplasmic space of gram-positive bacteria, however it is assumed to be an area densely packed with charge due to metabolic activity.<sup>31,81</sup> The concentration of mobile electrolyte ions was varied in this space and contributed a small percentage to normalised currents when containing concentrations 10 times that of bulk, suggesting that there could be an effect of transport across the cell wall. However, considering the lack of information about realistic parameterisation of transport into or out of this domain, this data has not been included.

## 4.5 Results and Discussion

To study local bioelectrical properties of the gram-negative and gram-positive bacterial cell envelopes, SICM pulsed-potential and scanned-potential procedures were applied to *E. coli* and *B. subtilis*. Detailed analyses of the bioelectrical response of the bacterial cell envelopes to these perturbations were then performed through FEM simulations.

### 4.5.1 Probing the gram-negative cell envelope: *E. coli*

Pulsed-potential SICM was first applied to live *E. coli* cells adhered to Cell-Tak in 50mM KCl electrolyte. The topographic map shows the bacterium to be  $\sim 2\ \mu\text{m}$  in length and  $\sim 1\ \mu\text{m}$  in height (Figure 4.9a), and the surface charge map reporting surface charge up to  $-140\ \text{mC}/\text{m}^2$  (Figure 4.9b). The morphological features of the bacterium concur with literature values and scanning electron microscopy images (Figure 4.10).<sup>88</sup>

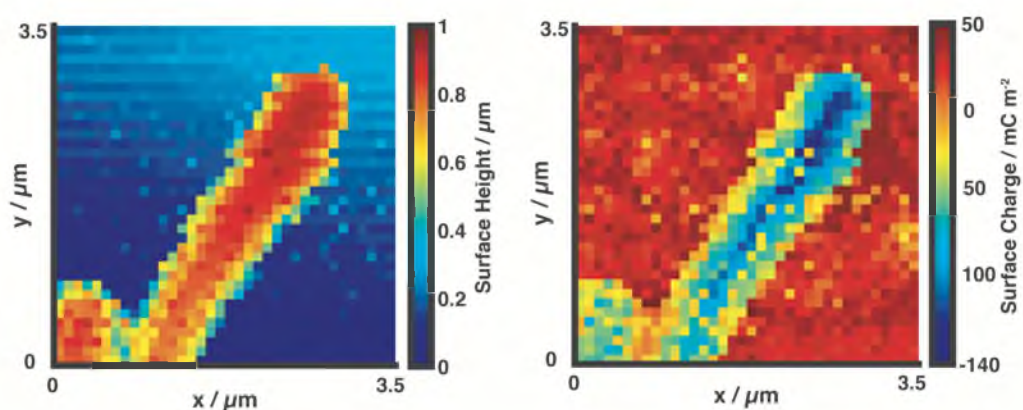


**Figure 4.9** SICM pulsed-potential scan of *E. coli*. (A) SICM topography and (B) local surface charge ( $\text{mC m}^{-2}$ ) following FEM simulation of *E. coli* collected simultaneously.



**Figure 4.10 Scanning Electron Microscopy (SEM) image of *E. coli* (wild type) cell.** Observed on carbon-laced copper TEM grids. EHT= 0.500 kV, Magnification x37950.

The structure of the gram-negative cell envelope provides an interface which is primarily an insulating lipid membrane (Figure 4.1). Therefore SICM scans of *E. coli* were expected to behave in a similar way to previous reports of this technique when applied to mammalian cells and lipid bilayers.<sup>17,25</sup> This is supported by the moderate range of normalised current values experimentally obtained (0.98-1.05, Figure 4.11) from which surface charges were calculated by FEM simulations which treat the surface as a charged insulator (Figure 4.6).<sup>19</sup>

A degree of variation can be observed over the bacteria with a strong topographical correlation, in which the central apex of the bacterium generates a higher normalised current than the curved edges. This differential response is likely to partially be due to the asymmetric tip-substrate separation and resulting surface angle and is generally higher in the regions corresponding most closely to a flat surface.<sup>89</sup> However there are also possible biological origins, bacteria are known to alter their external charge properties depending upon the substrate on which they sit and the resulting distribution of this charge over the bacterial surface is not known.<sup>90</sup> Charge distribution heterogeneities are also clearly observed with the areas of the bacterium with a similar topographical component, with variation between -80 and -140 mC/m<sup>2</sup> over the central apex of the cell.

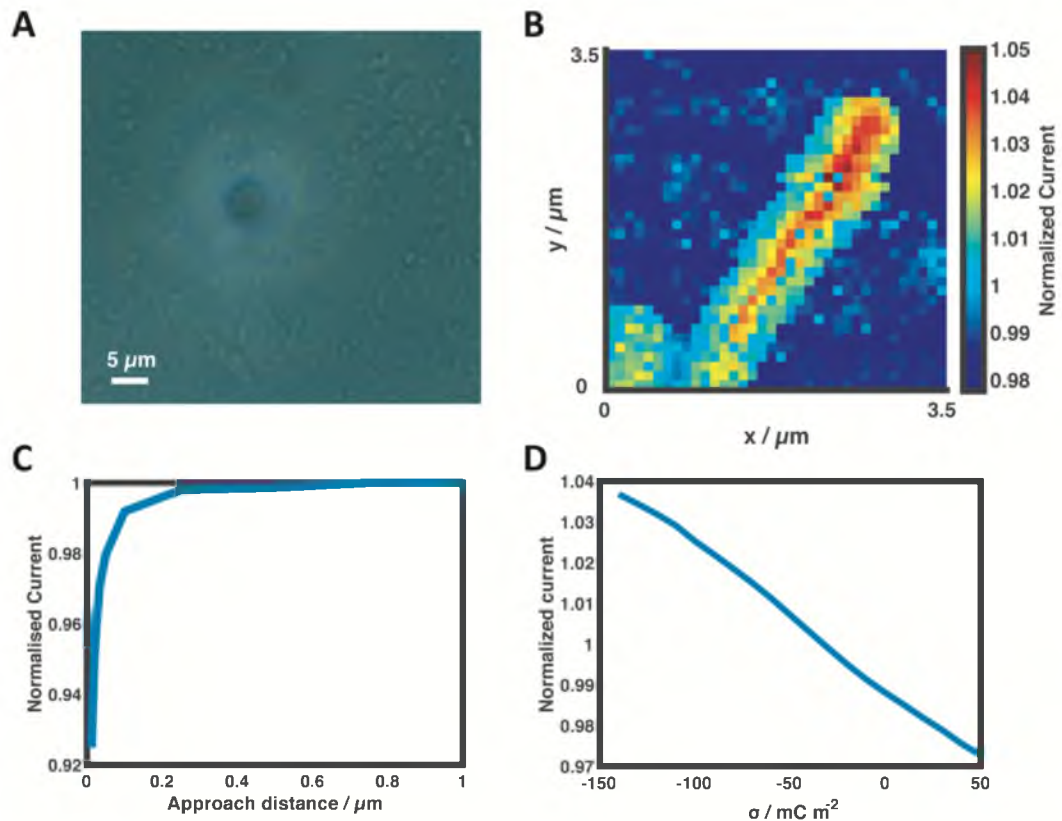


**Figure 4.11 *E. coli* pulsed-potential scan and simulations.** (A) Optical micrograph of the bacteria before scanning, scanned area is within the halo caused by the optical properties of the nanopipette. (B) Normalised current for *E. coli* wild type pulse scan (shown in Figure 4.9), taken from the end of the 20 ms pulse of -500 mV. (C) Simulated approach curve, and (D) calibration curve from FEM simulations to calculate surface charge from normalised current.

Non-topographic heterogeneities could be derived from the structure of the *E. coli* bacterial cell envelope, the ultrastructure structure of which is comprised of an outer membrane, underneath which is the periplasmic space containing the peptidoglycan cell wall, followed by the inner membrane.<sup>91</sup> *E. coli* outer membranes are primarily insulating phospholipid bilayers interspersed with lipopolysaccharides and proteins, forming a three dimensional structure with heterogeneous but generally negative charge density which could contribute to the observed experimental variation.<sup>34</sup> Sub-cellular surficial heterogeneities have also been demonstrated in adherence of *E. coli* to substrates, a phenomena which is highly dependent upon surface charge.<sup>92</sup> Among the outer membrane structures are the bacterial outer membrane porins (Figure 4.1c), these channels are up to 2 nm in diameter and allow

non-specific transport across the membrane, between the external environment and the ion dense periplasmic space.<sup>93,94</sup> However, due to the small pore size, net currents through these are expected to be low unless local pore aggregation occurs, a phenomena which has been reported.<sup>95,96</sup>

It is possible that ion transport through outer membrane channels could be induced by the biases applied within the experimental framework. However, depolarisation of this membrane is not considered to be likely due to the small voltages actually applied to the membrane; due to the high resistance at the pipette lumen (on the order of  $G\Omega$ ), the large majority of the voltage drop is in the first few microns within the pipette (Figure 4.12A).<sup>25</sup> The interfacial potential is therefore only altered by -15 to -25 mV (Figure 4.12B), below the expected depolarisation potential of *E. coli* ion channels ( $\sim$  -50 mV). This highlights the non-invasive nature of SICM functional mapping, however it also suggests that depolarisation potentials are within reach of SICM pulsed-potential measurements and could be exploited in further studies.

Pulsed-potential measurements do not readily distinguish current enhancement due to surface induced rectification from increased local ionic conductivity which could have a number of sources at bacterial interfaces. Ionic fluxes from the surface due to metabolic activity are also possible contributors to the electrochemical response of the bacterial cell, with a large number of redox active complexes present in the cell envelope.<sup>97</sup> Bacterial metabolism is generally dependent upon generation of a proton gradient by pumping of protons into the periplasmic space, there will be a gradient of metabolic and homeostatic products in proximity to the bacterium. We expect the contribution of this to be minimal due to the absence of a carbon source and the sub-isotonic electrolyte concentration driving homeostasis towards ionic retention.<sup>98,99</sup> However, these factors could equally cause a certain degree of cellular stress which has been shown to cause changes in the composition and charge of the bacterial cell envelope. Some contribution to sub-cellular heterogeneities from complex biological pathways and local ionic gradients cannot be ruled out but for the aforementioned reasons we expect the response to be dominated by charge effects.



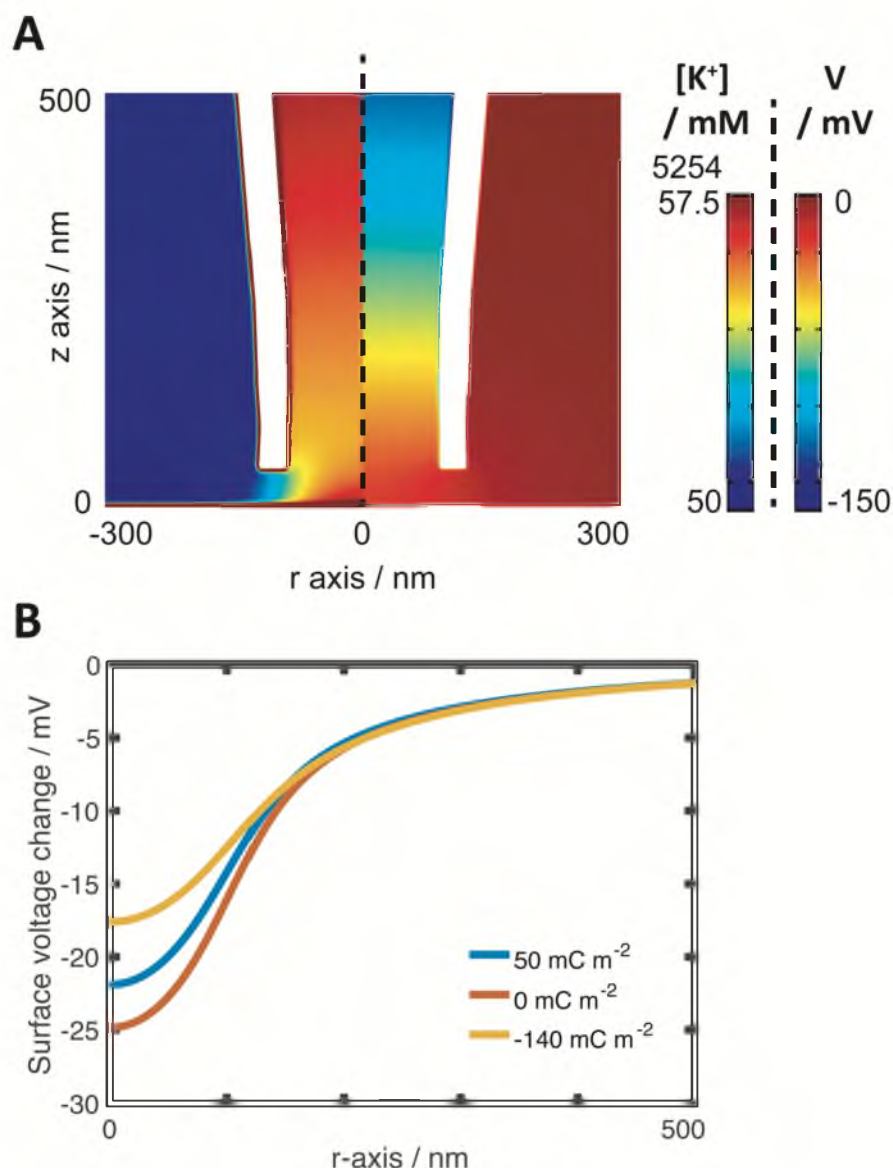


**Figure 4.12 FEM simulation of pulse-potential SICM measurements at charged surfaces.** (A) The  $[K^+]$  (left) at the end of a  $-500 \text{ mV}$  pulse for  $20 \text{ ms}$  at a  $-140 \text{ mC m}^{-2}$  surface, with (right) the corresponding electrostatic potential. Note  $[K^+]$  is presented up to  $57.5 \text{ mM}$  due to the high concentrations in the double layer. (B) The potential changes at differently charged surfaces relative to the equilibrium surface potential, demonstrating a small charge dependent potential drop at the surface.

#### 4.5.2 Scanned-Potential Measurements of Gram-negative *E.coli* Cells

SICM charge mapping capabilities can be further extended by employing a scanned-potential protocol instead (Figure 4.13) of a pulsed one (Figure 4.3). Although resulting in increased scanning times, it provides a greater depth of information about

the system and local ion concentration which can potentially help to elucidate more complex and dynamic processes. To further examine the origin of the currents and observed heterogeneities in the pulsed-potential scans, scanned-potential experiments were implemented in which  $i$ - $V$  curves are generated following approach to the substrate. The  $i$ - $V$  curves provide more information than the  $i$ - $t$  measurements which report mainly that there is a relative increase or decrease in current without giving a voltage dependency.

Figure 4.13 shows the results from the scanned-potential measurements, the topography corresponds well to that observed in other scans (Figure 4.13A). Normalized currents (Figure 4.13B and C) show clear differences between the bacteria and adherent in both the positive and negative extremes of the  $i$ - $V$  curve. The clear contrasts correspond to an enhanced current when surface counterions are driven into the nanopipette and a decreased current when the direction is reversed, indicating surface induced rectification (SIR). This current decrease at positive potentials demonstrates that the bacteria respond in a way similar to previous descriptions of SIR.<sup>19,100</sup> This is reflected in Figure 4.13D which shows the surface  $i$ - $V$  curves at selected pixels over the bacteria and substrate. These  $i$ - $V$  curves also demonstrate deviation from rectification which can be induced by a concentration differential between the inside and outside of the pipette as the high concentrations required would prevent approach to the surface.<sup>101</sup> Figure 4.13D also shows smooth current changes which indicate that voltage gating has not occurred as this would cause a sharp increase in current once the depolarization potential is reached. This shows that pulsed-potential current enhancements are not due to membrane depolarization, and the current response can be attributed mainly to surface charge.

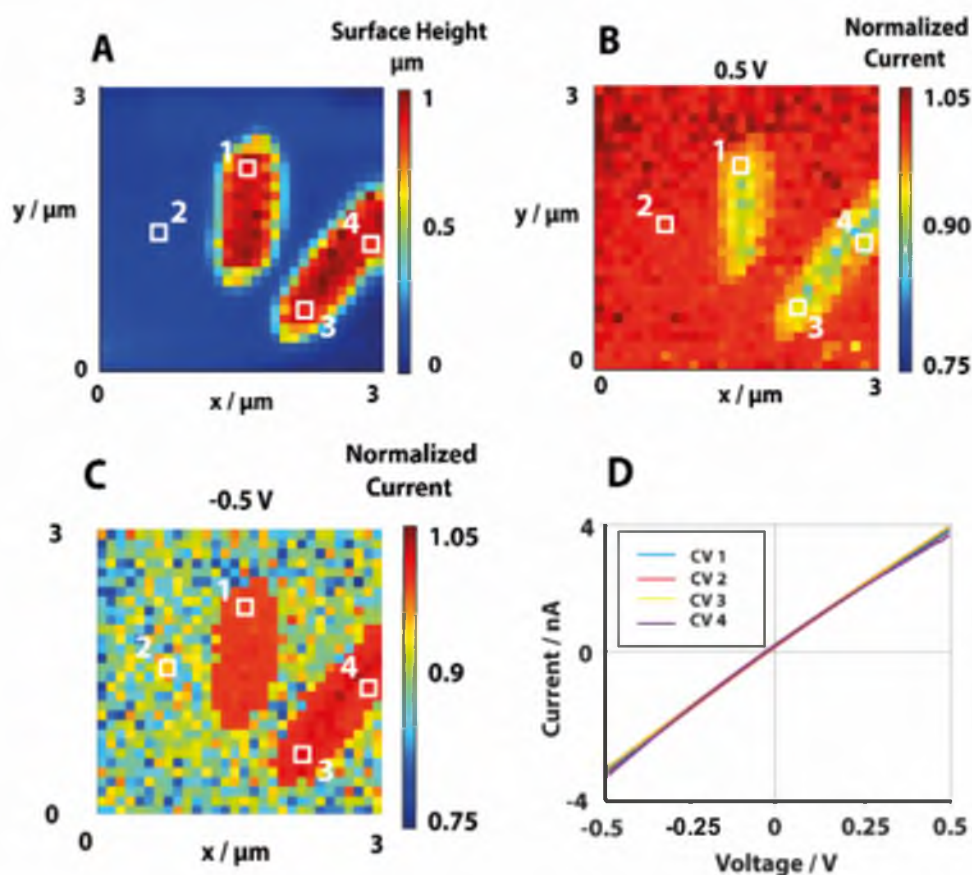


**Figure 4.13 Scanned-Potential SICM mapping of *E. coli*.** (A) Topography and normalised current maps of *E. coli* surface *i-V* curves at the extreme (B) positive and (C) negative potentials, with (D) *i-V* curves at selected pixels.

#### 4.5.3 Probing the gram-positive cell envelope: *B. subtilis*

We now consider experiments performed upon the gram-positive *B. subtilis*; typical pulsed-potential SICM results are displayed in Figure 4.14 and the topography corresponds well with microscopic images (Figure 4.16 - Figure 4.18). Normalized currents (Figure 4.14b) are significantly higher than in the *E. coli* case (Figure 4.11), this implies a high density of stationary negative charge at the interface and can be attributed to differences in the structure of the cell envelope between the gram-negative *E. coli* and the gram-positive *B. subtilis* (Figure 4.1). In this case, the permeable and ion dense peptidoglycan layer is not shielded by an insulating membrane and can therefore be a major contributor to the electrochemical response in SICM experiments. Inter-cellular heterogeneity in both size and normalized current

can easily be observed in Figure 4.14, this could have a number of causes, including microenvironment, cell physiology,<sup>102</sup> population variation, osmoregulation,<sup>98</sup> and differences in cell cycle stage.<sup>103</sup> The same mechanisms could also underpin the sub-cellular heterogeneities which can be observed across each cell.<sup>104</sup> Accessing information about these single entity heterogeneities demonstrate how powerful scanning probe techniques are in the fields of biology and materials science.<sup>6,8</sup>

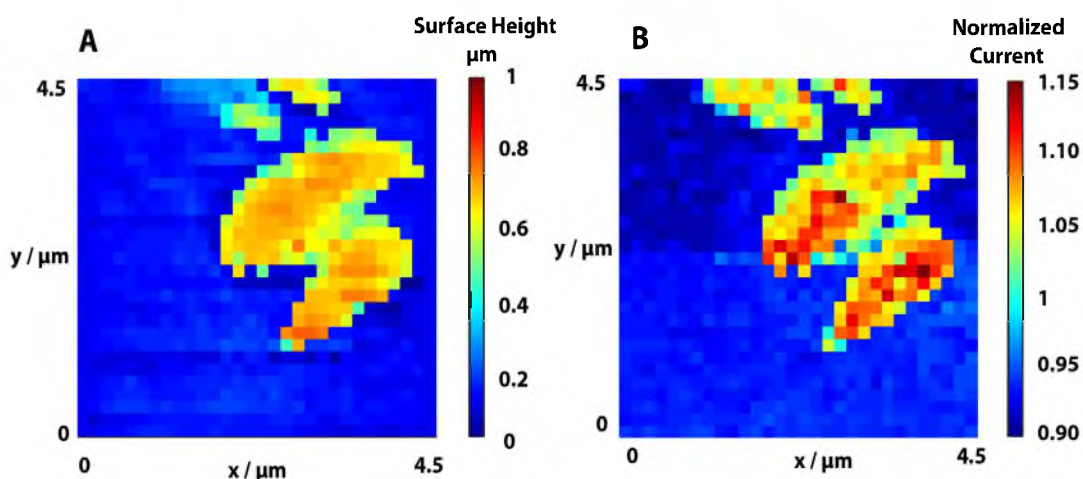


**Figure 4.14** SICM pulsed-potential mapping of *B. subtilis*. SICM topography (A) and normalised current (B) of *B. Subtilis* ( $\Delta$ hag) collected concurrently.

#### 4.5.4 Potential scans across gram-positive *B. subtilis* cells

Figure 4.15 shows the results of scanned-potential mapping for *B. subtilis* *i-V* curves above the bacterium and above the substrate demonstrate similar results to those generated due to surface induced rectification in the literature, indicating that the increased normalised current in pulsed-potential SICM is not due to a general increase in ionic strength near the cell.<sup>21</sup> Although ruled out already due to the low electric field at the pipette tip (Figure 4.12), the smooth rectification profiles provides further evidence that voltage induced depolarisation is not occurring, and no voltage-dependent ion transport mechanism is being gated by either the pulsed or scanned protocol employed herein.

The normalized current maps also exhibit features which do not correlate with the presence of bacteria in the topography map (Figure 4.14 and Figure 4.15), these features are clustered around the bacteria and have a similar current response (however typically to a smaller magnitude/less charged). This is attributed to a complex ion-

permeable matrix secreted by the bacteria, broadly termed the EPS, which we hope to further explore in future study.<sup>105–107</sup>

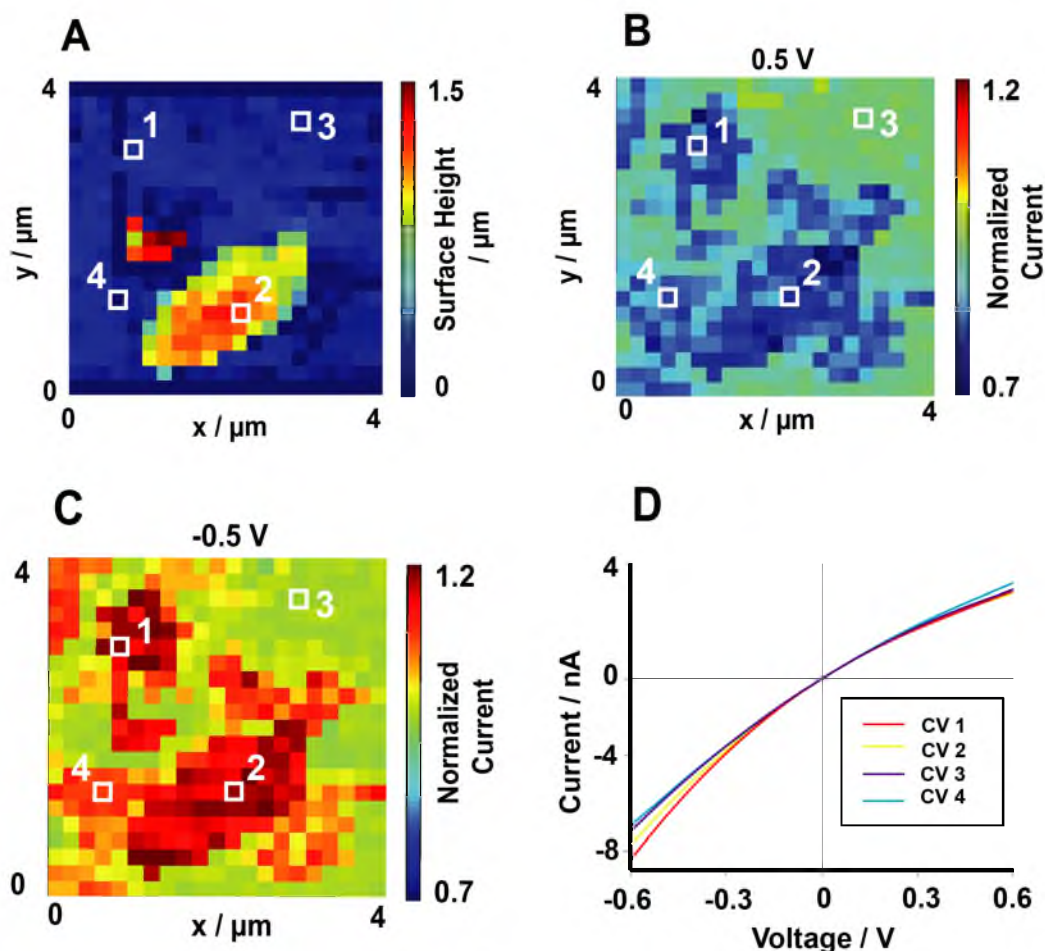


**Figure 4.15** Scanned-potential SICM maps of *B. subtilis*. (A) Topography and normalised current maps of *B. subtilis* surface *i-V* curves at the extreme (B) positive and (C) negative potentials, with (D) *i-V* curves at selected pixels.

EPS consists of polysaccharides, nucleic acids, lipids and polypeptides is released by bacteria,<sup>107,108</sup> and is reported to extend between several nanometres to microns from the cell surface. The EPS is known to aid bacterial adhesion,<sup>106</sup> is crucial in the formation of biofilms,<sup>109</sup> and can act as a nutrient trap.<sup>110</sup> More recently the EPS has been investigated to determine its electroactivity, in particular interest to the redox activity components such as heme-binding proteins, cytochrome-*c* and riboflavins.<sup>105,111</sup>

A coating of this substance explains the similar response between areas on the substrate and the bacterium, it could also contribute to the more homogeneous sub-

cellular response observed over *B. subtilis* compared to *E. coli*. It is worth noting that the EPS layer can be also seen on SEM images taken from the bacteria where a clear charged coating is observed over the cells (Figure 4.16 and Figure 4.17) and from the fluorescence images using an EPS stain (Figure 4.18).

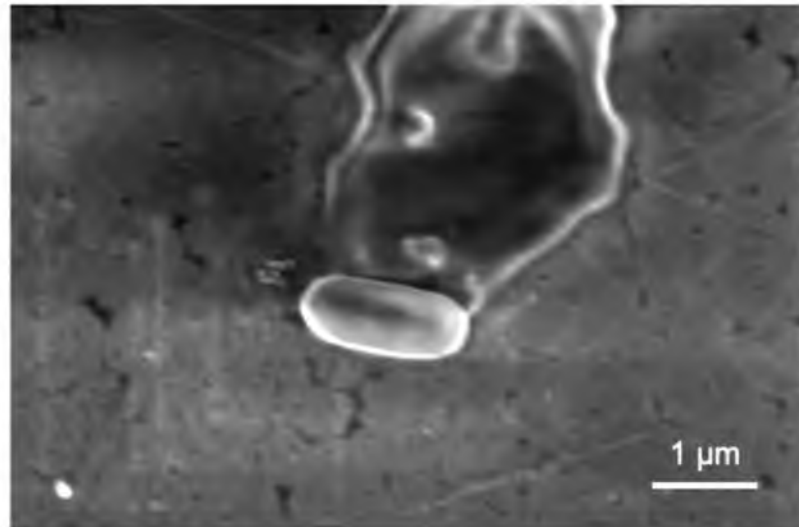


**Figure 4.16 SEM of *B. subtilis* (Δhag).** Observed on carbon-laced copper TEM grids. EHT= 2.00 kV, Magnification x37800.

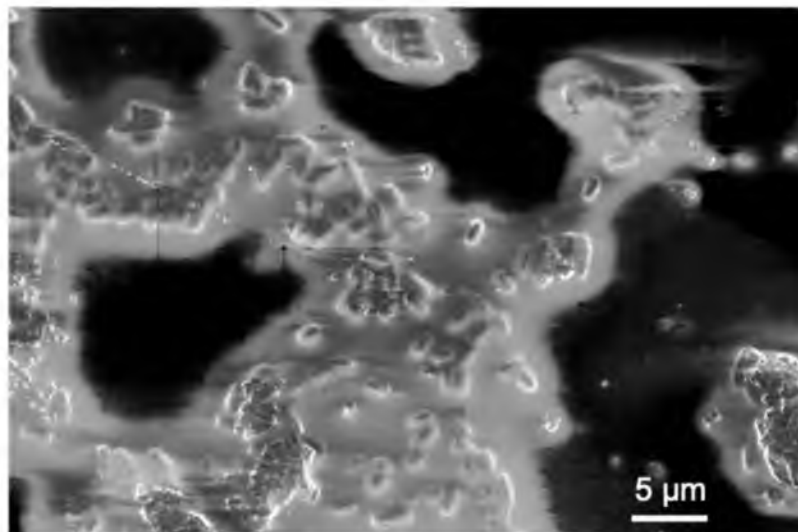


**Figure 4.17 Scanning Electron Microscopy (SEM) image of *B. subtilis* (Δhag).** Observed on carbon-laced copper TEM grids. EHT= 2.00 kV, Magnification x5520.



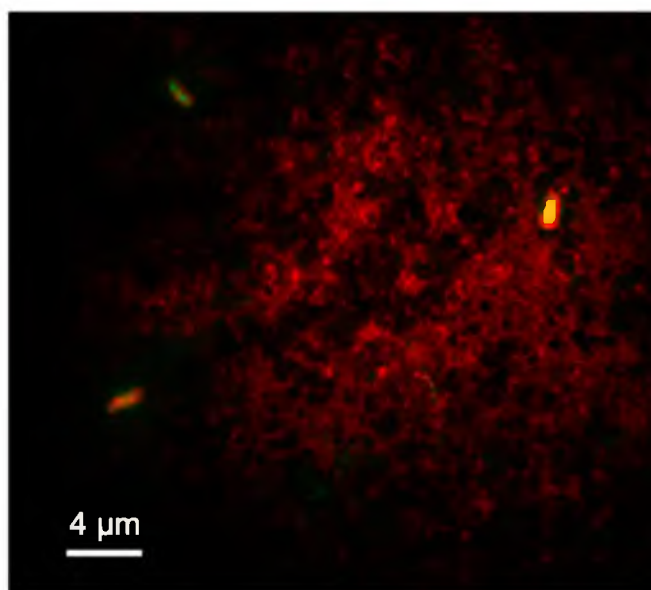


**Figure 4.18 Confocal microscopy of *B. subtilis* ( $\Delta h a g$ ).** Bacteria are stained with Alexa Fluor 594 (red) and SYBR Green (green) to show the location of EPS and bacteria, respectively.

#### 4.5.5 Further studies into the cell envelope-solution interface

To de-convolute the response of the excreted substances from that of the bacterial cell envelope, we used pulsed-potential SICM to investigate a mutant *B. subtilis* strain in which the genes for the *eps* operon; critical for the biosynthesis of the EPS exopolysaccharides have been deleted (*B. subtilis* NCIB 3610 -  $\Delta e p s$ , Asally lab) (Figure 4.19).<sup>75</sup> In these maps the normalised current is higher than when EPS secretion is active (Figure 4.14 and Figure 4.15), indicating that the response was actually dominated by the EPS layer which dampened the response of the cell wall itself. However, it is also possible that the charge in the wall is actually higher in this case due to knock on effects of the mutation or compensation for the lack of EPS by other mechanisms to allow the function of pathways and systems in which it is involved.

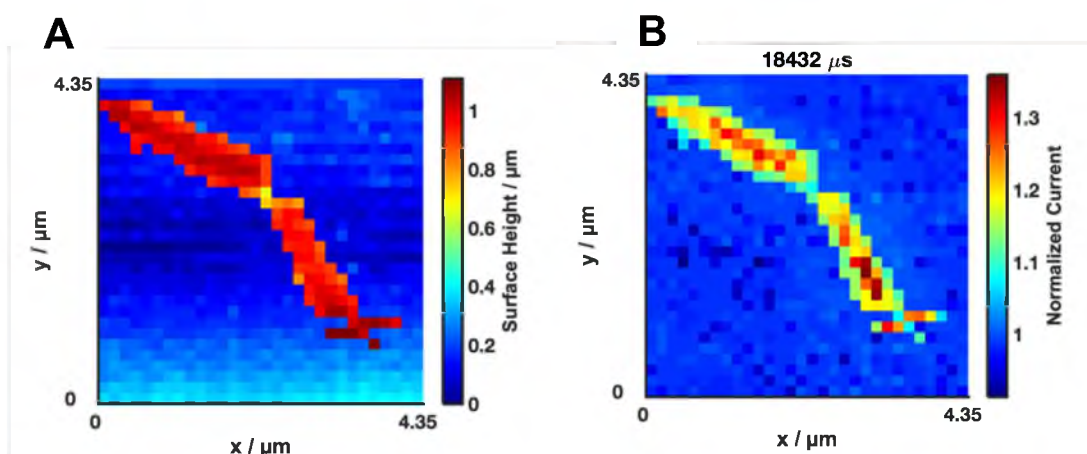


**Figure 4.19 Pulsed-potential SICM of a *B. subtilis* mutant with no EPS.** SICM topography (A) and normalised current (B) of *B. subtilis* collected concurrently.

#### 4.5.6 FEM simulations of the gram-positive cell envelope

The FEM model for the gram-positive bacterial cell wall considered herein was constructed as a semi-permeable domain with a homogeneous distribution of fixed stationary negative charge, and parameterised using literature values (Section 4.12.6). Parameters investigated that could influence the charge distribution were charge concentration ( $\rho_f/F$ ), ion partitioning, effective diffusion coefficient ( $\mu_{wall}D$ ), cell wall thickness, relative permittivity, and periplasmic ion concentrations. The majority of these parameters did not contribute significantly to the ionic current and have therefore not been extensively discussed.

The main contributors to the SICM response were the charge concentration, ion partitioning, and effective diffusion coefficient within the cell wall. The partitioning of  $\text{Cl}^-$  into the cell wall had large effects upon approach simulations, the ionic current approach threshold of 2% could not be obtained when  $\text{Cl}^-$  was able to partition into the cell wall unless mobility of ions was extremely low ( $<0.5$ ) or cell wall charge concentration was extremely high ( $>100$  mM). Pulse simulations at the heights calculated by this method resulted in normalised current values below 1.01, even when the pipette wall was in contact with the cell wall. Excluding  $\text{Cl}^-$  from the cell wall allowed approach independent of charge density and  $\text{K}^+$  mobility due to the increased effective resistance. This is considered a reasonable approximation as the spatial constriction of charges in the polyelectrolyte channels would significantly reduce partitioning of  $\text{Cl}^-$  into the cell wall beyond that of the mean field model used, particularly in relatively low electrolyte concentrations.<sup>62,112,113</sup> Therefore anions



would contribute only very small amounts to the ionic current through the cell wall, we do however acknowledge that this affects the calculated electrostatic potential arising from the Poisson-Nernst-Planck model applied within the cell wall compared to some other theoretical considerations of the cell wall.<sup>63</sup> Electrokinetic measurements have estimated the fixed charge concentration in the *B. subtilis* cell wall to be closer around 20 mM,<sup>83,114</sup> however this is based upon theory which ignores the effects of nanochannels upon partitioning.<sup>115</sup> These simulations suggest that the cell wall is more ion selective than previously considered and the Donnan potentials generated at approximately 100 mM do correspond to expected potentials in the cell wall (Figure 4.20). However, given the uncertainty in the transport phenomena within the wall these simulation results should primarily be taken as demonstrative of contributions from the possible effects in this system.

Figure 4.20A demonstrates the potential at different phases of the scanning procedure, showing that the interior of the cell wall reaches the Donnan equilibrium, the total potential across these interfaces is -17.5 mV for the unperturbed cell wall, -19.0 mV with approach potentials applied, and -9.4 mV when the pulse potential is applied. This is a result of the potential actually applied to the surface after the potential drop over the length of the nanopipette, also demonstrated in Figure 4.12, at the approach bias this potential is 2.16 mV, while at the pulse potential this is approximately -21 mV. This perturbation drives a flux of ions from the cell wall which increases the local ionic conductivity, resulting in the increased normalised currents shown in Figure 4.20B. The resulting  $[K^+]$  is shown in Figure 4.20C and the potential distribution caused by the perturbation and resulting ion flux is shown in Figure 4.20D.

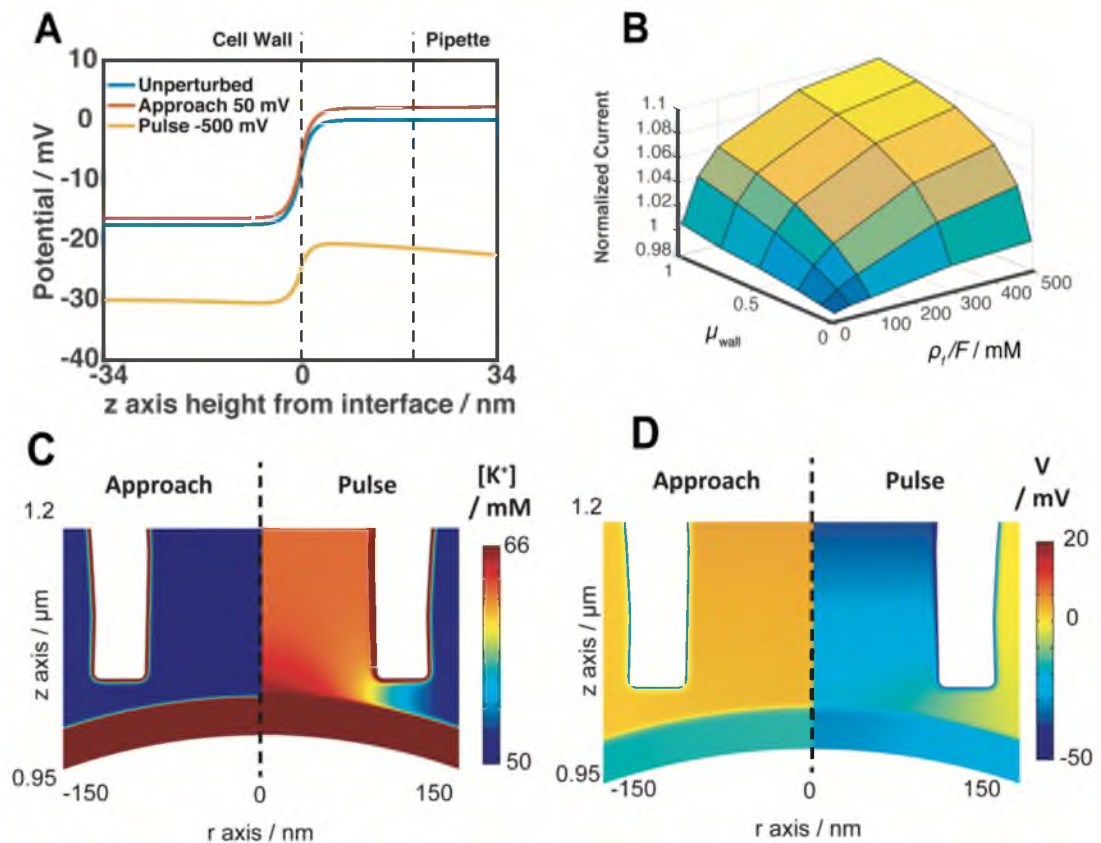


**Figure 4.20 FEM simulations of the pulse-potential SICM at the gram-positive cell wall with charge concentration of 100 mM.** (A) The potential gradient across the cell wall interface (along the axis of rotational symmetry, shown as a dashed line in C and D) with the externally applied potential subtracted. Potentials shown for the unperturbed cell wall (blue, pipette 2  $\mu m$  away), the pipette at the approach distance of 20 nm with the approach potential of +50 mV applied (orange), and at the end of the -500 mV pulse (yellow). (B) Normalised current plotted for combinations of  $\mu_{wall}$  and  $\rho_f/F$  showing diminishing normalised current feedback outside of expected physiological values. (C)  $[K^+]$  distribution and (D) potential gradient at the approach potential (left) and end of the pulse (right).

The normalised currents observed in Figure 4.20B do not correspond to the experimental normalised currents for the  $\Delta eps$  or the  $\Delta hag$  cell wall. The apparent logarithmic dependency of the normalised current upon  $\rho_f/F$  and  $\mu_{wall}$  demonstrates that these values cannot be reached by simply increasing each one and therefore there must be variables which have not been accounted for in this configuration of the

model. Modifying the cell wall thickness (Figure 4.8) causes only minor changes in the simulated normalised currents, suggesting that the technique is mainly sensitive to the interfacial region of the bacterial cell wall. These data suggest that the charge distribution could be an important factor; the interface appears to dominate the response and an enrichment of the charge concentration at the interface would increase the normalised current response. This fits with more detailed views of the bacterial cell envelope as they typically include charged components beyond those involved directly in the cell wall. Fixed glycoproteins and teichoic acids are present (Figure 4.1), and can be extremely densely packed as in the case of an S-layer,<sup>116</sup> this is alongside secretions which may be adhered to the cell surface.<sup>107,110</sup> The cell wall also acts as an ion-selective membrane between the periplasm and the external environment, while the exact composition of the periplasm is unknown, it is likely to be charge dense. It is also responsible for the membrane potential which is used to generate ATP through the proton motive force generating a flux of protons back through the membrane, therefore containing a high concentration of highly mobile charge.<sup>117,118</sup> The flux of ions from the periplasm across the cell wall could therefore contribute to the high currents observed herein.

The main models currently used to describe the bioelectrical properties of the cell wall are insufficient to describe the ion-current response observed in SICM. This indicates that a more complex view of the cell wall must be considered for meaningful interpretation of ion currents at the gram-positive interface. Various components of the bacterial system must be considered which cause charge inhomogeneity within the cell wall for example the existence of S-layers, extracellular polymeric substances, periplasmic contents, and excreted metabolites. The view of a relatively homogeneous cell wall is derived from bulk measurements, causing population and spatial averaging of the response, which must be considered in future work to capture the complexity of the bacterial cell envelope. SICM measurements reported here demonstrate the power to assess individual entities and better understand the charge distribution of a single cell, providing information which can be used to validate models, direct future studies, and help to build a more comprehensive bioelectrical view of the bacterial cell envelope.

#### **4.6 Conclusions**

The ability to interrogate the surface of live bacterial cells by employing different SICM potential scanning protocols is demonstrated. The data collected provide a wealth of information which can be used to assess and verify models of the bacterial cell envelope while also providing information on inter-cellular and sub-cellular heterogeneities. From our findings it is clear that the simplistic view of the cell envelope adopted enlarge is not sufficient to describe the charge nature of the bacterial cell wall and further developments on more comprehensive models are required. A more thorough understanding of the bioelectrical response at the interface of bacterial cells and their environments will benefit a broad range of research areas including bacterial adhesion, antibiotic resistance, and biofilm formation, with a significant impact on life science research and development. The proven ability of SICM to probe charged interfaces with sub-cellular resolution now extends to live bacterial samples and is a key tool towards further development in these fields.

#### 4.7 References.

- 1 P. K. Hansma, B. Drake, O. Marti, S. A. C. Gould and C. B. Prater, *Science*, 1989, **243**, 641–643.
- 2 Y. E. Korchev, L. C. Bashford, M. Milovanovic, I. Vodyanoy and M. J. Lab, *Biophys. J.*, 1997, **73**, 653–658.
- 3 Y. E. Korchev, Y. A. Negulyaev, C. R. W. Edwards, I. Vodyanoy and M. J. Lab, *Nat. Cell Biol.*, 2000, **2**, 616–619.
- 4 M. Miragoli, A. Moshkov, P. Novak, A. Shevchuk, V. O. Nikolaev, I. El-Hamamsy, C. M. F. Potter, P. Wright, S. H. S. A. Kadir, A. R. Lyon, J. A. Mitchell, A. H. Chester, D. Klenerman, M. J. Lab, Y. E. Korchev, S. E. Harding and J. Gorelik, *J. R. Soc. Interface*, 2011, **8**, 913–925.
- 5 A. Page, D. Perry and P. R. Unwin, *Proc. R. Soc. A*, 2017, **473**, 1–34.
- 6 D. Momotenko, K. McKelvey, M. Kang, G. N. Meloni and P. R. Unwin, *Anal. Chem.*, 2016, **88**, 2838–2846.
- 7 M. Kang, D. Perry, C. L. Bentley, G. West, A. Page and P. R. Unwin, *ACS Nano*, 2017, **11**, 44.
- 8 M. Kang, D. Momotenko, A. Page, D. Perry and P. R. Unwin, *Langmuir*, 2016, **32**, 7993–8008.
- 9 C.-C. Chen, Y. Zhou and L. A. Baker, *Annu. Rev. Anal. Chem.*, 2012, **5**, 207–228.
- 10 J. Seifert, J. Rheinlaender, F. Lang, M. Gawaz and T. E. Schäffer, *Nat. Sci. Reports*.
- 11 D. Perry, R. Al Botros, D. Momotenko, S. L. Kinnear and P. R. Unwin, *ACS Nano*, 2015, **9**, 7266–7276.
- 12 K. McKelvey, S. L. Kinnear, D. Perry, D. Momotenko and P. R. Unwin, *J. Am. Chem. Soc.*, 2014, **136**, 13735–13744.
- 13 D. Momotenko, K. McKelvey, M. Kang, G. N. Meloni and P. R. Unwin, *Anal. Chem.*, 2016, **88**, 2838–2846.
- 14 B. Chen, D. Perry, A. Page, M. Kang and P. R. Unwin, *Anal. Chem.*, 2019, **91**, 2516–2524.
- 15 B. Babakinejad, P. Jönsson, A. López Córdoba, P. Actis, P. Novak, Y. Takahashi, A. Shevchuk, U. Anand, P. Anand, A. Drews, A. Ferrer-Montiel, D. Klenerman and Y. E. Korchev, *Anal. Chem.*, 2013, **85**, 9333–9342.

- 16 S. Schobesberger, P. Jönsson, A. Buzuk, Y. Korchev, J. Siggers and J. Gorelik, *Biophys. J.*, 2016, **110**, 141–146.
- 17 C. Zhu, L. Zhou, M. Choi and L. A. Baker, *ChemElectroChem*, 2018, **5**, 2986–2990.
- 18 D. Perry, R. Al Botros, D. Momotenko, S. L. Kinnear and P. R. Unwin, *ACS Nano*, 2015, **9**, 7266–7276.
- 19 D. Perry, B. Paulose Nadappuram, D. Momotenko, P. D. Voyias, A. Page, G. Tripathi, B. G. Frenguelli and P. R. Unwin, *J. Am. Chem. Soc.*, 2016, **138**, 3152–3160.
- 20 A. Page, D. Perry, P. Young, D. Mitchell, B. G. Frenguelli and P. R. Unwin, *Anal. Chem.*, 2016, **88**, 10854–10859.
- 21 N. Sa and L. A. Baker, *J. Am. Chem. Soc.*, 2011, **133**, 45.
- 22 N. Sa, W.-J. Lan, W. Shi and L. A. Baker, *ACS Nano*, 2013, **7**, 11272–11282.
- 23 D. Perry, A. Page, B. Chen, B. G. Frenguelli and P. R. Unwin, *Anal. Chem.*, 2017, **89**, 12458–12465.
- 24 F. M. Maddar, D. Perry, R. Brooks, A. Page and P. R. Unwin, *Anal. Chem.*, 2019, **91**, 4632–4639.
- 25 A. Page, D. Perry, P. Young, D. A. Mitchell, B. G. Frenguelli and P. R. Unwin, *Anal. Chem.*, 2016, **88**, 10854–10859.
- 26 M. Gonsalves, A. L. Barker, J. V. Macpherson, P. R. Unwin, D. O’Hare and C. P. Winlove, *Biophys. J.*, 2000, **78**, 1578–1588.
- 27 A. Navrotsky, *Proc. Natl. Acad. Sci. U. S. A.*, 2004, **101**, 12096–12101.
- 28 H. Liu and H. H. P. Fang, *Biotechnol. Bioeng.*, 2002, **80**, 806–811.
- 29 R. Tedja, M. Lim, R. Amal and C. Marquis, *ACS Nano*, 2012, **6**, 4083–4093.
- 30 A. Adem Bahar, Z. Liu, M. Garafalo, N. Kallenbach and D. Ren, *Pharmaceuticals*, 2015, **8**, 696–710.
- 31 N. Malanovic, *Biochim. Biophys. Acta - Biomembr.*, 2016, **1858**, 936–946.
- 32 A. J. Park, J. P. Okhovat and J. Kim, *Clin. Basic Immunodermatology Second Ed.*, 2017, 81–95.
- 33 T. Koprivnjak, A. Peschel, M. H. Gelb, N. S. Liang and J. P. Weiss, *J. Biol. Chem.*, 2002, **277**, 47636–47644.
- 34 T. J. Silhavy, D. Kahne and S. Walker, *Cold Spring Harb. Perspect. Biol.*, 2010, **2**, 1–16.

- 35 D. J. Müller, D. Fotiadis, S. Scheuring, S. A. Müller and A. Engel, *Biophys. J.*, 1999, **76**, 1101–1111.
- 36 H. J. Wintle, *Meas. Sci. Technol.*, 1997, **8**, 508–513.
- 37 F. Wu, B. Zhou, J. Wang, M. Zhong, A. Das, M. Watkinson, K. A. Hing, D.-W. Zhang and S. Krause, *Anal. Chem.*, 2019, **19**, 5896–5903.
- 38 C. L. Bentley, J. Edmondson, G. N. Meloni, D. Perry, V. Shkirskiy and P. R. Unwin, *Anal. Chem.*, 2019, **91**, 84–108.
- 39 J. Gorelik, A. I. Shevchuk, G. I. Frolenkov, I. A. Diakonov, M. J. Lab, C. J. Kros, G. P. Richardson, I. Vodyanoy, C. R. W. Edwards, D. Klenerman and Y. E. Korchev, *Proc. Natl. Acad. Sci. U. S. A.*, 2003, **100**, 5819–22.
- 40 A. I. Shevchuk, G. I. Frolenkov, D. Sánchez, P. S. James, N. Freedman, M. J. Lab, R. Jones, D. Klenerman and Y. E. Korchev, *Angew. Chemie - Int. Ed.*, 2006, **45**, 2212–2216.
- 41 P. Novak, C. Li, A. I. Shevchuk, R. Stepanyan, M. Caldwell, S. Hughes, T. G. Smart, J. Gorelik, V. P. Ostanin, M. J. Lab, G. W. J. Moss, G. I. Frolenkov, D. Klenerman and Y. E. Korchev, *Nat. Methods*, 2009, **6**, 279–281.
- 42 *Editorial: Single-cell microbiology*, Nature Publishing Group, 2016, vol. 34.
- 43 S. Skylaki, O. Hilsenbeck and T. Schroeder, *Nat. Biotechnol.*, 2016, **34**, 1137–1144.
- 44 B. Tao, L. C. Yule, E. Daviddi, C. L. Bentley and P. R. Unwin, *Angew. Chemie - Int. Ed.*, 2019, **58**, 4606–4611.
- 45 G. Antczak and G. Ehrlich, *Surface Diffusion: Metals, Metal Atoms, and Clusters*, Cambridge University Press, Cambridge, 2010.
- 46 M. Schwab, C. Bergonzi, J. Sakkos, C. Staley, Q. Zhang, M. J. Sadowsky, A. Aksan and M. Elias, *Front. Microbiol.*, 2019, **10**, 611.
- 47 P. Sierocinski, F. Bayer, G. Yvon-Durocher, M. Burdon, T. Großkopf, M. Alston, D. Swarbreck, P. J. Hobbs, O. S. Soyer and A. Buckling, *Mol. Ecol.*, 2018, **27**, 4641–4651.
- 48 O. Gefen and N. Q. Balaban, *FEMS Microbiol. Rev.*, 2009, **33**, 704–717.
- 49 S. El-Kirat-Chatel, A. Puymège, T. H. Duong, P. V. Van Overtvelt, C. Bressy, L. Belec, Y. F. Dufrêne and M. Molmeret, *Front. Microbiol.*, , DOI:10.3389/fmicb.2017.01399.
- 50 C. W. Shields, C. D. Reyes, G. P. López and P. G. P. López, *Lab Chip*, 2015,

- 15**, 1230–49.
- 51 S. C. Bendall, E. F. Simonds, P. Qiu, E.-A. D. Amir, P. O. Krutzik, R. Finck, R. V Bruggner, R. Melamed, A. Trejo, O. I. Ornatsky, R. S. Balderas, S. K. Plevritis, K. Sachs, D. Pe'er, S. D. Tanner and G. P. Nolan, *Science* (80-. ), 2011, **332**, 687–696.
  - 52 D. Hebenstreit, *Biology (Basel)*., 2012, **1**, 658–667.
  - 53 A. Wagner, A. Regev and N. Yosef, *Nat. Biotechnol.*, 2016, **34**, 1145–1160.
  - 54 A. S. Stender, K. Marchuk, C. Liu, S. Sander, M. W. Meyer, E. A. Smith, B. Neupane, G. Wang, J. Li, J. X. Cheng, B. Huang and N. Fang, *Chem. Rev.*, 2013, **113**, 2469–2527.
  - 55 J. Y. Wong, R. Langer and D. E. Ingber, *Proc. Natl. Acad. Sci. U. S. A.*, 1994, **91**, 3201–4.
  - 56 H. J. Busscher and H. C. van der Mei, *PLoS Pathog.*, 2012, **8**, e1002440.
  - 57 H. C. Gram, *DMW - Dtsch. Medizinische Wochenschrift*, 1884, **10**, 234–235.
  - 58 R. Coico, in *Current Protocols in Microbiology*, John Wiley & Sons, Inc., Hoboken, NJ, USA, 2005, vol. Appendix 3, p. Appendix 3C.
  - 59 T. J. Beveridge and J. A. Davies, *J. Bacteriol.*, 1983, **156**, 846–58.
  - 60 W. A. Corpe, in *Adhesion in biological systems*, ed. R. S. Manly, Academic Press, Inc., New York, 1970.
  - 61 J. S. Dickson and M. Koohmaraie, *Appl. Environ. Microbiol.*, 1989, **55**, 832–836.
  - 62 A. Van Der Wal, W. Norde, A. J. B. Zehnder and J. Lyklema, *Colloids Surfaces B Biointerfaces*, 1997, **9**, 81–100.
  - 63 J. F. L. Duval and F. Gaboriaud, *Curr. Opin. Colloid Interface Sci.*, 2009, **15**, 184–195.
  - 64 X. X. Sheng, Y. P. Ting and S. O. Pehkonen, *J. Colloid Interface Sci.*, , DOI:10.1016/j.jcis.2008.02.038.
  - 65 Y. H. An and R. J. Friedman, *J. Biomed. Mater. Res.*, 1998, **43**, 338–348.
  - 66 T. J. Beveridge, *Int. Rev. Cytol.*, 1981, **72**, 229–317.
  - 67 J. Dankert, A. H. Hogt and J. Feijen, *Crit. Rev Biocompat*, 1986, **2**, 219–301.
  - 68 H. H. M. Rijnaarts, W. Norde, J. Lyklema and A. J. B. Zehnder, *Colloids Surfaces B Biointerfaces*, 1995, **4**, 191–197.
  - 69 M. C. M. van Loosdrecht, W. Norde, J. Lyklema and A. J. B. Zehnder, *Aquat.*



- Sci.*, 1990, **52**, 103–114.
- 70 F. Gaboriaud, M. L. Gee, R. Strugnell and J. F. L. Duval, *Langmuir*, 2008, **24**, 10988–10995.
  - 71 H. Ohshima, *Sci. Technol. Adv. Mater*, 2009, **10**, 13.
  - 72 J. F. L. Duval and F. Gaboriaud, *Curr. Opin. Colloid Interface Sci.*, 2010, **15**, 184–195.
  - 73 S. S. Dukhin, R. Zimmermann, J. F. L. Duval and C. Werner, *J. Colloid Interface Sci.*, 2010, **350**, 1–4.
  - 74 S. Mukherjee, P. Babitzke and D. B. Kearns, *J. Bacteriol.*, 2013, **195**, 297–306.
  - 75 D. B. Kearns, F. Chu, S. S. Branda, R. Kolter and R. Losick, *Mol. Microbiol.*, 2005, **55**, 739–749.
  - 76 M. Ehrenberg, H. Bremer and P. P. Dennis, *Biochimie*, 2013, **95**, 643–658.
  - 77 J. W. Young, J. C. W. Locke, A. Altinok, N. Rosenfeld, T. Bacarian, P. S. Swain, E. Mjolsness and M. B. Elowitz, *Nat. Protoc.*, 2012, **7**, 80–88.
  - 78 C. Zerfaß, J. A. Christie-oleza and O. S. Soyer, *bioRxiv*, , DOI:10.1101/294975.
  - 79 D. Perry, D. Momotenko, R. A. Lazenby, M. Kang and P. R. Unwin, *Anal. Chem.*, 2016, **88**, 5523–5530.
  - 80 A. Page, D. Perry and P. R. Unwin, *Proc. R. Soc. A*, 2017, **473**, 1–34.
  - 81 V. R. F. Matias and T. J. Beveridge, *Mol. Microbiol.*, 2005, **56**, 240–251.
  - 82 S. S. Dukhin, R. Zimmermann, J. F. L. Duval and C. Werner, *J. Colloid Interface Sci.*, 2010, **350**, 1–4.
  - 83 S. Okuda, R. Igarashi, Y. Kusui, Y. Kasahara and H. Morisaki, *J. Bacteriol.*, 2003, **185**, 3711–3717.
  - 84 D. Esteban-Ferrer, M. A. Edwards, L. Fumagalli, A. Juárez and G. Gomila, 2019, **13**, 9.
  - 85 R. E. Beck and J. S. Schultz, *BBA - Biomembr.*, 1972, **255**, 273–303.
  - 86 P. Demchick and A. L. Koch, *J. Bacteriol.*, 1996, **178**, 768–773.
  - 87 J. Cervera, P. Ramírez, J. A. Manzanares and S. Mafé, *Microfluid Nanofluid*, 2010, **9**, 41–53.
  - 88 D. G., *Introduction to Biochemical Engineering*, Tata McGraw-Hill, 2005.
  - 89 S. Del Linz, E. Willman, M. Caldwell, D. Klenerman, A. Fernández and G. Moss, *Anal. Chem.*, 2014, **86**, 2353–60.
  - 90 Y. Hong and D. G. Brown, *Appl. Environ. Microbiol.*, 2009, **75**, 2346–2353.

- 91 T. J. Silhavy, D. Kahne and S. Walker, *Cold Spring Harb. Perspect. Biol.*, 2010, **2**, 414.
- 92 T. Vissers, A. T. Brown, N. Koumakis, A. Dawson, M. Hermes, J. Schwarz-Linek, A. B. Schofield, J. M. French, V. Koutsos, J. Arlt, V. A. Martinez and W. C. K. Poon, *Sci. Adv.*, 2018, **4**, eaao1170.
- 93 O. D. Novikova and T. F. Solovyeva, *Biochem. Suppl. Ser. A Membr. Cell Biol.*, 2009, **3**, 3–15.
- 94 H. Nikaido, *J. Biol. Chem.*, 1994, **269**, 3905–3908.
- 95 D. Drew, L. Fröderberg, L. Baars and J.-W. L. de Gier, *Biochim. Biophys. Acta - Biomembr.*, 2003, **1610**, 3–10.
- 96 B. Martinac, M. Buechner, A. H. Delcour, J. Adler and C. Kung, *Proc. Natl. Acad. Sci. U. S. A.*, 1987, **84**, 2297–2301.
- 97 M. Babu, C. Bundalovic-Torma, C. Calmettes, S. Phanse, Q. Zhang, Y. Jiang, Z. Minic, S. Kim, J. Mehla, A. Gagarinova, I. Rodionova, A. Kumar, H. Guo, O. Kagan, O. Pogoutse, H. Aoki, V. Deineko, J. H. Caufield, E. Holtzapple, Z. Zhang, A. Vastermark, Y. Pandya, C. C. Lai, M. El Bakkouri, Y. Hooda, M. Shah, D. Burnside, M. Hooshyar, J. Vlasblom, S. V Rajagopala, A. Golshani, S. Wuchty, J. F Greenblatt, M. Saier, P. Uetz, T. F Moraes, J. Parkinson and A. Emili, *Nat. Biotechnol.*, 2018, **36**, 103–112.
- 98 J. M. Wood, *J. Gen. Physiol.*, 2015, **145**, 381–388.
- 99 A. Ly, J. Henderson, A. Lu, D. E. Culham and J. M. Wood, *J. Bacteriol.*, 2004, **186**, 296–306.
- 100 C. Zhu, L. Zhou, M. Choi and L. A. Baker, *ChemElectroChem*, 2018, **5**, 2986–2990.
- 101 L. Cao, W. Guo, Y. Wang and L. Jiang, *Langmuir*, 2012, **28**, 2194–2199.
- 102 E. M. Sonnenfeld, T. J. Beveridge and R. J. Doyle, *Can. J. Microbiol.*, 1985, **31**, 875–7.
- 103 A. Treuner-Lange and L. Søgaaard-Andersen, *J. Cell Biol.*, 2014, 206, 7–17.
- 104 J. Y. Wong, R. Langer and D. E. Ingber, *Proc. Natl. Acad. Sci. U. S. A.*, 1994, **91**, 3201–4.
- 105 Y. Xiao, E. Zhang, J. Zhang, Y. Dai, Z. Yang, H. E. M. Christensen, J. Ulstrup and F. Zhao, *Sci. Adv.*, 2017, **3**, e1700623.
- 106 S. Tsuneda, H. Aikawa, H. Hayashi, A. Yuasa and A. Hirata, *FEMS Microbiol.*

- Lett.*, 2003, **223**, 287–292.
- 107 H.-C. Flemming, *Microorganisms*, 2016, **4**, 41.
  - 108 H.-C. Flemming, J. Wingender, U. Szewzyk, P. Steinberg, S. A. Rice and S. Kjelleberg, *Nat. Publ. Gr.*, , DOI:10.1038/nrmicro.2016.94.
  - 109 S. Jachlewski, W. D. Jachlewski, U. Linne, C. Bräsen, J. Wingender and B. Siebers, *Front. Bioeng. Biotechnol.*, 2015, **3**, 1–11.
  - 110 A. Harimawan and Y. P. Ting, *Colloids Surfaces B Biointerfaces*, 2016, **146**, 459–467.
  - 111 S.-W. Li, G.-P. Sheng, Y.-Y. Cheng and H.-Q. Yu, *Nat. Publ. Gr.*, , DOI:10.1038/srep39098.
  - 112 F. Baldessari and J. G. Santiago, *J. Nanobiotechnology*, 2006, **4**, 12.
  - 113 A. Plecis, R. B. Schoch and P. Renaud, *Nano Lett*, 2005, **5**, 1147–1155.
  - 114 N. S. V Barbosa, E. R. A. Lima and F. W. Tavares, *Colloids Surfaces B Biointerfaces*, 2015, **134**, 447–452.
  - 115 H. Ohshima, *Curr. Opin. Colloid Interface Sci.*, 2013, **18**, 73–82.
  - 116 M. S. Sidhu and I. Olsen, *Microbiology*, 1997, **143**, 1039–1052.
  - 117 Y. Hong and D. G. Brown, *Appl. Environ. Microbiol.*, 2009, **75**, 2346–53.
  - 118 A. K. Khittrin, K. A. Khittrin and M. A. Model, *Chem. Phys. Lipids*, 2014, **184**, 76–81.

## 5 Conclusions and Outlook

SICM is a powerful technique which is able to access nanoscale information about the properties and processes at surfaces and interfaces. The work presented in this thesis builds upon SICM functional mapping techniques to facilitate the application of them to complex interfaces. The combination of experimental information with FEM modelling has been used to provide further understanding of the mechanisms which contribute to the SICM functional mapping response across a range of interfaces.

Chapter 2 presents an extensive study of the effects of substrate charge and reactivity upon EOF in the SICM regime. This improves understanding of the application of SICM delivery methodologies which employ EOF to control the flux of delivered species from the nanopipette. EOF at the tip-substrate interface was shown to be heavily influenced by the surface charge of the substrate at close approach distances, while larger tip-substrate separations result in less localised delivery. The effects of this and the surface reactivity were shown to influence delivered quantities during holding procedures. During delivery pulses the EOF was extremely dependent upon the surface charge, resulting in surface induced flow separation which has not previously been described. While this flow separation may not be as extreme in all cases, the effects upon delivery of neutral species are significant.

These factors are new considerations for SICM delivery protocols which have mostly assumed the fluxes from the nanopipette to be independent of the surface properties. SICM delivery protocols are generally applied to cells at which the local surface charge and surficial uptake is known to be heterogeneous and could therefore affect delivered quantities. This methodology is increasingly being applied to other substrates such as electrodes and catalysts for which accurate determination of local heterogeneous rate constants are important. Therefore, these new considerations are important when designing and interpreting SICM delivery experiments.

Future work in this area should incorporate surface charge for quantitative simulations of neutral species delivery and could be used for simultaneous surface charge and reaction mapping. This work also shows that the transport across the surface is important, diffusional broadening is significant and characterisation of the system may allow more information to be acquired. Further analysis of the ionic and substrate current transients during and after delivery could also be used to provide

information about the local transport and reactivity. With improvement of the sensitivity of detection in the ion current, the changes in local ionic conductivity due to surface reactions could be measured and quantified through the normalised ionic current. This would require scanning of the same sample without the neutral species present to control for differences in surface charge.

Chapter 3 builds upon delivery procedures for the controlled delivery of protons to induce dissolution of a surface while simultaneously tracking the resulting topographical changes. FEM simulations have proven valuable in understanding the underlying processes involved in the simultaneous dissolution and tracking of a surface. This has allowed calculation of the effective heterogeneous rate constants for the resulting dissolution reaction under different conditions. Comprehensive consideration of the reactions occurring allows the resulting buffering and fluxes from the surface to be taken into account. We have shown that the DM-SICM feedback is relatively insensitive to these processes allowing accurate tracking of the surface by maintaining tip-substrate separation. The high sensitivity of the DM-SICM feedback to the surface position and the control over proton delivery means that it can be tuned to track etching over a wide range of rates, from mainly surface sensitivity to rates limited by surface kinetics.

The power of this surface etching technique has been shown by the determination of the effects of different surface treatments upon effective heterogeneous rate constants for enamel dissolution. Combining this technique with other multifunctional or correlative microscopy techniques could allow for understanding of the underlying causes of the observed heterogeneities in this system. Linking the heterogeneities in the enamel response to the properties of the system could be possible through measurement of the relative hydroxyapatite and protein contents of individual sites. This technique is incredibly effective for nanoscale measurements of the dissolution process and could be applied to a wide range of complex substrates. Considering the flexibility of solutions with which the nanopipette can be filled, this could be used to investigate the dissolution of pharmaceutical formulations by biologically relevant solutions. It could also be possible to measure the response of metals to accelerated localised corrosion with the metal substrate grounded or at defined potentials or to deliver solutions to actively induce and track crystallisation.

The application of multiple functional SICM mapping methodologies to live bacteria was achieved in Chapter 4 to map of the bacterial bioelectrical response at the nanoscale for the first time. The underlying processes of the SICM response at live microorganisms has a wide range of possible contributing factors and FEM simulations were used to assess the underlying contributions. The strength of the SICM functional mapping perturbation to the surface was calculated by FEM and through this the expected effects upon substrate could be assessed. It was shown that the response at gram-negative bacteria is likely to be largely dominated by the surface charge due to their insulating outer cell membrane. Through these considerations the non-invasive nature of SICM functional mapping was demonstrated and it was indicated that significant perturbations could be generated if required to access more information from the substrate.

Gram-positive bacteria represent a much more complex challenge due to the large number of factors which contribute to the ionic currents through and near the cell envelope. The effects of mobility and charge density were shown to be insufficient to explain the bioelectrical response of the gram-positive cell wall. This suggests that more complex considerations of the gram-positive cell envelope are required to explain the response in SICM functional mapping, and that there is more to learn about the structure and function of the gram-positive cell envelope. This demonstrates the power of combined SICM methodologies supported by extensive theoretical consideration of the interfacial response.

SICM delivery and charge mapping could be combined to examine the effects of drugs or antibiotics upon the surface charge. This could also be combined with SECM measurement techniques to allow the simultaneous measurement of metabolites. In order to further understand the mechanisms underlying the SICM response of gram-positive bacteria it is necessary to further understand the system. Understanding of the SICM response at more simple polyelectrolyte materials would allow the flow characteristics in charged permeable layers to be properly characterised and then applied in more complex systems like the ones herein. This could be achieved with 3D SICM by measuring the ionic current response at multiple set distances from the surface, especially if a porous polymer of known charge density could be used. Similar information could be gained by using SICM-SECM, delivery of a fluorescent dye into the material, or by delivery-collection methodologies similar to Chapter 1

with permeable layer on top of an electrode. To fully understand the possible topographic effects of the bacterial cells upon the SICM response it is also necessary to build three-dimensional FEM simulations. The bacterial cells themselves could also be manipulated through the use of mutants or drugs to regulate the metabolic state of the bacteria to elucidate the contribution of ionic fluxes.

In summary, this work extends the application of SICM functional mapping to more complex substrates, providing methodologies and frameworks for the implementation of SICM functional mapping in real-world systems. In these systems combined experimental and theoretical approaches are invaluable for deconvoluting the underlying mechanisms. The multifunctional mapping capabilities of SICM can be used to provide complementary information which allows further understanding of interfaces *in situ*. This is shown to be extremely useful for investigation of a variety of medically and commercially relevant interfaces, with scope for expansion into a variety of disciplines. The continued development of this powerful, multifunctional mapping technique is a growing field which has a wide range of applications which are beginning to be realised.